CRANFIELD UNIVERSITY

SCHOOL OF ENGINEERING

PhD THESIS

Academic Year 2007-2008

GEORGIOS C. DOULGERIS

Modelling & Integration of Advanced Propulsion Systems

Supervisor: Pericles Pilidis

March 2008

Abstract

This research study focuses on the design of advanced propulsion cycles, having as primary design goal the improvement on noise emissions and fuel consumption. In this context, a preliminary cycle design method has been developed and applied on four novel propulsion systems; ultra high bypass ratio, recuperated, intercooled-recuperated, constant volume combustion turbofans. The analysis has shown significant improvement in jet noise, and fuel consumption, as a result of high bypass ratio. Additionally, a comparison to future fuel-optimised cycle has revealed the trade-off between noise emissions and fuel consumption, where a reduction of ~30dBs in jet noise may be achieved in the expense of ~10% increase of mission fuel.

A second aspect of this study is the integration of the propulsion system for improving fan noise. A novel approach is followed, by half-embedding the turbofan in the upper surface of the wing of a Broad Delta airframe. Such an installation aids in noise reduction, by providing shielding to component (fan) noise. However, it leads to significant inlet distortion levels. In order to assess the effect of installation-born distortion on performance an enhanced fan representation model has been developed, able to predict fan and overall engine performance sensitivity to three-dimensional distorted inlet flow. This model that comprises parallel compressor theory and streamline curvature compressor modelling, has been used for proving a linear relation between the loss in fan stability margins and engine performance. In this way, the design engineer can take into consideration distortion effects on off-design performance, as early as, at the stage of preliminary cycle design.

Acknowledgements

First of all, I would like to express my gratitude to my supervisor and mentor, Professor Pilidis, for his continuous support, in every aspect, over these three years.

My special thanks go to Sunil Mistry, with whom we have spent loads of hours during this study and it has been a real pleasure working with him.

Additionally, I would like to thank Professor Kalfas, for all his psychological support during this ‘difficult’ period in Cranfield.

I feel really lucky for meeting certain people during my stay in Cranfield. Thank you Costas and Kostas for all the good and bad times we had together.

I would, also, like to thank Friederike Mund for the excellent, pleasant cooperation we had while working together. Additionally, all the people (MSc and exchange students) that have worked closely with me in the past years and made this project a success:

Dos Santos Mauricio
Medicina Diego
Truffi Daniele
Rousselot Sylvain
Javed Adeel
Nettis Dino

My special gratitude goes, of course, to my family; my parents Christos and Irini and my brother Panos, for helping me take this step to England, supporting me and tolerating me during the past 26 years. Finally, I would like to thank Katerina for invading in my life.

List of Contents

List of Figures

List of Tables

Notation

Abbreviations

AIP	Aerodynamic Inlet Plane
ANCF	Active Noise Control Fan
AR	Aspect Ratio
BPR	By-Pass Ratio
BD	Broad Delta
BDVT	Broad Delta V-Tail
BWB	Blended Wing Body
CFD	Computational Fluid Dynamics
COT	Combustor Outlet Temperature [K]
CVC	Constant Volume Combustion
CW	Compressor Work
DP	Design Point
EAS	EquiAngle Skew
EPNL	Effective Perceived Noise Levels
EVS	EquiSize Skew
FAA	Federal Aviation Administration
FAR	Federal Aviation Regulation
FPR	Fan Pressure Ratio
GT	Gas Turbine
HPC	High Pressure Compressor
IPC	Intermediate Pressure Compressor
LPT	Low Pressure Turbine
MDO	Multi Disciplinary Optimisation
MFR	Mass Flow Ratio
MTOW	Maximum Take-Off Weight
OD	Off Design

OF	Objective Function
OPR	Overall Pressure Ratio
OEW	Operational Empty Weight
PaCo	Parallel Compressor
PNLT	Perceived Noise Levels Tone Corrected
PRF	Pressure Recovery Factor
SAI	Silent Aircraft Initiative
SF	Sensitivity Factor
SLC	StreamLine Curvature
SM	Surge Margin
SPL	Sound Pressure Level
SFC	Specific Fuel Consumption
ST	Specific Thrust
ToC	Top of Climb
TTDF	Tip Turbine Driven Fan
UHBPR	Ultra High Bypass Ratio

Symbols

AP_{noise}	Accoustic Power
C_p	Specific Heat Capacity at Constant Pressure
D_M	Maximum Diameter
D_H	Highlight Diameter
dB	DeciBel
K	Distortion Index
KS_{PR}	Pressure Ratio Sensitivity Factor
KS_{MF}	Mass Flow Sensitivity Factor
L_F	Total Forebody Length
M	Mach Number
M_D	Drag Rise Mach Number
$M_{D,A}$	Afterbody Drag Rise Mach Number

n_p	Polytropic Efficiency
n_{prop}	Propulsive Efficiency
n_{th}	Thermal Efficiency
n_{ov}	Overall Efficiency
P	Pressure [Pa]
R	Gas Constant
R_A	Afterbody Circular Arc Radius
Rc	Compressor Pressure Ratio
Rf	Fan Pressure Ratio
T	Temperature [K]
V	Velocity
W	Mass Flow [kg/s]
α	Speed of Sound
γ	Ratio of Specific Heat Capacities
θ_{crit}	Critical sector angle
ΔPRS	Loss in surge pressure ratio
ΔT_{rec}	Recuperator temperature drop
ΔWS	Loss in surge mass flow

Subscripts

$_t$	Total
$_s$	Static

Engine Stations

$_0$	Far Upstream
$_1$	Nacelle Highlight
$_2$	Fan Face
$_3$	IPC Inlet

4	Intercooler Inlet
4.1	HPC Inlet
5	Recuperator Inlet
6	Combustor Inlet
7	Combustor Outlet
8	HPT Inlet
9	IPT Inlet
10	LPT Inlet
11	Recuperator Hot Part Inlet
12	Nozzle Inlet
13	Nozzle Exit

1 Introduction

The major propulsion system in modern aviation is the gas turbine. Whether in military or civil applications, the gas turbine dominates, mainly, due to its high compactness and ability of operation under extreme conditions –altitude and speed. Moreover, it is expected to continue serving aviation, at least as long as fossil fuel reserves remain in sufficient levels and it is economically viable. Additionally, in recent years, the effect of propulsion systems on environment has become of major concern. In this direction, contemporary research focuses in ways of reducing gas turbine's dependence on fossil fuels and improving its environmental impact.

The gas turbine is a heat engine. This definition means that it converts thermal energy to useful work, which in the case of propulsion systems is thrust. As an idea, it is quite old, since the first patent of the gas turbine belongs to John Barber in 1791, while it was first patented as turbojet engine by Sir Frank Whittle in 1930. Since the dawn of the jet era, several improvements have taken place, especially in the area of structures and materials. However, the thermodynamic cycle remains in principle the same, with the only significant step-change the introduction of turbofan engines in mid sixties.

The market of gas turbines is intensively growing, following the growth of civil aviation. However, this condition highlights the essence for intensive research on efficiency and environmental impact. A close study on the potential of further improvement, unveils the need for strategic decisions for future propulsion systems; the need for investigating and developing alternative thermodynamic cycles, in a way that future goals of fuel consumption, noise and emissions will be easily attained.

1.1 Silent Aircraft Initiative

In the scope of an environmentally friendly aircraft C-MIT Institute launched the Silent Aircraft Initiative (SAI) project. In this project doctoral and MSc researchers from Cambridge and MIT joined powers to design from scratch an aircraft, having as prior design target low aircraft noise [Manneville et al., 2004], [Crichton et al., 2007]. The selected configuration is a Blended Wing Body (BWB), with embedded high bypass ratio, variable nozzle, multiple-fan turbofans. Several technological solutions have been investigated by the 40-member team and significant noise and fuel burn reduction has been calculated from the novel design, leading to a significant reduction in terms of noise and fuel consumption.

1.2 Project Objectives

This thesis reports the findings from the research study conducted in the scope of Cranfield University's contribution to Silent Aircraft Initiative. The rationale behind this was to provide alternative configurations of airframes and propulsion systems to the SAI team. As a result, the author's work on advanced propulsion cycles evolved in association to Sunil Mistry's work [Mistry, 2008], on novel airframes.

The intellectual contribution of this study can be summarised in the three milestones, listed below.

- Development of a preliminary gas turbine cycle design method, targeting at low noise novel configurations.
- Study of the installation of an advanced propulsion system into a novel airframe.
- Development of a tool, able to predict the sensitivity of propulsion systems to highly distorted inlet flows.

A preliminary design method has been developed, with prior target the reduction of engine noise. In this scope, several tools have been coupled in order to investigate the attributes of advanced propulsion systems. In this direction, the method is based on parametric analysis, as such a process allows for identifying overall performance attributes and the trade-offs that are involved in every design-related decision. As so, it was decided that a parametric analysis tool is the most suitable as it allows the user to see the evolution of performance and noise while varying the main cycle parameters. This analysis, aids the engineer in defining the optimum cycle design and it has been applied on four novel thermodynamic cycles; ultra high bypass ratio, recuperated, intercooled-recuperated and constant volume combustion.

In a further step, the close collaboration, between the airframe and the engine designer, has led to a novel installation that has been computationally investigated. The design drive of such installation is to provide maximum possible noise attenuation in order to reduce noise from major sources such as the fan. In this direction, the propulsion systems are half-embedded in the upper surface of the wing of a Broad Delta Wing Airframe. A three dimensional RANS CFD simulation has been conducted by two exchange students under the author's guidance, based on performance-CFD boundary-exchange iterative method, for calculating the levels of inlet distortion associated to the particular novel integration.

The three dimensional flow analysis in the half-embedded intake has shown significant inlet distortion levels, during the whole flight envelope. As a result, in order to assess the effect of installation-born inlet distortion on overall engine performance and stability, a high fidelity fan representation model has been developed. This model comprises two well established modelling methods; the streamline curvature (SLC) and the parallel compressor (PaCo). The rationale of the method is to increase simulation fidelity, by accounting for three dimensional effects. As a result, the parallel compressor method is used to divide the circumference in parallel sectors, according to the levels of circumferential distortion. Moreover, each sector is represented by streamline curvature code [Pachidis, 2006] which covers the radial direction. In such way, the sensitivity of the fan and engine to inlet distortion is assessed and conclusions relative to the forfeit of low noise installation are derived.

1.3 Thesis Structure

This thesis is divided into 7 chapters, with each chapter consisting of several sections and subsections.

The second chapter ‘Propulsion System Configurations for Noise Reduction’ contains the findings of a literature research that has been conducted on propulsion systems for low noise. It starts with some fundamentals on noise, continues with a discussion on the advanced cycles that have been studied and concludes with contemporary research on noise reduction techniques.

The third chapter ‘Advanced Propulsion System Analysis’ presents the various methods that have been developed. It starts with the low-noise cycle design that contains modules for gas turbine performance, aircraft performance, noise prediction, and engine weight and length prediction. In a further step, the development of the high fidelity fan model, for assessing installation effects, is discussed, including the parallel compressor the streamline curvature and their coupling. Finally the chapter includes the validation process for both engine-design and distortion-prediction methods.

In the fourth chapter ‘Propulsion System Preliminary Design Analysis’, the results of the cycle design method are presented. The method is applied to four thermodynamic cycles, an ultra high bypass ratio, a recuperated, an Intercooled-recuperated and a constant volume combustion turbofan. Optimum engines for the four cycles are installed on a baseline and a novel airframe (Broad Delta Wing) and they are assessed in terms of total noise and mission fuel consumption.

The fifth chapter ‘Airframe-Engine Integration’ assesses the design of a novel, low-noise, half-embedded installation and the study of its performance with the use of 3D CFD modules. A quasi-3D map of the intake has been created to be used in the enhanced parallel compressor model in the sixth chapter.

The sixth chapter ‘High Fidelity Engine Performance Analysis Under Inlet Distortion’ presents the analysis of the sensitivity of the fan and overall engine performance to inlet distortion. As a result useful conclusions are derived, relative to the stability of the low pressure compression system at off-design condition and the extent of the effect on engine OD performance.

Finally, the seventh chapter ‘Conclusions and Future Work’ includes a discussion on the findings of this research study. Additionally, recommendation for further improvement are listed and discussed in depth.

2 Propulsion System Configurations for Noise Reduction

A literature study on several propulsion systems and novel configurations with emphasis on reducing noise emissions has been conducted. It starts with a discussion on noise fundamentals, as this is the main design criterion. In a further step, the novel propulsion cycles that are studied in the design process are presented. Finally, it concludes with contemporary, state of the art research on noise reduction technologies.

2.1 Aviation Noise

The launch of the first jet engine (de Havilland Ghost MK I, 1949) was a milestone in the history of civil aviation, boosting air-travelling in terms of cost and time efficiency [Spearman 2002], [Ballal 2003]. However, it rendered the airplane to be one significant noise source of modern time [centennialofflight.com], something that became of major concern since the early years of the jet era.

The use of jet engine, in early '50s, allowed a number of innovations, such as the low thickness, swept wing, leading to higher cruise speed, or the increased aircraft dimensions, resulting in lower operating costs. In the next decade, the launch of commercially successfull Boeing 707 and Douglas DC-8 led to a dramatic growth of civil transport making apparent the issue of 'noise pollution' in the airport surrounding areas and in 1966 the first conference on noise was organised in London. As a result, in 1971 the Federal Aviation Administration (FAA) imposed the first noise certification scheme, the Federal Aviation Regulation (FAR), Part 36 [Smith, 1989].

The extensive research on gas turbine technology led to significant progress in the field of propulsion. As a result, the introduction of turbofan engines -Rolls Royce Conway, or GE CF700, followed by propulsion systems like RR RB-211, GE CF6, or PW JT9D-, combined with the application of lining in the intake, led to a ~15dB reduction by year

1985 – Figure 2-1. It can be noticed, however, that the rate of noise improvement reduces with time, as component efficiencies and material quality levels get close to theoretical limits. On the other hand the continuous growth of air transport will inevitably lead to unacceptably high noise levels in the airport suburbs. Thus, the consequent demand for significant future noise abatement makes essential the need of drastic changes in aircraft and propulsion design. From the propulsion engineer's perspective, a redesign of the thermodynamic cycle could lead to promising result, and this is the objective of this research study.

2.2 Aircraft Noise Regulations

In the year 1971, the FAA introduced the first aircraft noise regulation (FAR Part 36, stage 1). Since then, and following the advances in airframe and engine technology, a number of revisions have been imposed. The most recent noise standard adopted by FAA is the FAR Part 36, stage 4, introduced on January the 1st 2006, the same date with ICAO Annex 16 Chapter 4 regulation.

Figure 2-2 illustrates the noise limits at three certification positions. It can be noticed that the limit varies with the total aircraft take-off weight from low to high, with the slope of the curves being totally empirical. The differences between FAA and ICAO limits shown in Figure 2-2 rely on the fact that different power setting and flight conditions have been imposed by the two regulations. However, recent updates have rebated this deviation.

2.3 Noise Metrics

Noise can be described as pressure fluctuations resulting from non-periodic vibrations and perceived by human beings as disturbing. The measuring unit is the deciBel (dB), which is a logarithmic ratio of sound intensity. The reason for using such a unit is that it was found that the human response to sound follows logarithmic rule. According to that, a doubling of sound intensity corresponds to 3 dBs.

The range of the frequencies involved in any noise study is between 50 and 10000 Hz, as it is found that out of these bounds, noise is not annoying. Additionally, there is another important condition, which is the level of irritation caused by loudness. Human hearing systems are highly irritated, by sound levels in a frequency range between 2 and 4 kHz. For this reason the A-weighted scale - shown in Figure 2-3 - has been invented, applying weight factors in the integral of the sound pressure levels (SPL). In this way, low and high frequencies are attenuated in order to correlate to the way human ears assess loudness. dB(A) is a simple scale used by several airports to set noise restrictions, according to FAR part 150.

In addition to dB(A), other more complex scales are used, such as perceived noise tone corrected (PNLT) and effective perceived noise scale (EPNL). Perceived noise, similarly to dB(A) takes into account human beings' annoyance, based on audiometric tests, where the audience annoyance was quantified into 'Noys' [Kryter, 1959]. Furthermore, the tone correction factor adds a penalty to certain tones, according to their intrusion to human hearing system. While PNLT is measured for time-independent noise, EPNL takes into consideration the duration of the noise source, being the integral of PNLT, for a certain certification flight segment -take off or approach. EPNL and dB(A) are both used for aircraft certification [www.faa.gov], depending on the particular airport's policy. In the present study dB(A) has been used for validating aircraft and engine noise prediction tools, due to its simplicity and the lack of full mission data.

2.4 Aircraft Noise Sources

An aircraft is a vehicle that utilises a considerable number of components. Every air-interacting component is a potential noise source by disturbing the ambient air and causing pressure fluctuations. However, some of these components have a distinct role in noise production.

The present thesis is focused on propulsion noise, thus the airframe will be considered as one unified noise source as shown in Figure 2-4. In the same figure the engine noise is split to fan, compressor, turbine and jet. The contribution of each one of these sources is clearly shown, justifying the fan and the jet as the two primary turbofan noise sources. Due to the preliminary nature of the analysis and the use of low fidelity noise codes, the results have been presented in dBA. Additionally they are comparable to the FAA estimates [www.faa.gov], as a lot of airports use dBA as noise certification criterion.

2.4.1 Jet Mixing Noise

Jet noise or 'jet mixing noise' is the noise created when high temperature, high velocity exhaust jet gases mix with ambient air. The three main mechanisms that contribute to jet noise are listed below:

- Turbulent mixing of the exhaust gases with the ambient air. When a high velocity stream is mixing with ambient air, turbulence increases considerably, leading to generation of noise with acoustic power (AP) as shown below

  Equation 2-1

  $$AP_{noise} \approx \frac{p \cdot V^8 \cdot D^2}{a^5}$$

  As discussed by Lush [Lush, 1971], high density, or jet diameter are connected with higher mass flow, increasing jet-mixing noise, while ambient speed of sound is inversely proportional to sound, making apparent that during a hot day less noise will occur.

- Jet shock noise is formed when the jet plum is not fully expanded. As shown in Figure 2-5, the shocks that form in the vicinity of the exhaust plane interact with the turbulence, producing broad band noise.

- Jet entropy noise, caused by the high temperature of the jet. It is usually negligible, except in low flight-speed conditions.

Jet noise is the predominant noise source in turbojet applications. In the case of turbofans, however, where large mass of air is accelerated to low jet velocity another component plays major role; the fan.

2.4.2 Fan Noise

The fan is a low hub-tip ratio, one stage compressor, positioned at the face of the engine. It is identified as the second major noise source in an aero-engine, while it is easily recognised, especially when an aircraft approaches towards an observer (forward propagating noise). In a further detail, the noise produced by the fan features three main mechanisms.

- Broadband noise, which is produced from the interaction between rotating blade and incoming air. This interaction results to high levels of turbulence (see Figure 2-6), generating pressure fluctuations in a wide range of frequencies. Significant role is played by the fan-tip, which is rotating at maximum speed and within the turbulent boundary layer of the wall, something that increases further turbulence intensity.

- Blade-passing noise is apparent at the fan rotational speed frequency and its higher harmonics. The main generation mechanism is the forward propagation of each blade pressure field, when the blade speed is supersonic. A mechanism of equal importance is, also, the interaction between rotor and stator. In a further detail, when rotor blade wakes meet stator vanes, pressure fluctuations form, at the blade-passing frequency. This phenomenon is affected by the rotor-stator distance and the number of blades as discussed in [ESDU, 2002] and [Smith, 1989].

- Combined tone, or 'buzz-saw' noise originates from small geometrical differences between consequent fan blades, as shown in an exaggerated manner in Figure 2-7. Strong tones of lower shaft-order are generated due to the variation of blade pressure fields, or shock patterns, as illustrated in Figure 2-7. 'Buzz-saw' noise is produced at multiples of the fan rotational frequency and depends on the number of blades and the rotational speed.

Further information on engine noise sources can be found in Smith, [Smith, 1989].

2.5 Ultra High Bypass Ratio (UHBPR)

Since the launch of turbofans propulsion systems have evolved towards higher bypass ratio, as a result of the benefits in terms of fuel consumption and environmental impact. For this reason, the assessment of UHBPR cycles has a major role in this noise reduction preliminary study, where BPRs up to 30 have been evaluated.

2.5.1 Cycle performance considerations

Bypass Ratio (BPR) is defined as the ratio of the bypass to core massflows. Therefore, the increase of bypass ratio leads to higher bypass mass flow compared to the air that enters the core. This condition has a number of effects in terms of engine performance and noise emissions.

The increase of fan size, relative to core leads to higher power requirement from the low pressure turbine. As a result, at constant combustor outlet temperature the turbine exit temperature reduces when BPR increases leading to lower core jet velocity. Moreover, the optimum fan pressure ratio decreases, leading to lower bypass exhaust velocity. For every set of BPR, OPR and COT there is an optimum FPR where specific thrust is maximum and SFC minimum, as discussed by Walsh [Walsh, 2004, pp.304]. Another effect of high BPR is the reduction of exhaust velocity that leads to lower specific thrust and jet noise. Additionally, propulsive efficiency is improved, with a positive effect on specific fuel consumption.

The rise of BPR affects the off-design performance of the engine, as well. Firing temperature variation from top of climb to take off is affected by the BPR level. A common flight condition for designing a jet engine is top of climb (ToC), where the engine is operating under maximum temperature ratio (COT/T_{amb}). Moreover, when at static take-off, the combustor temperature is allowed to go to higher levels, in order to produce the required maximum thrust. However, at ultra high BPR the design point will comprise the increased ram drag – due to higher mass flow –, having as a result the need for lower take off throttle settings – where ram drag is zero. The benefit from reduced COT at take-off is lower NO_x and noise emissions.

2.5.2 Ultra High BPR Turbofan Applications

Several issues emerge from the implementation of ultra high BPR. The increase of fan diameter is one and combined with the need for low tip speed leads to very low fan rotational speed. As a result, an increase of turbine stages is needed, in order to satisfy the increased power requirement, having a strong impact on engine weight. To overcome this constraint, a number of applications are suggested below:

Tip Turbine Driven Fan

A proposed configuration is the Tip Turbine Driven Fan (TTDF). TTDF was originally proposed for VSTOL applications; NASA reports by Rolls [Rolls, 1969], Jaklitsch [Jaklitsch, 1971] and Lowe [Lowe, 1972] have concluded to detailed mechanical design, static testing and flight evaluation of such a machine in early 70s. Some decades later, its application on remote propelling large fans was assessed in Cranfield University. Huete [Huete, 1997], King [King, 1999], Noirot [Noirot, 1999], Higson [Higson, 1999] and

Medicina [Medicina, 2006] have investigated the aerodynamic, thermodynamic, mechanical design, noise and installation issues, relative to tip turbine driven remote fan.

As shown in Figure 2-8, the TTDF features a low pressure turbine, positioned at the tip of the fan. In this way the turbine is rotating at higher circumferential velocity producing more work, per turbine volume and satisfying the high load requirement. Additionally, the proposed configuration depicts two turbine stages on the same rotor, splitting the circumference into two sections; the first fed with high enthalpy gas and the second fed with the exhaust gas of the first. In this way, the rotor blades are self cooled and maximum enthalpy may be extracted from the turbine. However, issues concerning the thermal fatigue on the blades should be subject to further research.

Another benefit from such a concept is the shroud of the fan that eliminates tip leakage losses and also, provides with higher fan integrity. However, special care should be given on adequate shielding at the fan tip, for the deterioration of leakage.

There are two variations of TTDF; the exhaust and the bleed. Their main difference is the type of gas that feeds them. In the exhaust type, part of the core exhaust gases is led to the entry of the tip turbine. In the bleed type air is bled from the high pressure compressor and is guided to a tip combustor. This gives operational flexibility in addition to the capability of retracting the remote fan in variable cycle applications [Arnulfo et al., 2001], [Huete, 1997]. However, the bleed flow out of the core leads to significant performance deterioration. On the other hand, the exhaust-type TTDF is simpler to construct as there is no need for tip combustor. A drawback in this configuration is the need for large diameter ducts, due to lower density gas-flow, where there is a higher possibility of leakage.

<u>Mechanically driven fan</u>

An alternative, to TTDF, is the geared turbofan. Its definition implies that a gearbox is fitted on LP shaft, reducing the fan and increasing the turbine rotational speeds. In the scope of 'SAI' project, a gearbox study on a UHBPR turbofan has been performed by De la Rosa et al. [de la Rosa et al., 2007], where two designs have been evaluated in terms of noise and total weight. It was found that a configuration featuring planetary gearbox would add less than 10% to total weight. Additionally, a number of European projects, like VITAL and NEWAC take into consideration such a configuration, while Pratt&Whitney is already in the process of ground testing PW 8000, a high bypass ratio geared turbofan – shown in Figure 2-9 – claiming a 9% reduction in fuel consumption and lower noise emissions [SAE/Top 15 Technology Innovations, 1998].

Electrically driven fan

A much more unconventional solution to the UHBPR issues could be the all electric propulsion system. In that case the main gas turbine acts as an electric power generator and the main propulsor – the fan – is electrically driven, or electric power storage devices are used – fuel cells. Research by NASA has been conducted in the direction of magnetically levitated fans [Emerson, 2004], however the main disadvantage is the increased weight of such a configuration that can be tackled when electric generator and fuel cell specific power gets to competitive magnitude.

Remote fan

All of the above described configurations have a common characteristic. They bear the possibility of changing the position of the fan – related to the core –, or even increasing the number of fans driven by a single gas generator. This condition has two advantages. Firstly, it allows for lower fan diameters, giving an aid to low-speed fan design and lower noise. Secondly, it allows unconventional fan installation – semi or fully embedded –, for improved aerodynamic performance and noise emissions – see installation section.

.

2.6 Variable Geometry

In addition to high BRP at design point, further noise reduction can be achieved by further increasing BPR at off design – take-off and approach. Variable geometry is a means of accomplishing such a target, by controlling the engine exhaust velocity at these conditions.

Conventional turbofans operate under lower BPR during take-off. This happens due to the engine operating at high power level. As a result, the core tends to increase more its flow capacity than the by-pass propelling nozzle. However, high core mass flow, leads to high jet noise.

In order to eliminate such behaviour, variable nozzle and intake configurations are assessed for minimum noise emissions during take-off and landing. The main principle is that variable by-pass nozzle can lead to high BPR during take-off, as the fan operates at higher mass flow and lower pressure ratio, while the core mass flow reduces, due to lower inlet pressure. This condition is beneficial for jet noise, as lower mass flow of hot gases is exhausted and is also, surrounded by higher mass flow of cold air. Similar attribute can be achieved by using auxiliary fan air inlets.

The work of Nascimento [Nascimento, 1992] and Aleid [Aleid, 1997] on variable cycle turbofans has shown the off design engine performance and the gain in fuel consumption for supersonic vehicles. On the other hand, Crichton [Crichton, 2007] investigated the noise reduction potential of variable bypass nozzle technology, for a subsonic airliner. Moreover, the work of Woodward and Hughes [Hughes, 2004], have shown a 2 dB reduction of effective perceived noise by 5% increase in fan nozzle area.

Considerable research has been undergoing on the application of variable nozzles on modern turbofans. Rey [Rey et al., 2001] has proposed a shape memory alloy actuator system that is two times lighter than other conventional actuators.

A technology that can be applied in parallel to variable nozzle is the variable pitch fan. Variable pitch technology is well-established in propellers, where blade pitch varies during operation for keeping the propeller rotational speed at optimum. Additionally, in ultra high bypass –thus large diameter– turbofans variable pitch fan can be used for reversing the thrust during landing, by reversing blade angles. In this way, considerable noise reduction can be achieved. Significant research has been performed during the 70s, with the works of Ashill, [Ashill1972], Schaefer, [Schaefer et al.,1977] and Moore and Osborn, [Moore & Osborn, 1979] being some representative examples. Ashill, [Ashill, 1972] experimentally investigated the effect of thrust reversing on wing aerodynamics, showing a 5.5% reduction of maximum lift for fully blocked engine inlet. The experiments from Schaefer, [Schaefer et al.,1977], showed that rapid reverse-thrust transients are not limitating engine performance and investigated the performance dynamics during feather-pitch operation. Moreover, in 1979 a complete aerodynamic performance investigation of a variable pitch fan was presented by NASA researchers, Moore and Osborn.

2.7 Constant Volume Combustion (CVC)

A CVC cycle includes constant volume combustion in comparison to classic Brayton cycle, where heat addition occurs under constant pressure – see Figure 2-10. As a result, significant improvement in specific fuel consumption and specific thrust can be achieved. Previous studies on the field by Snyder, [Snyder et al., 2002], Smith, [Smith et al., 2002] and Won and Waters [Won & Waters, 2003] indicate the potential benefit of constant volume combustion engine incorporating a wave rotor combustor, which utilizes pressure wave dynamics combined with combustion within wave rotor tubes.

A Turbomatch model of a CVC turbofan has been created to predict the theoretical performance benefit from increasing the pressure at the exit of the combustor. In order to model the behaviour of a wave-rotor CVC, a linear expression – Equation 2-2 – has been proposed by Won and Waters, matching results from Snyder, [Snyder et al., 2002] and has been implemented into the engine model.

Equation 2-2:

$$\frac{P_7}{P_6} = 0.502 \cdot \frac{T_7}{T_6} + 0.445$$

Figure 2-11 illustrates a comparison between a conventional and a CVC turbofan, where it becomes obvious that no length, or weight penalty as stated by Smith, [Smith et al., 2002] is applied. The reason is the fact that less compressor stages are required, as part of the compression takes places inside the burner. Moreover, the CVC is found to be 15% more efficient. The Turbomatch model of a CVC engine can be found in the Appendix.

2.8 Recuperated Turbofan

A recuperated cycle is considered to be part of this study because of its high efficiency and low noise potential. In a conventional gas turbine, a considerable amount of enthalpy is scattered to the environment through the hot gases. Recuperation is the process of limiting the exhaust gas temperature, by transferring heat from the turbine exit to the compressor delivery air, in a way that less fuel is required for the combustion. In addition to this, the reduced exhaust total temperature T_j (Equation 2-3) results in reduced jet velocity V_j –Equation 2-4–, thus jet noise. Equation 2-3 illustrates the effect of core and fan pressure ratio, COT and BPR on the value of nozzle total temperature; a rise in COT increases T_{11}, while a rise of pressure ratios and BPR leads to lower T_{11} with beneficial effects on jet noise. Another parameter affecting T_j is the effectiveness of the heat exchanger, where a high value allows maximum heat transfer and reduces further T_j.

Equation 2-3

$$T_j = T_{11} - \Delta \mathrm{T}_{rec}$$

where $$T_{11} = COT - \frac{Cp_a}{Cp_g}\left[\left(R_c^{\frac{\gamma-1}{\gamma \cdot n_p}} - 1\right)\cdot R_f^{\frac{\gamma-1}{\gamma \cdot n_p}} + BPR \cdot \left(R_f^{\frac{\gamma-1}{\gamma \cdot n_p}} - 1\right)\right]\cdot T_o \cdot \left(1 - \frac{\gamma-1}{2}\mathrm{M}_o^2\right)$$

and $$\Delta T_{rec} = \left(T_{11} - T_5\right)\cdot eff$$

Equation 2-4 $$V_j = \sqrt{\gamma R t} \cdot M_j$$

Equation 2-5 $$\frac{T}{t} = 1 - \frac{\gamma - 1}{2} \mathrm{M}_j^2$$

where $\mathrm{M}_j = 1$, when nozzle is choked

or, $$\mathrm{M}_j = \sqrt{\frac{2}{\gamma - 1}\left(1 - \left(\frac{P_{nozzle}}{P_o}\right)^{\frac{\gamma - 1}{\gamma}}\right)}$$

Equation 2-6 $$n_{th} = \frac{T_{j\_c} - T_o + BPR \cdot \left(T_{j\_B} - T_o\right)}{T_{11} - T_5}$$

A major difference between the Brayton and the recuperated cycle is the effect of OPR on thermal efficiency. Unlike the Brayton cycle, where a high OPR always improves SFC, the increase of compressor delivery temperature reduces the heat transfer from the exhaust gas, counteracting the recuperation benefit. COT has a major role in improving this attribute by increasing the temperature difference inside the recuperator.

A drawback in such configuration is the impact of recuperation on specific thrust, which is proportional to exhaust velocity. Intense recuperation leads to higher emgome dimensions and weight. As a result the positive effect of higher SFC is limited when it comes to overall aircraft performance.

2.9 Intercooled-Recuperated Turbofan

When a recuperated cycle is enhanced with intercooling –shown in Figure 2-12–, the issues of limited OPR and low specific thrust are resolved, as the compressor exit temperature is cooled down by cold air stream from the bypass duct. In this way, its enthalpy is transferred to the bypass stream and the heat transfer in the recuperation is of higher degree. As a result, improved specific thrust and SFC is achieved –as discussed by Boggia, [Boggia, 2005]. The effect of COT, compressor pressure ratios and BPR on turbine exit temperature (T_{11}) is shown in Equation 2-7.

Equation 2-7

$$T_{11} = COT - \frac{Cp_a}{Cp_g}\left[\begin{matrix}\left(R_{c1}^{\frac{\gamma-1}{\gamma\cdot n_p}}\cdot(1-eff_{ICR})+eff_{ICR}\right)\cdot\left(R_{c2}^{\frac{\gamma-1}{\gamma\cdot n_p}}-1\right)+ \\ \left(R_{c1}^{\frac{\gamma-1}{\gamma\cdot n_p}}-1\right)+BPR\cdot\left(1-\frac{1}{R_f^{\frac{\gamma-1}{\gamma\cdot n_p}}}\right)\end{matrix}\right]\cdot R_f^{\frac{\gamma-1}{\gamma}}\cdot T_o\cdot\left(1-\frac{\gamma-1}{2}\mathrm{M}_o^2\right)$$

A Turbomatch model has been created, implementing two heat exchangers and allowing for varying their effectiveness, in order to quantify the potential benefit of this innovative cycle.

A drawback in such configuration is the need for heat exchangers that weight and pressure losses to the machine. Additionally, increased turbulence may lead to higher noise, issues that need to be subjected to further research. For the purposes of the present preliminary study, a weight penalty of 20% has been imposed on the weight prediction module, in order to account for the mass of the heat exchangers.

2.10 Subsonic tip fan

All of the above mentioned cycle configurations aim, mainly, to jet noise suppression, having a little effect on fan. For this reason and due to the fact that total noise is not the algebraic but the logarithmic sum of all sources, a noise treatment for the fan is requisite. In addition to the acoustic treatment of noise through lining and noise shielding, significant improvement can be achieved by designing a subsonic tip fan.

Figure 2-13 illustrates the effect of inlet relative rotor-tip Mach number on fan noise. In the figure, fan noise is plotted against off-design tip Mach number, having as parameter the design-point tip Mach. As expected, a decreasing Mach number leads to significant noise reduction up to 7dB. The reason of such an attribute may be identified in Figure 2-14, which shows the Sound Pressure Level (SPL) spectrum for two cases. The peaks in the high Mach spectra are connected to tonal noises – refer to § 2.4.2. As a result, those peaks in parallel with broadband noise diminish for fan operation under subsonic conditions. For this reason, the cycle design process uses fan geometric data equivalent to subsonic fan design.

2.11 Contemporary Research on Noise Reduction Technologies

Significant research has been recently conducted on the development of novel low-noise devices for improving noise signature of future engines without vast modification of the thermodynamic cycle. In the following section state-of-the-art research on noise reduction is presented.

2.11.1 Jet Noise

In addition to the cycle design for low noise, various mixing devices can be used as the chevron nozzle shown in Figure 2-15. Moreover, Figure 2-15 demonstrates the noise spectra of a chevron nozzle compared to a conventional, where considerable noise suppression up to 5dB is noticed as discussed by Saiyed [Saiyed et al., 2000].

Another mixing device is the one proposed by Papamoschou [Papamoschou, 2003], utilizing the deflection of the bypass stream in order to suppress the downwards directed noise and demonstrating a 5dB noise reduction.

Another noise reducing configuration is the bevelled nozzle, proposed by Viswanathan [Viswanathan, 2004] and shown in Figure 2-16, can result in a 5-7dB noise reduction.

2.11.2 Fan Noise

As discussed previously, the increase of BPR makes the fan the primary noise source, as the mass flow and size increase. This is partially offset by the reduction of the optimum fan pressure ratio (FPR), combined with low rotating speed. Additionally, liners at the inlet and the exhaust duct add in the direction of fan noise suppression.

The tonal and broadband noise can be suppressed, also, by increasing the rotor-stator spacing as proposed by Dalton [Dalton, 2003]. However there is a limit in such solution, as the increase of the spacing may lead to extremely long cowl, having an impact on the installation drag of the engine. Furthermore, the implementation of leaned and swept stator vanes – Figure 2-17– may improve further the tonal and broadband noise levels.

Another novel configuration of special interest is the ducted, subsonic, variable pitch fan proposed by Dittmar, [Dittmar et al., 1999], shown in Figure 2-18. This experimental study investigated the noise benefit from operating the fan under subsonic conditions, eliminating tonal noise, using variable pitch blading.

The idea of cancelling an acoustic field by introducing an acoustic field of the same amplitude but opposite phase inspired the research on Active Noise Control Fans

(ANCF). Such a device comprises an actuator array to produce the cancelling noise field, a microphone to monitor the noise levels, and an algorithm to provide input to the actuator. A system like this is presented in detail by Parente, [Parente, 1999] – Figure 2-19.

Another field of further development is the rotor-stator interaction. Extended work ([Brookfield, 1998], [Sutliff et al., 2002], [Halasz, 2005], [Woodward et al., 2007]) has shown that blowing air at the trailing edge of the fan can reduce the velocity deficit, and thus the tonal noise produced by the interaction of the rotor wake with the stator. In 2002, Sutliff, [Sutliff et al., 2002] following the work of Brookfield [Brookfield, 1998], showed that a maximum of 2% of the fan mass flow can be directed through the fan to fill the wake and achieve a far field noise reduction of ~10dB. Three years later Halasz [Halasz, 2005] investigated alternative configurations for reducing the amount of blown air, while Woodward, [Woodward et al., 2007] applied various TE blowing scenarios on a modern fan and documented a 2dB improvement when 2% of the total flow was blown at the full span of the trailing edge. Figure 2-20 shows a fan blade meridional cut where the air passages are clearly shown.

A different strategy is followed in the scarfed inlet configuration for under-the-wing podded engines. In this case, an extension of the lower lip of the intake, redirects some of the fan noise upwards reducing the noise reaching the ground, as discussed by Raman [Raman, 1999].

2.12 Engine-Airframe Integration

The installation of the propulsion system on the airframe is a supplementary approach for reducing engine noise that is received at the ground. The rationale is instead of eliminating the source of the noise, to improve the impedance of noise and shield it, in order not to reach urban areas at high intensity. Especially in the present study noise shielding is regarded as crucial for fan noise reduction. The reason is that fan noise is not strongly affected by the increase of BPR. Additionally, there are a number of other benefits that accompany a close integration of engine and airframe in civil applications.

The idea of embedding the propulsion system dates back to mid-forties. Frick, [Frick et al., 1945] introduced and conducted an experimental study on submerged-duct entrances, as alternative solutions to wing leading edge inlets. Mossman and Randall [Mossman & Randall, 1948] continued this work and investigated the performance and the design of submerged intakes, showing the large effect of boundary layer thickness on pressure recovery factor. In the following years, embedded installations were implemented mainly on military applications. However, in the recent years, the interaction between engine and airframe has been subject of research, with an example being the white paper produced by Yaros et al. [Yaros et al., 1998] for NASA. This paper reviews several technologies for their potential of improving aircraft aerodynamics, (i.e. the wing lift coefficient) among them being distributed propulsion, blown flaps and the channel wing aircraft.

Recently, in the scope of Silent Aircraft Initiative, embedded propulsion systems have been theoretically investigated, for their ability of improving aircraft aerodynamics, by ingesting the boundary layer of the wing and re-energising it. The benefit, in terms of fuel consumption and aircraft performance, from embedding the engine in the airframe has been investigated and highlighted by Hall & Crichton [Hall & Crichton, 2005], while Plas [Plas et al., 2007] have quantified the effect of boundary layer ingestion on the performance of the propulsion system. Other works on embedded intakes are Rodriguez [Rodriguez, 2000] and Ko [Ko, 2003], regarding optimisation of boundary layer ingesting intakes, and distributed propulsion, respectively. Embedding the propulsion system can be combined with novel engine configurations, such as multiple fans per engine-core. Splitting the main flow to a number of fans is shown by Hall [Hall, 2005] to have a beneficial effect on total installation drag and fuel consumption, especially if it is combined with embedded engines into a novel airframe such as a blended wing body (BWB). Moreover, Lundbladh, [Lundbladh, 2005] compared distributed propulsion configurations and showed a 4% fuel reduction, for fully embedding 8 engines into a conventional wing. In this project a half embedded installation has been study for improving fan-noise shielding.

2.13 'Slow & Steep' Approach

In the scope of SAI project, the author has participated in the 'Steep & Slow Approach' exercise. The aim of this exercise was to highlight possible ways of reducing community nuisance from aircraft noise, by changing the approach flight path. The effect of speed and angle of approach on noise have been investigated, as shown in Figure 2-21, for an engine provided by SAI team.

Figure 2-22 illustrates the effect of flight angle and speed on thrust requirement. It becomes obvious that steep and slow approach may reduce thrust by 40%. This allows for throttling back the engines and thus reducing jet and fan noise, as shown in Figure 2-23 and Figure 2-24, where a noise reduction in excess of 25 dBs for the jet and 15 dBs for the fan is noticeable.

Figures of Chapter 2

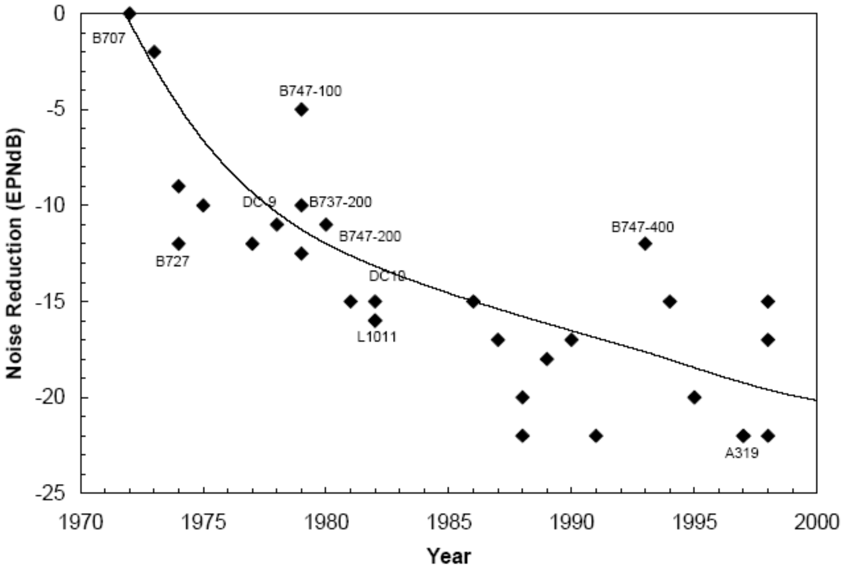

Figure 2-1: Noise abatement improvement in civil aviation [Ballal, 2003].

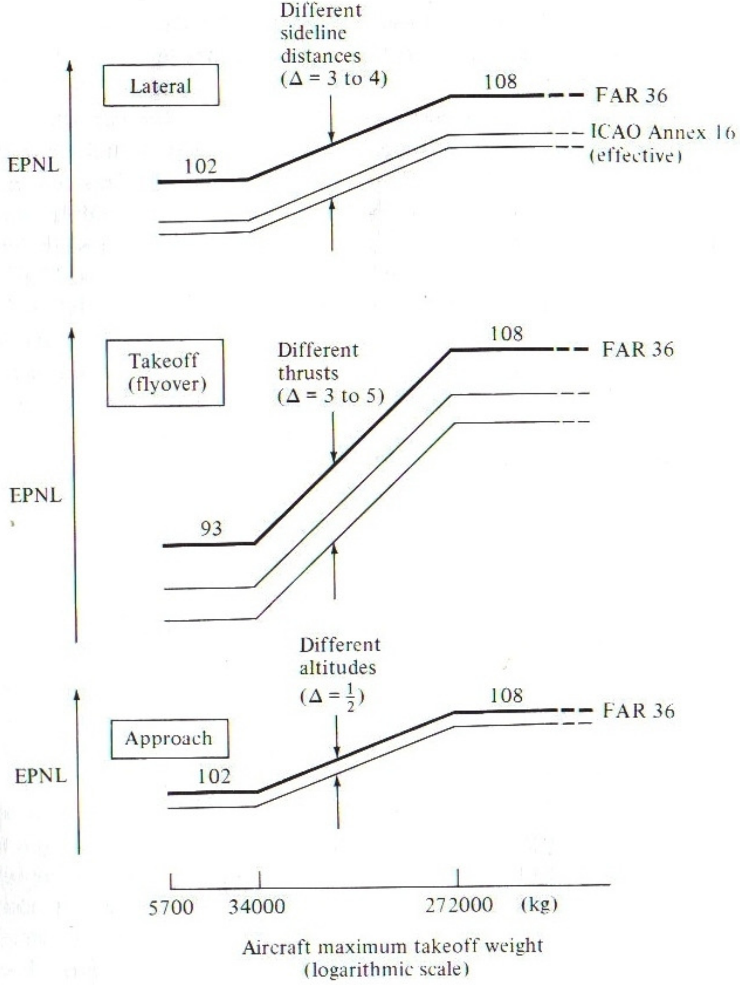

Figure 2-2: FAR Part 36 and ICAO Annex 16 noise limits.

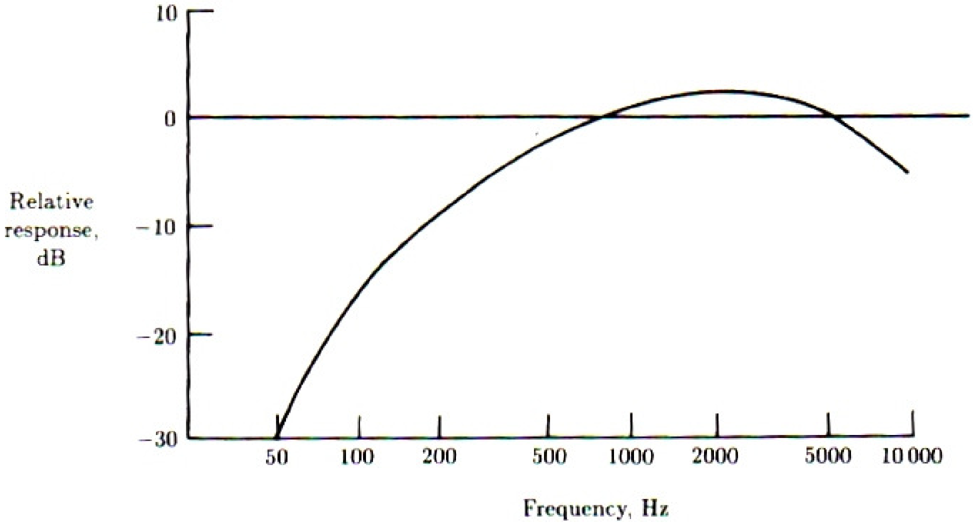

Figure 2-3: Relative response to the A-weighted filter [Hubbard, 1991]

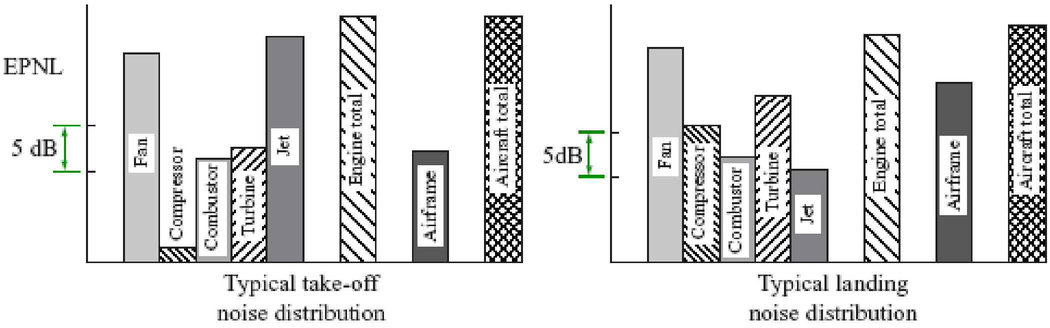

Figure 2-4: Noise breakdown for take-off and landing. [ESDU, 2002]

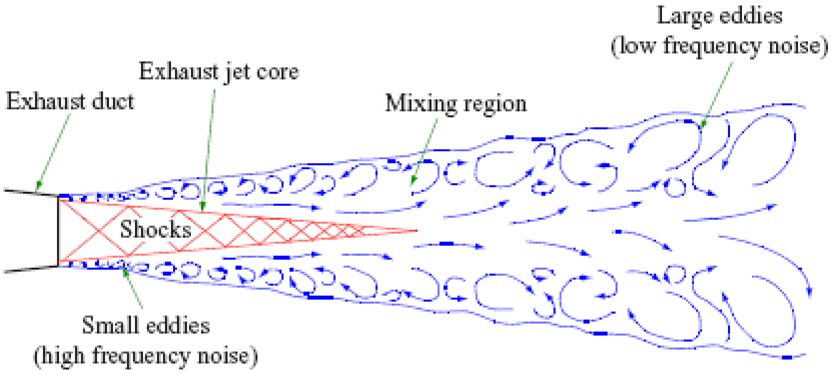

Figure 2-5: Representation of jet noise mechanisms [ESDU, 2002].

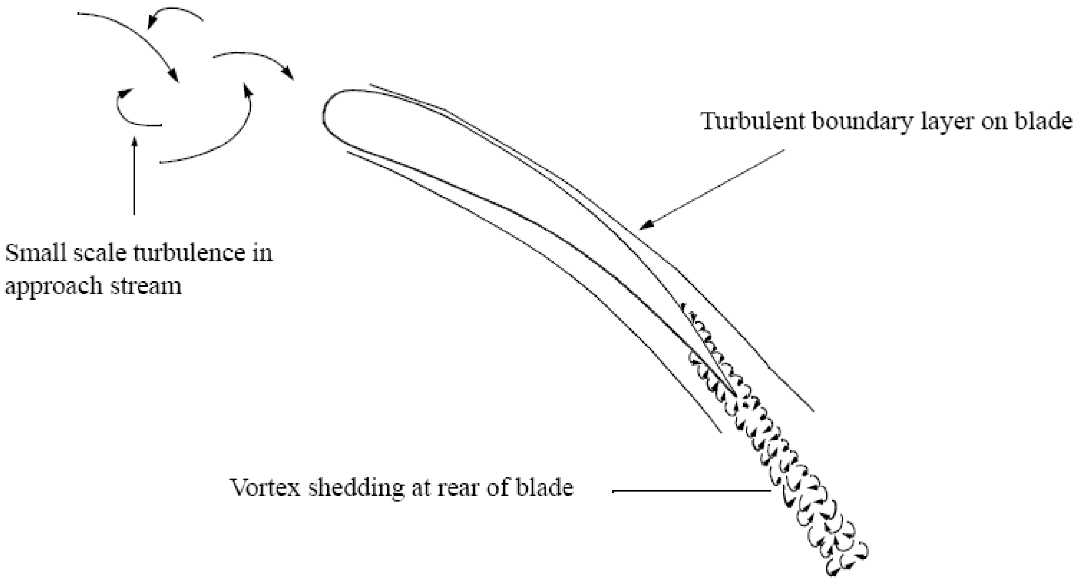

Figure 2-6: Representation of broadband fan noise mechanism, [ESDU, 2002].

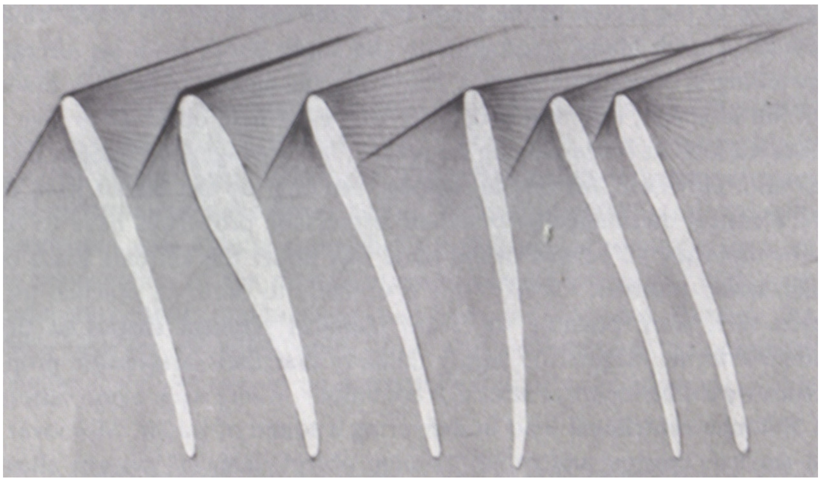

Figure 2-7: Representation of 'buzz-saw' noise generation [Smith, 1989].

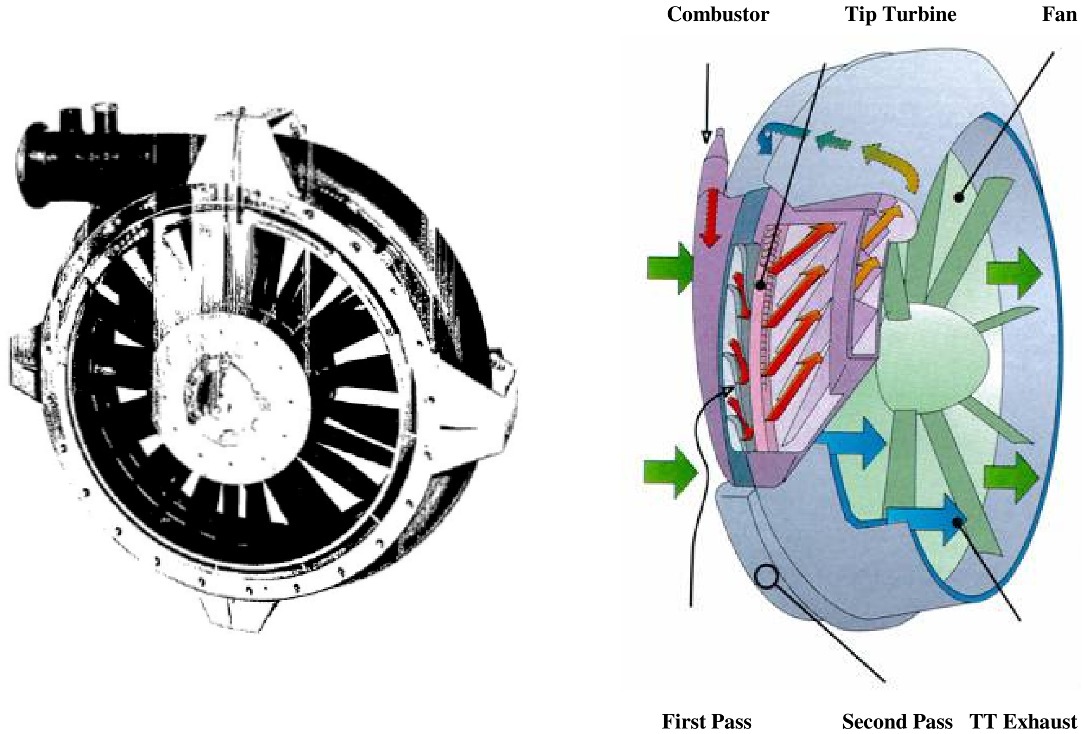

Figure 2-8: Tip Turbine Driven Fan (Bleed type)

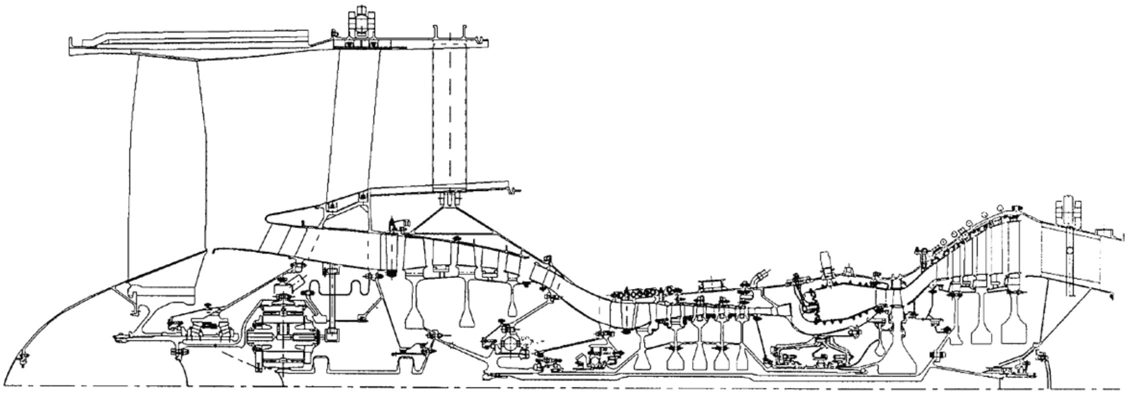

Figure 2-9: PW 8000 geared turbofan [Courtesy of P&W].

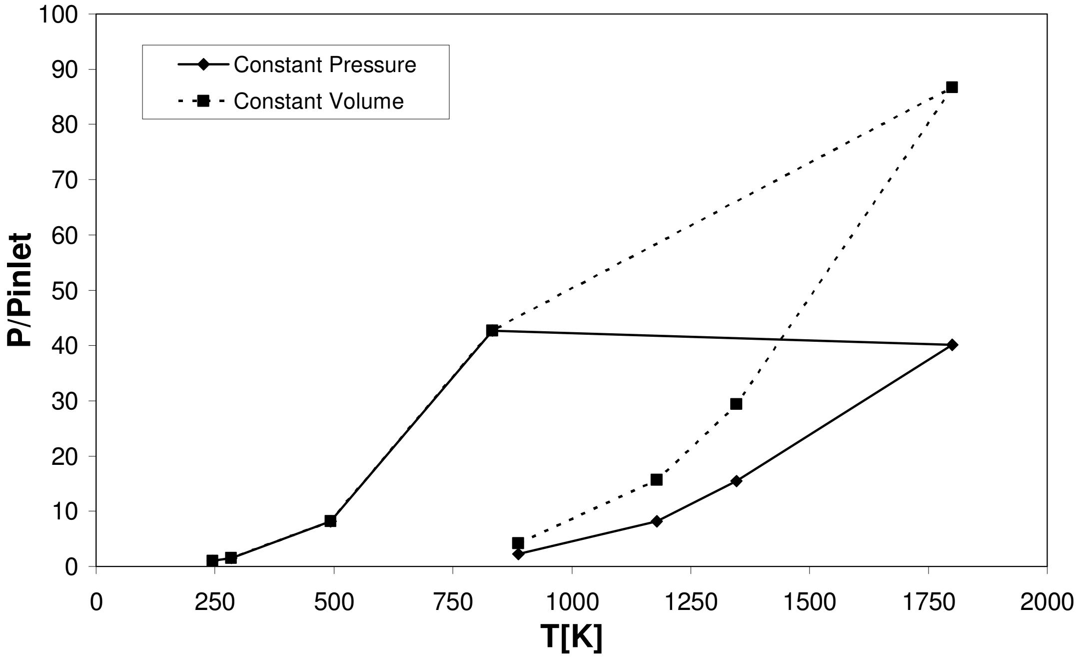

Figure 2-10: Brayton versus CVC cycle.

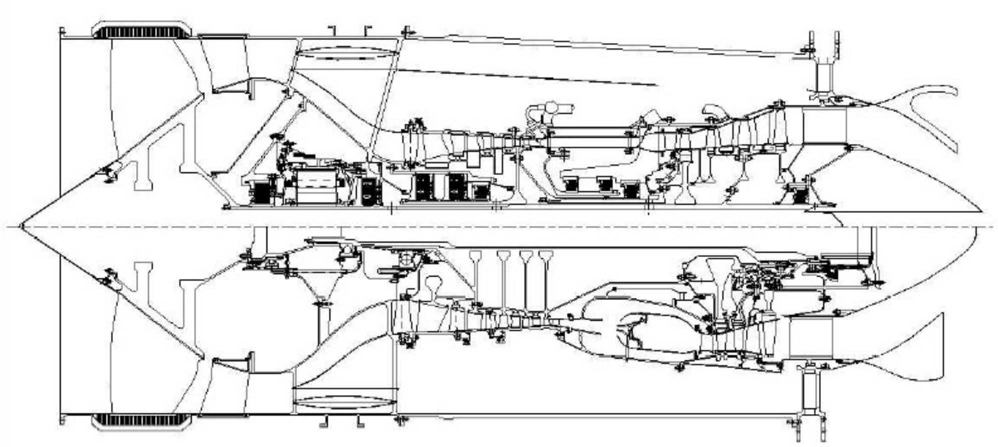

Figure 2-11: Conventional versus CVC turbofan [Courtesy of AADC].

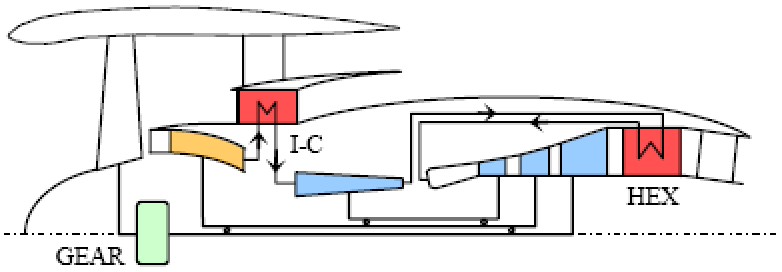

Figure 2-12: Intercooled recuperated turbofan, [Boggia, 2005].

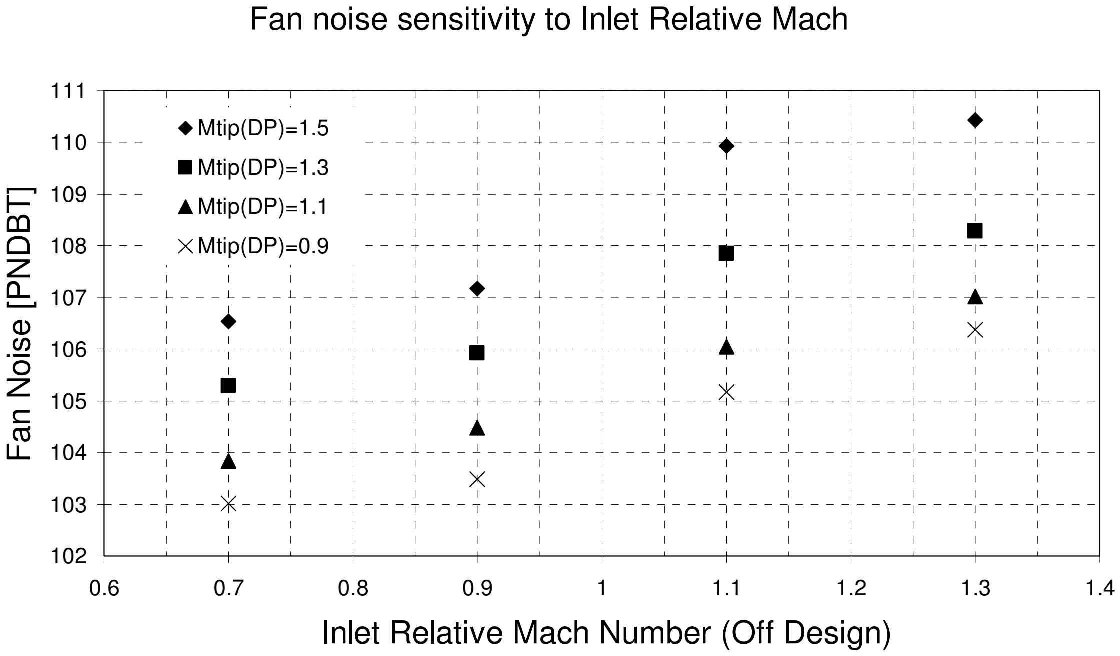

Figure 2-13: Fan noise variation with inlet relative Mach number.

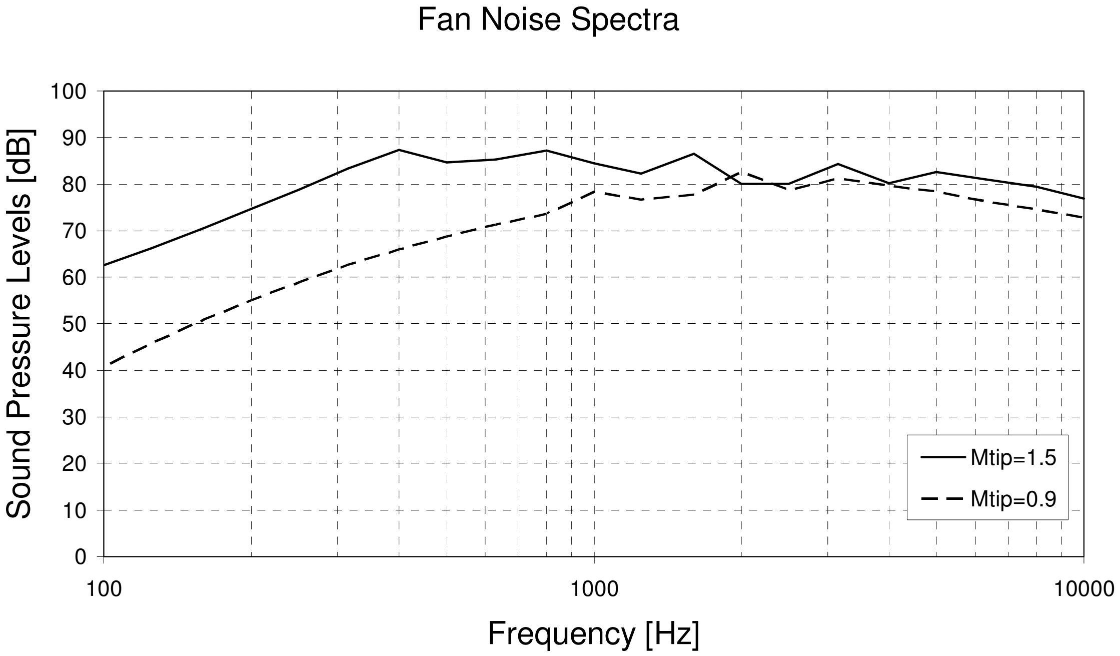

Figure 2-14: Fan noise spectra for various inlet relative Mach numbers.

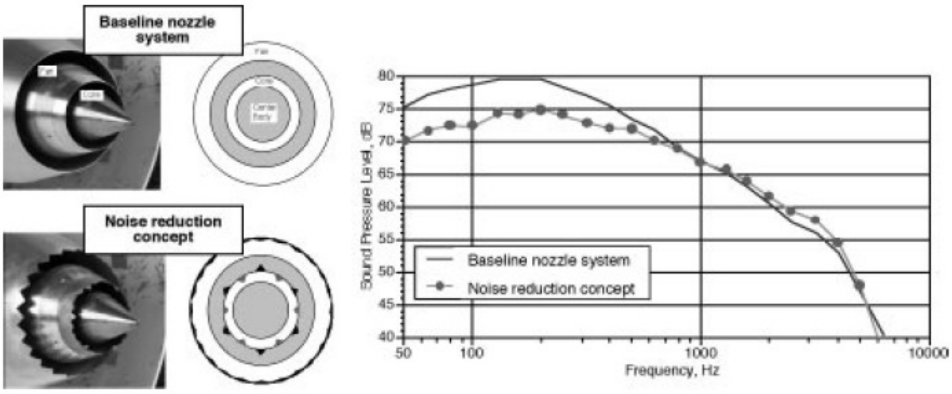

Figure 2-15: Noise reduction concept noise spectra [Saiyed et al., 2000].

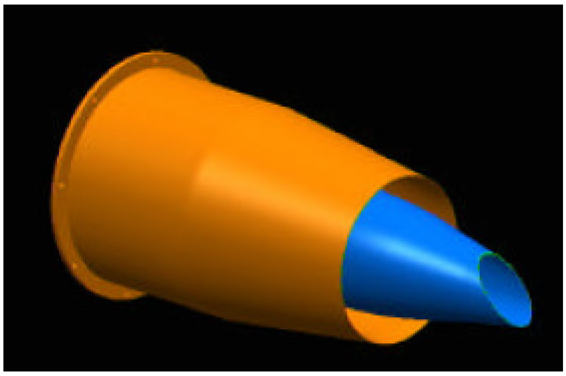

Figure 2-16: Beveled nozzle [courtesy of Boeing].

Figure 2-17: Leaned and swept stator vanes.

Figure 2-18: The advanced ducted propulsor fan. (Courtesy of NASA, P&W)

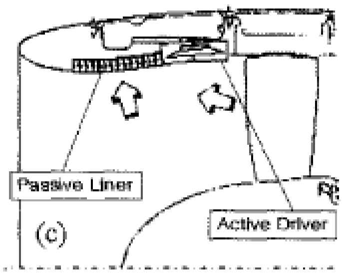

Figure 2-19: Hybrid active-passive system

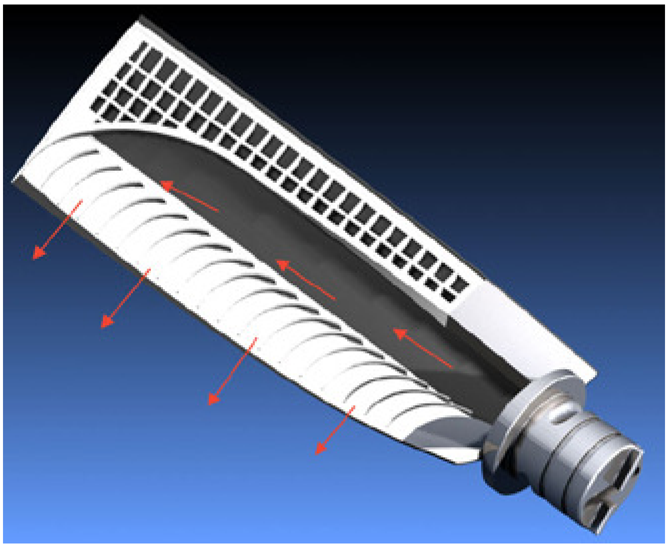

Figure 2-20: Blown rotor and internal passages, [Sutliff et al., 2002].

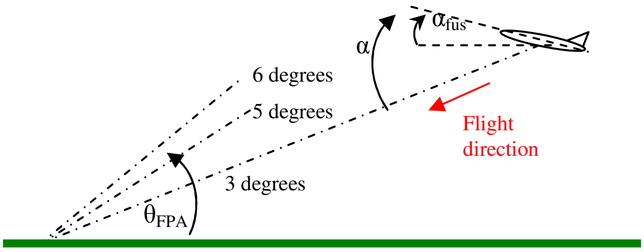

Figure 2-21: Approach flightpaths.

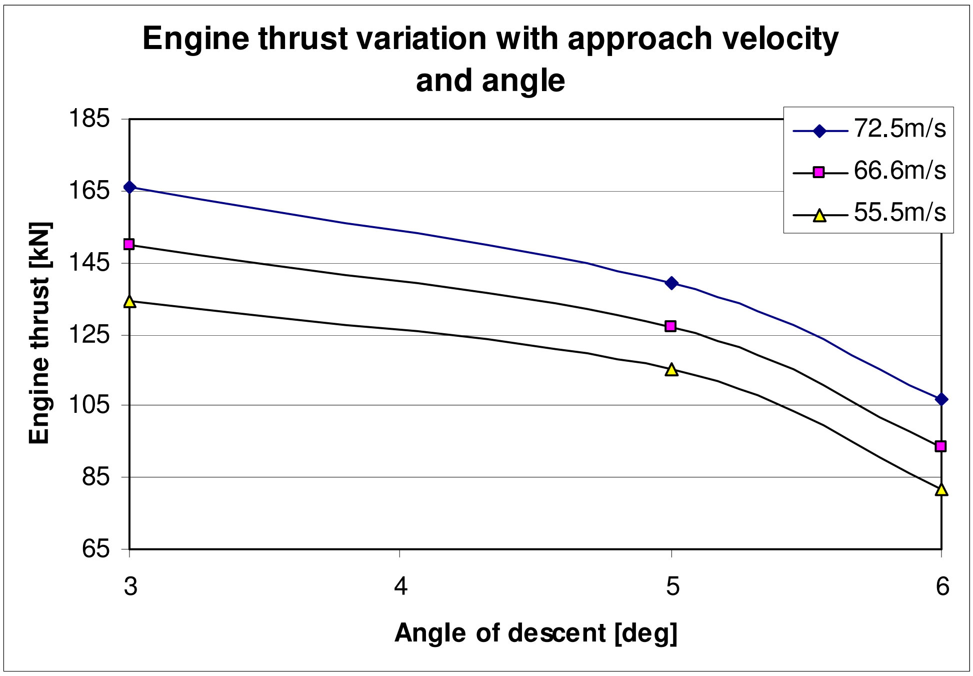

Figure 2-22: Net thrust during approach.

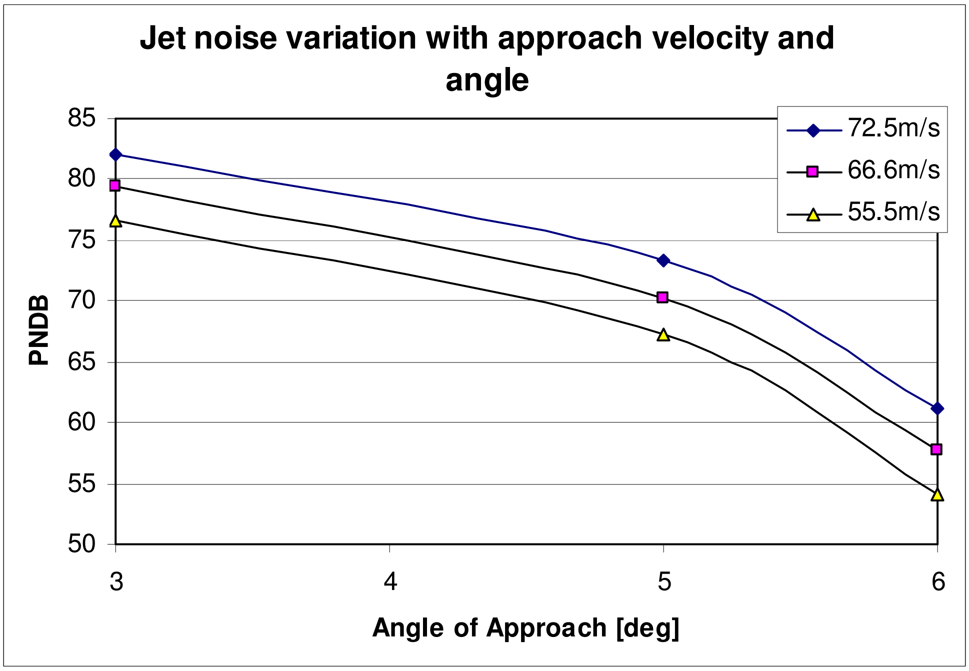

Figure 2-23: Jet noise during approach.

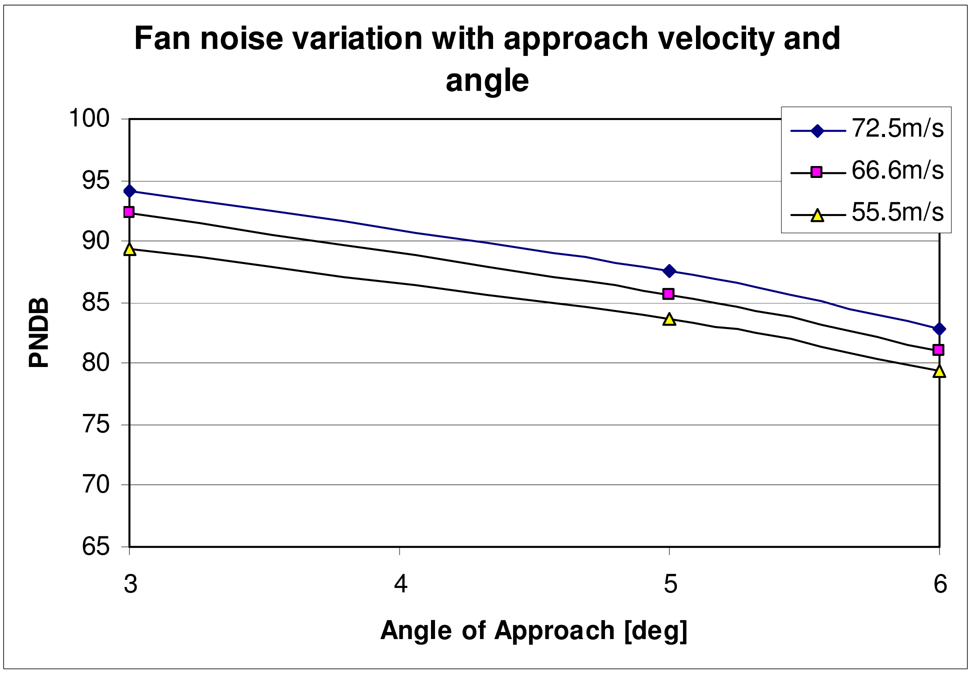

Figure 2-24: Fan noise during approach.

3 Advanced Propulsion System Analysis

The preliminary design of a modern propulsion system can be discerned into a number of steps. The first is the evaluation of design targets and the statement of requirements, followed by a design point analysis, based on existing scaled component maps. The results of the initial analysis are input to component design analyses that enable a more detailed prediction of the engine performance. This thesis focuses on the design of advanced propulsion systems, with primary target noise reduction. In this manner, a noise-reduction cycle design method is presented, along with higher fidelity gas turbine performance tools. The development of all of the GT component design tools is out of the scope of this thesis, which focuses on components that have the most significant effect on noise emissions. These are the intake and fan of the engine.

A preliminary gas turbine design method takes into account the total mission fuel and noise emissions, for providing optimum propulsion systems. Moreover, the effect of noise-reducing airframe-engine integration on gas turbine performance is predicted using an enhanced representation model of the fan component.

In this chapter, the methods that have been developed in the scope of the project are presented. The design point GT cycle design method is first detailed, including gas turbine performance, aircraft performance and noise emissions modules. Furthermore, it is followed by a validation of the modules against real aircraft data. The chapter concludes with the presentation of an enhanced parallel compressor model, integrated in a 0D GT performance code. This model has been developed to assess the effect of installation-born distortion on engine stability and performance.

3.1 Low Noise DP Cycle Design

3.1.1 Literature Review

It is a common practice in aviation industry to use fuel consumption as primer design drive. The noise has always been a secondary target, where any concern has been directed in attaining safe margins from limits set by international noise legislation. In recent years, however, noise has become an issue due to exponentially increasing air-traffic. As a result, a number of research studies have focused on noise oriented design methodologies for lowering airborne noise.

A work on multi-disciplinary optimisation (MDO) on preliminary aircraft design, for low noise and emissions has been performed by Antoine [Antoine, 2004]. The design process was focused on conventional airframe and engine configurations, while the only engine varying parameter was the bypass ratio. The result was a propulsion system with BPR of 14.7 and noise reduction up to 8 dB. Another low noise aircraft design study has been conducted by Leifsson [Leifsson, 2006], where the propulsion system is not taken into account.

Extended studies on noise reduction design methods have taken place in the context of the ‘Silent Aircraft Initiative’ (SAI) project, such as the report from Benveniste, [Benveniste et al., 2005] and the publication of Diedrich, [Diedrich et al., 2006]. Benveniste shows an initial optimisation based on blended wing body and multiple fan propulsion system, focusing on the benefits and the challenges from using single and multi objective optimisers. However, basic engine cycle parameters, such as the Combustor Outlet Temperature (COT) and overall pressure ratio (OPR) are not included in the methodology. A different approach is followed by Diedrich, utilising a matrix to represent the propulsion system in the aircraft design method. The data of this matrix are produced by a commercial gas turbine performance code and are based on predefined engine cycle parameters.

Taking into consideration the conducted literature research, the present thesis proposes a noise oriented gas turbine design method that takes into account all of the thermodynamic parameters, targeting at a low noise, fuel efficient engine.

3.1.2 Parametric Analysis Description

The present work focuses on the preliminary design of innovative propulsion cycles, installed on novel airframes provided by the airframe team [Mistry, 2008]. In this context, the optimisation process has been focused on a detailed design-point engine analysis.

The tools that have been implemented and developed are framed by a parametric analysis module. This module uses an objective function in order to identify and quantify the trade off between noise and fuel consumption for defined mission. The decision of using parametric analysis instead of an optimiser has been taken because of the better understanding that such a process gives to the engineer. Moreover, any tradeoffs between conflicting targets, such as noise and diameter, become easily identifiable and handled.

The modules involved in the analysis are displayed in Figure 3-1 and are discussed in depth in following sections, while an outline of the method is given below.

The three main design variables; the engine bypass ratio (BPR), the overall pressure ratio (OPR) and the combustor outlet temperature (COT) are input to the first module; the Turbomatch gas turbine performance scheme. Having these variables determined, Turbomatch calculates the thermodynamic cycle at design point. This point has been set at Top of Climb (ToC), which is the most demanding condition of the flight envelope for the engine - maximum COT to inlet temperature ratio -, thus the most appropriate for sizing the propulsion system. For this reason, the thrust requirement and flight conditions at ToC are inputs to the method. In spite of this, the noise evaluation takes place at take-off, making imperative the need for defining thrust requirement, Mach number and altitude at off-design conditions, as well. As a result, the code is able to predict off design performance and noise emissions, at any off design point.

Essential input to the process is the polytropic efficiency of the components. In order to assume similar technological levels and be able to compare the various cycles, their polytropic –and not isentropic– efficiency is kept constant during the parametric analysis. In this manner, isentropic efficiency is calculated according to the pressure ratio of each component, using Equation 3-1. Additionally, the user has the option of determining the Compressor Work (CW) ratio for the Intermediate Pressure Compressor (IPC) and High Pressure Compessor (HPC) respectively. This ratio is expressed in pressure ratios that have an effect on isentropic efficiencies as well.

Equation 3-1

$$n_{is} = \frac{R_c^{\frac{\gamma-1}{\gamma}} - 1}{R_c^{\frac{\gamma-1}{\gamma \cdot n_p}} - 1}$$

In turbofan design the split of the flow into bypass and core adds an extra parameter to be taken into consideration; the fan pressure ratio (FPR) that affects the bypass-nozzle pressure ratio. However, FPR is not an independent variable. It is proven [Walsh, 2004] that any set of BPR, OPR and COT corresponds to an optimum value of FPR, which leads to maximum specific thrust and minimum specific fuel consumption. This condition is the result of the energy balance between the bypass duct and the core. In order to take this into consideration, an iterative loop of DP calculations is performed in order to obtain the optimum FPR. It should be noted that for varying FPR, core pressure ratio varies as well, in order to keep the OPR equal to the value defined by the optimiser.

At this point, it is worth mentioning that Turbomatch is not able to converge for any combination of the 4 parameters; i.e. for low COT and high FPR the low pressure turbine (LPT) that drives the fan can not provide the required work. As a result an error occurs. In order to solve this condition a self adopting process has been implemented in the routine, imposing empirical boundaries to FPR according to the values of BPR, COT and OPR.

After defining the fan pressure ratio, a Design Point calculation provides with the specific cycle characteristics. Following this, the engine mass flow is specified in order to satisfy the thrust requirement at ToC condition. In this scope, an iterative process has been implemented, as shown in Figure 3-1.

In a further step, off-design (OD) performance is calculated. The desired thrust, at off design altitude and flight velocity, is achieved by iterating the COT. For the purposes of this study, the off design flight condition has been set at the FAA noise measuring certification point for take-off, as shown in Table 3-4, while the thrust requirement is based on the airframe provided by the airframe design team [Mistry, 2008].

The results from Turbomatch are used as input to the Geometry module. This module provides with all essential engine geometric data and prepares the input files for the noise routine. As geometric data are described the fan annulus, velocity triangles, blade angle and blade thickness. The noise calculation is performed for coaxial jet and fan at take-off. In the case of installation above the wing - novel concepts - , the shielding effect is quantified, reducing inlet and aft fan noise levels received at the ground.

In order to predict the installed performance of the engine and the aircraft performance of the new configuration an aircraft performance module called 'Hermes' is implemented in the process. The inputs to this module are the airframe geometry, the flight mission and engine off- design performance data for the whole flight envelope. The result is the total mission fuel that has been consumed and the time duration. Something to be underlined is that during the design process, the engine size and weight vary substantially along with the cycle parameters affecting the installation drag and the aircraft empty weight. In order to take this effect into consideration, two models have been implemented in the method, providing 'Hermes' with engine weight and length, while the diameter is provided by the geometry module discussed in previous paragraph. The above presented process is repeated for a certain number of iterations, according to the range and step size of the design variable. A typical input file is found in the appendix.

3.2 Focusing Technique

A focusing technique has been implemented in the parametric method, aiming at considerable reduction of computational time. The idea behind this can be summarized in the following; instead of performing the calculations for the full range of the design parameters, the code focuses on the areas in the proximity of previous step's optimum, according to the objective function that is used. Such a condition reduces dramatically the number of iterations, achieving lower computational time, without losing in accuracy. The reason is that small incremental steps in BPR, OPR and COT correspond to small changes in the optimum solution. As a result, each set of iterations focuses on the proximity of previous steps optimum.

In further detail the process could be described as consisting of three main loops, one for each cycle parameter. The OPR loop is nested in the COT loop that is nested in the BPR loop. As a result, when the process begins an initial bypass ratio is defined. Followingly, COT is kept constant, while OPR iterates. After an optimum OPR is identified, COT increases, and OPR iterates, this time not for the full range but in the proximity of the previous COT-step's optimum OPR. The iteration for COT continues and an optimum COT is found. In a further step, BPR increases and the above process is repeated. The only difference is that COT range has decreased and focused on the proximity of previous BPR-step's optimum COT.

This technique, leads to a six fold reduction of computational time, without compromising the validity of the results, as the behaviour of the system is consecutive for the three design variables.

3.3 Objective Function

The main objective of the developed method is the minimisation of take-off jet noise and burnt fuel for a given mission. An objective function has been implemented in the process, in order to investigate the balance between these counteractive targets.

Jet noise has been chosen as the primary design goal, because of the nature of the study. Fan noise has not been taken into account, as it is strongly dependent on fan design parameters, such as tip Mach number, lining absorption, or even wing shielding rather than on the thermodynamic cycle. Moreover, fuel consumption represents the efficiency, the CO_2 emissions - linear relation with fuel - and the economic performance of the configuration. Equation 3-2 includes the definition of the objective function, while the design parameters and their range are illustrated in Table 4-4.

Equation 3-2
$$F(X) = \min\left(a_1 \cdot \frac{Fuel}{Fuel_{ref}} + a_2 \cdot \frac{Jet\_Noise}{Jet\_Noise_{ref}} \right)$$

where,

$$X = (BPR, OPR, COT)$$

and

$$a_1 + a_2 = 1$$

The reference values in the objective function correspond to baseline engine data, while the weight factors 'a_i' are set by the designer in order to determine the prime goal of the process. In the present study 'a_2' that corresponds to jet noise takes a higher value than 'a_1'. A typical module input file is discussed in detail in the Appendix (§9.3).

The range of the design variables imposes certain boundaries on the calculation. Additionally, an extra boundary condition is imposed. This condition, is related to the maximum diameter of the engine, and follows recommendations from the airframe team [Mistry, 2008]. The cycle design study has been performed for two airframes; a baseline and an advanced design. In the first case the parametric analysis is limited by the engine diameter and the process stops when this limit is exceeded. On the other hand, in the novel configuration, where alternative installation is proposed, the diameter limit plays a different role. When this limit is exceeded, the code changes the number of fans per engine, leading to distributed propulsion configurations.

3.4 Turbomatch Gas Turbine Performance Scheme

Turbomatch is an in-house one dimensional gas turbine performance code. It has the capability of design point and off design calculations, while its modular structure allows the user to assembly any engine configuration from a number of individual GT components (bricks). These attributes allow for using Turbomatch to model advanced propulsion cycles. As a result it Turbomatch is the core of the cycle design method, aiding into the design of novel thermodynamic cycles.

The working principle of Turbomatch is based on mass and energy balance, carried out through an iterative method, based on component maps. It has been validated against commercially sensitive data and further details can be found in the Turbomatch manual [Pachidis, 1999]. Additionally the Thermal Power MSc course notes from Pachidis [Pachidis, 2004] and the books from Walsh & Fletcher [Walsh & Fletcher, 2004] and Saravanamuttoo, [Saravanamuttoo et al., 1989] may give a further insight into the background of Turbomatch.

3.5 ‘Hermes’ Aircraft Performance Model

Another model that has been used in the present study is ‘Hermes’ Aircraft Model. It is able to predict the flight performance of any airframe-engine configuration. For any given mission profile, it produces data such as fuel burned, or flight duration. The implementation of Hermes in the design method, allows the engineer to optimise for minimum total fuel burned, instead of specific fuel consumption. This condition is beneficial, as the actual amount of fuel can be translated to operating cost, leading to useful conclusions relatively to the economic viability of the novel configuration. Moreover, fuel consumption is directly proportional to CO_2 emissions. An index of CO_2 can be calculated, assuming complete combustion of kerosene, at a value of 3.13169 kilos of CO_2 per kilos of fuel. As a result, the environmental impact is taken into account in the design.

The method includes the calculation of aerodynamic values of the airframe, according to aircraft theory [Jenkinson, 1999] and the implementation of Turbomatch for providing with engine performance data - fuel consumption and thrust - , for the three main flight segments; climb, cruise and descent. At each segment, an iterative process matches the airframe thrust requirement with engine thrust, calculates the mass of the burned fuel and subtracts it from the total aircraft mass. The model is in depth described by Laskaridis [Laskaridis, 2005a] and has been validated against published data, showing a deviation less than 1% [Laskaridis et al., 2005b].

In Figure 3-2 the flow diagram of 'Hermes' is illustrated. The main input to the code is the flight mission, containing details such as altitude, Mach number and engine settings for all the flight segments. The same file is used as input to the Turbomatch code, which calculates the thrust and SFC of the engine and produces a matrix that covers the whole flight envelope. Another file contains all the airframe geometry data, such as fuselage and wing dimensions, needed to predict the drag polar of the aircraft. The input files can be found in the Appendix (§9.6). The rest of the input is relative to the engine geometry - weight, length and diameter, crucial for the estimation of installation drag - produced by three empirical models, which will be discussed below.

3.6 Engine Weight Model

3.6.1 Model Description

As it has been previously mentioned, the weight of the propulsion system is significantly affected by parameters such as the BPR, OPR, COT and the year of manufacturing. Additionally, the effect of engine weight on total aircraft mass and performance is not negligible, inevitably leading to the need of a weight prediction method. On the other hand, in a preliminary study that covers a broad range of cycle parameters, a detailed calculation of the mass of the gas turbine is considered to be impractical, due to the need of a thorough geometrical design for each component. As a result, the implementation of a semi-empirical generalised procedure has been decided.

The method that has been proposed by Gerend [Gerend, 1970] is based on statistical correlations derived from a broad engine database. It takes into account the effect of bypass ratio, combustor outlet temperature, overall pressure ratio, air mass flow, or even technology level. Even though, the model dates back to 1970, moderate projections to future configurations have been found to give reasonable results. In this direction, the shift of the reference engine from a 1962 turbojet to the baseline of the present study (1985 turbofan), reduced the extrapolation-born cumulative prediction error. Additionally, for reasons of consistency with the present study, the air mass flow is defined at design point, which is top of climb, as opposed to sea level static used by Gerend.

As shown in Equation 3-3 the mass of the propulsion system is proportional to the air mass flow and to a number of correction factors. In order to implement these factors in the model, a number of mathematical expressions have been used, that have been found to fit the data published by Gerend. The correlation equation and its factors are summarised below:

Equation 3-3
$$WT = \left(\frac{WT}{Wo}\right)_{ref} \cdot Wo \cdot KENG \cdot \left[K_{gg} \cdot KHP + \left(1 - K_{gg}\right) \cdot KLP\right]$$

where,

WT	The total engine weight.
WT/Wo_{ref}	The reference engine weight divided by the air mass flow.
Wo	The air mass flow of the engine under examination.
KENG	=[KBPR][KY][KLIFE][KM][KDUCT] The correction factor referring to the whole engine.
K_{gg}	The ratio of core engine weight to total.
KHP	=[KT_4][KR_p][KW_e][KHX] The correction factor referring to the core.
KLP	=[KWo] The correction factor referring to the fan.

The analytical expressions and further discussion on the above mentioned correction factors can be found in Appendix(§9.1).

3.6.2 Model Validation

In order to obtain a level of confidence regarding the error involved in this method, the weight of the baseline engine (GE CF6-80C2 type) has been predicted and compared to GE CF6 certified weight. It is worth mentioning that the reference engine for this calculation is the one proposed by Gerend [Gerend, 1970], where the air mass flow is calculated at sea level static condition.

The results are summarised in Table 3-1. The table is divided in two columns, with the one at the left containing the values of the correlations and correction factors, and the second column illustrating the variable that has been used to derive each factor from the corresponding graph in [Gerend, 1970]. Finally, the calculated weight has shown a deviation less than 1.5% from the certified engine weight, documented in the FAA data sheet [FAA, 2000].

3.7 Engine Length Model

3.7.1 Model Description

In addition to weight, another engine dimension important to aircraft performance prediction and affected by the cycle parameters is the length. ‘Hermes’ uses as input the turbofan length and diameter in order to predict the installation drag, based on a semi-empirical method [Laskaridis, 2005a]. For that reason, a length evaluation model has been implemented into the cycle design method.

Gerend [Gerend, 1970] has proposed a semi-empirical method for evaluating the bare length of the propulsion system. This correlation is derived from a statistical analysis on a large engine database and is illustrated in Equation 3-4.

Equation 3-4 $L_{engine} = L_{ref} \cdot KLW_e \cdot KLBPR \cdot KLY \cdot KLR_p \cdot KIGV$

L_{ref} is the length of the reference engine, while the correction factors for air mass flow, year of manufacturing, BPR and OPR are discussed in Appendix (§9.2).

3.7.2 Model validation

The length prediction of the baseline engine has been evaluated against certified data – FAA data sheet [FAA, 2000]. The results are summarised in Table 3-2, which follows the same structure with Table 3-1. The reference engine in this calculation is the one proposed by Gerend [Gerend, 1970]. Moreover, the finally implemented length model utilises the baseline engine as reference, using the certified length – instead of the predicted – in order to eliminate the error of 4.6%.

3.8 Noise Estimation Tool

The noise calculation is performed by a tool prepared by G. Santos [Santos, 2005] in the framework of his dissertation thesis. This Fortran code implements a collection of semi-empirical noise routines found in the open literature. The generic structure of the code allows the simulation of test cases including fan and jet noise, atmospheric attenuation, ground reflection, flight correction and liner attenuation.

3.8.1 Jet Noise

The prediction of coaxial jet - apparent in turbofans - noise is based on SAE AIR 1905-3. This is a method developed by NASA in 1983 and published by SAE [SAE, 1985]. It determines the sound pressure levels (SPL) by interpolating from a model data base, taking into consideration a number of parameters, such as, velocity, area and temperature ratios, as shown in Table 3-3. It has been chosen because of its broad range of valid operation, essential for a study on ultra high bypass ratio cycles, where the area and velocity ratios take high values. Additionally, the maximum error involved in the noise prediction, as discussed in [SAE, 1985], is +2 dB.

During the parametric analysis some of the parameters shown in Table 3-3 reach or exceed their valid limits. In order to avoid such a condition, a number of check points in the code ensure smooth operation of the noise routine, by changing the number of fans per engine - reducing in this way the area ratio - and giving warning messages for the awareness of the user.

3.8.2 Fan Noise

A fan noise method based on Heidmann's model [Heidmann, 1979] and including further improvements from Kontos [Kontos et al., 1996] has been used for predicting the inlet and aft fan noise. This model is, also, a part of NASA's ANOPP code for aircraft noise [Gillian, 1982].

According to Heidmann, the calculation of fan forward noise is separated to broadband, discrete tone and 'buzz-saw', while the rearward propagating noise is the sum of broadband and discrete tone noise, only. The total noise is derived by adding up on an energy basis the above mentioned component spectra.

The main parameters of the calculation are:

- the fan mass flow,
- the total temperature rise,
- the relative inlet Mach number at the tip (at design and operating point),
- the rotor-stator spacing and
- the number of rotor and stator blades, connected to the tone cut-off effect.

Regarding the accuracy of Heidmann model, a maximum rms error of 5 dBs is involved in the calculation, according to [ESDU, 1998].

3.8.3 Additional Noise-Related Models

An accurate noise prediction needs to take into account a number of natural phenomena that occur during a noise certification process. In order to obtain a high level of accuracy, several routines from the open literature have been used and are discussed below:

Atmospheric attenuation

Atmospheric attenuation is the reduction of a wave's acoustic energy when it propagates through the atmosphere. It depends on ambient temperature, pressure and relative humidity and decreases for high values of these variables. Additionally, sound absorption is more evident at high frequencies. The model for the prediction of this effect is described in [ESDU, 1977] and is based on tabulated data, derived from experimental and real engine tests.

Ground reflection correction

The ground reflection correction takes into account the position (height) of the sound receiver. It adds a spectrum correction to the free field estimates, according to the reflection of noise at the ground, in order to provide with the measured spectrum. A method based on semi-empirical equations developed by Chessel [Chessel, 1977] and discussed in [ESDU, 1994] has been used in the noise code. Some parameters, important for the calculation, are the distance between noise source and receiver, the height of the receiver and the type of the ground.

Liner attenuation

Acoustical liners are a significant aid in noise suppression, especially in modern turbofans, where the fan is the major noise source. A model able to predict the noise absorption from current technology liners [ESDU, 2000] has been implemented in the noise code. A number of variables, such as the duct diameter and length, Mach number, or the type of the liner, strongly affect the noise attenuation. Finally, a validation against experimental data in [ESDU, 2000], has shown a maximum rms error of 2.5 dB.

Noise Shielding

Over-the-wing engine installations act beneficially in reducing forward and aftward propagating fan noise. In order to study this effect, the ESDU-79011 [ESDU, 1979] routine has been implemented in the noise model. As illustrated in Figure 3-3, the routine is able to predict the sound pressure levels spectrum attenuation, caused by noise diffraction round a barrier, which in this case is the wing leading and trailing edge, respectively. The most critical values in the calculation are the distances of the source and the observer from the barrier and the wedge angle β. The model has given attenuation levels in agreement to the calculations of Berton [Berton, 2000] and the measurements of Agarwal, [Agarwal, 2005], as discussed in §4.5.1. Further details on the method can be found in [ESDU, 1979] and [Pierce, 1974].

Combination of Noise Levels

As it has been previously discussed, the aircraft is considered as a group of noise sources, each one calculated separately. In order to predict total aircraft noise, the ESDU-66017 [ESDU, 1966], routine is used. This method determines the combined sound level resulting from two sources of known dBs. Any number of sources can be added by repeated combination of pairs of levels. Further details are available in [Harris, 1957].

3.9 Aircraft Noise Validation

The noise estimation tool has been validated against FAA noise data for the baseline aircraft. In this manner, useful conclusions have been made on the accuracy and the error involved in the noise predictions.

3.9.1 FAA Federal Aviation Regulation Part 36 Reference Procedure

The noise calculation is following reference procedures, according to Federal Aviation Regulation (FAR). These procedures and conditions are specified in FAR Part 36 and are presented below:

Reference atmosphere:

Sea level atmospheric pressure	101325 Pa
Sea level static temperature	298 K
Atmospheric relative humidity	70%
Zero wind	

Takeoff reference flight path, according to section B36.7:

- Maximum available thrust
- Thrust cutback at 300m
- Climb gradient of 4%
- Reference speed V2+19km/h

Approach reference flight path according to section B36.7:

- Approach angle of 3 degrees
- Steady approach speed at Vref+19km/h

Reference noise measurement positions, as shown in Figure 3-4:

- Sideline measuring point lies on a line, parallel to runway and at a distance of 450m, after lift-off of the aircraft.
- The maximum noise is calculated at an altitude of 442.5m for Stage-2 two engine aircraft, for maximum thrust available.
- Flyover reference noise measurement point is set at 6500m from start of takeoff roll. Approach measurement point is at a height of 120m.

Maximum noise is received when the aircraft is at minimum distance from receiver and that is the position chosen for the calculation of the dB(A) noise estimates. Table 3-4 shows the flight conditions (take-off and approach) that have been used for the prediction of dB(A) estimates, according to the above mentioned directives.

Baseline Aircraft

The CF6-80C2 settings are shown in Table 3-4. The table contains information for Bypass Ratio (BPR), Overall Pressure Ratio (OPR) and Combustor Outlet Temperature (COT) at three operating points. Finally, Table 3-4 depicts the engine thrust levels and the Specific Fuel Consumption (SFC). It is apparent that the engine operates at 51.4% of static thrust at the take-off condition, while it is throttled back at 19.4% at the approach certification point. The chosen thrust levels are in agreement to Bielak, [Bielak et al., 1999]. Full details of the noise calculation can be found in the Appendix (§9.5), while the baseline airframe and engine are discussed, in detail, in chapter 4.

The engine noise estimations, which have been produced according to the data of Table 3-4, are shown in Table 3-5. A breakdown of the noise into jet, inlet-fan and aft-fan gives a better understanding on the results of the individual noise routines that have been used. Additionally, it indicates the relative effect of each source on total engine noise, where fan appears to be the dominant noise source in both take-off and approach conditions.

The first row in Table 3-5 illustrates the aircraft noise estimations in dBA for a Boeing 767-300ER, powered by two GE CF6-80C2B6 turbofans, at take-off and approach condition, according to FAA/FAR-36. The comparison between predicted and FAA data shows a very good agreement for the approach case, where the error is less than 0.1%. In the take-off condition, however, a deviation of 6.6 dB is observed, due to the higher noise estimation of the fan, which is in agreement to [ESDU, 1998], where a maximum rms error of 5dB is documented. It should be, also, noticed that a number of assumptions in the design of the baseline fan - tip Mach number, rotor-stator spacing - may have caused this declination, in addition to the tendency of the Heidmann model to over-predict fan noise, as discussed by Antoine [Antoine, 2004] and Kontos, [Kontos et al., 1996].

The comparison with FAA data has shown that the noise tool can be used with confidence at lower engine settings, while at high power settings a maximum error of ~7% may be involved in the noise evaluation process.

3.10 Enhanced Parallel Compressor – Streamline Curvature Model

Gas turbine off-design performance is predicted by zero dimensional analysis methodologies –i.e. Turbomatch. Such methodologies are based on discrete component maps, treated as black boxes with inlet and outlet stations for exchanging averaged fluid values. As a result, any non-uniformities of the flow can not be taken into account. However, inlet distortion on the first compression system of a gas turbine can be critical for the operation of the engine. Moreover, this study involves the design of a half-embedded installation for providing noise shielding and reducing fan noise. However, such design leads to permanent distortion of inlet flow. Therefore, a method is needed for predicting the performance of the propulsion system.

In this direction, an enhanced representation of the fan component has been introduced in Turbomatch code, in order to provide with qualitative estimates of gas turbine performance under inlet distortion. This method is based on the combination of two techniques; streamline curvature (SLC) and parallel compressor (PC). The resulting model is a quasi 3D representation of the fan component in the following manner: the SLC predicts the fan performance under radial inlet profiles, while the parallel compressor simulates the effect of the inlet total pressure circumferential distortion. In this way, three dimensional input from CFD simulation can be used to assess the effect of half-embedded installation on engine performance and stability.

3.10.1 Literature Review

The severity of the effect of inlet distortion on compressor and gas turbine performance has been realised since the early stages of jet aviation, during the design of the first generation lift engines for VTOL applications. Since the initial observation that compressor stability limits are affected by non uniform inlet flows, various models have been proposed, in order to predict with accuracy, the results from extended experiments.

The work of Lieblein [Lieblein, 1957] is representative of the experimental research on the inception of surge on compressor blades, where the effect of incidence angle on loss characteristics is investigated. The attenuation of circumferential flow distortion, through multistage compressors has been studied by Plourde [Plourde et al.,1968], while Callahan and Stenning [Callahan & Stenning, 1969], have presented experimental and theoretical results on the attenuation of the distortion that takes place upstream the compressor.

The Parallel Compressor Model that is discussed, thoroughly, in following sub section was firstly proposed by Pearson & McKenzie [Pearson & McKenzie,1959] and has been extensively used since then. The capabilities of the Parallel Compressor have been investigated by Reid, [Reid, 1969], who showed the effect of the angle of spoiling on compressor surge limits and the deviation between experimental and theoretical results. Following this, he identified the critical distortion angle (θ_{crit}) –unique for every compressor– above which, the loss in surge margin reduces significantly.

During the seventies, significant research has been undertaken by NASA. The effect of circumferential distortion on the performance of the gas turbine has been investigated by Calogeras, [Calogeras et al., 1971] and Milner, [Milner et al., 1975]. Their reports present the shift of the operating line of the J85-GE-13 turbojet, due to various distortion patterns. The stability of the same engine under combined inlet temperature and pressure distortion has been studied by Braithwaite and Graber [Braithwaite & Graber, 1973]. A simple Parallel Compressor Model was used to predict the loss in surge margin and a reasonable agreement was achieved between experimental and theoretical results. As an extension to the Parallel Compressor Method, analytical expressions of compressor stability and compressor-diffuser interaction have been developed, such as the paper from Greitzer and Griswold [Greitzer & Griswold, 1976].

Another direction of expanding Parallel Compressor theory has been presented by Wenzel and Blaha [Wenzel & Blaha, 1977]. They investigated the dynamic response of a J85-13 compressor to various transient inlet distortion patterns. The model uses in parallel a steady-state uniform inlet compressor and a stage by stage model (able to calculate dynamic perturbations), both discharging to the same plenum. Similarly to Wenzel, that coupled a dynamic compressor model using Parallel Compressor theory, Mazzawy [Mazzawy, 1977] suggested a multiple segment parallel compressor model. This model utilises several dynamic models in order to account for the cross-flow between the segments upstream and through the compressor, along with any other unsteady phenomena. In the same direction, Elder, [Elder, 1985] presented a dynamic model, based on parallel compressor theory, that takes into account sector interaction. In this way this model does not require a predefined value for θ_{crit}. In the mid-seventies, while the interest was turned to turbofans, NASA focused on the study of transonic fans. As a result, radial [Schmidt et al., 1978] and circumferential [Sanger, 1976] distortion effects were measured on a transonic fan [Urasek et al., 1979].

In the direction of studying the transient performance –rotating stall– of compressors, Moore and Greitzer developed a model [Moore & Greitzer, 1986(a)], [Moore & Greitzer, 1986(b)] in order to predict the growth and decay of a rotating stall cell. This model comprises three non-linear 3rd order partial differential equations for pressure ratio, average and disturbed values of mass flow coefficient and it accounts for circumferential distortion, only. Followingly, Moore-Greitzer's model, surge inception has been subject of research, with some examples being Longley and Hynes [Longley & Hynes, 1990], McDougall, [McDougall et al., 1990] and Markopoulos, [Markopoulos et al., 1999]. Further information on stability of compression systems and rotating stall can be found in the papers of Greitzer [Greitzer, 1981] and Moore [Moore, 1983].

Even though most of the past research has focused on circumferential distortion, significant work on the effect of radial perturbations has been undergoing in Cranfield University. A 2D turbofan model able to predict the engine performance under radial inlet profiles has been presented, [Yin & Pilidis, 2002], [Yin et al., 2001]. In such model the fan is represented by experimentally derived radial maps. A different approach has been followed by Pachidis, [Pachidis et al., 2007], who proposed a 2D streamline curvature method for predicting compressor performance. This model is fed with inlet radial profiles and can be used in coupling the simulation of an axisymmetric intake by CFD with a gas turbine performance code [Pachidis, 2006]. This thesis provides an enhancement to the prediction method, by extending the streamline curvature to quasi 3D, through coupling Parallel Compressor theory with streamline curvature, enabling it to accept 3D inlet profiles from a CFD simulation.

3.10.2 Parallel Compressor

The Parallel Compressor (PaCo) method was a breakthrough in compressor-under-distortion modelling, when proposed by Pearson and McKenzie, [Pearson & McKenzie, 1959]. It has been referenced and applied in several models since then, as discussed in the previous section. The reason is its simplicity that allows the engineer to account for inlet distortion effects with relatively low computational effort.

Parallel Compressor Theory

The rationale of the model is the split of the compressor into two separate compressors, as shown in Figure 3-5. Both of these compressors operate separately and discharge to a common plenum. Their main difference, though, is the inlet condition that varies. As a result, one segment operates under clean inlet flow, while the second one is subject to low inlet pressure. This assumption is based on the observation that there exist areas of low and high pressure on the Aerodynamic Inlet Plane (AIP) and the application of averaged pressure on simple compressor can not predict accurately the effect of distortion. On the other hand, these two areas can be connected to two separate segments, with no mixing between them, which is valid for modern compressors with narrow rotor-tip clearance and relatively small rotor-stator spacing.

The main assumption that connects the two compressor segments is their discharge to common plenum. This means that outlet static pressure and flow angle are the same for both sectors, as no mixing is assumed. Such an assumption is valid, due to the presence of stator blades, which are designed for creating uniform exit flow conditions, while it is established by several experimental studies, such as the one from Sanger, [Sanger, 1976]. In this study, very low deviation of static pressure was shown at the fan exit plane.

Under the above mentioned assumptions, each sector operates on the same rotational speed, as they have the same non-dimensional map. As a result, the ‘clean’ segment (high inlet total pressure) operates at higher mass flow and lower pressure ratio, in order to give the same exit static pressure with the ‘distorted’ compressor segment (low inlet total pressure). The dimensional mass flow is calculated using Equation 3-5. In a further step the overall compressor performance is calculated after appropriate averaging between the two sectors. Exit P_t and mass flow are defined by area averaging (Equation 3-6 and Equation 3-7), while T_t by mass averaging (Equation 3-8). The term ‘θ’ is the angle of extend of each sector (Equation 3-9) and it represents area, due to circumferentially constant radius.

Equation 3-5

$$m_i = \frac{Q_i P_{ti}}{\sqrt{T_{ti}}} \cdot \frac{\theta_i}{360^o}$$

Equation 3-6

$$P_t = \frac{\theta_1 P_{t1} + \theta_2 P_{t2}}{360^o}$$

Equation 3-7

$$m = m_1 + m_2$$

Equation 3-8
$$T_t = \frac{m_1 T_{t1} + m_2 T_{t2}}{m}$$

Equation 3-9
$$\theta_1 + \theta_2 = 360^o$$

The aforementioned method has been widely used for defining the surge limit of the compressor. In this process, the surge limit of the 'clean' speedline is assumed to be the same for 'clean' and 'distorted' sectors. As a result, when the 'distorted' one reaches this limit, the compressor is assumed to enter the surge region and the averaged values of P_t and non-dimensional mass flow are the 'distorted' surge limit. This surge criterion has been broadly used in bibliography, such as [Cumpsty, 1989] and [Seddon, 1985]. It is based on the assumption of using the same non-dimensional map for both sectors as stated in the previous paragraph. As a result a reduction of the surge margin can be qualitatively analysed.

Parallel Compressor Performance & Enhancement

In the scope of this thesis several modifications have been applied on simple parallel compressor method. One is the increase of the number of circumferential segments to more than two, which necessitates the application of a correction factor, while the model has been modified in order to account for varying fan nozzle area.

In order to realise the necessity of the various modifications, a discussion on the simple parallel compressor performance follows. Figure 3-8 illustrates the effect of magnitude of distortion on surge pressure ratio and mass flow. It is obvious that inlet distortion has a linear effect on loss in surge pressure ratio, as higher distortion leads to lower 'distorted' exit static pressure, pushing to higher mass flow the 'clean' sector operating point. This is not the case for the mass flow, though, because surge margin loss is limited by choking. Therefore, in each case it depends on the gradient of the corresponding speedline. This observation, highlights the dependency on speedline gradient and the strong effect of distortion on pressure ratio, thus special interest is given in the loss of surge pressure ratio.

In addition to the magnitude of distortion, the area of the distorted sector has a critical effect on the performance prediction of the model, as discussed by Longley & Greitzer, [Longley & Greitzer, 1972] and Reid, [Reid, 1969]. This attribute is clearly shown in Figure 3-9, where parallel compressor prediction is compared to experimental data provided by Reid, [Reid, 1969]. From these data, the existence of a critical angle becomes obvious. For extent of distortion, lower than this angle, the negative effect on surge pressure ratio diminishes. This attribute can not be predicted by simple parallel compressor model. The reason is that parallel compressor presents a linear relation between the extent of spoiled sector and surge pressure ratio loss, as this is the result of area averaging between the two compressors. In order to minimise this over-prediction of surge pressure ratio loss, a correction is suggested, based on the critical angle θ_{crit}, which in the case of Figure 3-9 appears to be 90^o. This correction affects the averaging between the circumferential sectors. The angle of extent of the most spoilt sector is modified according to the following equation.

Equation 3-10 $\theta'_{dist} = \theta_{crit} + (\theta_{crit} - \theta'_{dist})$ for $\theta_{dist} < \theta_{crit}$

$\theta'_{dist} = \theta_{crit}$ for $\theta_{dist} > \theta_{crit}$

The implementation of the aforementioned correction allows for the modelling of narrow distorted areas and thus the use of more than two circumferential sectors, where applicable. As a result, the number of circumferential sectors can vary according to the inlet flow pattern, as it is discussed in §3.10.5.

Another modification on the parallel compressor corresponds to predicting in a qualitative way the distortion amplification downstream the fan due to varying fan nozzle area. This model uses Q-function at the stator exit and nozzle exit, having as input the area ratio between these two stations. A significant assumption is made, regarding no cross-flow between the parallel segments. However, as discussed by Longley & Greitzer, [Longley & Greitzer, 1972], this model is able of producing realistic results. Figure 3-10 illustrates the effect of nozzle area on loss in surge limits. It becomes obvious that the use of convergent nozzle with area 80% of fan exit, leads to ~50% improvement in surge loss for PR, ~25% for mass flow and ~100% for isentropic efficiency.

3.10.3 Streamline Curvature

The core of this distortion prediction method is the streamline curvature (SLC) compressor model, developed by Pachidis, [Pachidis, 2006] and Templalexis, [Templalexis, 2006]. This model, has replaced the default 0D compressor map in the Parallel Compressor model. In such way, higher fidelity is achieved, through analysing the effect of radial distortion inlet patterns on compressor performance. This section discusses briefly the method, while full description can be found in [Pachidis, 2006] and [Templalexis, 2006].

The SLC is an inviscid through-flow analysis method, in which empirical correlations are used to account for viscous losses. The equations implemented in the model are based on axisymmetric, compressible, inviscid flow through the compressor. As a result, the law of conservation of angular momentum (Equation 3-11) includes terms for pressure forces, derivative of velocity, centripetal acceleration and coriollis acceleration. In a further step, the gradient of meridional velocity is calculated from the full radial equilibrium equation (
Equation 3-12), which is derived from Equation 3-11.

Equation 3-11

$$-\frac{1}{\rho}\nabla P = \frac{DW}{Dt} + \omega\times\omega\times r + 2\omega\times W + F$$

Equation 3-12

$$\frac{\partial V_m^2}{\partial s} = V_m^2 2\cos^2\alpha \left[\begin{array}{l} \dfrac{\cos(\varepsilon+\gamma)}{R_c} - \dfrac{\tan\alpha(\partial\alpha/\partial s)}{\cos^2\alpha} + \\ \sin(\varepsilon+\gamma)\left(-\dfrac{1}{\cos(\varepsilon+\gamma)}\dfrac{\partial\varepsilon}{\partial s} + \dfrac{\tan(\varepsilon+\gamma)}{R_c} - \dfrac{\partial\ln(rp)}{\partial m} \right) \end{array} \right] +$$

$$2\cos^2\alpha\left(\frac{\partial I}{\partial s} - 2\cos\gamma\omega(V_w - U) - T\frac{\partial S}{\partial s} \right)$$

Equation 3-13 $$m_j = \int \overline{\rho_j}\,\overline{V_{mj}}\,dA$$

The meridional velocity is calculated by solving the above equation, with mass continuity as constraint.

Equation 3-12 and Equation 3-13 are solved iteratively. After a first guess of the curvature of the streamlines, the radial distribution of the meridional velocity at the blade leading edge is calculated. Taking into account blade geometry, the velocity triangles, entropy and enthalpy rise are calculated and the meridional velocity distribution at blade trailing edge is used for establishing the mass flow, in order to check for continuity. The iterations are based on mass flow convergence, while the streamtube mass flow is used to determine the radial position of each streamline.

The SLC model has been validated against published data by Pachidis, [Pachidis, 2006] and Templalexis, [Templalexis, 2006]. They have used fan published data, [Urasek et al., 1979], [Schmidt and Ruggeri, 1978], and good quantitative and qualitative agreement between measured and SLC results has been shown, [Pachidis et al., 2007].

3.10.4 Coupled PaCo-SLC model

In the previous two sections two widely used models have been described; the parallel compressor, able of predicting performance under circumferential inlet distortion and the SLC for high fidelity compressor modelling with radial inlet profiles. Coupling these two methods can provide a quasi 3D fan representation tool that can account for 3D distortion phenomena. Figure 3-6 illustrates this extended parallel compressor model.

The rationale behind this method is to replace the non-dimensional fan map with an SLC fan model. As a result, each segment's operating point is not the result of interpolation from a map, but it is calculated by the SLC code which is embedded in the Parallel Compressor model. In this way, any interpolation-related errors are avoided, especially in the case of inlet temperature distortion and the code implementation of the method is described below.

The PaCo-SLC code is written in Fortran 90 and has four main subroutines (Figure 3-7); one for reading the input data (pc_data_input.f90), one for defining the parallel sectors (pc_divide_circumference.f90), one for the main parallel compressor process (pc_main.f90) and a subroutine for writing the outputs (pc_write_results.f90). In the subroutine 'pc_data_input.f90' data such as mass flow, inlet pressure and temperature profiles, number of segments or angle of extend of each sector are input to the code. A typical input data file (pc_input.dat) is shown in the Appendix (§9.8). Subroutine 'pc_divide_circumference.f90' is used for dividing the fan annulus according to the extent of distortion and the desired number of circumferential segments. After all input is defined the parallel compressor method is executed in 'pc_main.f90', where the 'Compressor2D_MainProgram.f90' SLC model is called several times. Finally the results, such as radial distributions of exit values for each circumferential sector and averaged compressor performance are written in 'pc_output.dat' data file. A typical output file is shown in the Appendix(§9.14).

As already discussed in §3.10.2, the parallel compressor model is assuming two or more circumferential sectors, operating under different inlet conditions and discharging to the same plenum, thus static pressure. This is modeled by an iterative process, where the initial mass flow from the input is used for running SLC for the most distorted section. In a further step, the exit static pressure of this section is calculated and the operating point of each one of the rest of the circumferential sectors is found after an iterative process. In this process Newton Raphson method is used for varying the sector mass flow and calculating the deviation of the sector's mass flow averaged P_{st} from the distorted sector's P_{st}. It should be noted that averaged values of static pressure have been used, as a complete radial concurrence of P_s for all segments would be impossible. This is due to large deviations of inlet radial profiles between the sectors. Additionally, constant fan geometry leads to a monotonic relation between averaged outlet pressure and mass flow. After every sector's operating point is defined, averaging takes place according to the equations presented in §3.10.2.

3.10.5 Code Versions of PaCo-SLC

In the scope of this thesis several versions of the PaCo-SLC model have been created. Firstly, a reference parallel compressor model decoupled from the SLC model was built. It was followed by a coupled PaCo-SLC version for validation and calibration and a PaCo-SLC version using a quasi 3D intake map –§5.5. Further versions refer to the coupling of PaCo-SLC with Turbomatch gas turbine modelling code, with a coupled and a decoupled versions existing.

Decoupled PaCo Model

This model is built in order to be used as a reference to the rest. It is operating on speedlines provided by several runs of the streamline curvature code and uses linear interpolation. No corrections are taken into account, as it is a demonstrator of basic parallel compressor theory.

PaCo-SLC (Validation/Calibration)

This model uses all the corrections that have been presented and is used for the validation and the calibration of the fan model of this study. As a result, radial profiles for all the circumferential sectors are input manually, in the 'pc_input.dat' file, and the user has absolute control over the number of segments and the circumferential extend of the most distorted area. This allows the, in depth, investigation of the model.

PaCo-SLC (Intake Map)

This version of the model has been used for the prediction of engine performance under distortion produced from a real half-embedded intake –§5.5. An intake map data file is input to the code providing with radial profiles in 8 circumferential positions at several operating points. The number of sectors and the extent of spoiled sector are not chosen, but calculated, based on the distortion index K. In further detail, the distorted area θ_{dist} is the area of the AIP operating under inlet –radially area weighted– P_t, lower than the averaged P_t of the whole annulus. Consequently, the number of segments is related to this minimum area; i.e. a θ_{dist} 180^o does not allow for more than 2 circumferential sectors, while a θ_{dist} of 45^o would allow for 8 segments.

Equation 3-14

$$K = \frac{\overline{P_t} - \overline{P_{t\_distorted}}}{\overline{P_t}}$$

PaCo-SLC (Turbomatch)

The aim of the PaCo-SLC model is to aid in the prediction of the effect of inlet distortion on overall performance of the propulsion system. As a result, a version of the 'PaCo-SLC_Intake_Map' model has been created and embedded in Turbomatch Code. A new subroutine has been created in the Compressor brick of Turbomatch, calling the PaCo-SLC executable, instead of performing linear interpolation from standard compressor maps.

An issue relative to this model is that PaCo-SLC returns a different mass flow from the one given from Turbomatch. As a result, convergence problems to Turbomatch would occur, as the fan would operate under different mass flow than the one guessed by Turbomatch main loop. In order to surpass this obstacle, an iterative loop has been added, iterating PaCo-SLC for mass flow. The result is a fully coupled Turbomatch-PaCo-SLC engine model, able to predict any gas turbine operating point. A major drawback, though, is the high computational time, as the parallel compressor calls SLC several times for each sector, and compressor brick calls PaCo-SLC several times, while, Turbomatch may iterate several times before convergence occurs, leading to high computational effort. In addition to this, during the iterations, there is the risk of SLC falling in convergence oscillations, something that prevents convergence.

PaCo-SLC (Fan Map Production)

This version is based on the 'PaCo-SLC_Intake_Map' and differs from the aforementioned in the fact that it is not embedded in Turbomatch but it is manually used for producing a detailed map of the fan. In this direction an extra output data file is created, listing the operating point for each run. This version is useful for plotting the full fan map. In a further step the map is installed in Turbomatch in order to produce the full operating line of the engine model.

3.10.6 Model Validation-Calibration

This section describes the validation and calibration process of the PaCo-SLC model. It has been already mentioned that the SLC software has been validated in [Pachidis, 2006] and [Templalexis, 2006] for uniform and radially distorted inlet. Additionally, validation of the parallel compressor model can be found in several publications such as [Pearson & McKenzie, 1959] and [Reid, 1961]. In the following paragraphs, the combined PaCo-SLC model is compared to measured data.

For the purposes of validation, fan experimental data are compared to the model. The fan is the NASA TP 1294, presented in [Sanger, 1976], while the SLC geometry is based on the first stage of the NASA TP 1493 two-stage fan. The design point data of the fan are listed in Table 3-6, where their close similarities are obvious. For this reason and due to the fact that SLC model had strong convergence issues with any other geometrical input the validation and calibration of the model was based on these two fans.

The process of validation/calibration includes the comparison of plain parallel compressor and PaCo-SLC results to experimental data from Sanger, [1976]. In a further step, the number of circumferential sectors, thus the extent of the distorted sector, has been varied in order to identify the critical angle of the fan. This angle is expected to be the one, for which, the correction will give results closest to the experimental. The rationale behind this process is that the critical angle which is unique for every compressor gives the best matching between modeled and measured data, as shown in Figure 3-9. In such way, the model is calibrated to the experimental results for further use, such as under computationally obtained inlet profiles.

Figure 3-11 illustrates the total pressure inlet profiles at the AIP of the fan. These profiles are obtained from [Sanger, 1976] and show a region of step reduction of P_t due to the presence of a 90^o-extent screen upstream the fan inlet. The distorted area angle 'θ_{dist}' equals to 120^o, and the distortion index 'K' is calculated at 7.75%. The radial variation of total pressure is taken into consideration in the model, and P_t at each radial position is the product of area averaging, according to the number of circumferential sectors. Some representative examples are shown in Figure 3-12, Figure 3-13 and Figure 3-14 for two, three and four sectors, respectively.

Several models have been created from these data –the input data is included in the Appendix (§9.8). In a first step, a plain parallel compressor is used, with two or four circumferential segments, and area-weighted inlet total pressure for each segment. This model has the role of baseline. Additionally, several PaCo-SLC models for 2, 3 and 4 circumferential sectors have been created, corresponding to sector angles of 180^o, 120^o and 90^o respectively. The use of various sector areas gives an insight into the performance of the PaCo-SLC. Moreover, various inputs are used in the PaCo-SLC model. Constant inlet P_t distribution for each circumferential sector has been compared to radial distribution of P_t, in order to asses the effect of radial distortion on the solution. In a further step, the 'θ_{crit}' correction is applied to be compared against the experimental data and the plain version, after defining 'θ_{crit}'.

The calibration process involves the identification of compressor critical angle, as discussed above. In this scope, a range of critical angles is decided, varying from 90^o to

180^o. In a further step, the correction range is applied to PaCo-SLC results with two, three and four segments, as shown in Figure 3-15. The critical angle of the particular fan is the one exhibiting lowest deviation from the experimental results, for all the models as illustrated in Figure 3-16. In Figure 3-16, it becomes obvious that 'θ_{crit}' equals to 130^o. This value is used in the comparison of the models that follows.

Following the calibration of the model, final results are illustrated in Figure 3-17 and Figure 3-18 where pressure ratio and Δ(efficiency) (Equation 3-15) are plotted against corrected mass flow per unit area and the following conclusions are extracted. In a first step a comparison between clean inlet speedlines shows good agreement between experimental and numerical results, especially in the near-surge region. This allows for using with confidence the model for comparing the loss in surge limit from the various models. As shown in Figure 3-17 the standard parallel compressor and the PaCo-SLC with and without radial distribution exhibit similar levels of surge pressure ratio loss. This is because radial distortion is relatively low compared to circumferential. On the other hand, the standard PC exhibits much lower levels of loss in efficiency, according to Figure 3-18, while efficiency prediction from PaCo-SLC is very close to the experimental result. Figure 3-17 shows a significant difference between the 2-sector models and the rest. This happens due to the fact that the low-pressure sector is greater than the extent of circumferential distortion. As a result, the circumferentially averaged total pressure includes regions of higher pressure resulting in lower distortion (higher averaged values). This condition is established by comparing Figure 3-12, Figure 3-13 and Figure 3-14, where it is obvious that distortion levels are lower in the case of two-segments.

Equation 3-15

$$\Delta(efficiency) = \frac{\eta_{clean} - \eta_{distorted}}{\eta_{clean}}$$

The implementation of 'θ_{crit}' correction moves surge limit towards the experimental value, as it is clearly shown in Figure 3-17 and Figure 3-18. Especially the models with 3 and 4 sectors (which include in one sector the whole region of low inlet pressure), when corrected, lay in the close proximity of the actual value of surge limit (pressure ratio mass flow and isentropic efficiency). This gives a strong confidence for using the PaCo-SLC model for the prediction of the effect of distortion on fan performance, at least in a qualitative manner.

Tables of Chapter 3

CF6-80C2

Coefficient		Variable	
WT/Wo_{ref}	14	1962 turbojet	
Wo [kg/s]	795	Take-Off	
KBPR	0.45	BPR	5.15
KY	0.45	Year	1985
KLIFE	1.07	Long Life	
KM	1	Subsonic	
KDUCT	1	Short Duct	
KENG	0.21668		
KT4	1.3	δCOT [^{o}F]	800
KR_p	1.45	OPR	31.5
KW_e	1.1	We [kg/s]	154.4
KHP	2.0735		
KLP	1.6	KW_o	1.6
K_{gg}	0.41	BPR	5.15
Weight	4326.7	Predicted	
Weight	4386.2	Actual	
Error	1.36	%	

Table 3-1: Engine weight model validation.

CF6-80C2

Coefficient		Variable	
Lref	2.159	1962 turbojet	
KLBPR	1.39	BPR	5.15
KLY	0.73	Year	1985
KLRp	1.41	OPR	31.5
KLWe	1.32	We [kg/s]	154.4
Length	4.078	Predicted	
Length	4.274	Actual	
Error	4.6	%	

Table 3-2: Engine length model validation.

Parameter		Min	Max
Jet velocity to ambient sound speed	Vjet/ao	0.3	2
Jet temperature to ambient	Tjet/To	0.7	4.5
Bypass(secondary) velocity to core(primary)	Vs/Vp	0.02	2.5
Bypass area to core	As/Ap	0.5	10
Bypass temperature to core	Ts/Tp	0.2	4

Table 3-3: SAE AIR 1905 Method 3 parameters and recommended range.

Baseline Engine	SLS	Take Off	Approach
According to FAR-36			
Altitude [m]	0	442.5	120
Mach	0	0.3	0.23
Engine Settings			
BPR	5.15	5.69	5.88
OPR	31.5	23.5	12.6
COT [K]	1615	1446	1200
Performance			
Thrust [kN]	267.5	137.5	51.9
SFC [mg/(Ns)]	9.8	12.3	14.4

Table 3-4: Baseline engine parameters at the FAA noise certification points.

Baseline Engine	Take Off	Approach
FAA B767-300ER	79.1	89.3
Jet	70.8	60.1
Inl Fan	81.9	80.7
Aft Fan	82.6	87.9
Total Engine	85.6	88.7
Airframe	70.1	80.0
Total Aircraft	85.7	89.3

Table 3-5: Baseline engine noise breakdown estimations [dBA] against FAA data.

	NASA TP 1493	NASA TP 1294
Pressure Ratio	1.59	1.574
Temperature Ratio	1.167	1.17
Is. Efficiency	0.848	0.816
Mass Flow [kg/s]	33.248	29.484
RPM	16042.8	16100.0
Tip Speed [m/s]	428.9	424.6

Table 3-6: Design point data comparison between NASA TP 1493 and NASA TP 1294 fans.

Figures of Chapter 3

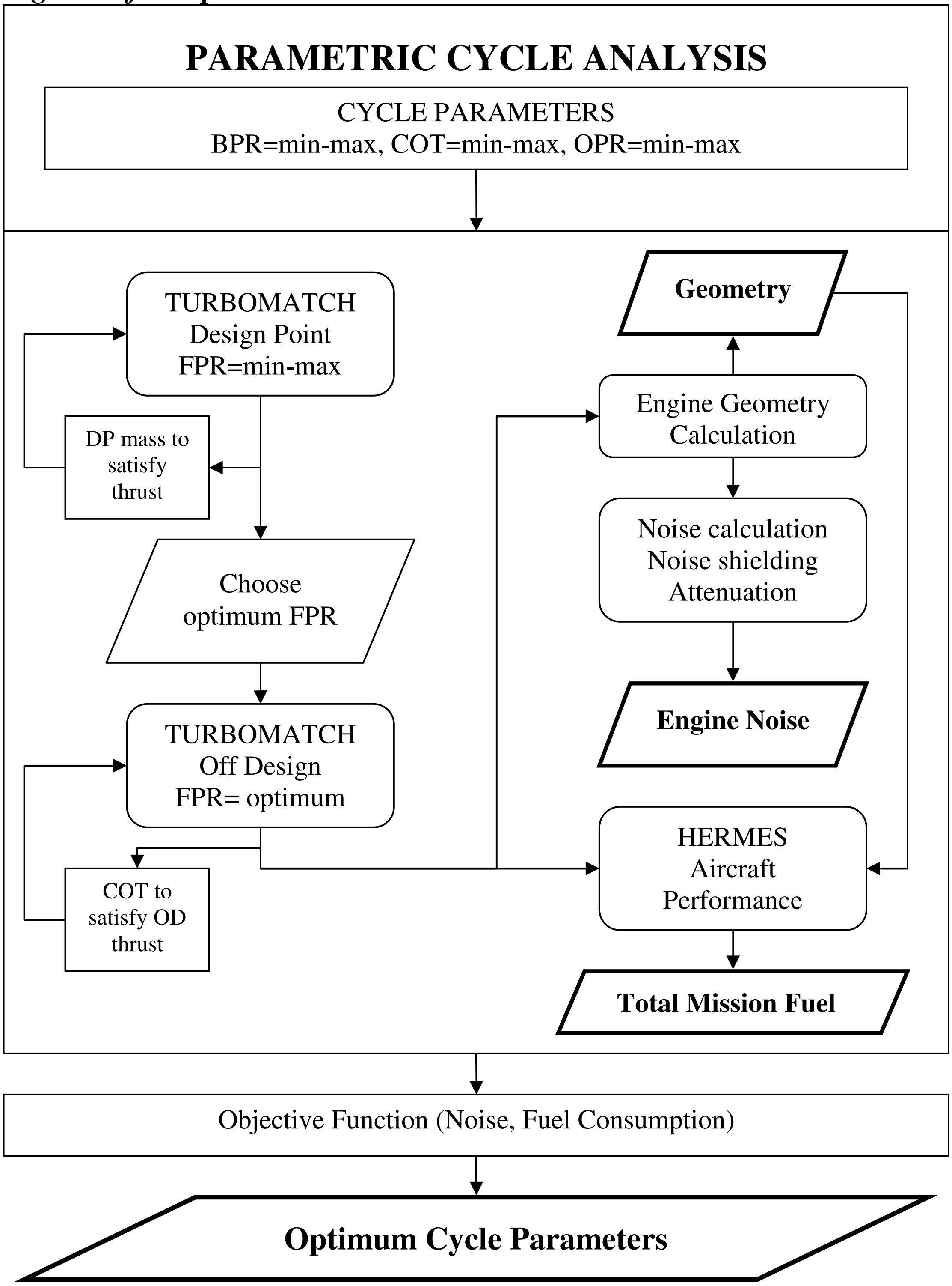

Figure 3-1: Parametric analysis flow diagram.

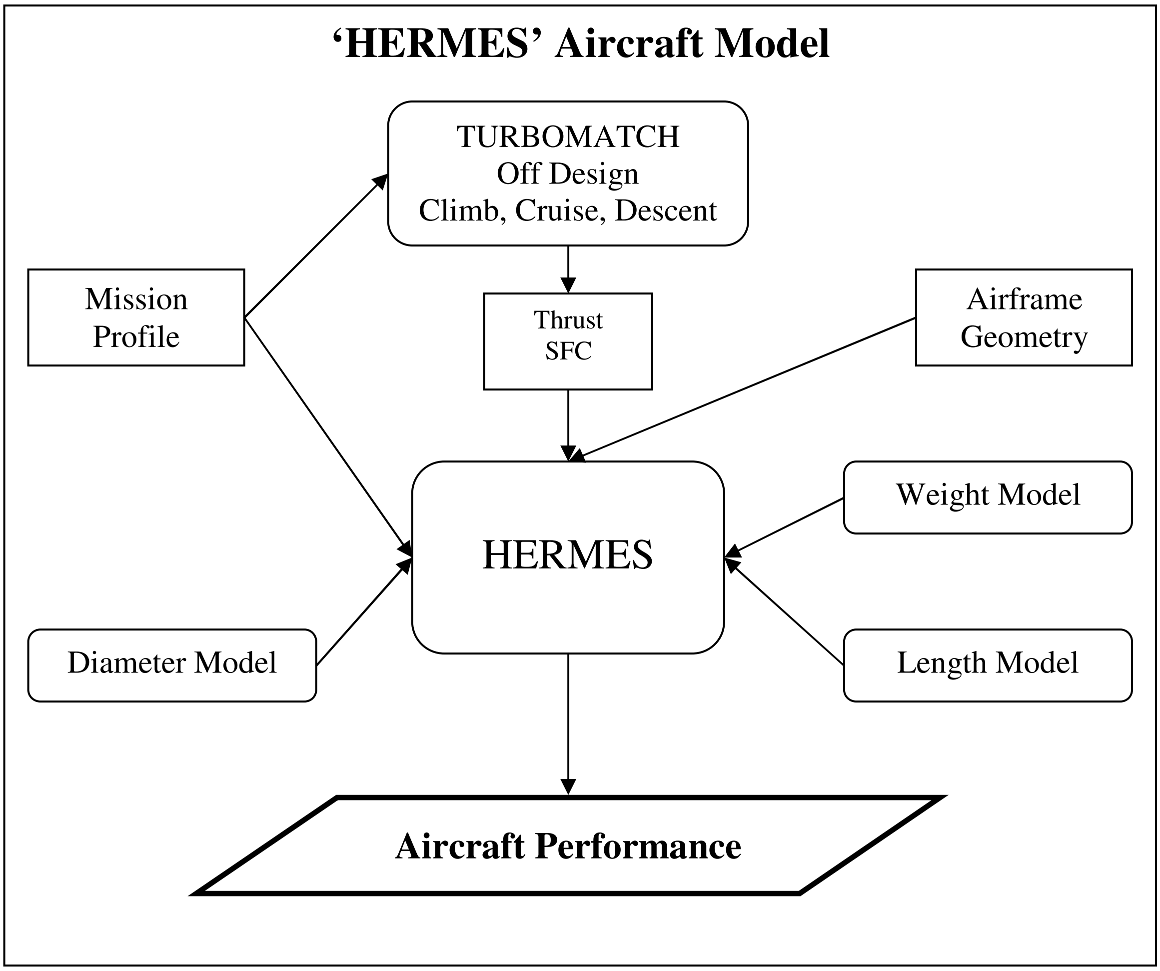

Figure 3-2: 'Hermes' flow diagram.

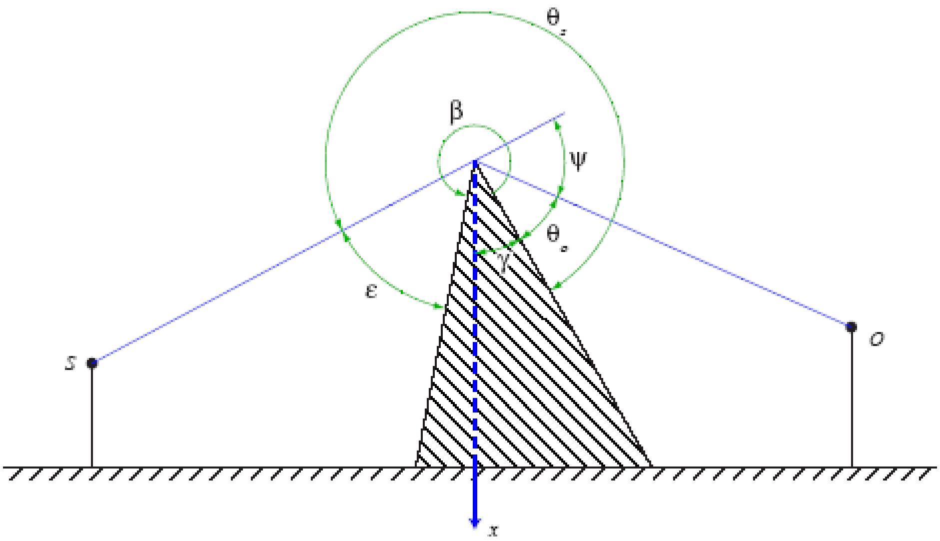

Figure 3-3: Schematic of wing leading edge, acting as a noise barrier, [ESDU, 1979]

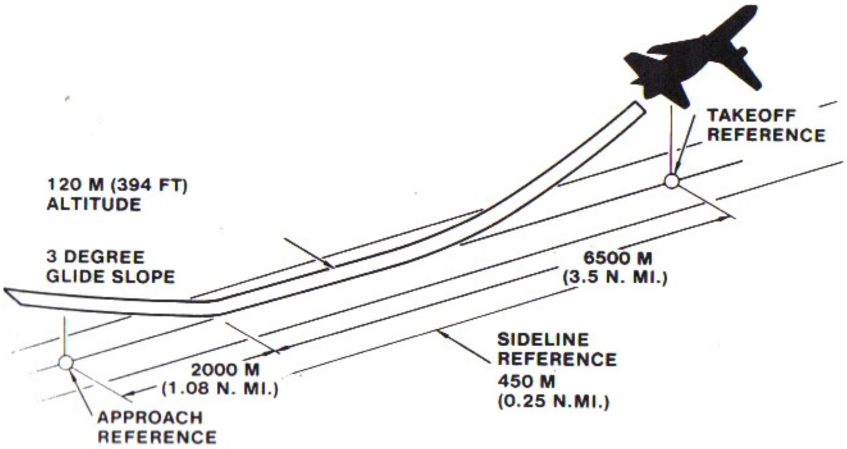

Figure 3-4: Noise certification reference positions [Smith, 1989].

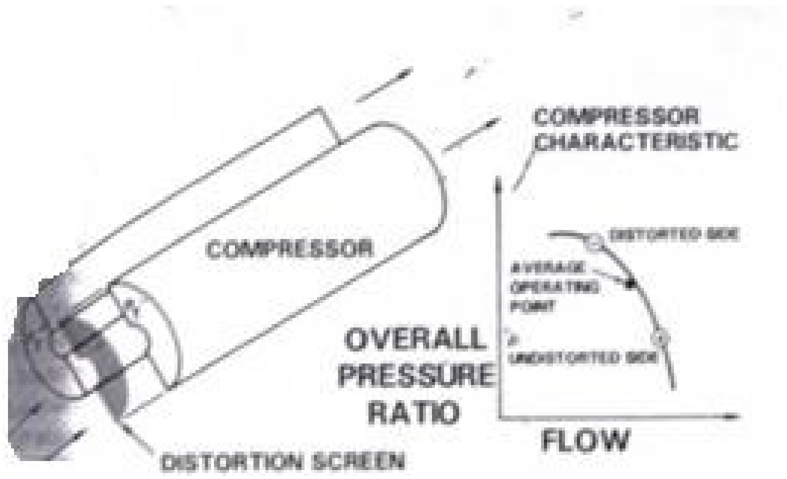

Figure 3-5: Parallel compressor concept.

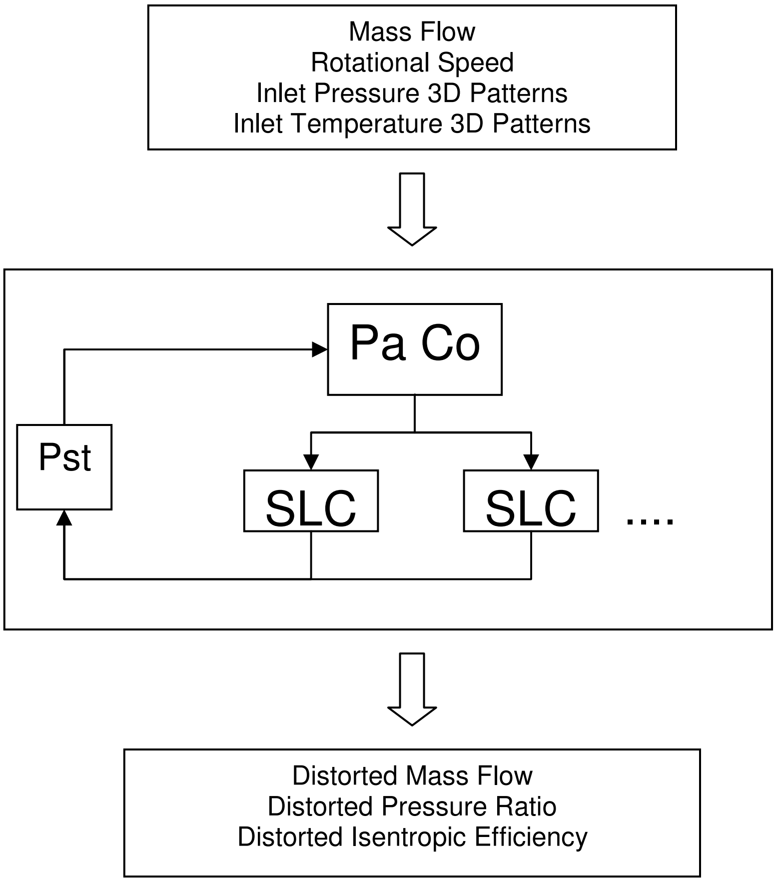

Figure 3-6: Enhanced PaCo-SLC model.

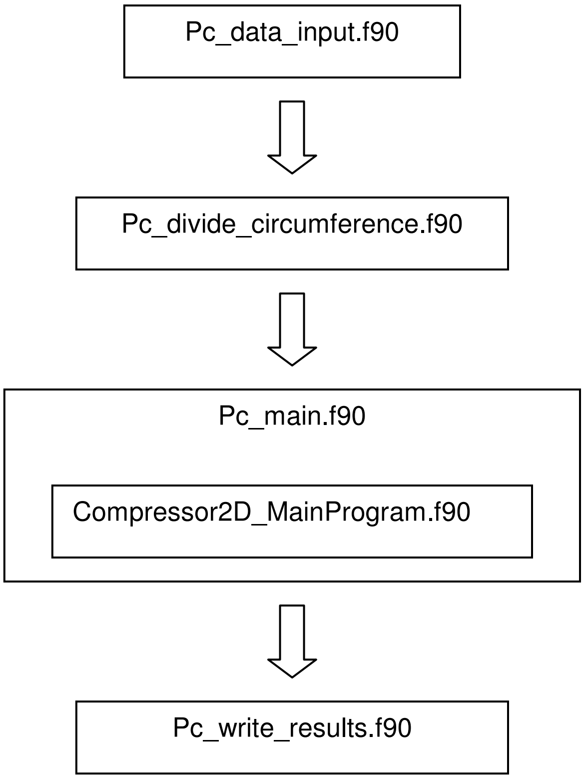

Figure 3-7: Enhanced PaCo-SLC code structure.

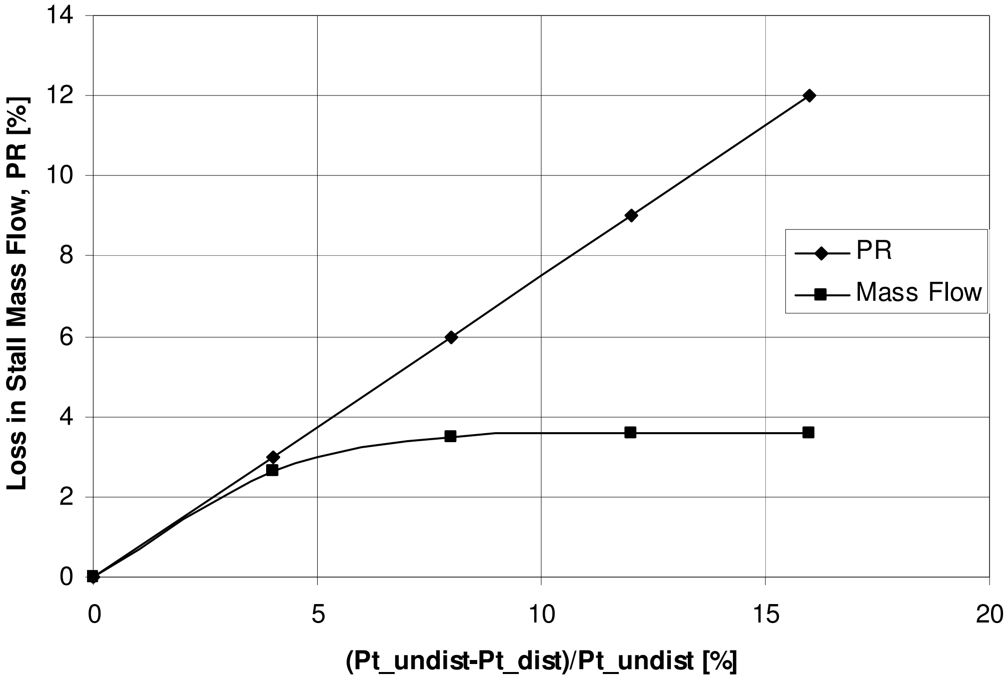

Figure 3-8: Basic PaCo compressor response to distortion.

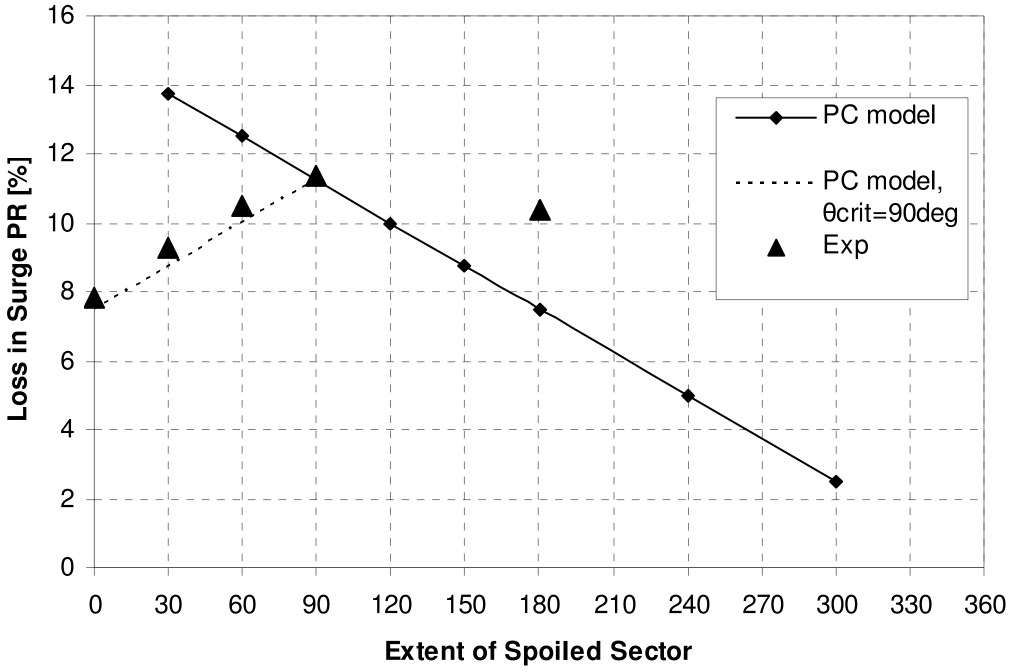

Figure 3-9: Basic and corrected PaCo models against experimental data from [Reid, 1969].

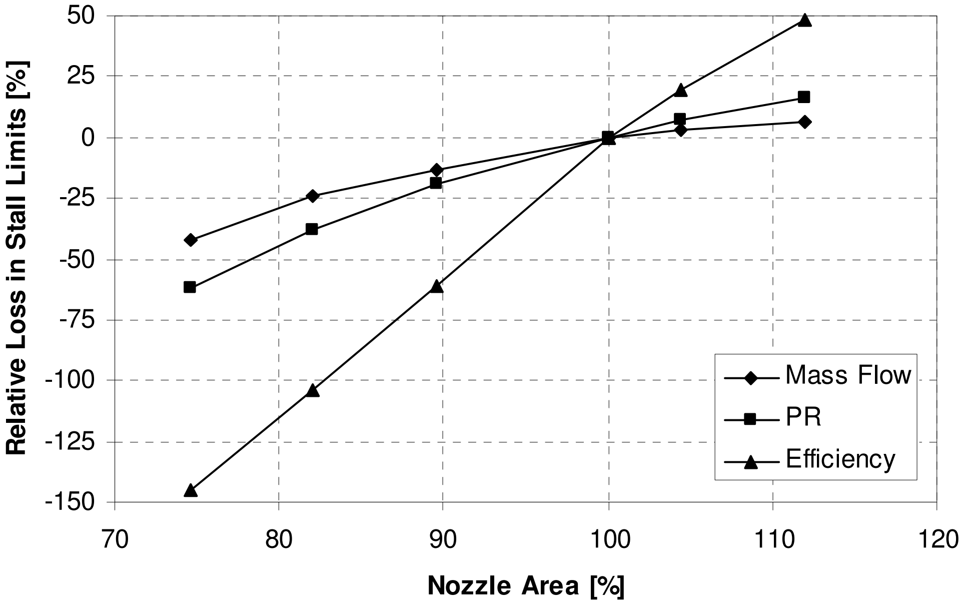

Figure 3-10: Effect of variable nozzle on loss in surge mass flow, PR and efficiency.

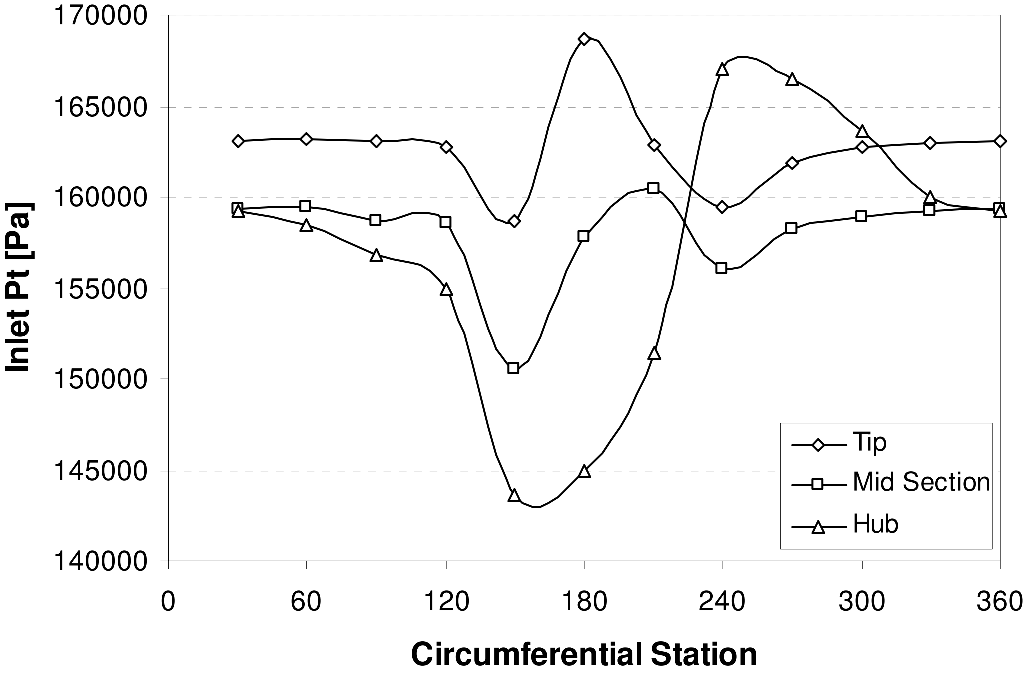

Figure 3-11: Inlet total pressure circumferential distribution, [Sanger, 1976].

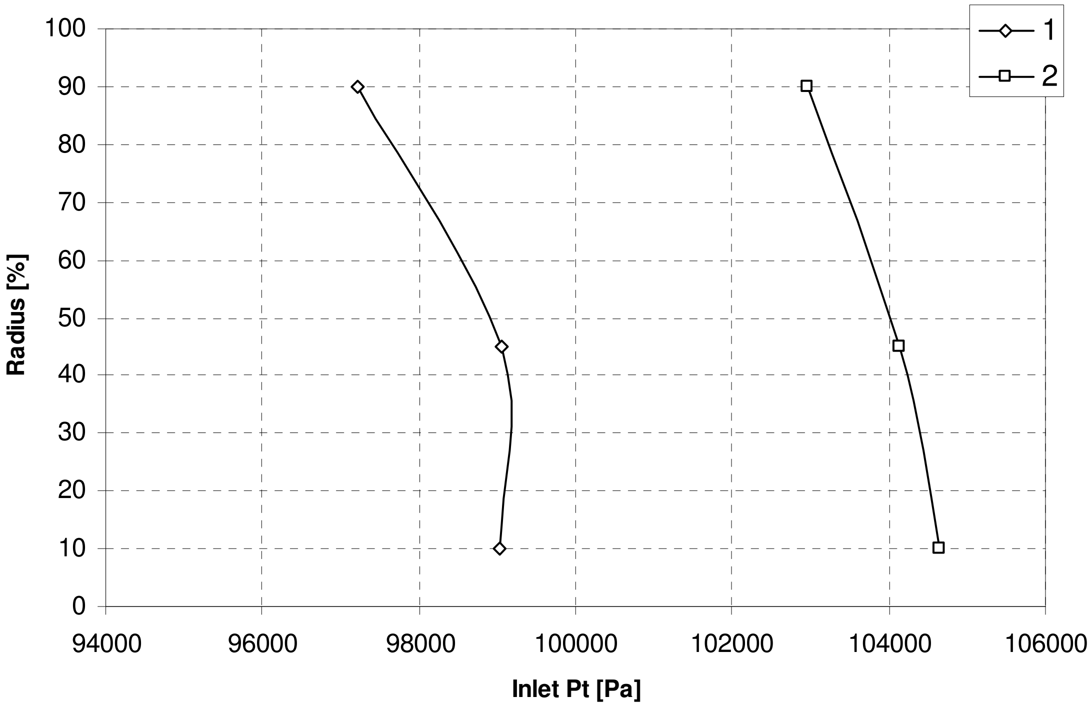

Figure 3-12: Radial profiles of inlet Pt at 2-segment version.

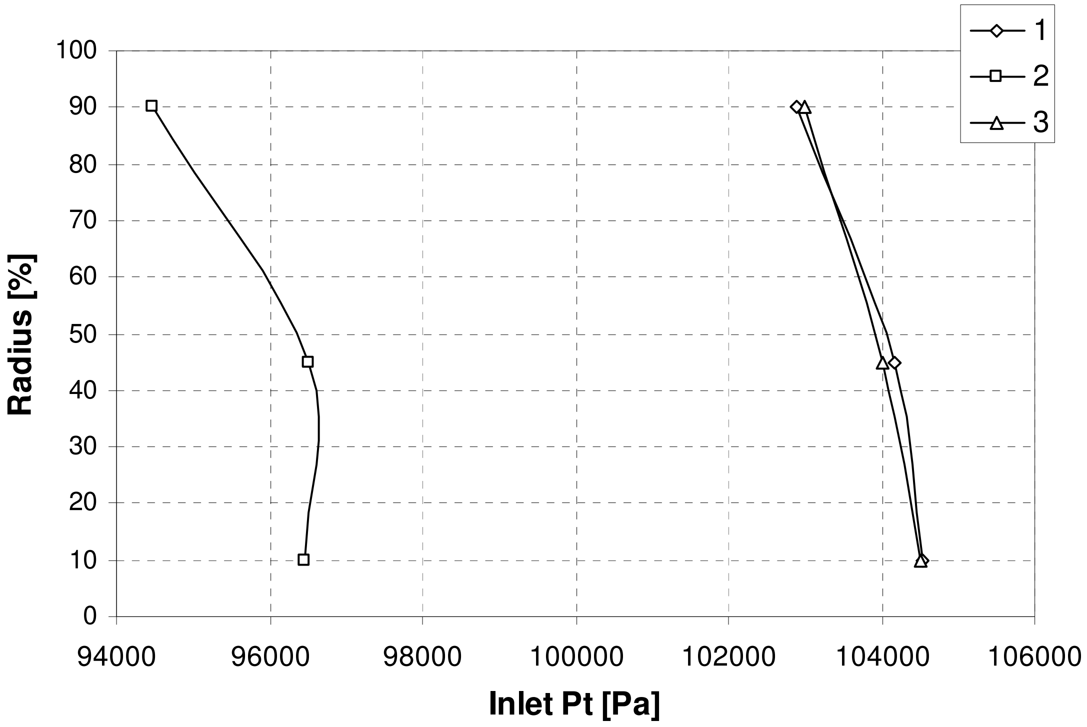

Figure 3-13: Radial profiles of inlet Pt at 3-segment version.

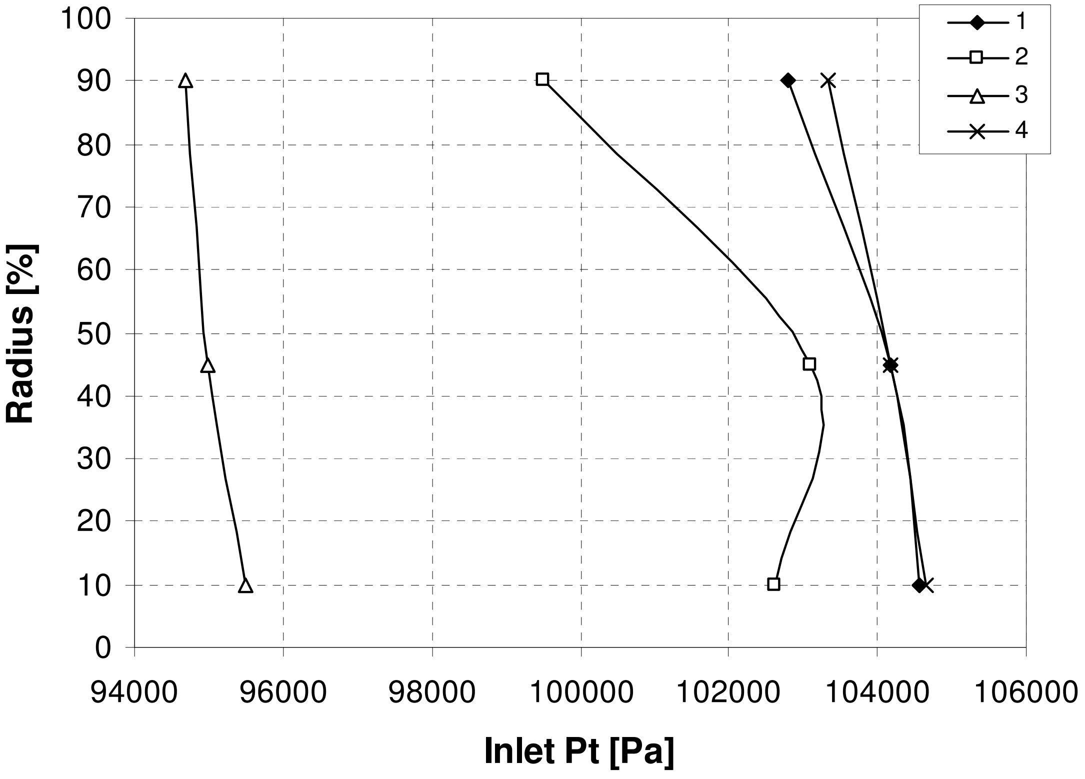

Figure 3-14: Radial profiles of inlet Pt for 4-sector version.

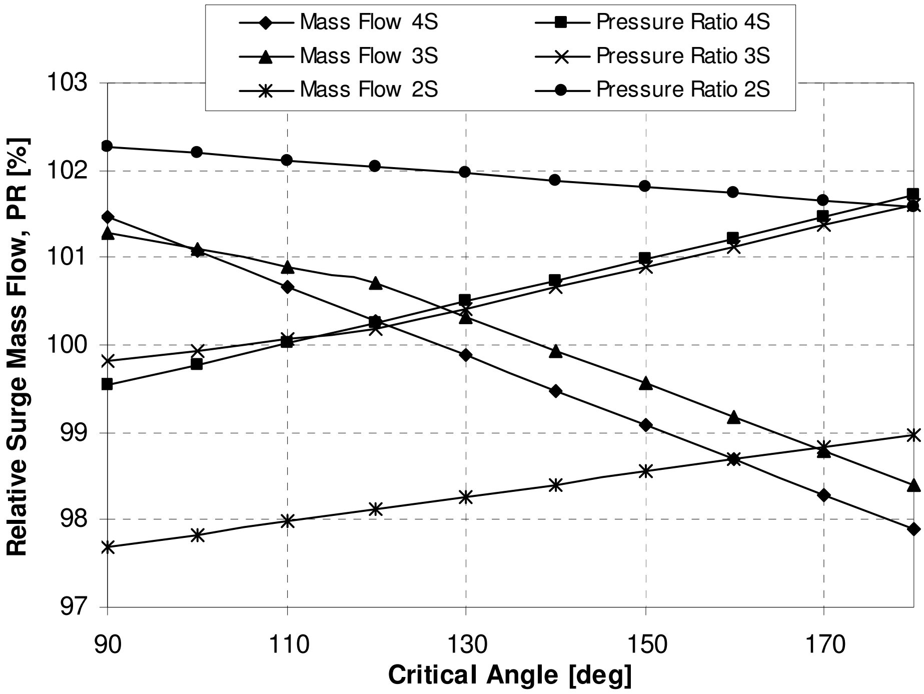

Figure 3-15: Effect of θ_{crit} on PaCo-SLC results.

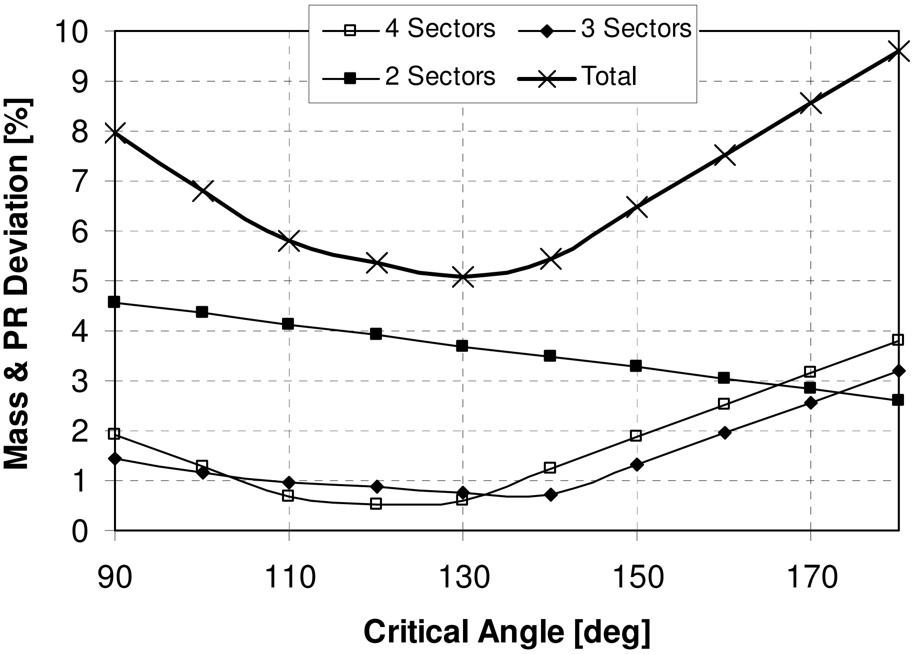

Figure 3-16: Deviation from experimental data Vs θ_{crit}.

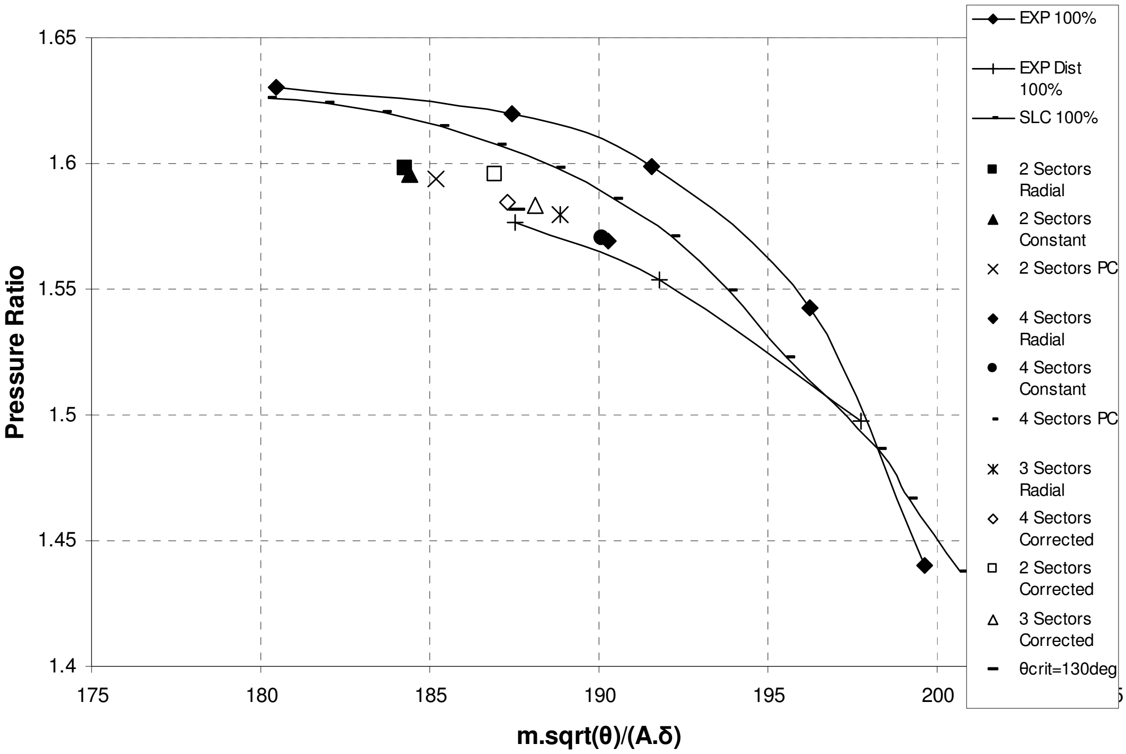

Figure 3-17: 100% speedline; pressure ratio theoretical and experimental results.

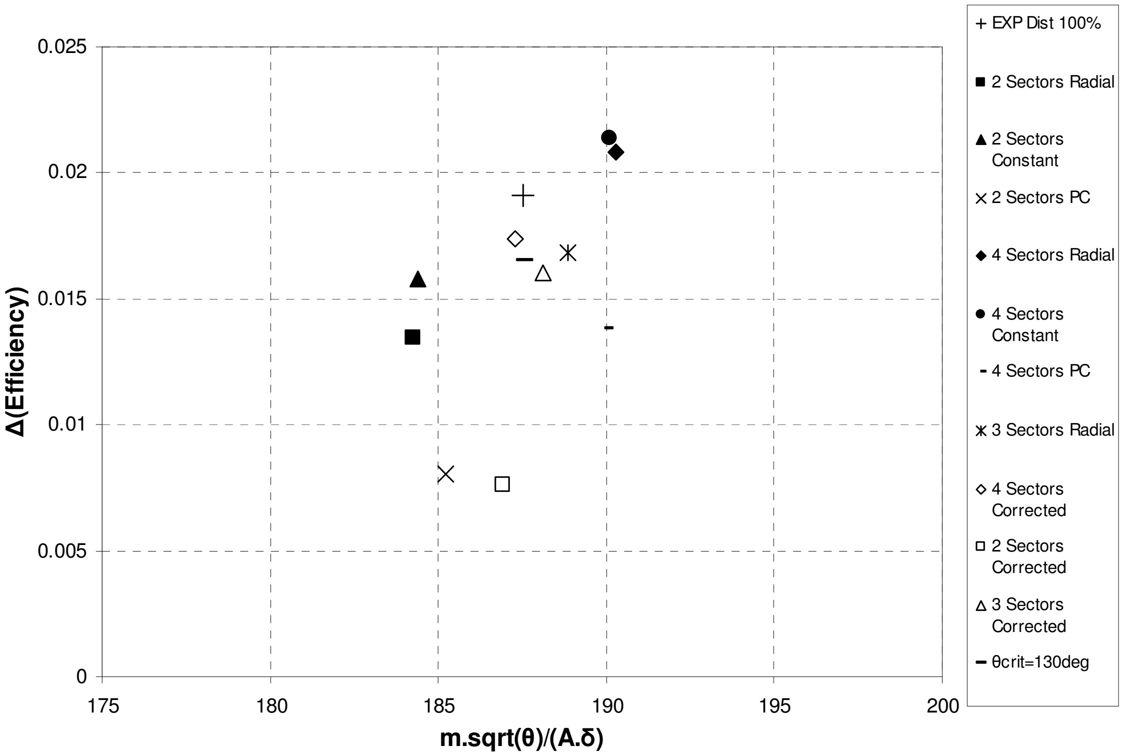

Figure 3-18: 100% speedline; isentropic efficiency theoretical and experimental results.

4 Propulsion System Preliminary Design Analysis

The novel cycle design method has been applied on propulsion systems featuring ultra high bypass ratio, constant volume combustion, recuperation and intercooling. These engines are integrated in a conventional and a novel airframe. The results of the parametric analysis are presented and discussed. In a further step, final aircraft configurations are compared in terms of noise, fuel consumption and CO_2 emissions.

4.1 Baseline Airframe

The baseline configuration has a critical role in any preliminary design study. It forms the basis upon which novel designs are ranked. Therefore, it has to represent mature, well approved and widespread technology levels, in a way that useful outcomes, in terms of noise, and fuel efficiency, may be derived by comparing it to novel configurations.

For the purposes of engine sizing and flight performance calculation, a baseline airframe has been used, provided by Mistry, [Mistry, 2008]. This airframe is used as the platform for applying the low noise design method on all novel propulsion systems.

In accordance to SAI targets, the main specifications of the aircraft are medium range (4000nm), 250-passenger, twin engine airliner, with a cruise Mach of 0.8. These data classify the baseline aircraft in the class of Boeing 767-300. The rationale behind the choice of range and capacity is based on the principle that a medium range aircraft spends a higher percentage of its life in take-offs and landings (TO&L), than a long range. In this essence, the choice has been taken after considering that any noise benefit would appear at TO&L.

The design of the baseline airframe is based on a semi-empirical conceptual design method, developed by Howe [Howe, 2000]. A parametric study, based on this method, has provided high level analysis results, using a database of existing aircraft, alongside the specification. The baseline configuration is the optimum result from this top-level analysis, leading to the design data that are illustrated in Table 4-1. Its Maximum Take-Off Weight (MTOW) in the range of 150 tons and Operational Empty Weight (OEW) at about 90 tons classify the aircraft in the same class with airliners such as the Boeing 767-300. Additionally, the dimensions of the fuselage and the wing make it directly comparable to B-767. The geometry of the aircraft is input to 'Hermes' code and an input file is included in the Appendix (§9.6). Moreover, four views of the baseline aircraft are illustrated in Figure 4-1.

4.2 Broad Delta V-Tail Body Airframe

The Broad Delta V-Tail (BDVT) airframe, designed by Mistry [Mistry, 2008], is a novel configuration, developed for low noise and fuel consumption. Therefore, it is the airframe to be powered by the advanced propulsion cycles, and is used as the planform for the novel cycle design method.

The Broad Delta (BD) configuration has been chosen after a brainstorming session [Mistry, 2008], where several types of aircrafts were evaluated in terms of noise, cost and safety. Collecting a considerably high score, the BD is a tube-and-wing class of aircraft, similar to the baseline, with a conventional fuselage combined with a low aspect ratio delta wing. Derived from the legendary Avro Vulcan tailless bomber, the broad delta wing is featuring low noise and drag, due to its increased stability allowing for reduced use of secondary lift surfaces – flaps, slats. Even though its low aspect ratio wing is expected to result in higher induced drag than a conventional, the implementation of winglets at the wing tips, leads to enhanced performance as shown in the results section.

Table 4-1 contains some indicative geometry data of the BDVT airframe, as opposed to the baseline. These two airframes have common fuselage dimensions and are designed for the same payload. However, the BDVT features a considerably lighter airframe, something that has an impact on its maximum take-off weight. A comparison between the lift surfaces indicates increased area, low span and low aspect ratio for the BDVT wing, due to its delta shape. In the same table the V-Tail dimensions are depicted, in the form of projections on the X (Tail) and Y (Fin) axis. From these it is derived that the total tail area is lower than the baseline, leading to reduced noise generation. It should be noted that the substantial area of the winglets is included in the Fin dimensions.

A view of the broad delta airframe is included in Figure 4-2, where some of the novel features of the BDVT are revealed; the increased wing-root thickness, the winglets, the reduced size V-tail and the novel fuselage-nose, designed for improving lift. Moreover, the geometry data file of the BDVT that was input to 'Hermes' aircraft performance module can be found in the Appendix (§9.6).

4.3 Baseline Propulsion System

The baseline engine has been appointed mainly by the baseline airframe. In this manner, the engine has been chosen to match one of the propulsion systems that propel the Boeing 767-300, a General Electric CF6-80C2. This two-spool medium bypass ratio turbofan represents well approved, widespread technology standards, being a very good candidate for the baseline configuration.

The main characteristics of the baseline model have already been discussed in §3.9, in the scope of validating the noise modules of the design method. Moreover the baseline engine data are included in Table 4-2. As stated above, the levels of bypass ratio, overall pressure ratio and combustor outlet temperature represent well established technology. In a similar manner, the combustor pressure losses and the isentropic efficiency of the compression and expansion systems represent contemporary technological standards in component design.

Lower in the table, the geometrical data of the engine are shown, according to the FAA datasheet [FAA, 2000]. Special emphasis should be given on engine design point thrust, due to its effect on engine size. Furthermore, the optimum designs are challenged to complete the given mission, consuming less fuel and producing lower noise levels than the baseline.

4.4 Parametric Propulsion Cycle Design

In the following section the design method has been applied for low noise and fuel consumption on Ultra High Bypass Ratio (UHBPR) turbofan. It investigates the effect of increasing bypass ratio on engine noise and mission fuel burnt. Two airframes have been used in the analysis, a conventional and a broad delta wing, while the mission targets are the same to the baseline aircraft.

4.4.1 Constant Input Values

The first step in a preliminary design study is to define those variables that remain constant during the process, whether they are design targets, constraints, or lower level analysis characteristics – i.e. component efficiencies. These variables are listed in Table 4-3. It should be noted, though, that all the component values –in a preliminary stage– are approximate guesses and are fully defined by component-design teams after detailed studies. However, in a preliminary stage, where the configurations are evaluated relative to each other setting constant values for some parameters is found to be satisfactory. Moreover, extra confidence on the results is obtained by performing a sensitivity analysis on selected parameters [§ 4.4.6].

Fan/Compressor/Turbine polytropic efficiency

According to Saravanamuttoo [Saravanamuttoo, 2001, pp.61], “When performing calculations over a range of pressure ratio, it is reasonable to assume constant polytropic efficiency; this automatically allows for a variation of isentropic efficiency with pressure ratio. In simple terms, the polytropic efficiency may be interpreted as representing the current state-of-the-art for a particular design." For this reason the polytropic instead of isentropic efficiency is constant through the process.

Heat Exchanger effectiveness and pressure loss

As already discussed in §2.8 and §2.9, two of the four novel cycles, utilise heat exchanging processes for enhanced performance and noise emissions. For this reason, relevant data such as pressure loss and effectiveness of the heat exchanger are input and kept constant through the design process, for simplicity purposes. The value given to the effectiveness is representative of a moderate prediction of future technology at ~70%, while the pressure loss is set at 2%.

Combustor efficiency and pressure loss

The combustor characteristics are kept constant through the design process. A high value of efficiency has been set –see Table 4-3– accounting for highly mixed flames and low dissociation, while the pressure losses are estimated at 6%, due to the cooling process of the combustor.

Inlet pressure recovery

The total pressure losses in the inlet are represented by the inlet pressure recovery factor – see [Walsh & Fletcher, 2004]. A value of 0.99 is easily achievable for future podded engines, while for the case of embedded, where friction losses increase, a lower value of 0.97 has been used.

Ducting pressure loss

The four engine models include several ducts. A duct imposes pressure losses, estimated to be 1%. This value should be updated after detailed design of all ducts.

Ratio of pressure ratios of two core compressors

This variable represents the balance of work input between the intermediate and high pressure compressors. During the optimisation of the fan pressure ratio, the core pressure ratio varies in order to keep the overall pressure ratio constant. The value of this ratio defines the final size of each of the two compressors and their off design performance – i.e. the tendency of the high pressure compressor of reaching surge earlier than intermediate pressure compressor. A value of 1 has been used assuming equal pressure ratio for both intermediate and high pressure compressors. In addition to this, in the case of ICR turbofan, the intercooler is positioned between the two compressors.

Fan air inlet Mach number

Inlet Mach number is a major fan design variable, as it determines the annulus of the fan. High Mach would lead to reduced fan frontal area. However, it would increase the part of the fan operating under supersonic conditions, having a radical impact on fan noise, as discussed in §2.10. For this reason, in the present study it has been kept as low as possible with an effect on fan diameter.

Fan-tip blade Mach number

The fan-tip blade Mach number that is blade speed by speed of sound (Equation 4-1), along with the air inlet Mach, play a critical role in the generation of fan noise, in a sense that they affect the inlet relative velocity, which has a direct effect on tonal noise. The reason for this, lies on the relation between supersonic relative velocity and shock waves, source of tonal noise [§ 2.4.2]. However, the constraint of fan tip Mach to less than 1, leads to fan design issues, connected with low rotational speed and high blade loading.

Equation 4-1

$$M_{tip} = \frac{V_{BladeTip}}{\alpha}$$

Fan hub/tip ratio

Hub/tip is the ratio of hub diameter to the tip (Equation 4-2). It demonstrates the relative height of the blade, compared to total dimensions. In the direction of limitng tip speed, a low h/t is desired, in order to attain minimum possible tip diameter. In this study, a h/t of 0.3 has been applied, in accordace to modern fan technology. A further reduction of h/t would meet structural limitations, such as high stress loading at the root of the blade.

Equation 4-2
$$h/t = \frac{D_{Hub}}{D_{Tip}}$$

Maximum Fan diameter

The maximum diameter of the fan is a constraint imposed by the airframe team. Various reasons, such as landing gear height, or the possibility of embedding the engine in a novel airframe – i.e. BDVT – necessitate the control over the dimensions of the propulsion system. In the case of the baseline airframe, maximum diameter delimits the process. On the other hand, in the case of BDVT, the limit is satisfied by increasing the number of fans per engine. In the initial preliminary study, a limit of 2.7 meters has been set, in accordance to the broad delta wing thickness, enabling a half-embedded installation. Moreover, the limit for the baseline analysis has been set at 3.7m as a higher diameter would cause considerable issues on podding the engine under the wing, such as ground vortex ingestion, or increased under-carriage. Additionally, it is taken into account that engine maximum diameter is expected to be higher by ~0.5m, due to secondary equipment and nacelle design.

Flight conditions at design point (DP)

The design point is the condition for which individual engine components are designed. It is, usually, the most power demanding condition of the flight envelope. For this reason, in civil aviation top of climb is chosen as design point, where the temperature ratio of the cycle is maximal. The two main variables for specifying the flight condition are the Mach number and the altitude.

Thrust requirement at design point

The thrust requirement at design point is the value that defines the engine mass flow ratio, thus dimensions, for given thermodynamic cycle. A cycle is defined by specific values such as specific thrust and specific fuel consumption. In order to obtain net thrust an extra parameter is needed; the mass flow rate which affects the dimensions, the weight, the noise and the total fuel consumption of the propulsion system. Therefore, the thrust requirement is an input to the design process. It is derived from the airframe design method and it is part of the exchange data between airframe and engine teams.

Flight conditions at off design (OD)

Whilst designing the engine at top of climb, the most critical conditions of the flight envelope, in terms of noise, are take off and approach. In a direction of simplifying the optimisation process, the take-off condtion, only, is taken into account. Therefore, in order to predict the noise emissions at take off, the performance calculation at off design is crucial. As a result, an off design condition –flight Mach number and altitude– is specified, depicting the noise measuring point, according to FAA, FAR Part 36 [§ 3.9.1].

Thrust requirement at off design

The engine thrust at the noise certification point has a major effect on the noise produced by the turbofan. Moreover, the thrust cutback during the second climb segment targets at noise reduction, as the combustor firing temperature has a direct effect on mass flow ratio, exit velocity and rotational speed, affecting fan and jet noise. As in the case of design point, the thrust requirement is provided by the airframe team and is kept constant during the design process. In this way, the configurations are designed at the same thrust, while OD-COT changes accordingly.

Aircraft and flight mission data

A number of input variables to the process are relative to the aircraft performance module. Such variables are the airframe geometry, the flight mission – range, flight speed, altitudes – and the operational weight of the aircraft – maximum take-off weight, maximum fuel weight and maximum payload. These conditions are input from the result of the airframe parametric analysis discussed in [Mistry, 2008]. The values of these parameters are summarised in Table 4-3, while the data referring to airframe design are presented in Table 4-1.

4.4.2 Design Variables

As previously discussed, the three main design parameters are BPR, OPR and COT, while their optimisation is the desired outcome of the method. The limits of their variation and the incremental step are shown in Table 4-4. The choice of the step lies upon the desired level of accuracy. Since this is a preliminary design study, a step of 1 for BPR, 2 for OPR and 10 K for COT has been decided.

The upper limits of these variables have been chosen with respect to current and future technology limits. As a result, in the analysis using the twin-engine baseline aircraft as planform, a maximum BPR of 18 has been set. Additionally, a diameter limit of 3.7m has been imposed as suggested by the airframe team [Mistry, 2008]. On the other hand, the BPR upper limit for the case of the Broad Delta airframe has been set at 30 and the fan diameter limit at 2.7m. This diameter limit has been chosen for best engine-airframe compatibility in a half-embedded configuration. Moreover, the code provides the possibility of increasing the number of fans per engine, a condition that is not possible in the baseline aircraft. Finally, the values of maximum OPR and COT are the result of extrapolation based on data presented by Ballal, [Ballal, 2003] and referring to year 2030 technology levels.

4.4.3 Total population results

A parametric analysis is a process of varying the design variables, creating a large population of results and choosing the optimum one. This section presents the total population results, as derived from the method. A discussion follows concerning the behaviour of the propulsion cycles relative to the three main variables. The results shown in this section are derived from one of the 12 test cases presented in §4.4.4 and are used for exhibiting the analysis structure.

Design Variables

The parametric analysis includes a number of module executions, for varying bypass ratio, overall pressure ratio and combustor outlet temperature. This variation is depicted in Figure 4-3 to Figure 4-5. Each line in these figures represents a group of points, where each point stands for an execution of the engine modules –design point calculation. The parametric study strategy is clearly depicted in these three figures; OPR increases linearly, for each COT, COT increases linearly for every BPR and BPR increases linearly through the process.

It can be observed in Figure 4-3 that more than 300 executions are completed for the first BPR, while the rest of BPRs are including about 100. The reason of this difference is identified in Figure 4-4, where at the initial BPR the code iterates for the full range of COT and after identifying the optimum in the area of 1600K, the next BPR uses a refined COT range in the proximity of 1600K –as in this test-case optimum results appear at the lowest COT. In this point it should be noticed that for increasing BPR the range of COTs increases. Such attribute is explained by the fact that the code iterates in a range of 100K below and above the optimum value –as discussed in §3.2. As a result, when optimum COT increases, the range for the next step adjusts accordingly.

In a similar manner, OPR iterates in full range for the first COT of each BPR, while when moving to higher COTs, OPR iterations focus on the optimum region, which is found to be around OPR of 60. For this reason, the number of executions in the region of 50 to 60 is so high that the discrete points are illustrated as continuous lines. Additionally, as it has been previously pointed out, when the optimum OPR is other than 60 –i.e. 58– the next step will range between 48 and 60. If the optimum OPR was found to be 40, the range would adjust to 30 to 50.

Performance Results

The variation of engine performance characteristics is illustrated in Figure 4-6 to Figure 4-10 . Figure 4-6 shows the evolution of SFC during the process. Increasing bypass ratio leads to reduced specific fuel consumption up to BPR 20. When BPR increases further, though, SFC appears to increase. This happens, because the improvement in propulsive efficiency becomes lower than the reduction of thermal efficiency. On the other hand, Figure 4-8 depicts the reducing trend of jet noise with increasing BPR. A comparison between Figure 4-7 and Figure 4-8 makes apparent the direct relation between jet noise and specific thrust due to their dependence on exhaust gas velocity.

Whilst Figure 4-6 and Figure 4-7 show general trends, the effect of COT and OPR on performance is not clear. For this reason, two extreme BPRs have been picked and enlarged in Figure 4-9 and Figure 4-10, showing the detailed behaviour in terms of SFC and specific thrust respectively. In this way, the reader may compare the design point performance between baseline and ultra high bypass ratio and extract a number of useful conclusions, as discussed below.

Low COT results in SFC improvement at low BPR, similarly to turbojet cycle. However, SFC increases for decreasing COT at high BPR, similarly to shaft power cycle. This occurs because of the overall cycle efficiency dependence from propulsive and thermal efficiency, according to the following equation.

Equation 4-3

$$n_{ov} = n_{prop} \cdot n_{th}$$

COT reduction has an impact on thermal efficiency. However, at low BPRs, the reduction in exhaust gas velocity gives significant improvement in propulsive efficiency resulting in higher overall efficiency and lower SFC. For BPRs higher than 20 –where propulsive efficiency is already high– the improvement on propulsive efficiency is less significant than the decrease of thermal efficiency.

Figure 4-10 illustrates the variation of specific thrust with OPR and COT. Specific thrust reduces with increasing OPR, as it depends on jet exit velocity. This happens due to the increase of compressor work at high OPR, but it diminishes for increasing COT, because of the increase in turbine work excess. High COT results in high specific thrust. In Figure 4-10, it becomes apparent that the effect of COT is less intense at high BPRs. The explanation is that COT affects, mainly, core exhaust velocity, at constant OPR. However, at high BPR, the proportion of core thrust to total is much lower. As a result, any change in core thrust plays less critical role in total net thrust.

In addition to the specific values of the cycle, the most critical result in an engine analysis is the fuel demand for a defined mission. In this manner, the fuel consumption variation for the whole engine population is plotted in Figure 4-11. A comparison between Figure 4-6 and Figure 4-11 reveals the similarities and the differences between the specific and the actual fuel consumption. Their attribute is similar up to BPR of 14. However, when BPR increases further, the increased engine weight –shown in Figure 4-12– has an impact on aircraft mass, lift, thrust and fuel demand. As a result, significant increase of fuel consumption is observed at high BPRs.

The engine weight prediction results are illustrated in Figure 4-12, where –as discussed in Appendix– high COT improves weight, through reducing engine size, while high OPR increases weight, due to higher number of compressor stages. Moreover, a rising BPR, increases engine mass flow, thus weight.

4.4.4 Cycle Comparison

The parametric analysis cycle design process has been applied on four gas turbine cycles using a baseline and a novel planform. The results from these sixteen test-cases are presented –Figure 4-13 to Figure 4-40– while several powerplant design issues have been addressed.

For reasons of simplicity and clarity the cycle evaluation is based on diagrams illustrating the variation of the engine parameters with BPR. Every parameter is presented in two plots, one for the baseline and one for the BDVT airframe. Each plot contains four subplots –one for each novel cycle– where three data-sets are depicted. The first is the result of optimising for noise –objective function governed only by jet noise–, the second for fuel –objective function governed only by fuel consumption– and the third has been produced for combined fuel-noise optimisation. In this way, a range of possible solutions is created, allowing the designer to choose the appropriate values, according to the project priorities. It should be noted that the following graphs represent the optimum solution –COT and OPR– for each bypass ratio. As a result, each point is the result of the balance between conflicting attributes; i.e. lower SFC against higher weight, or jet noise. Moreover, the points highlighted with the 'triangle' sign stand for the global optimum solution for each of the three data-sets.

A comparison between baseline and BDVT shows that the design evolution of each cycle is not affected –in general– by the airframe. As an example, the UHBPR turbofan exhibits optimum noise at maximum overall pressure ratio, as already discussed in §4.4.3 and this behaviour is apparent in both baseline and BDVT airframes –Figure 4-15, Figure 4-16. Moreover, this attribute is apparent in most of the cycle characteristics, with some exceptions. Such exceptions are the weight and dimensions –length, diameter– of the engine, due to the difference in the number of propulsion systems of each aircraft –two for baseline, four for BDVT. As a result, the four-engine configuration leads to lower engine dimensions, compared to a twin engine, due to lower thrust requirement per engine. Moreover, another difference appears, in terms of fuel. BDVT's superior aerodynamic performance leads to lower total mission fuel consumption and CO_2 production.

A critical difference between baseline and BDVT configurations is the effect of diameter limit on the process, as discussed in §3.3. As a result, the BPR-range of the analysis is limited to much lower values than the upper BPR-limit. Figure 4-29 depicts this effect, where it is obvious that maximum BPR is affected by two conditions; the type of the cycle and the nature of the objective function. More specifically, cycles that present enhanced specific thrust, such as ICR and CVC have higher BPR limits than cycles with lower specific thrust such as the recuperated. Additionally, when noise is governing the objective function, optimum cycles show low specific thrust, thus high diameter and the maximum diameter limit is reached at low BPRs.

In this point, the role of the objective function (OF) –page 134– in the 'focusing' technique of the design method becomes apparent. During the process, the optimum cycle for each BPR depends upon the OF definition –the values of a_1 and a_2 in Equation 3-2– redirecting the solution accordingly. As a result, when optimising i.e. for fuel, the solver chooses the most fuel efficient solution, neglecting any other parameter; i.e. jet noise. This attribute becomes apparent in Figure 4-13 and Figure 4-14 where the global optimum for fuel lays in the area of BPR of 15 and the global optimum for noise, takes the maximum possible value. Moreover, when both noise and fuel are used in the objective function, the optimum solution is found in the proximity of optimum noise. This happens, because during the process –BPR varying from 5 to 30– engine noise reduces in a much higher rate than fuel consumption, having a more strong effect on the value of the objective function. However, this is allowed, as the primary goal of the present study is noise reduction.

The figures in pages 135 to 147 illustrate the effect of BPR on cycles, despite the values of the other two parameters. Preciselier, increasing BPR leads to lower Specific Thrust (ST), jet noise and Fan Pressure Ratio (FPR), as a result of low jet velocity. Additionally, low FPR results in improved fan noise, but low ST increases engine weight, length and diameter. Specific Fuel Consumption (SFC) exhibits a minimum value at BPR of ~20. An optimum value exists, also, for the total fuel consumption, at BPR of ~15. The optimum BPR for fuel is lower than SFC, due to the negative effect of increasing engine weight. It is, therefore, realised that engine weight plays a critical role in the design process.

A figure useful in understanding the performance of each cycle during the design process is Figure 4-17, where the variation of the main cycle parameters with OPR is illustrated. As shown in the figure, OPR has a detrimental effect on specific thrust, due to increasing compressor work. On the other hand, SFC improves with OPR, as a result of higher thermal efficiency. It should be noted, though, that the increase of OPR, higher than a critical value, would lead to marginal SFC increase, due to high relative magnitude of component losses, compared to work output (net thrust). Moreover, it becomes obvious that this critical value has a strong dependency on COT.

The recuperated cycle exhibits lower than conventional turbofan SFC, which improves up to an optimum OPR. When this optimum is exceeded the available temperature rise in recuperation is diminished and SFC rises. Moreover, recuperation has a detrimental effect on ST, compared to other cycles. For increasing OPR, ST rises up to a point, beyond which, the increase in nozzle exit temperature is limited by the high compressor work, in addition to the relative increase of component losses. Such an attribute is not observed in the Intercooled-recuperated cycle, where ST increases continuously –though, asymptotically– with BPR due to the beneficial effect of intercooling, that reduces compressor work. However, minimum SFC appears at low OPR and increases at higher OPR, despite high thermal efficiency, due to poor propulsive efficiency, resulting from enhanced exit velocity.

In addition to Figure 4-17, Figure 4-18 depicts the effect of increased weight, due to high OPR, on aircraft performance. Two data sets have been plotted, illustrating performance for OPR of 30 and 60. High engine weight, increases total aircraft mass, leading to higher thrust requirement during cruise, thus higher COT, which results to high SFC and fuel consumption for each cruise segment.

The discussion about the effects of COT and OPR on engine parameters branches to four sections, one for each propulsive cycle. The first section exhibits in detail the attributes of turbofan, while the rest three focus in deviations that alleviate from the change in the thermodynamic cycle.

Ultra High BPR Turbofan

The ultra high bypass ratio turbofan has been studied to be used as a baseline for the other three novel cycles, as it demonstrates mainly the effect of BPR on conventional gas turbine cycle.

When target is ‘noise’ the optimum cycle is represented by maximum possible OPR and minimum COT –Figures in pages 135 and 137–, as such combination leads to low jet velocity, thus low noise –page 143. These cycle settings have a detrimental impact to ST –page 139–, leading to higher fan diameter –page 142–, engine length –page 146– and weight –higher due to increased mass flow –pp. 145. On the other hand, specific fuel consumption –pp.139– remains at low levels, at BPRs between 5 and 18, due to the beneficial effect of OPR on thermal efficiency and low COT on propulsive. However, further increase of BPR exaggerates the negative effect of low COT on thermal efficiency, resulting in increasing SFC. Moreover, low COT affects optimum fan pressure ratio (FPR) –pp.141–, as the ratio of core and bypass jet velocities is constant [Walsh&Fletcher, 2005, pp. 305], resulting to lower fan noise –pp.144. Finally, despite low SFC, total mission fuel –pp.147– is increasing with BPR, because of high engine weight, but it is not taken into account in the design process. As a result, the noise-optimum BPR is found to be the maximum possible.

As opposed to ‘noise’ optimising, a different optimum is predicted when optimisation target is low fuel consumption. In this case, jet noise is not taken into consideration, and the process targets at low SFC and engine weight. As a result, a rising COT up to maximum is observed, leading to high specific thrust, high FPR and fan noise, low fan diameter and low engine weight –as opposed to other two cases. A comparison to noise-optimums shows higher lower propulsive efficiency, higher jet noise –due to high ST– and higher fan noise –due to high FPR. On the other hand, OPR exhibits a tendency to high values, due to its beneficial effect on SFC. However, at low BPR, where COT is low –to improve SFC–, OPR decreases, in order to maximise the reduction in engine weight. The effect of weight on total fuel is apparent in the BPR of the optimum cycle, which is in the proximity of 15, much lower than the optimum solution for ‘noise’. Figure 4-24 illustrates higher SFC than the other two test-cases up to a BPR of ~18. When BPR increases further than 18, SFC continues falling, in contrast to the rest test-cases. Generally, low weight and SFC lead to low fuel consumption, throughout the whole BPR range.

In order to bridge the gap between the two test-cases, a third has been performed, in the scope of accounting for a cycle that combines low jet noise with low fuel consumption. As already discussed, the relevant optimums exhibit little diversion from 'noise' test-case. Some differences are detected for high BPRs, where the benefit in fuel consumption from increasing COT and decreasing OPR, overcomes the noise penalty. The overall optimum appears at lower BPR than 'noise', due to the effect of fuel consumption. However, fuel consumption is, still, considerably higher than the fuel-optimised test-case.

Recuperated Turbofan

The addition of recuperation to Brayton cycle has two major effects. It reduces SFC, but also, specific thrust, as shown in Figure 4-17. Low specific thrust affects strongly the evolution of optimum OPR and COT –pp.135, pp.137. As a result, in the case of noise-optimising, where low exhaust speed is the target, optimum overall pressure ratio takes values in the proximity of 60, combined with lowest possible COT. This attribute is similar to conventional turbofan cycle. A significant difference, though, is the apparent scattering of OPR that is evident in Figure 4-16. This is the result of two conflicting behaviours, due to the nature of the recuperated cycle. In a further detail, low noise is generated by high OPR that increases turbine work, lowering exhaust temperature, or by moderate OPR that allows for considerable exhaust temperature reduction, due to recuperation. As a result, scattering values of optimum OPR appear throughout the BPR range.

When objective function is driven by 'fuel', OPR is taking values between 40 and 50, where ST is maximum, though quite lower than other cycles, as shown in Figure 4-17. As a result, high COTs survive the selective process, in order to attenuate the weight increase caused by low specific thrust. Finally, the combined noise-fuel test case shows limited increase in COT in order to prevent noise increase. However, this leads to even lower OPR. The main reason is that low OPR leads to low noise and weight. As a result mission fuel consumption is low despite the high SFC.

Intercooled Recuperated Turbofan

Intercooling has been added to the recuperated cycle in order to counteract the specific thrust reduction. This happens by reducing the compressor work and also, adding the intercooler heat to bypass stream, leading to a completely different relation between OPR and ST, as illustrated in Figure 4-17. As a result, when designing for low noise, low overall pressure ratios survive, due to the positive effect of OPR on specific thrust. Moreover, combustor exit temperature remains in lowest levels, in similar manner with the rest of the cycles. High ST, combined with low OPR contributes to low engine weight, despite the application of correction factor for heat exchangers in the weight module. This weight benefit is noticeable in the burnt fuel, enhanced by the fact that optimum SFC is achieved at low OPRs. However, high ST, thus high jet velocity result to high jet noise, combined with high fan noise, due to high FPR.

For ‘fuel’ optimising, OPR starts at low levels, because of its beneficial effect on SFC and weight and increases with BPR, while COT increases as well up to the maximum allowed value. The increase of OPR happens because high COT traverses the optimum – for SFC and ST– overall pressure ratio to higher values, as more energy is available for recuperation at the turbine exit. As already discussed in the previous paragraph, low SFC, high ST and low weight lead to more than 10% lower fuel burnt compared to the simple turbofan cycle.

The ‘noise-fuel’ optimisation process, exhibits attributes similar to the ‘noise’ test-case and some deviation appears at high BPRs, where the process is mainly ‘fuel’ driven, having an impact on noise; otherwise the impact on fuel consumption would be much more severe.

Constant Volume Combustion Turbofan

The novelty in CVC cycle lies in the substitution of constant pressure combustion with constant volume, leading to significant pressure rise inside the combustor. This condition enhances mainly SFC, through increasing the pressure ratio of the turbines. The ‘noise’ optimisation process presents similar to conventional turbofan attributes, as the need for lowest possible ST leads to minimum COT and maximum OPR. As a result, parameters such as FPR, jet noise, engine weight and length vary in a similar manner to baseline turbofan.

In the case of 'fuel' optimising, though, optimum cycle (OPR in particular) is affected by the ultra low specific fuel consumption. More specifically, OPR remains at low levels, in order to minimise engine weight. This condition has a penalty on SFC which is negligible, as SFC variation with OPR is much less intense than in conventional cycle. The result is low weight –pp. 145– and ~25% less total fuel burnt –pp. 147–, compared to conventional.

When both fuel and noise are involved in the objective function the following attributes appear. Combustor outlet temperature remains low in order to keep exit velocity low, while OPR ranges between low and high values in order to achieve a balance between low engine weight –thus minimum fuel– and low jet noise, respectively. It should be noted that optimum BPR –28– is higher than the rest cycles, due to less intense fuel increase with BPR.

Effect of OPR on cruise performance

The cruise performance of the cycles has been evaluated at cruise OD condition in terms of specific thrust and SFC. The analysis has been conducted for two extreme OPRs in order to identify the effect of OPR in this condition. A baseline setting has been chosen; BPR 5 and COT at 1600K. The COT reduces from 1680K to 1200K and the changes in SFC and ST are shown in % of design point values.

In the case of baseline turbofan throttling back the engine leads to linear reduction of specific thrust, as illustrated in Figure 4-44. On the other hand, SFC initially improves, as propulsive efficiency outweighs the drop in thermal efficiency –due to lower COT and lower isentropic component efficiencies–, and then rises again. Overall pressure ratio affects mainly specific thrust, leading to lower ST for reducing COT, because of the reheating effect –diverging constant pressure lines in h-s diagram; i.e. at lower pressure, a change in the cycle has smaller effect.

A different attribute is observed in the recuperated turbofan test-case –Figure 4-45–, where SFC does not improve with lower COT, due to the elimination of recuperation. As a result, a throttling back in the excess of 100K leads to higher specific fuel consumption, having an impact on mission fuel burnt. Additionally, low OPR results in lower compressor delivery temperature, giving higher temperature difference in the heat exchanger and allowing for higher COT reduction. As a result, improved off design SFC is exhibited by the low OPR engine.

The intercooled-recuperated turbofan, exhibits improved performance, compared to the other two cycles, due to high specific thrust at design points, which allows for considerable improvement in propulsive efficiency for descending COT. As a result, the throttling of the engine up to 200K improves SFC, as shown in Figure 4-46. while ST reduction is less intense compared to conventional and recuperated cycles. Moreover, low OPR engine exhibits superior performance in terms of SFC and ST. The reason is that recuperation effect is more intense in the low OPR, as more energy excess is available at low COT.

The negative effect of high OPR on off-design cruise performance affects fuel onsumption during cruise. It is, therefore, taken into account in the present study, by using total mission fuel consumption in the objective function.

4.4.5 Optimum cycle results

The parametric analysis leads to an optimum design for each thermodynamic cycle, according to the OF value. The final cycle designs for baseline and BDVT airframes are compared with the baseline aircraft in Table 4-5. These final designs are based on an objective function that accounts for both noise and fuel.

However, the use of two conflicting values –fuel consumption and noise– in the objective function allows for more than one optimum solution. As a result, a Pareto front is created, as shown in Figure 4-43. From this set of data, the most fuel efficient cycle is chosen, which is, also, of relatively lower BPR, lower dimensions and better installation drag.

A comparison between novel cycles and the baseline, installed on the baseline airframe, shows a ~15% reduction in total mission fuel –translated to ~15% lower CO_2 emissions– and a ~ 30dBs in jet noise. The main reason is the increase in BPR, which leads optimum COT to higher values, resulting in better SFC, while exhaust jet noise reduces. Maximum BPR, though, is governed directly by the engine diameter limit and the type of the cycle as discussed in §4.4. As a result, the maximum allowed BPR for the recuperated engine is 10, because higher BPR would infringe the imposed diameter limit. Moreover, the same fan design principles have been applied to all cycles. Similar specific thrust is, therefore, produced by all cycles. As a result, all four cycles produce noise levels of similar magnitude, despite the fact that the ICR cycle is designed at BPR of 17, while the recuperated cycle has a BPR of 10. This is not the case for the SFC –mission fuel consumption–, where a strong dependence on the type of cycle is observed. In a further detail, the most efficient cycle is the CVC, with the ICR following and the Recuperated exhibiting the highest SFC levels. The constant volume combustion leads to high efficiency due to pressure rise inside the combustor. Moreover, ICR's high BPR, enhances its thermal efficiency.

The data in Table 4-5 present large diameters for all cycles, in relation to conventional engines; i.e. doubling BPR leads to ~40% diameter increase. This happens, partly, because the fan diameter –which affects maximum engine diameter–, is strongly dependent on fundamental fan design values, such as fan inlet Mach number and hub to tip ratio. Due to the nature of this study, the fan design values correspond to low tip Mach number, for improving fan noise. As a result, low inlet velocity leads to large fan-face area, thus diameter.

As it has been previously mentioned, cycle design has not a significant effect on fan perceived noise. This is apparent in Table 4-5, where a maximum reduction of 6 dBs is achieved by increasing BPR in the baseline airframe. Even though 6dBs is considered a significant reduction of noise, it is much less than the 18dB reduction in jet noise. In this point, it should be noted the difference between the tools validation, where A-averaged decibels have been used to measure noise. Perceived noise tone corrected [PNDBT], leads to much higher values of dBs, due to the various corrections that take place –see §2.3.

A comparison of the two airframes reveals the aerodynamic superiority of the broad delta body, as a fuel consumption reduction of ~13% in is observed in all four cycles in Table 4-5, despite higher SFC. The CVC cycle is the most fuel efficient. In terms of jet noise, though, it becomes obvious the critical role of BPR that is much more intense than the effect of cycle type. In a further detail, the increase of BPR diminishes the relative benefits from recuperation or, CVC low temperature and the UHBPR turbofan produces the lowest jet noise levels. However, the engine that scores the lowest OF is the CVC, being the most fuel efficient and 'silent'.

Finally, in order to obtain an insight into the trade-off between noise and fuel consumption the fuel-optimum cycles for BDVT airframe are presented in Table 4-6. Table 4-7 includes a comparison between final cycles and fuel-optimised ones. Every cycle value has been expressed in % of its fuel-optimised equivalent. Bypass ratio increases significantly from ~15 to 25. On the other hand, no significant changes appear at OPR as high OPR is favourable for both noise and SFC. Moreover, COT has the maximum allowed value in the case of fuel-optimisation, while taking moderate values in the other case, due to its effect on exhaust velocity. Another interesting comparison is the SFC, where it appears that the noise-optimised simple turbofan and recuperated cycles exhibit lower SFC, in comparison to the fuel-optimised ones. However, specific thrust in these two cycles is more than double in the fuel-optimised configurations, affecting engine weight –almost half– and leading to a 10% improvement in total mission fuel consumption. On the other hand, the ICR and the CVC exhibit lower SFC in their fuel-optimised versions. As a result a ~30dB reduction in jet noise is achieved on the expense of ~15% increase on fuel consumption and CO_2 emissions.

4.4.6 Sensitivity Analysis

In order to obtain a level of confidence regarding certain values that have been kept constant through the process a sensitivity-analysis has been conducted. In a further detail, the effect of component efficiency, bleed, and weight on fuel consumption, noise and other parameters has been evaluated. It should be noted that each point on the following figures represents a design point calculation.

Compression polytropic efficiency

Figure 4-47 depicts the dependence of cycle parameters on polytropic efficiency of the compression process. The points in the figure have been joined with polynomial lines for reasons of clarity. The variation of efficiency from 0.8 to 1 shows a 40% increase in specific thrust –affecting weight, length, diameter and jet noise–, assorted with more than 15% SFC improvement. Both of them outweigh the ~10% increase in jet noise, leading to improved objective function value, by 5%. This observation leads to the conclusion that a worse cycle efficiency would have lower jet noise as well, however, it is found to be uneconomical and the implementation of highest possible efficiency a one-way route.

Expansion polytropic efficiency

In the same manner to compressor, the turbine polytropic efficiency has been plotted against the main engine parameters –Figure 4-48. As in the case of compressor, a 10% rise in efficiency, leads to ~5% higher noise but ~12% lower fuel consumption, justifying the research for highest possible efficiency.

Recuperating effectiveness

In Figure 4-49 the effect of recuperation effectiveness is plotted. The increase of effectiveness reduces jet exit velocity. This results in improved SFC and jet noise, but worse specific thrust, leading to higher weight. However, objective function improves, making apparent the need for highest possible effectiveness. Regarding the sensitivity of the solution, a 25% increase in effectiveness results to less than 4% improvement in OF, a value that can be considered low, in relation to the error margins of the preliminary design modules.

Intercooling/Recuperating effectiveness

A sensitivity analysis of the effect of heat exchanger effectiveness on the intercooled recuperated turbofan is illustrated in Figure 4-50. Specific fuel consumption has been plotted against specific thrust for varying intercooler and recuperator effectiveness. It is obvious that high recuperator effectiveness leads to a significant improvement in SFC, but also, reduces ST, due to energy extraction from exhaust nozzle. On the other hand, a more effective intercooler improves specific thrust, while its effect on SFC depends on the extend of recuperation. For recuperation effectiveness values higher than 0.4, higher intercooling improves SFC. This happens because more effective intercooling reduces compressor work and delivery temperature, while leads to higher turbine exit temperature, subject to enhanced temperature drop in the recuperator. It can be seen that the value of 70% for both heat exchangers results in considerable improvement of both SFC and ST. The plot in Figure 4-51 shows the effect of effectiveness on the design results. It is obvious that a change of the effectiveness for both recuperator and intercooler from 0.5 to 0.75 results in a 2% change of the objective function.

Compressor bleed

Another variable affecting the performance of the cycle is the bleed from high pressure compressor for the purposes of turbine cooling and cabin air-conditioning. The amount of this flow depends on the type of the airframe –size of passenger cabin– and on the detailed design of the turbine stages. As shown in Figure 4-52, the main effect of increasing bleed flow is the reduction of specific thrust, as it reduces turbine entry temperature, due to the cool flow that mixes with the combustor outlet main flow. On the other hand the reduction in thermal efficiency is counteracted by the improvement in propulsive efficiency, leading to small improvement in SFC. The outcome of this analysis is that an increase of cooling flow by 10% leads to ~0.2% reduction in fuel, 3.5% noise improvement and the OF is lower by ~2%, values that are considered low in a preliminary stage.

4.5 Installed Engine & Total Aircraft Noise

In section 4.4 various configurations have been designed for low noise and fuel consumption. However, the noise emissions that have been discussed are referring to uninstalled engine. This section presents the effects of installation on noise and the final total aircraft noise emissions, in order to highlight the total benefit of the study. The following sub-section describes the effect of noise shielding on fan noise.

4.5.1 Noise Shielding

As it has been already discussed, cycle design affects mainly jet noise. As a result, at ultra high BPR configurations, fan becomes a significant noise source. In order to obtain low overall noise levels a different approach is followed. Fan noise is shielded by installing the engine on top of the wing.

The intercession of the wing between the engine and the ground increases the effective distance that sound needs to travel. Moreover, it redirects a significant amount of sound waves upwards. Such a configuration exhibits the potential of strong reduction on fan noise for two reasons. A significant portion of fan noise is tonal –§2.4.2– and it can be easily attenuated by shielding. Additionally, fan noise can be regarded as spot source, thus a valid prediction of shielding can be applied.

As discussed in §3.8.3, a noise-shielding routine has been used for predicting the installed fan noise levels. Figure 4-56 illustrates the effect of shielding on the whole SPL spectrum. Sound pressure levels are attenuated in the full frequency range. As shown in the figure, higher frequencies experience a stronger effect of shielding and the averaged noise reduction exceeds 20dBs.

It should be noted that the axial distance between the fan and the leading edge has been chosen to be 3meters, after performing a sensitivity analysis by varying the distance, as shown in Figure 4-57. This parameter is considered of high significance for shielding as an increase by 2 meters can provide up to 4dBs of noise reduction. During this process the position of the engine on the wing has been chosen in order to allow adequate space upstream and downstream the engine for shielding both forward and aftward propagating fan noise.

Another critical parameter in noise shielding is the vertical distance from the wing surface. It is assumed to be less than 1 meter as the engine is half-embedded in the wing – see §5.1. As shown in Figure 4-58, less than 1 dB is gained in noise shielding by reducing this distance. However, half-embedding the engine, has a strong impact on side noise as well. However, it can not be quantified by this code.

A third parameter in the calculation is the wedge angle of the edge. This is derived from the wing geometry and is provided by the airframe team. Thus, a value of 330^o has been used in the calculation, due to high thickness of the wing leading edge. Even though the angle is fixed, a sensitivity analysis –Figure 4-59– has shown that a change by 10^o leads to ~1dB change in noise shielding.

In this study noise shielding has been applied on fan noise only, despite the fact of expecting some reduction on jet noise as well. The effect of shielding on jet noise though, is less intense and difficult to quantify. The reason is that jet noise is a distributed sound-source downstream the exhaust plane, as discussed by Berton, [Berton, 2000]. As a result, due to the lack of available prediction model, the most pessimistic scenario has been considered, where no jet noise reduction occurs.

4.5.2 Installed Engine Noise

Following the calculation of installed fan noise the two main engine noise sources are presented for all the novel configurations. These are presented in Figure 4-60 and Figure 4-61 for engines installed on the baseline and the BD airframes respectively. The calculation has been performed for two flight conditions according to FAR regulations – see §3.9. Moreover, in order to allow direct comparison the figures show noise levels in A-averaged decibels (dBA).

As shown in Figure 4-60, considerable jet noise reduction is achieved in take off and approach. However, this is not the case for fan noise, where the increase of BPR leads to a relatively small improvement. Additionally, it is observed that no significant difference appears between the novel cycles, as already discussed in §4.4.5. Moreover, it can be noticed that baseline fan noise at approach is higher than take-off. This happens due to the, fact that fan noise is not so strongly affected by throttle setting, while the distance from the observer is much less in the approach, than the take-off measuring point. However, this is not the case for the high BPR engines, where increased diameter leads to stronger mass flow reduction at part load conditions. As a result a slight noise reduction appears during landing. On the other hand, a comparison between take-off and approach jet noise, shows a stronger effect in the case of baseline. Such a condition may be explained by the fact that high BPR engine throttling is less intense, due to higher ram drag.

Figure 4-61 presents jet and fan noise of the novel propulsion systems installed on the broad delta airframe. The major differences from baseline airframe are lower design-thrust, ultra high bypass ratios and noise shielding for the fan. Ultra high BPR leads to considerably low jet noise levels. On the other hand, fan noise is reduced due to effective shielding, but a comparison to the baseline engine shows less than 5dBs. This is consistent to the fact that thermodynamic cycle mainly affects jet noise.

4.5.3 Total Aircraft Noise

In a further step, after predicting noise from all sources at the two critical flight conditions, the calculation of total aircraft noise emissions is performed. This calculation follows the method described in §3.8.3 and the results are illustrated in Figure 4-62 and Figure 4-63. They include aircraft noise at take-off and approach for both baseline and broad delta airframes.

Airframe noise data have been provided by Mistry, [Mistry, 2008] and have been added to combined engine noise levels, in order to produce total aircraft noise emissions. A comparison between BD and baseline shows an approximately 20dB reduction in take-off and ~12dB in landing noise. However, this is achieved in the expense of higher fuel consumption. A comparison between fuel-optimised and final cycle designs for the broad delta shows a 10-17% increase in mission fuel consumption, as it has been previously discussed.

Compared to take-off, lower improvement is achieved in approach condition, as it is, mainly, affected by airframe noise and no reduction lower than 69dB(A) could be achieved for the airframe, [Mistry, 2008]. Finally, it could be concluded that the four novel propulsion systems do not present major variations in the between them noise.

4.6 Tables & Figures of Chapter 4

Airframe data	**Baseline**	**BDVT**
MTOW [kg]	149000	137000
Airframe weight [kg]	86803	64060
Payload [kg]	18550	18550
Max. Fuel weight [kg]	43000	43000
Fuselage Length [m]	53.67	53.67
Fuselage Max. Width [m]	5.03	5.03
Wingspan [m]	45.47	33.20
Wing Area [m^2]	258.45	354.60
Wing Aspect Ratio	8.0	3.11
Tailplane Span [m]	17.80	10.10
Tailplane Area [m^2]	65.16	65.9
Fin Height [m]	18.62	3.5
Total Fin Area [m^2]	39.09	28.4

Table 4-1: Baseline and Broad Delta V-Tail airframe geometry data.

Baseline Engine (CF6-80C2 type)	
BPR (SLS)	5.15
OPR (SLS)	31.5
FPR (SLS)	1.7
COT (SLS)[K]	1615
Mass Flow (SLS) [kg/s]	695
Fan, Compressor is. Efficiency	0.895
$\Delta P_{combustor}$	0.05
Turbine is. Efficiency	0.91
Weight [kg]	4386.7
Length [m]	4.274
Diameter [m]	2.7
Thrust (SLS) [kN]	267.5
Take-off Noise [dbA]	85.6
Approach Noise [dbA]	88.7
4000nm Mission Fuel [kg]	42729
4000nm Mission Duration	9h 3min

Table 4-2: Baseline engine data.

Constant Values	**Baseline**	**BDVT**
Fan polytropic efficiency	0.91	0.91
Compressor polytropic efficiency	0.9	0.9
Turbine polytropic efficiency	0.92	0.92
Combustor efficiency	0.998	0.998
Heat exchanger effectiveness	0.7	0.7
Combustor $\Delta P/P_{in}$	0.06	0.06
Heat exchanger $\Delta P/P_{in}$	0.02	0.02
Ducting $\Delta P/P_{in}$	0.01	0.01
Inlet pressure recovery	0.99	0.97
HPC/IPC pressure ratio	1	1
Fan air inlet Mach number	0.55	0.55
Fan-tip blade Mach number	0.95	0.95
Fan hub/tip ratio	0.3	0.3
Fan maximum diameter [m]	3.7	2.7
Altitude at ToC [m]	12192	12192
Flight Mach at ToC	0.8	0.8
Thrust at ToC [kN]	55	26
Altitude at Take-Off (FAR 36) [m]	442.5	442.5
Flight Mach at Take-Off	0.3	0.3
Thrust at Take-Off [kN]	135	63

Table 4-3: Values of constant input to parametric analysis method.

Design Variables Range

Min	Variable	Max	Step
5	BPR	18 / 30	1
30	OPR	60	2
1600 K	COT	2100 K	10 K

Table 4-4: Range of cycle design variables.

Airframe Type	**Baseline**					**Broad Delta V-Tail**			
Propulsion System Type	**Baseline**	**UHBPR**	**Recup**	**ICR**	**CVC**	**UHBPR**	**Recup**	**ICR**	**CVC**
BPR	5.15	11	10	17	12	24	25	25	25
OPR	31.5	58	34	32	32	60	56	30	29
COT [K]	1615	1610	1700	1870	1610	1680	1880	1660	1620
COT (OD) [K]	1446	1512	1570	1744	1492	1566	1726	1562	1484
SFC [mg/(Ns)]	16.5	14.507	15.147	13.904	10.883	14.378	14.341	14.31	10.889
Specific Thrust [N/(kg/s)]	160	105.1	111.15	110.63	109.98	55.62	57.29	64.74	56.92
Fuel [kg]	42729	39677	39426	37119	29982	36075	35782	35004	28950
Jet Noise [PNDBT]	85.1	68.1	69.8	68.7	68.7	44.7	47.0	52.7	45.3
Fan Noise [PNDBT]	118.1	112.6	112.7	112.8	112.2	106.6	107.0	108.1	106.6
CO2 [kg]	134036	124462	123675	116438	94050	113163	112244	109804	90813
Diameter [m]	2.7	3.69	3.63	3.65	3.65	2.47	2.46	2.29	2.47
Number of Fans/Engine	1	1	1	1	1	2	2	2	2
Number of Engines	2	2	2	2	2	4	4	4	4
Weight [kg]	4386.2	8198.6	5577.6	5466	4982.4	5518.8	5597.9	3562.5	4002.1
Length [m]	4.274	6.13	4.19	5.01	4.33	8.66	8.39	5.59	5.66
OF	1	0.89	0.896	0.861	0.768	0.713	0.722	0.744	0.625

Table 4-5: Optimum cycles for baseline and BDVT airframes

Fuel Optimised (BD airframe)

	UHBPR	Recup	ICR	CVC
BPR	15	11	20	15
OPR	60	50	42	36
COT [K]	2100	2100	2100	2000
COT (OD) [K]	1960	1940	1960	1850
SFC [mg/(Ns)]	14.596	14.755	13.512	10.669
Specific Thrust [N/(kg/s)]	137.83	142.25	118.77	137.6
Fuel [kg]	32.545	32.608	29.894	24.795
Jet Noise [PNDBT]	76.424	76.135	71.446	75.117
Fan Noise [PNDBT]	114.49	114.33	110.26	114.05
CO_2 [kg]	102090	102288	93774	77779
Diameter [m]	2.215	2.206	1.705	2.242
Number of Fans/Engine	1	1	1	1
Number of Engines	4	4	4	4
Weight [kg]	2486.1	2486.4	2286.7	1737.6
Length [m]	5.899	4.607	5.454	4.266
OF	0.839	0.84	0.77	0.638

Table 4-6: Fuel optimised propulsion cycles on Broad Delta airframe.

$(X_{final}-X_{fuel})/X_{fuel}$	UHBPR	Recup	ICR	CVC
BPR	60.0	127.3	25.0	66.7
OPR	0.0	12.0	-28.6	-19.4
COT [%]	-20.0	-10.5	-21.0	-19.0
COT (OD) [%]	-20.1	-11.0	-20.3	-19.8
SFC [%]	-1.5	-2.8	5.9	2.1
Specific Thrust [%]	-59.6	-59.7	-45.5	-58.6
Fuel [%]	**10.8**	**9.7**	**17.1**	**16.8**
Jet Noise [%]	**-41.5**	**-38.3**	**-26.2**	**-39.7**
Fan Noise [%]	-6.9	-6.4	-2.0	-6.5
CO_2 [%]	10.8	9.7	17.1	16.8
Diameter [%]	11.5	11.5	34.3	10.2
Weight [%]	122.0	125.1	55.8	130.3
Length [%]	46.8	82.1	2.5	32.7
OF	-15.0	-14.0	-3.4	-2.0

Table 4-7: Comparison between final cycles and fuel-optimised cycles [% of fuel-optimised].

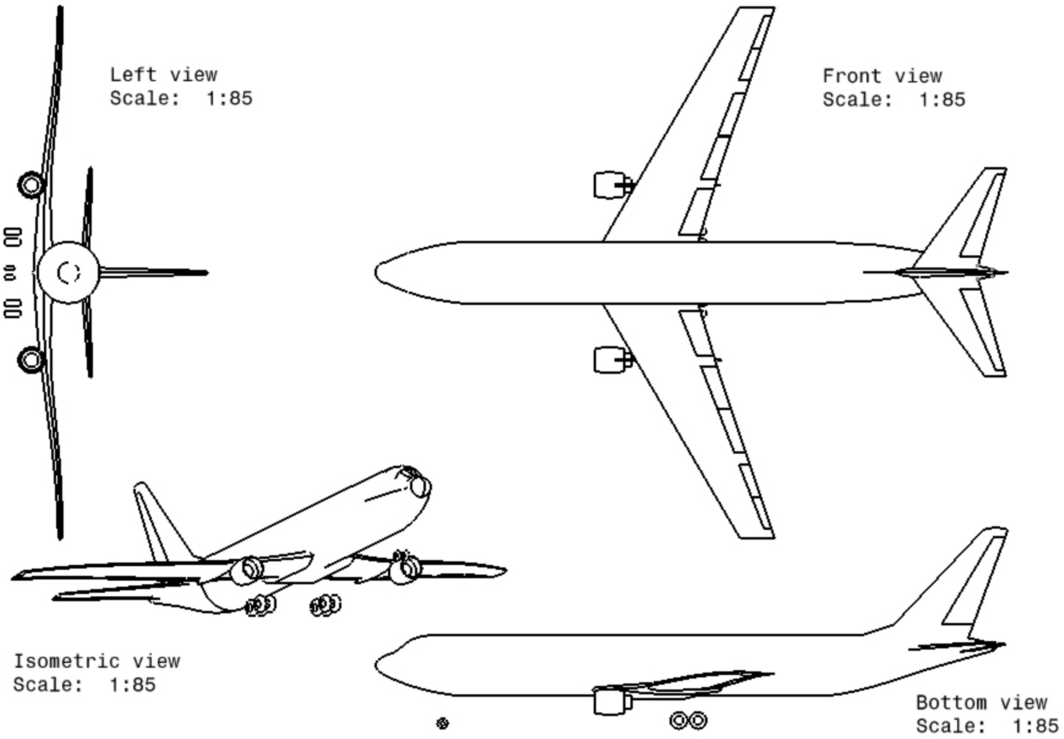

Figure 4-1: Baseline airframe design [Mistry, 2008].

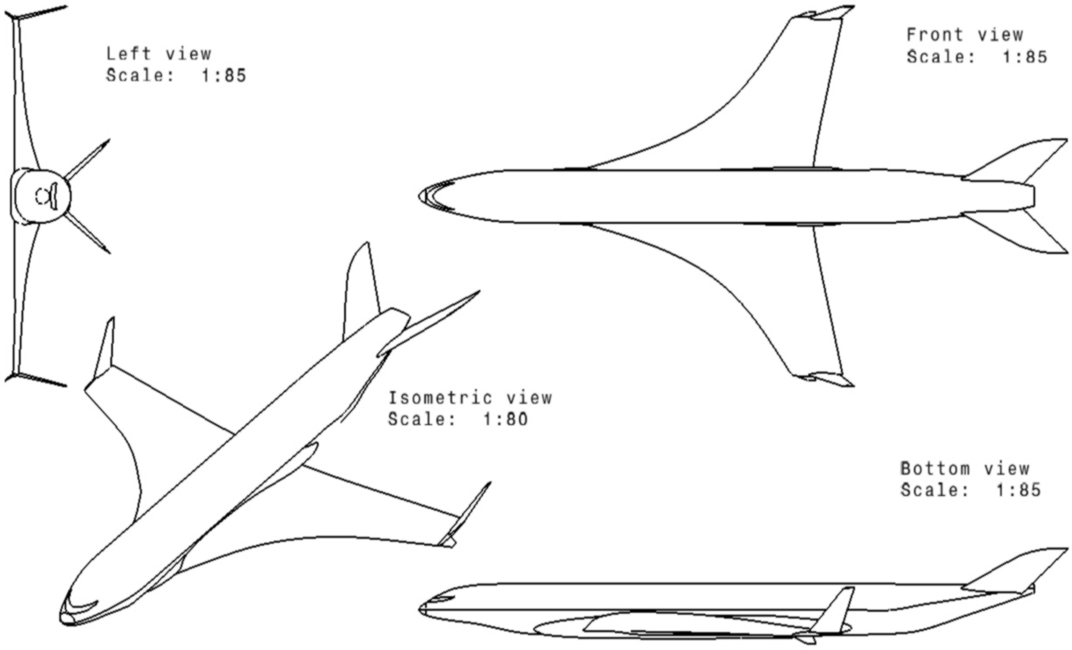

Figure 4-2: Broad Delta V-Tail airframe design [Mistry, 2008].

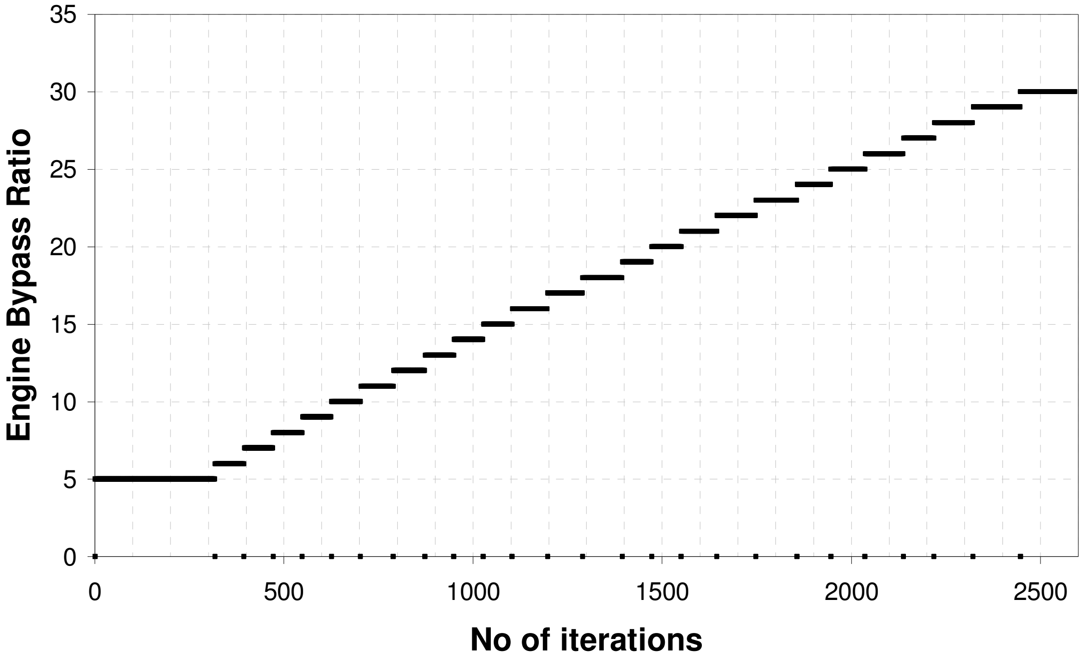

Figure 4-3: Variation of design point BPR during parametric analysis.

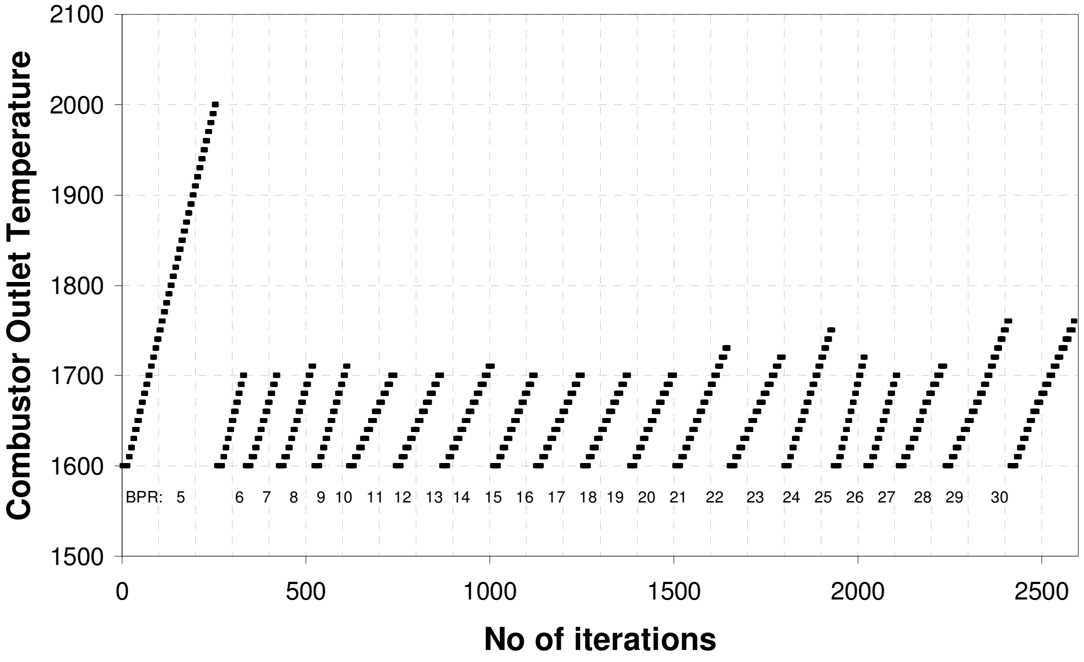

Figure 4-4: Variation of design point COT during parametric analysis.

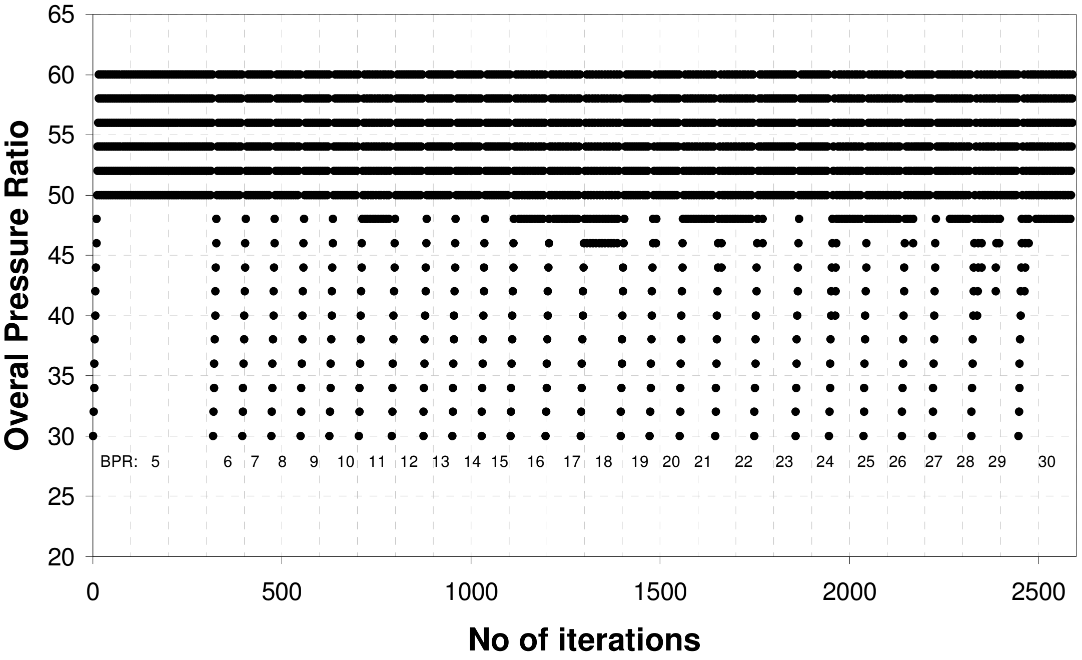

Figure 4-5: Variation of design point OPR during parametric analysis.

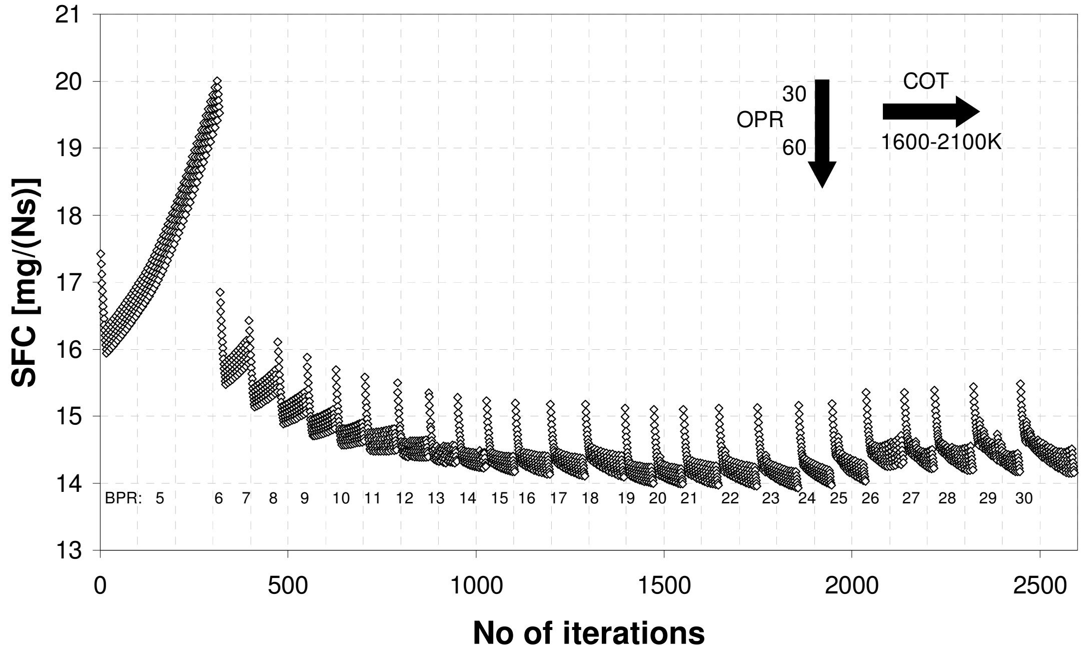

Figure 4-6: Variation of design point specific fuel consumption during parametric analysis.

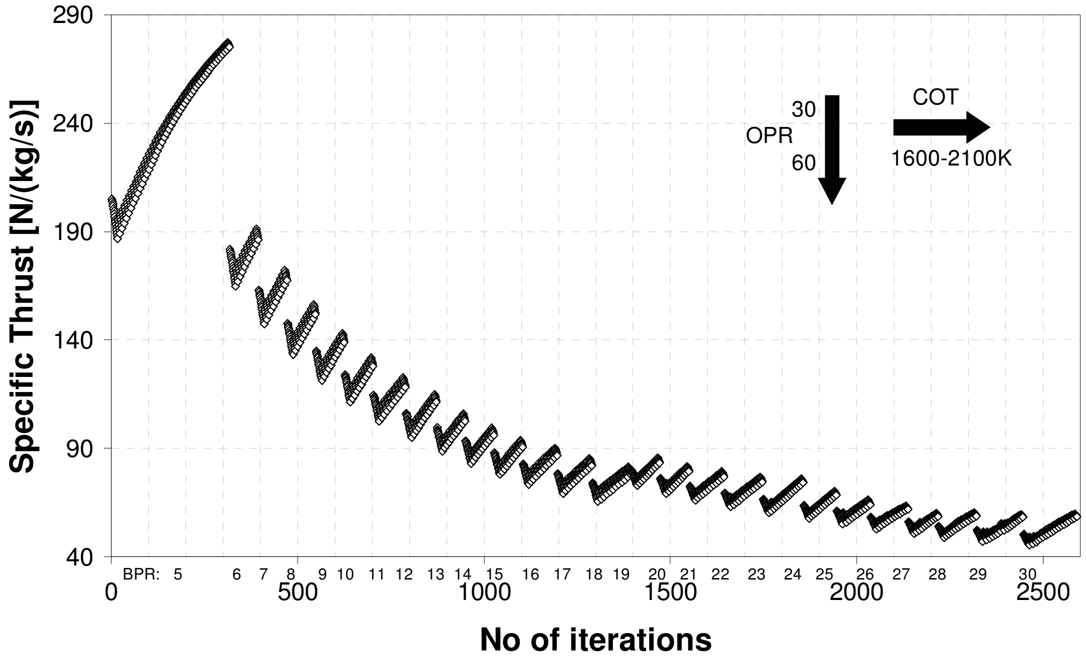

Figure 4-7: Variation of design point specific thrust during parametric analysis.

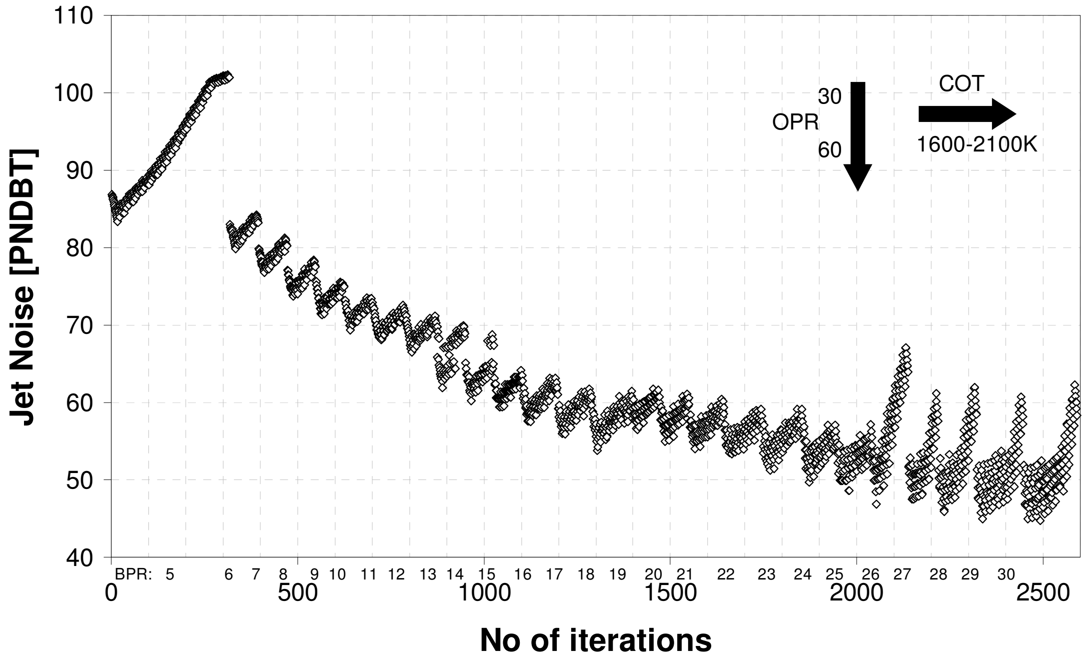

Figure 4-8: Variation of jet noise during parametric analysis.

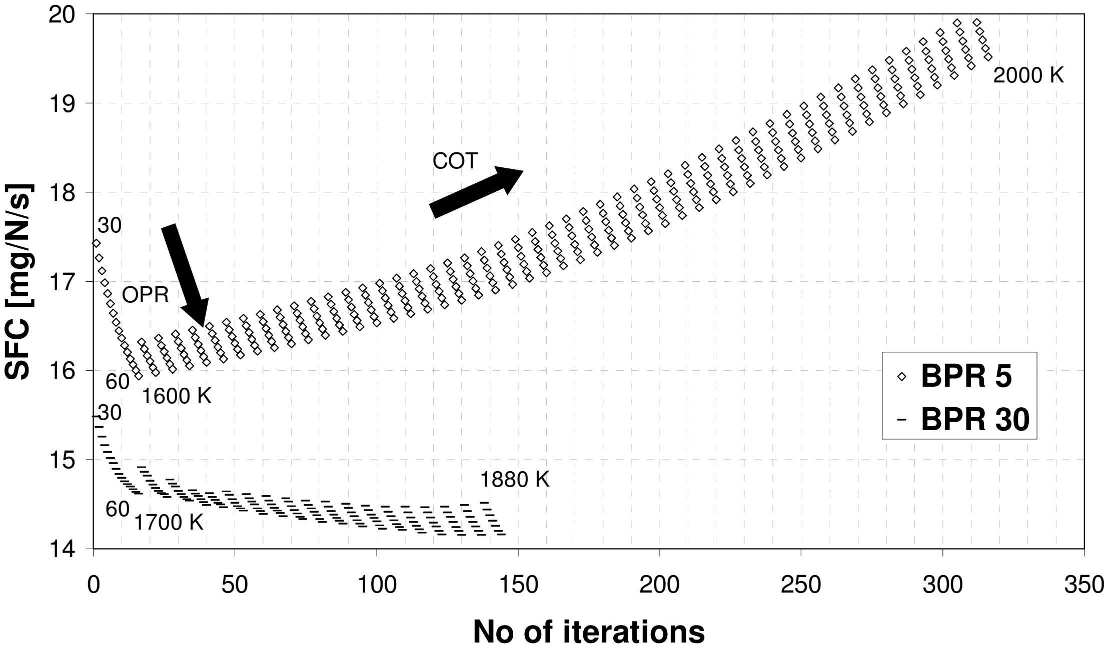

Figure 4-9: Variation of design point specific fuel consumption for two extreme BPRs.

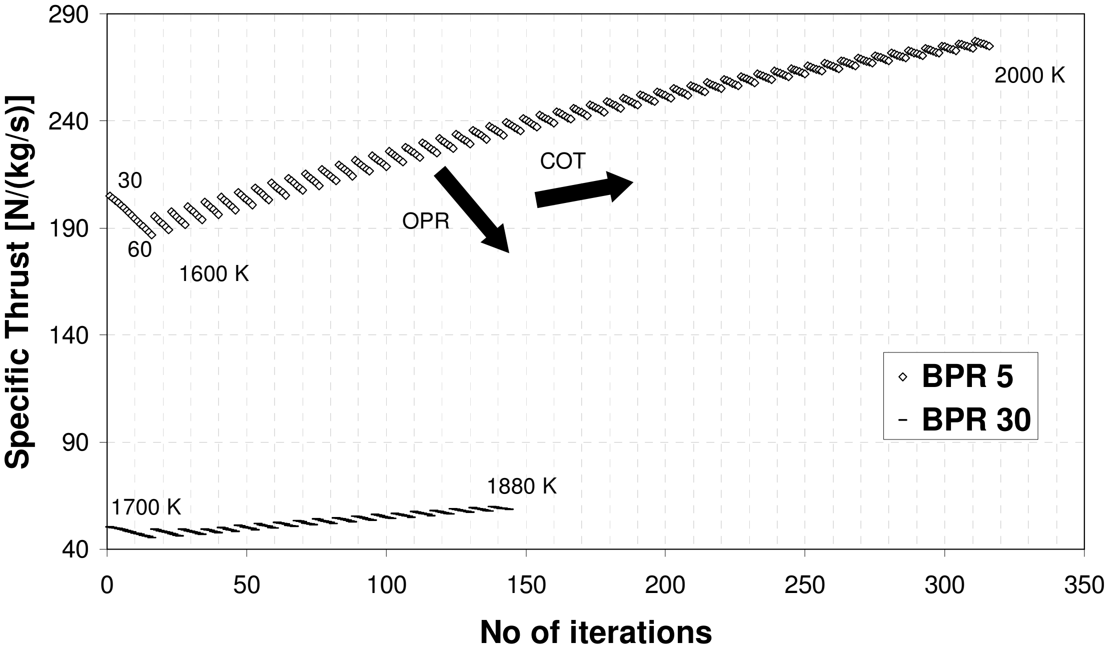

Figure 4-10: Variation of design point specific thrust for two extreme BPRs.

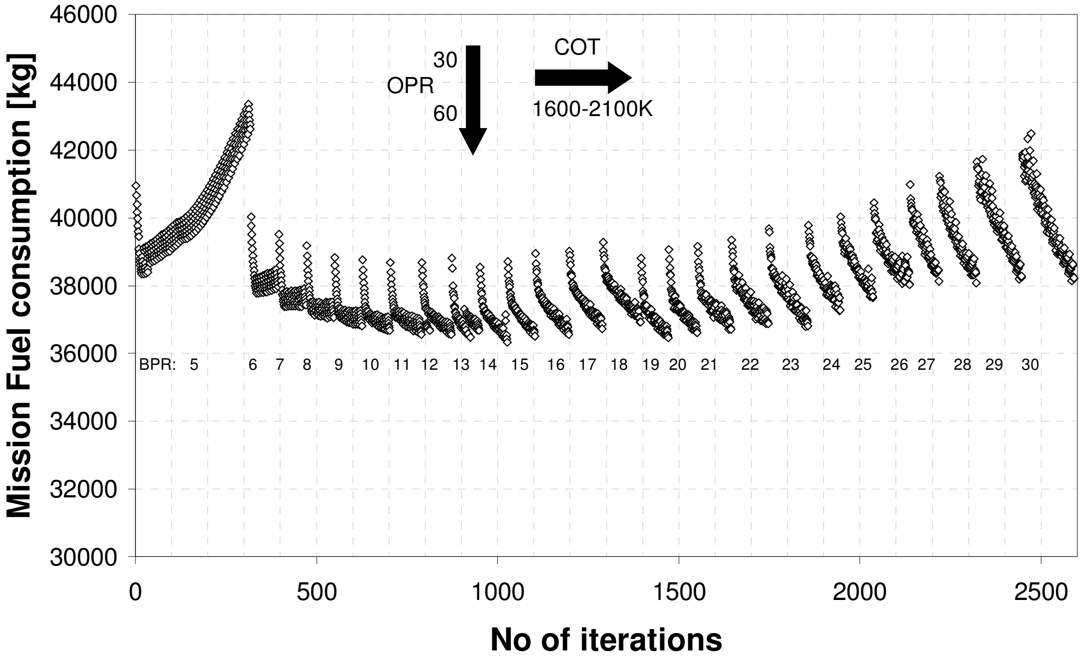

Figure 4-11: Variation of mission fuel during parametric analysis.

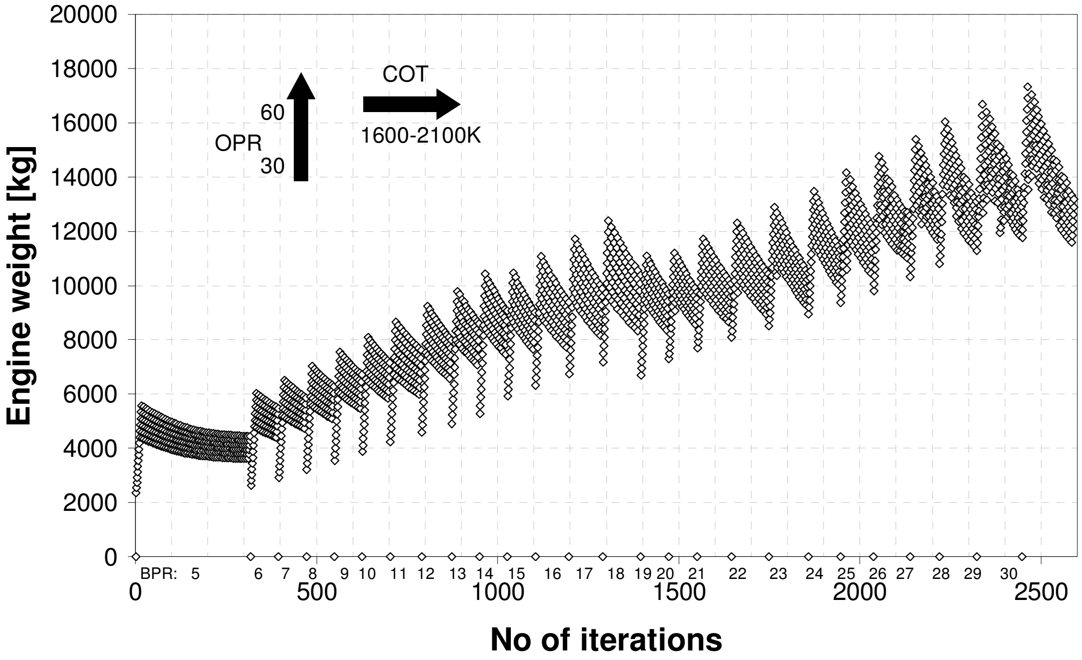

Figure 4-12: Engine weight prediction during parametric analysis.

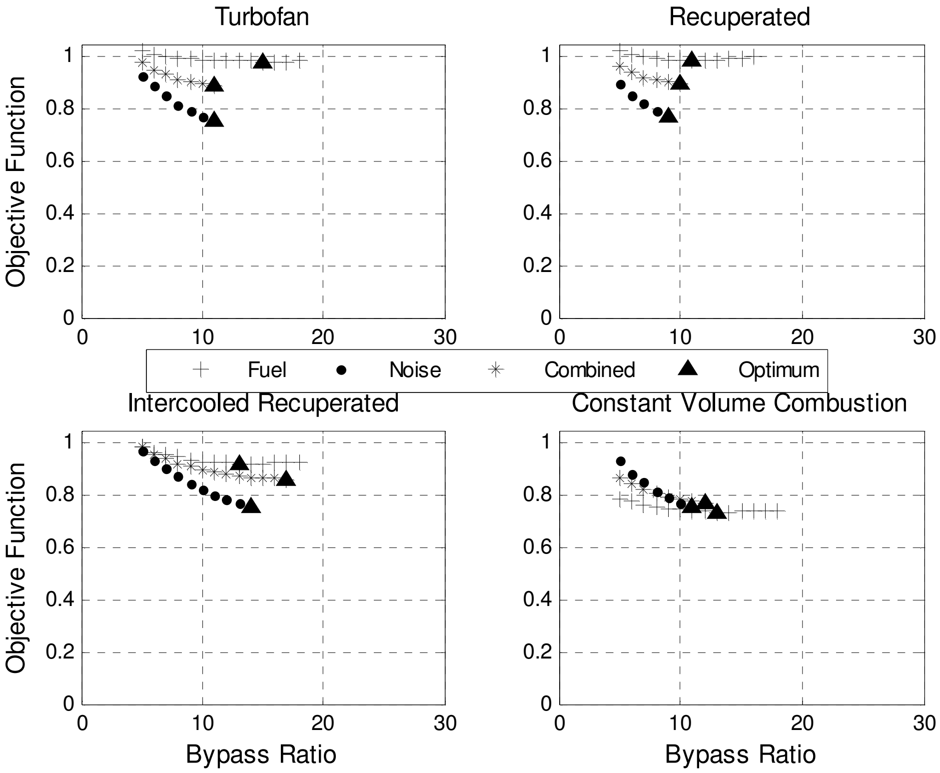

Figure 4-13: Objective function for baseline airframe.

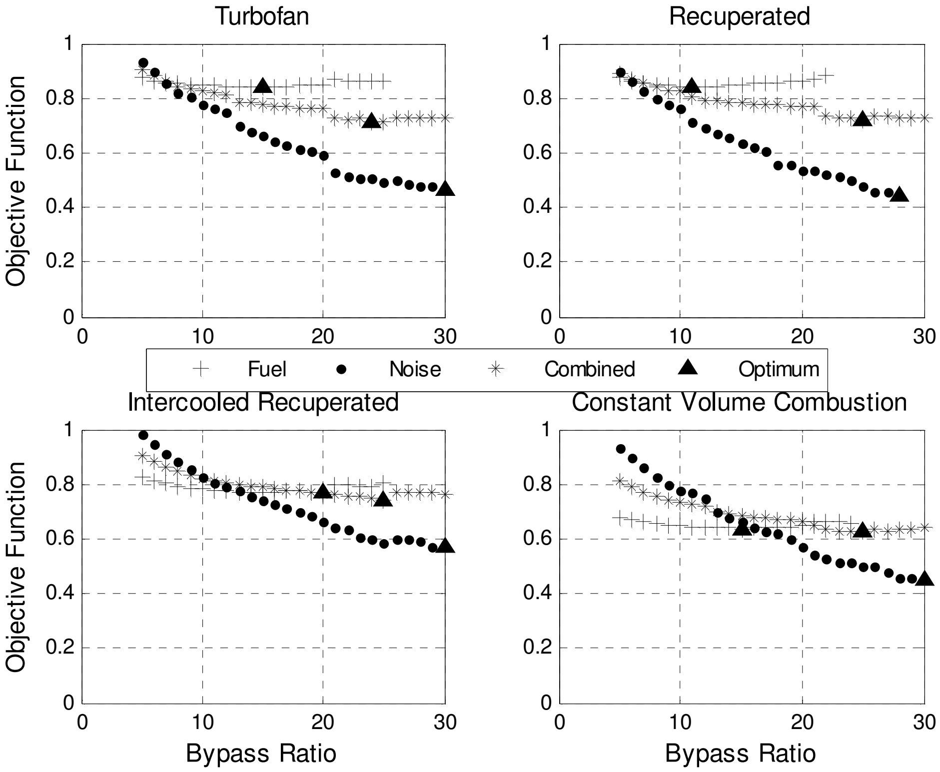

Figure 4-14: Objective function for BDVT airframe.

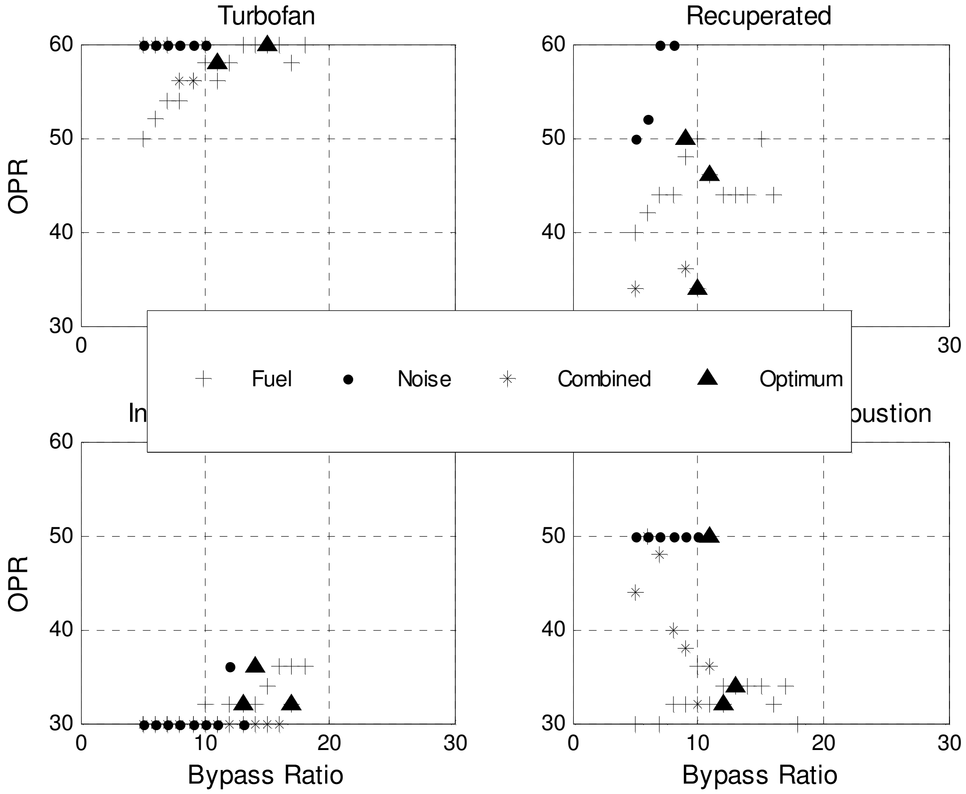

Figure 4-15: Overall pressure ratio for baseline airframe.

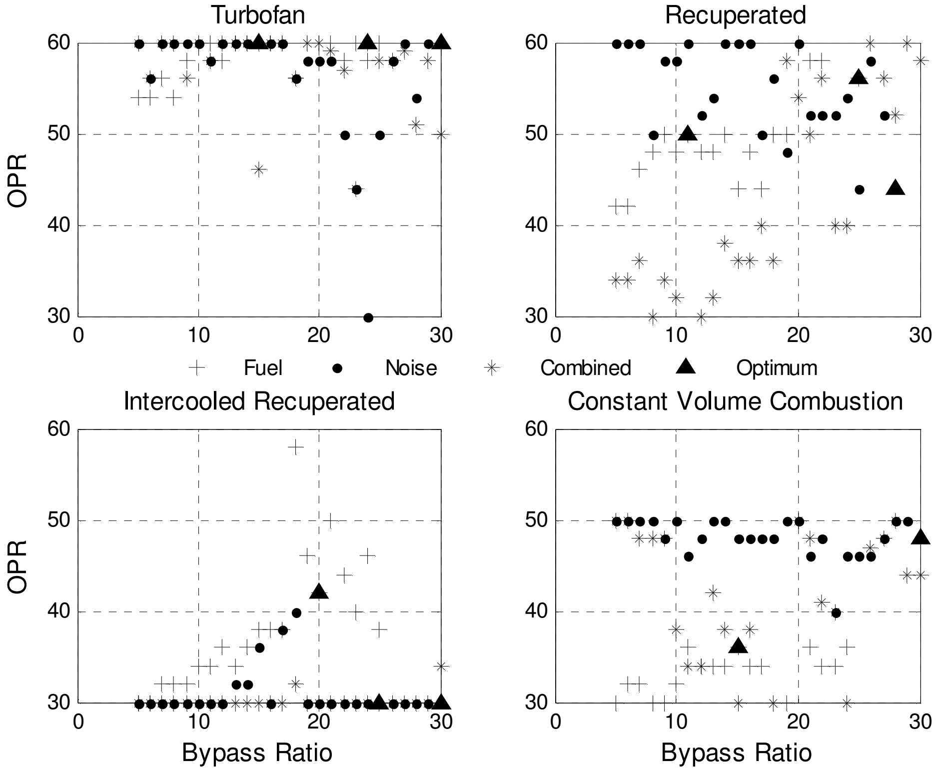

Figure 4-16: Overall pressure ratio for BDVT airframe.

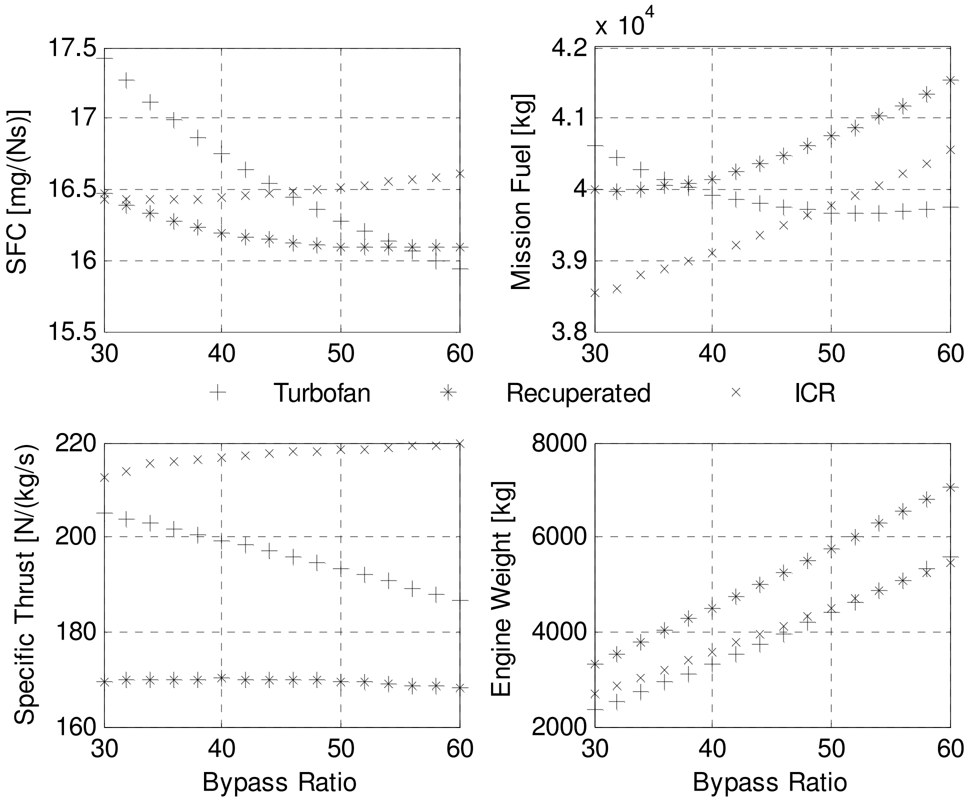

Figure 4-17: Parameter variation with OPR at BPR=5 and COT=1600K for turbofan.

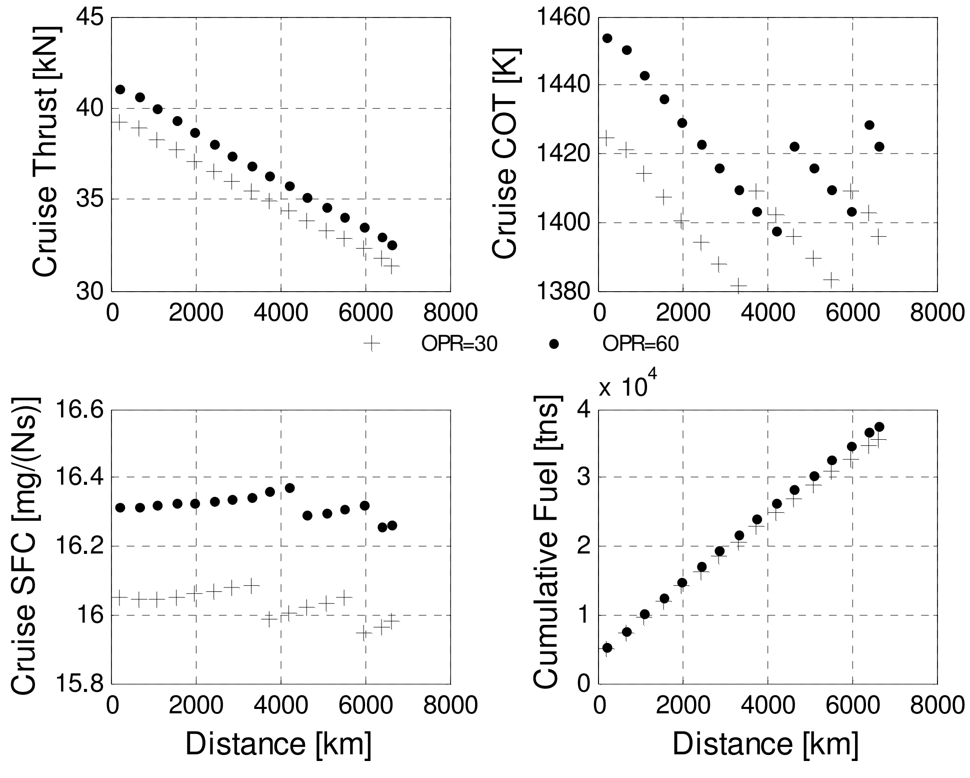

Figure 4-18: Effect of increased weight on aircraft performance at BPR=5 and COT=1600K.

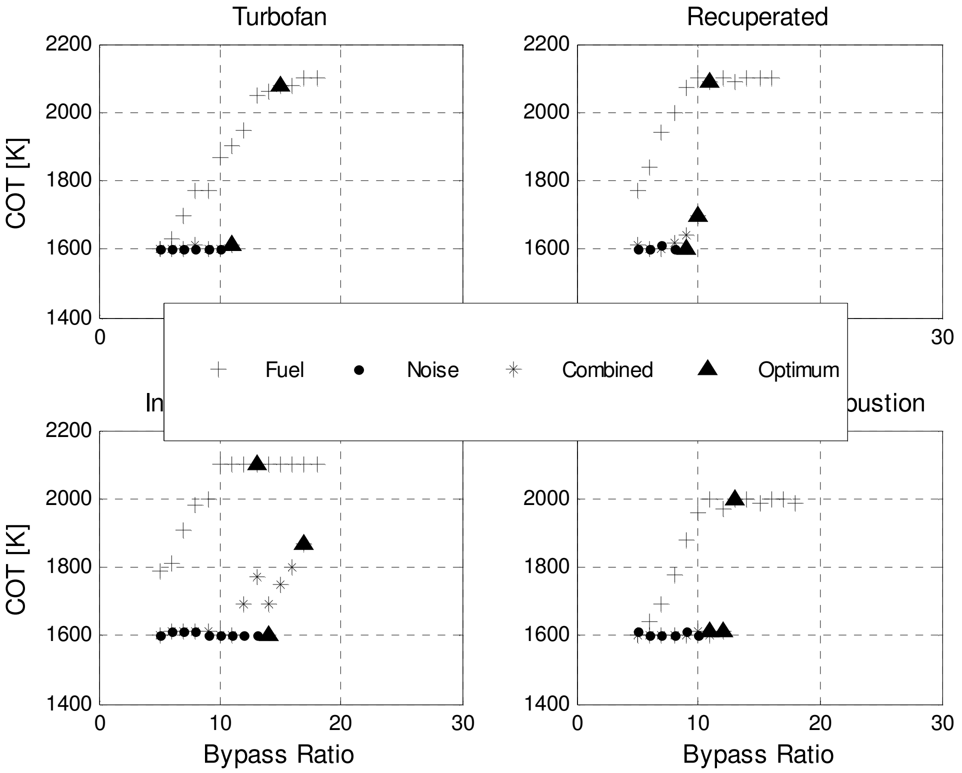

Figure 4-19: Combustor outlet temperature at design point for baseline airframe.

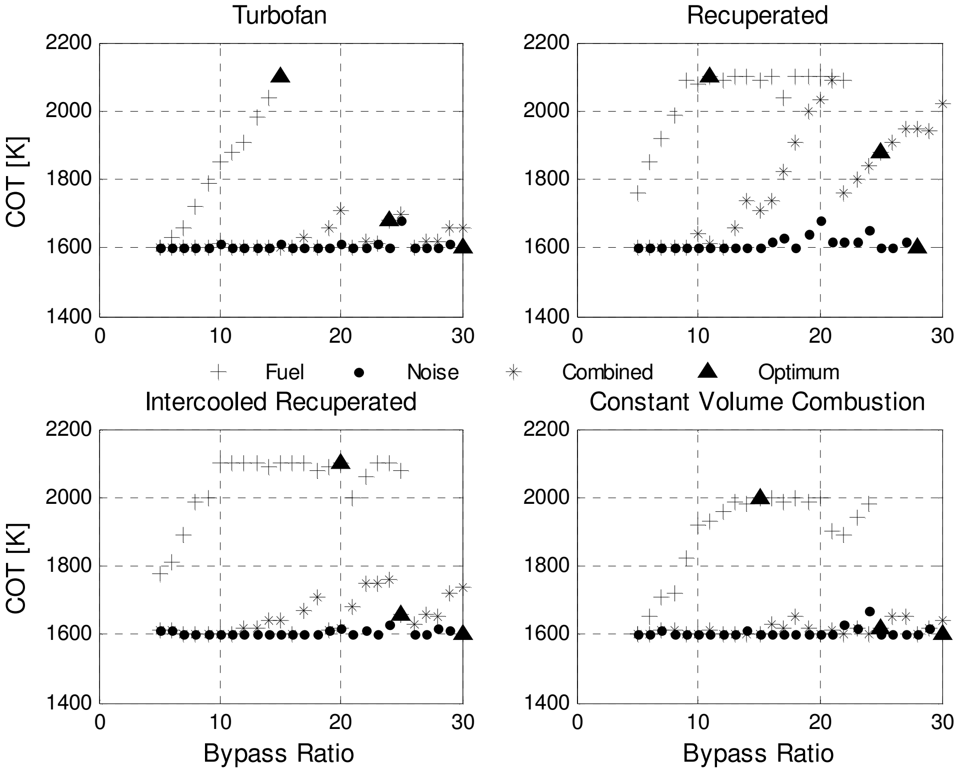

Figure 4-20: Combustor outlet temperature at design point for BDVT airframe.

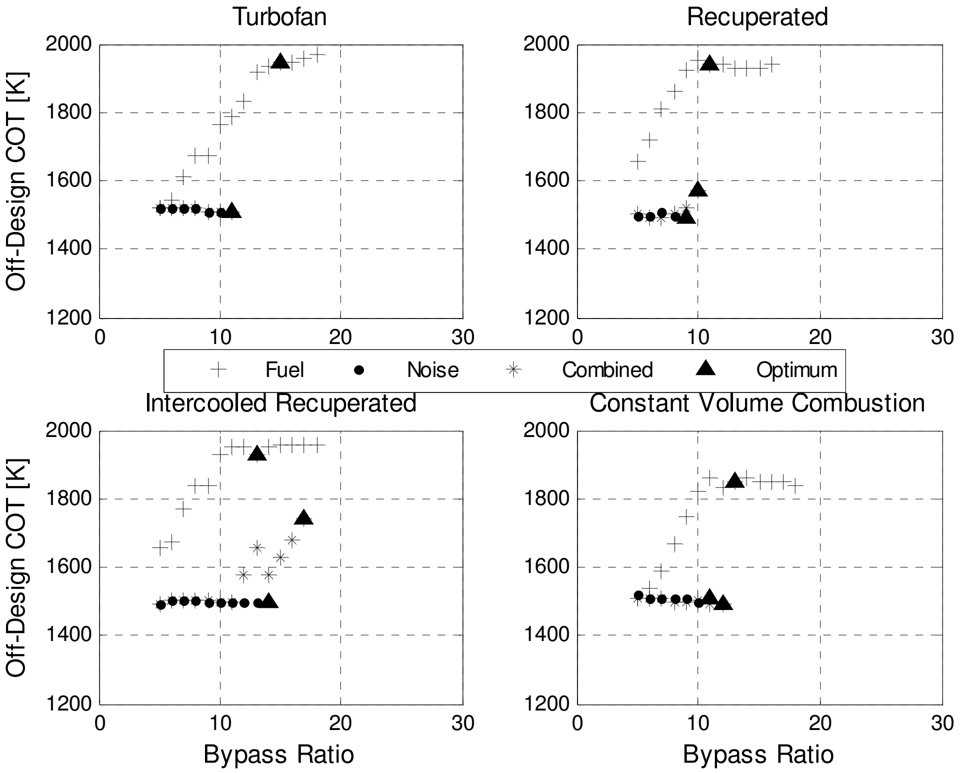

Figure 4-21: Combustor outlet temperature at off-design for baseline airframe.

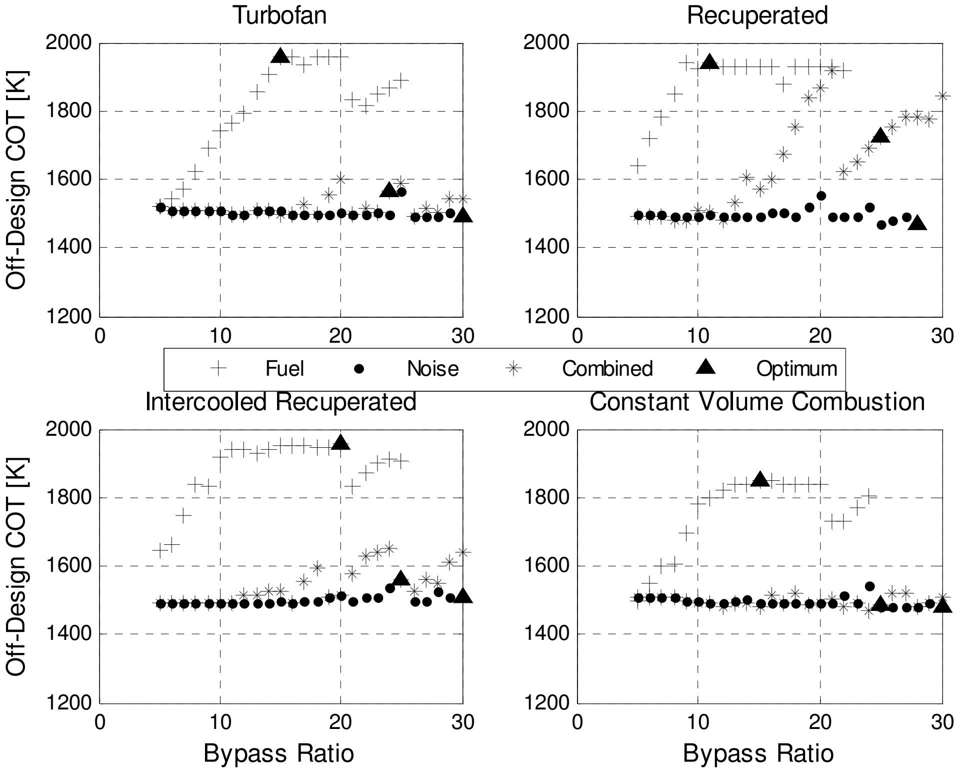

Figure 4-22: Combustor outlet temperature at off-design for BDVT airframe.

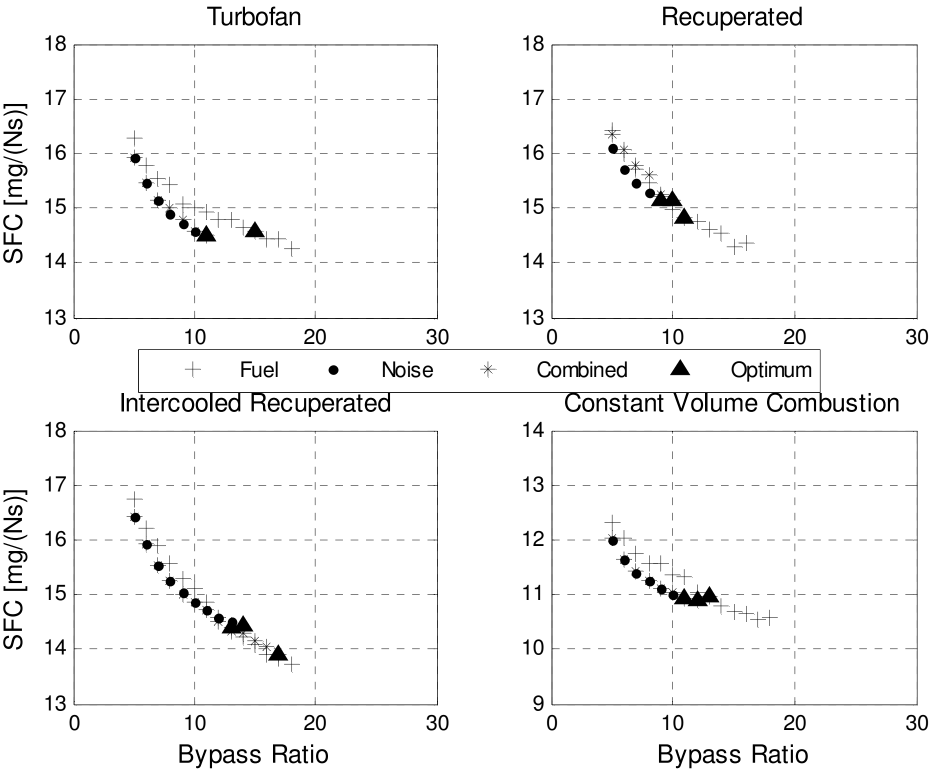

Figure 4-23: Specific fuel consumption for baseline airframe.

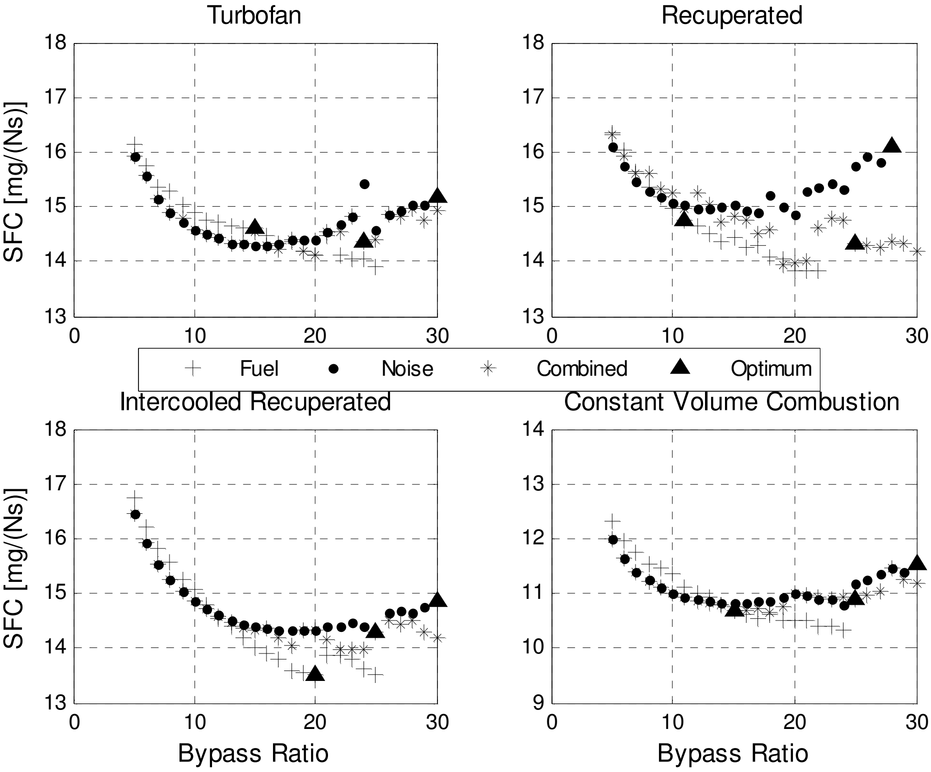

Figure 4-24: Specific fuel consumption for BDVT airframe.

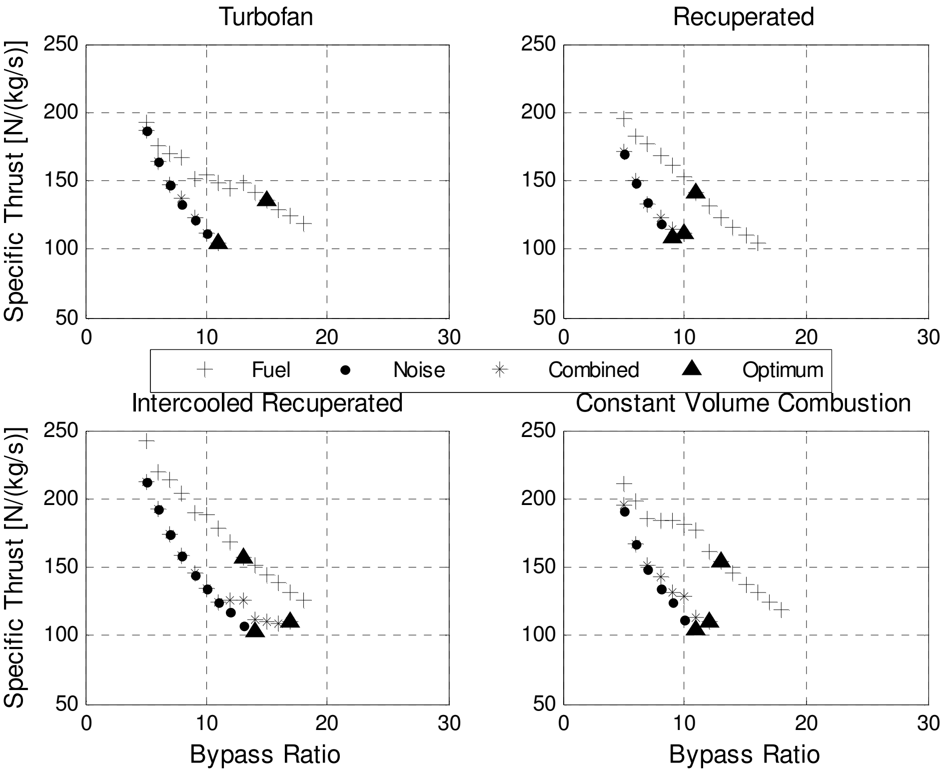

Figure 4-25: Specific thrust for baseline airframe.

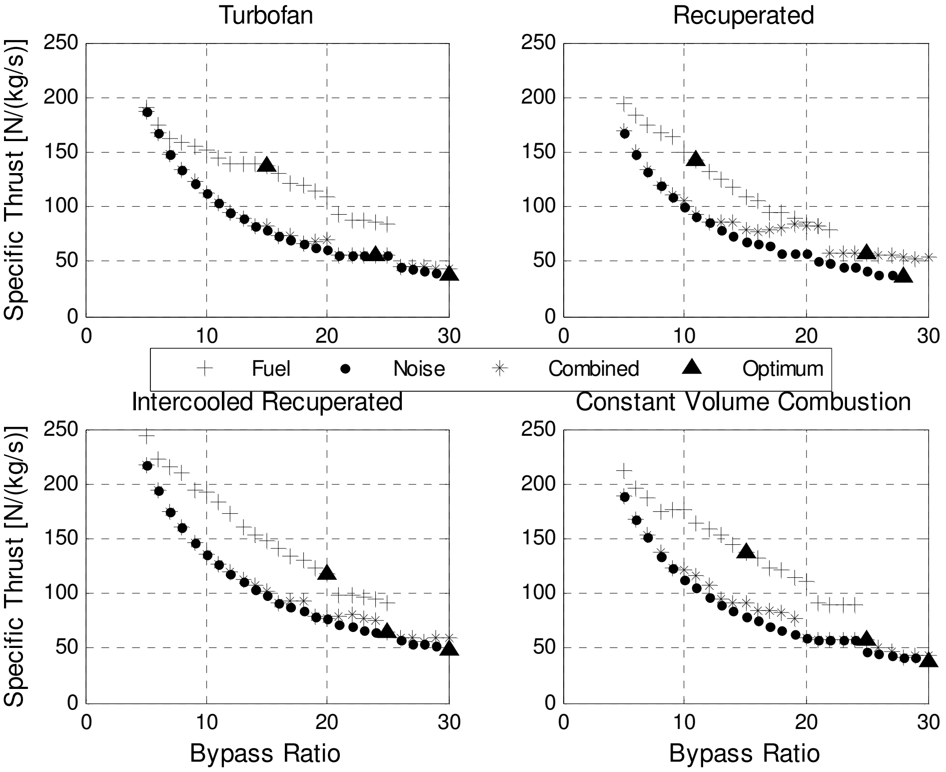

Figure 4-26: Specific thrust for BDVT airframe.

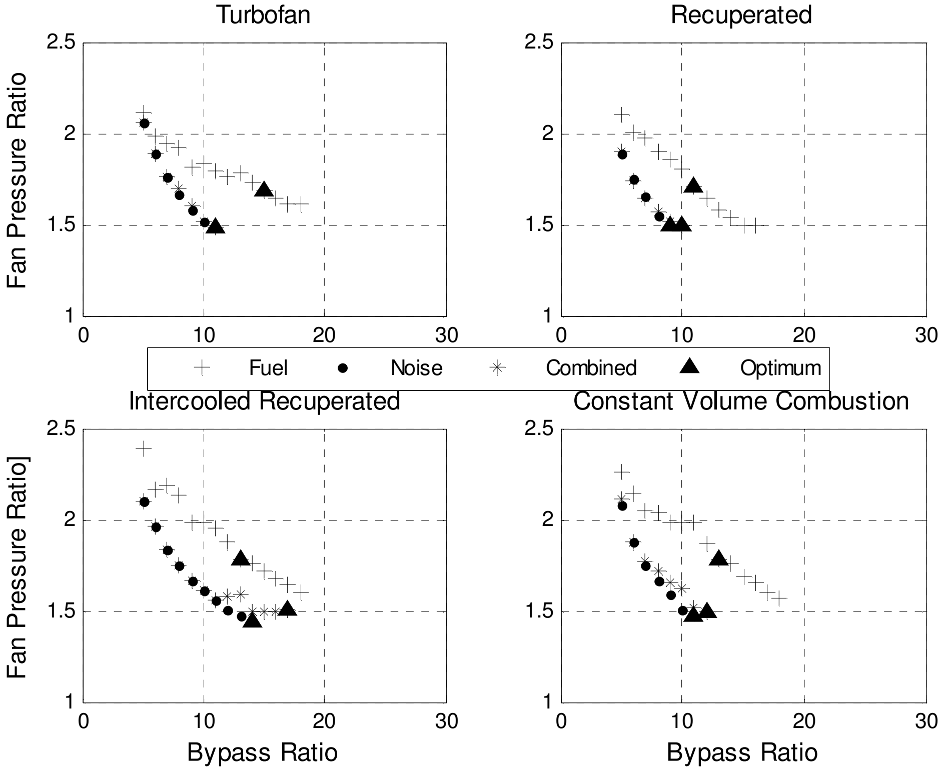

Figure 4-27: Fan pressure ratio for baseline airframe.

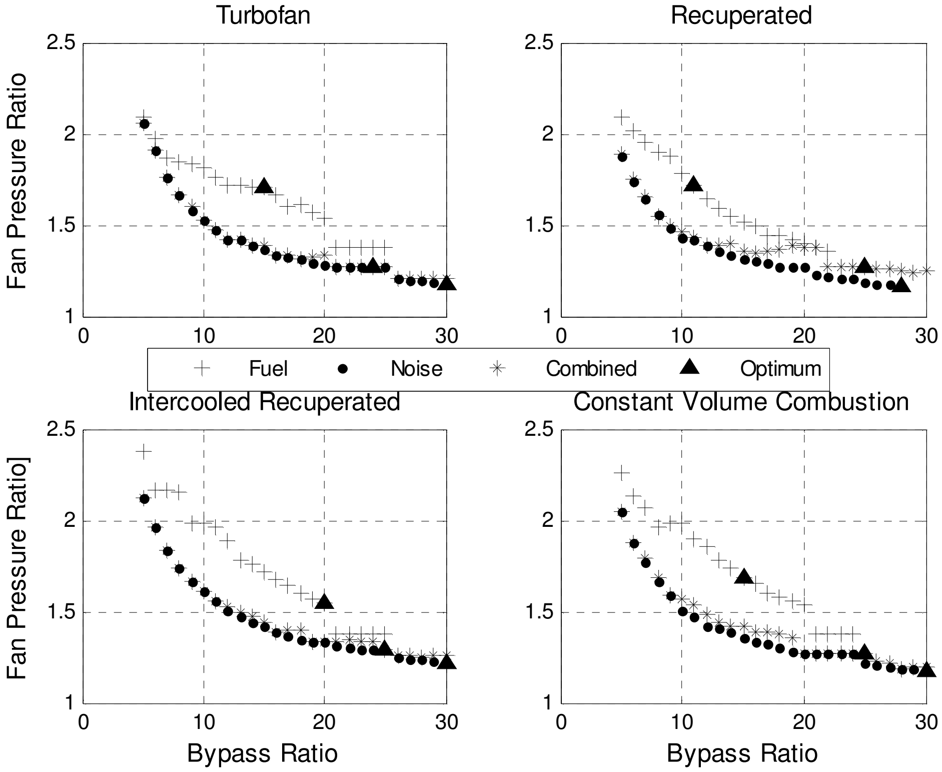

Figure 4-28: Fan pressure ratio for BDVT airframe.

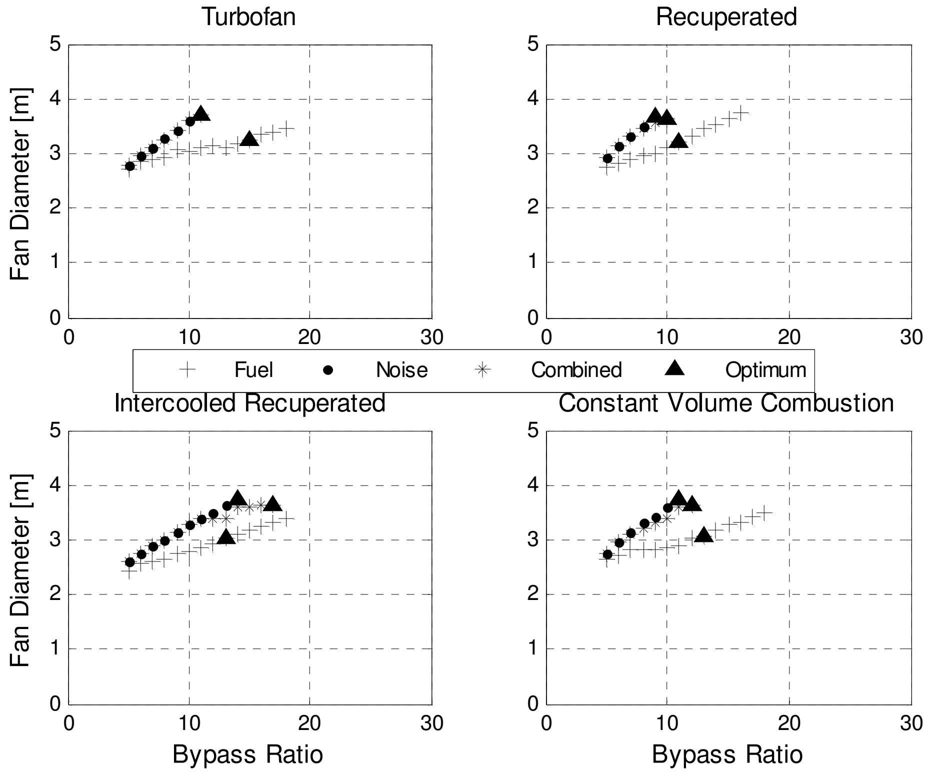

Figure 4-29: Fan diameter for baseline airframe.

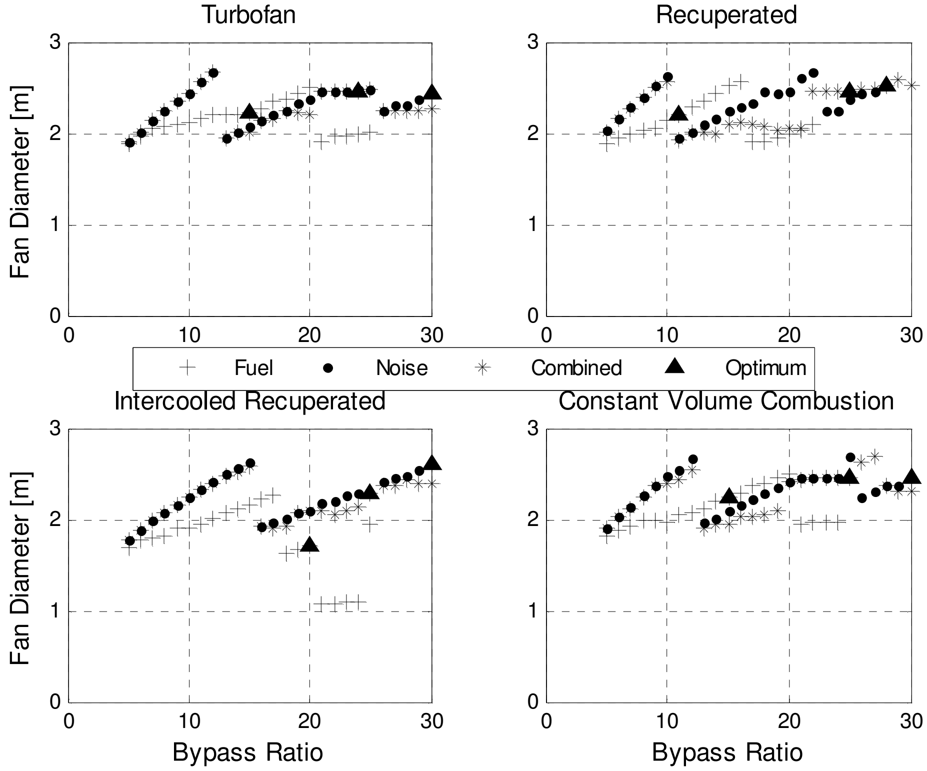

Figure 4-30: Fan diameter for BDVT airframe.

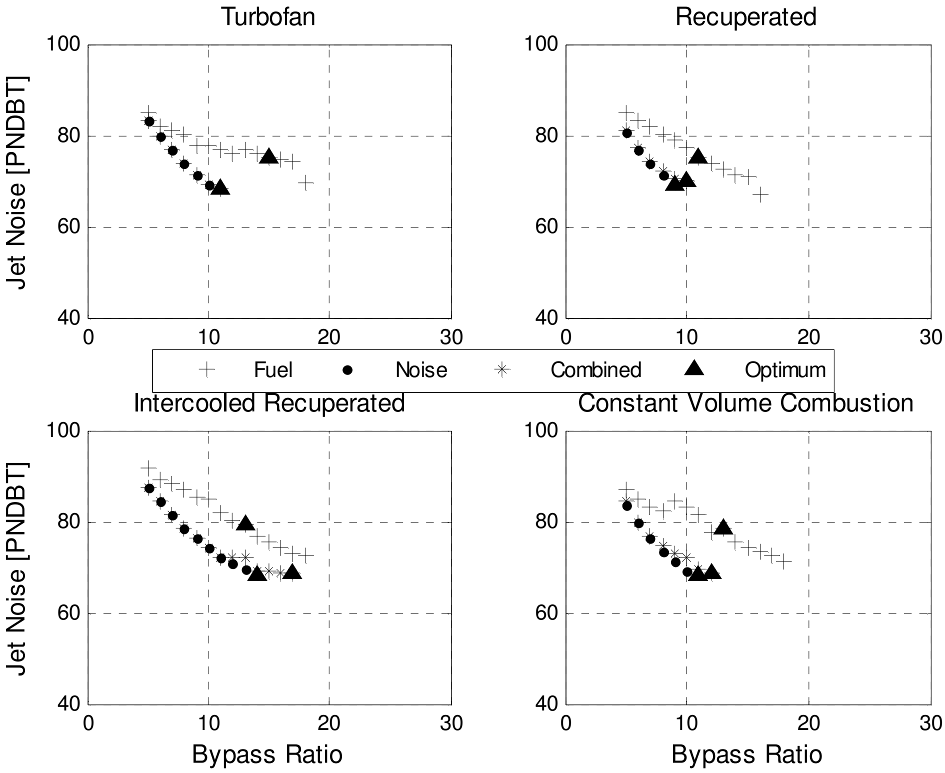

Figure 4-31: Jet noise for baseline airframe.

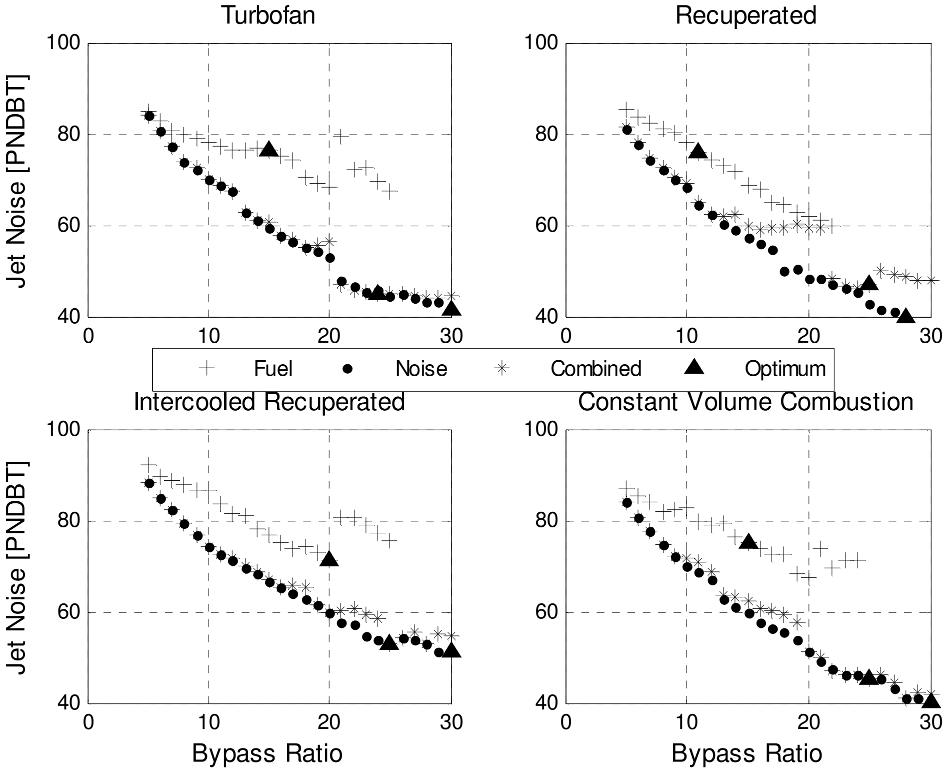

Figure 4-32: Jet noise for BDVT airframe.

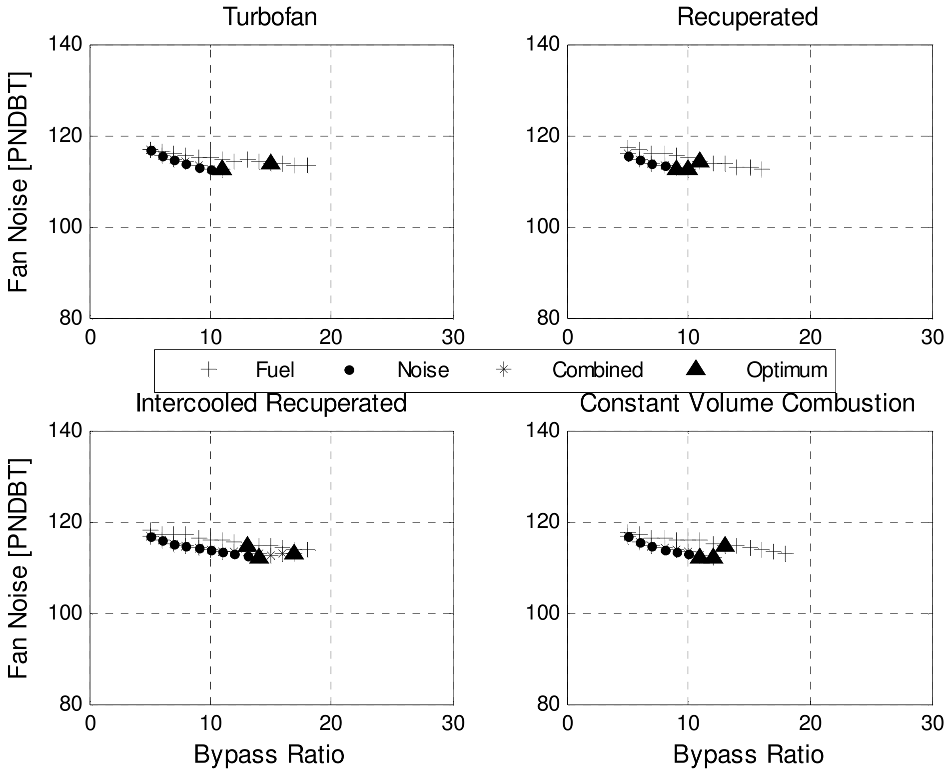

Figure 4-33: Fan noise for baseline airframe.

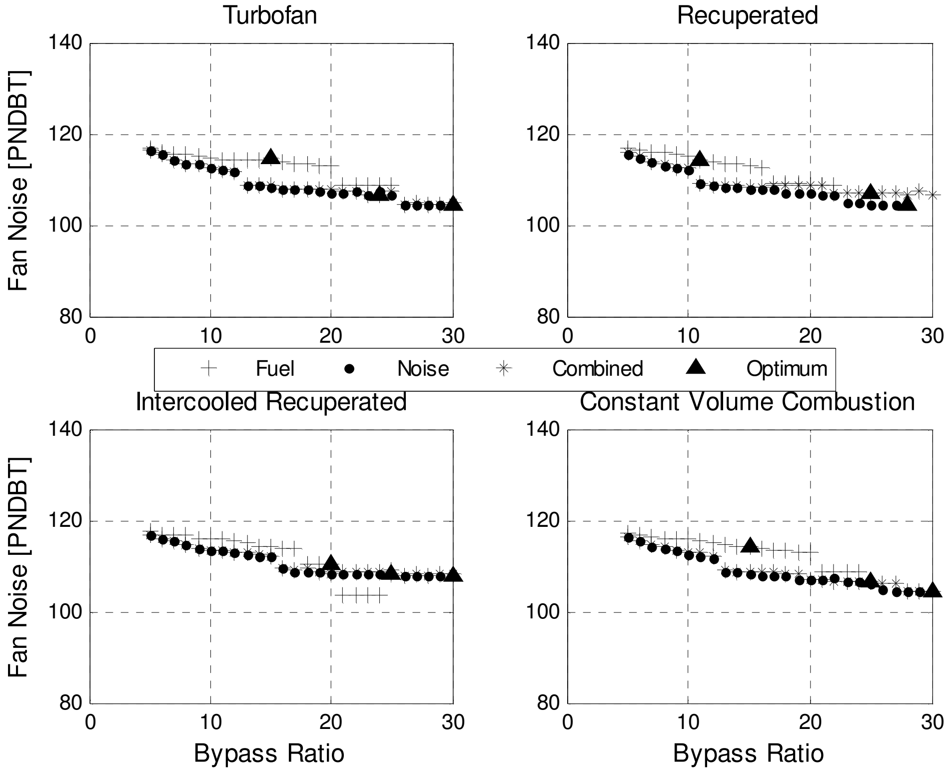

Figure 4-34: Fan noise for BDVT airframe.

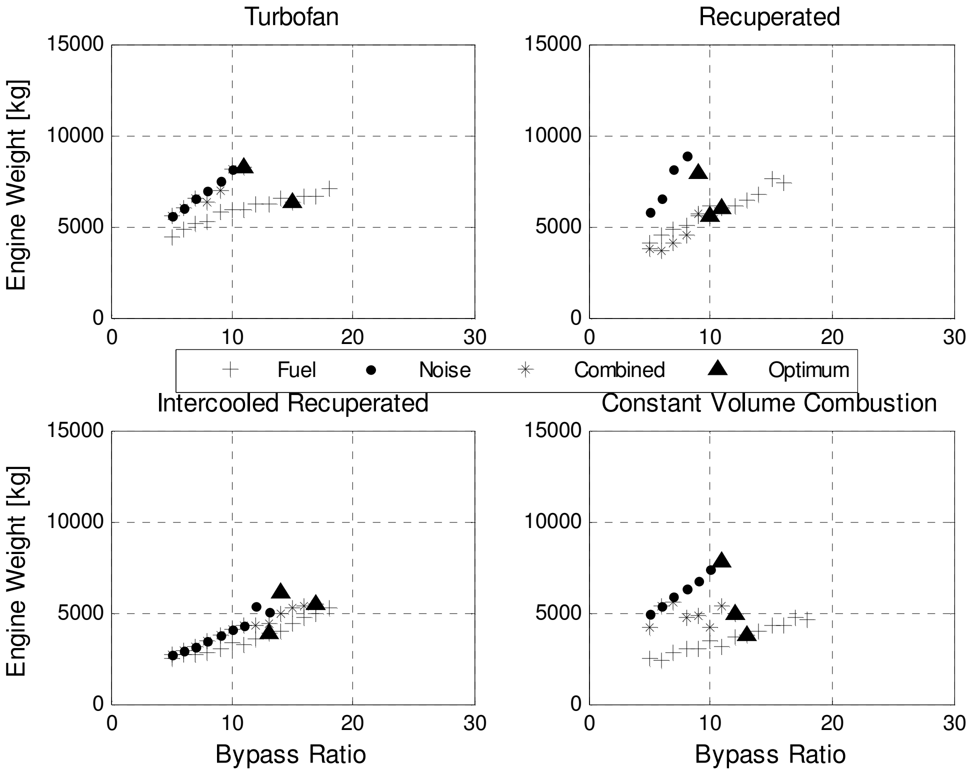

Figure 4-35: Engine weight for baseline airframe.

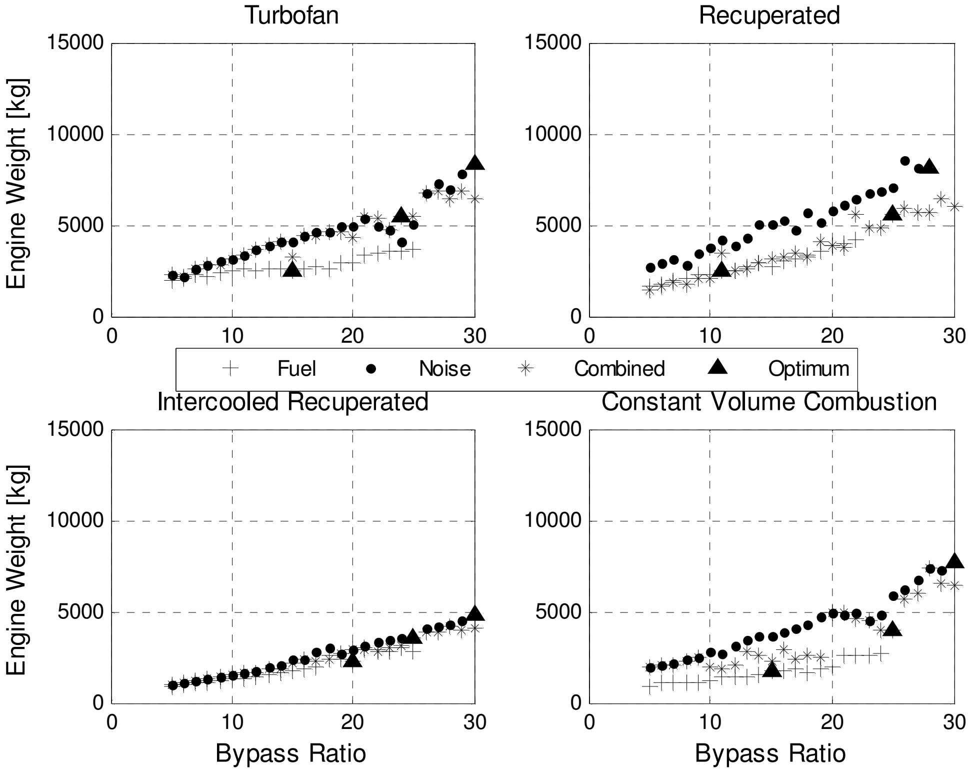

Figure 4-36: Engine weight for BDVT airframe.

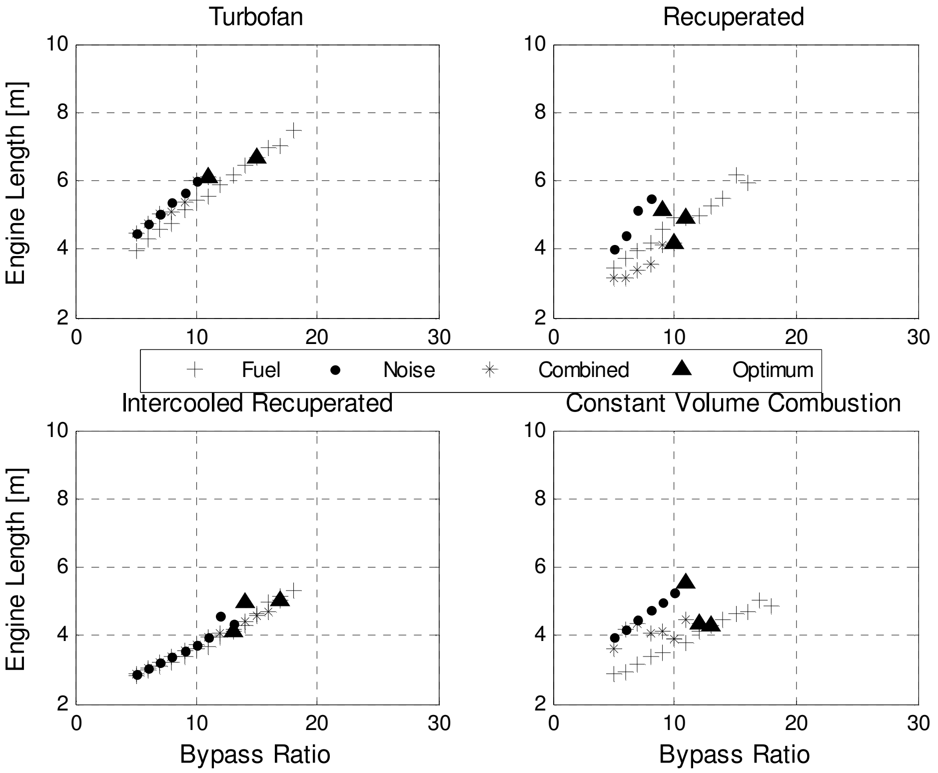

Figure 4-37: Engine length for baseline airframe.

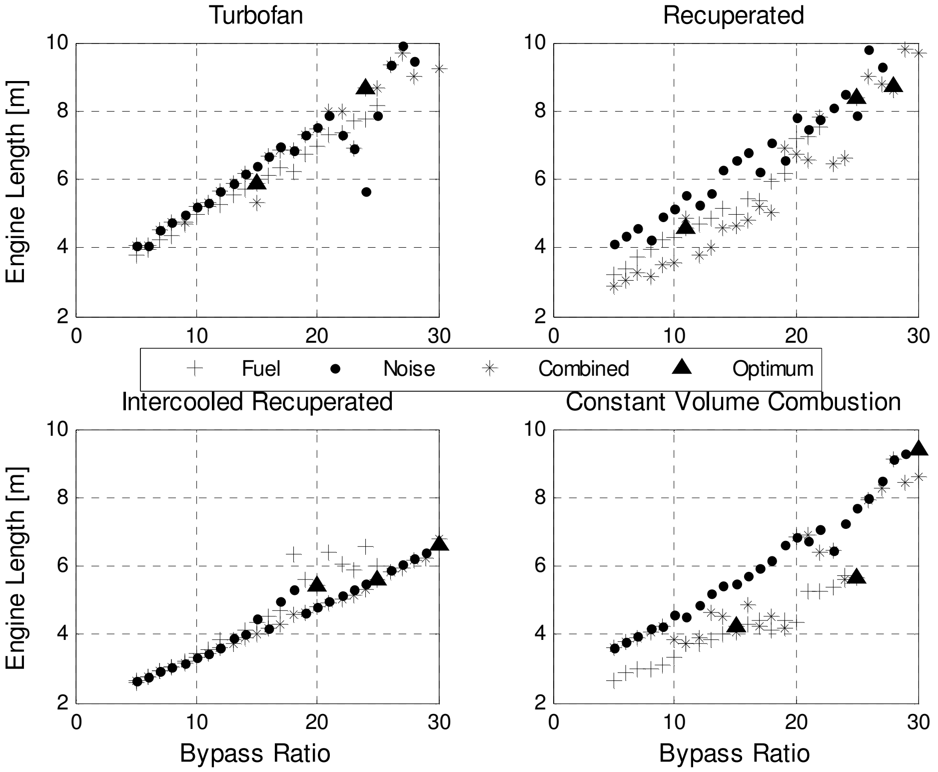

Figure 4-38: Engine length for BDVT airframe.

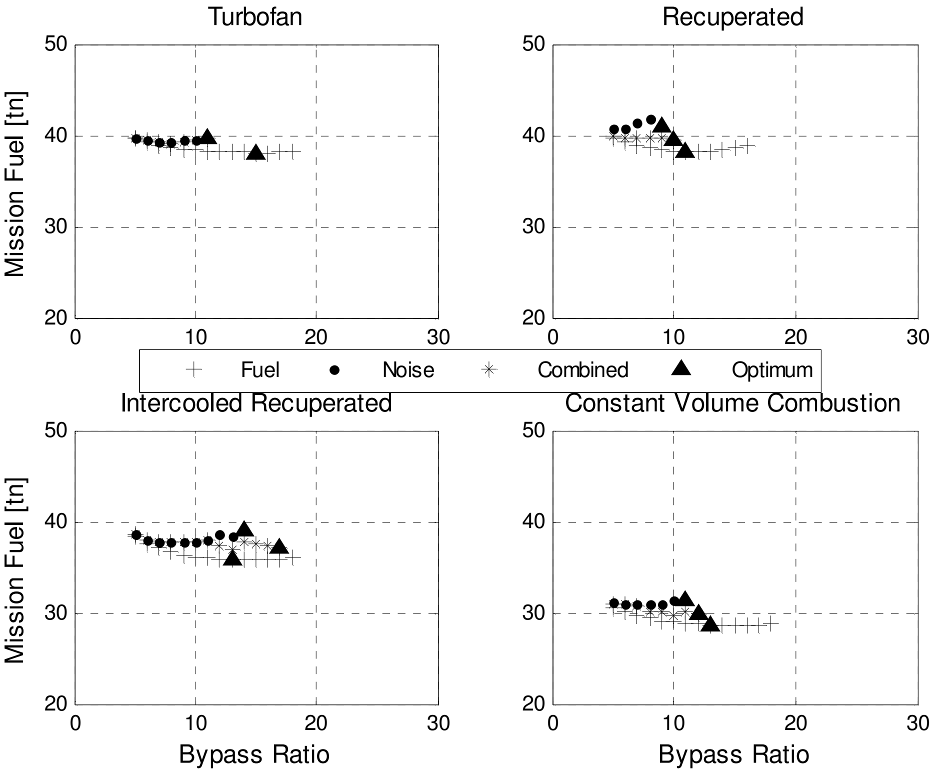

Figure 4-39: Mission fuel for baseline airframe.

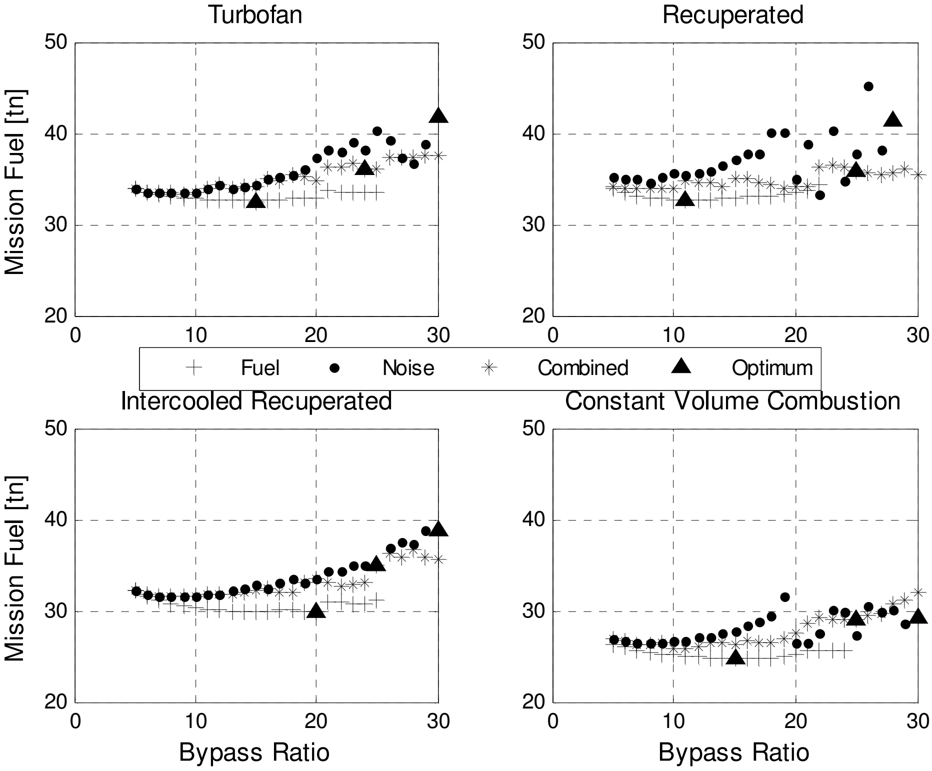

Figure 4-40: Mission fuel for BDVT airframe.

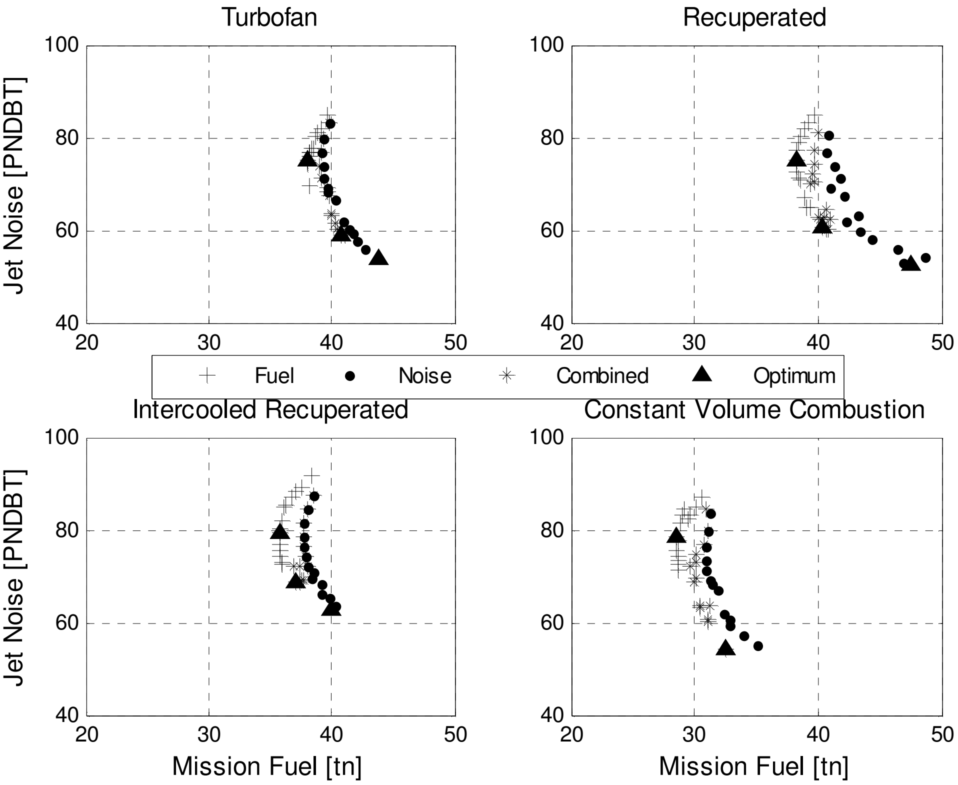

Figure 4-41: Fuel and jet noise for baseline airframe.

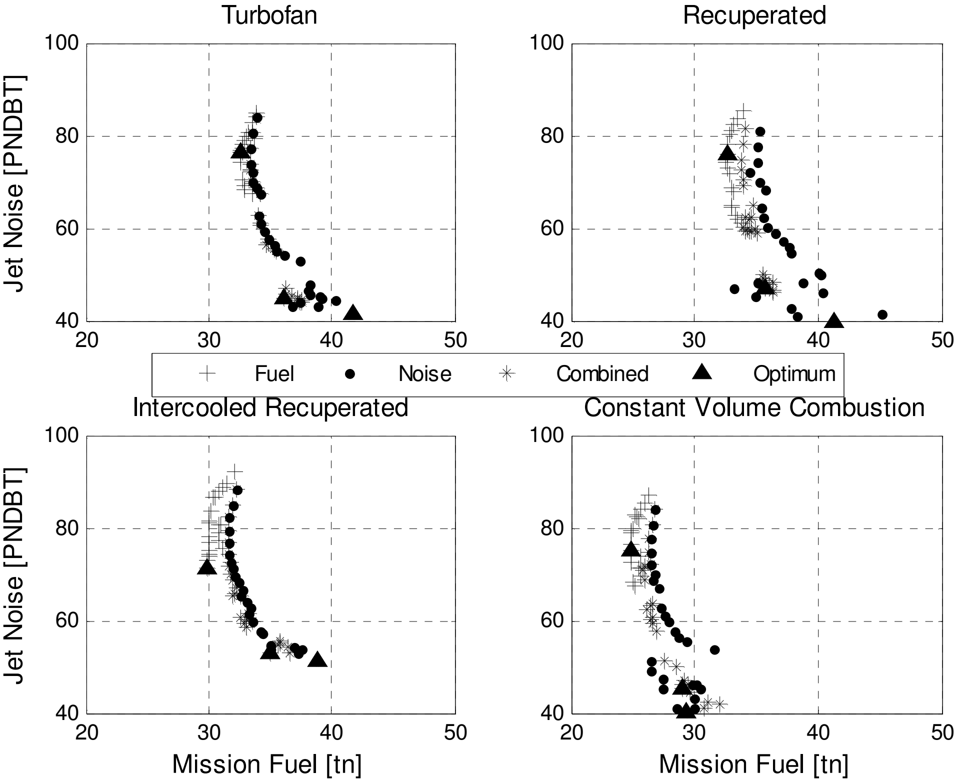

Figure 4-42: Fuel and jet noise for BDVT airframe.

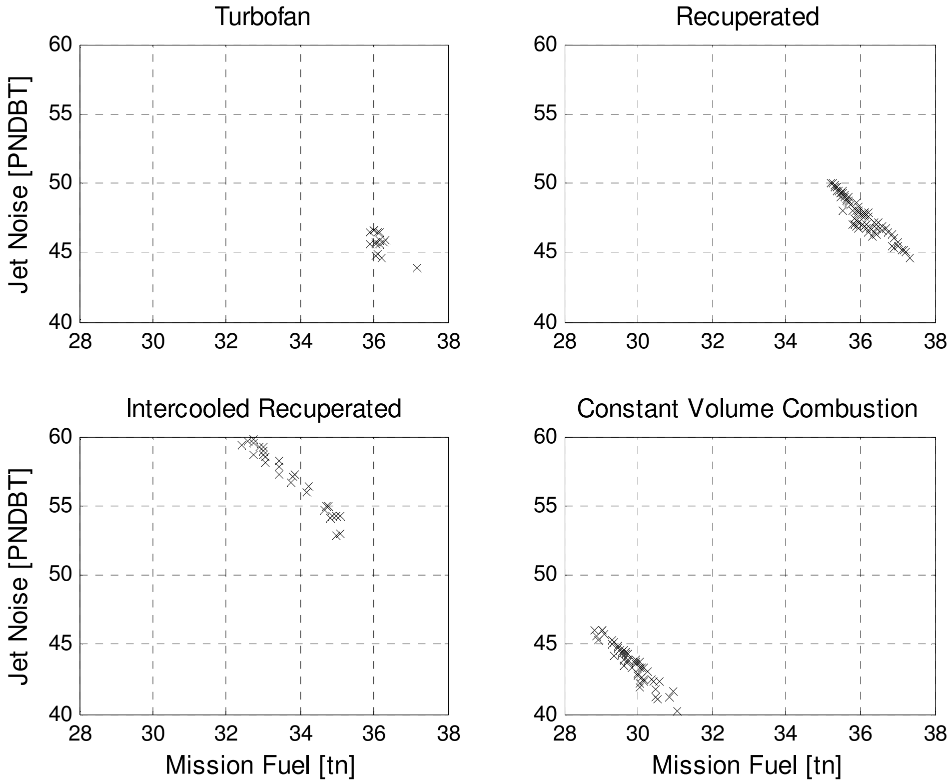

Figure 4-43: Pareto front for BDVT airframe.

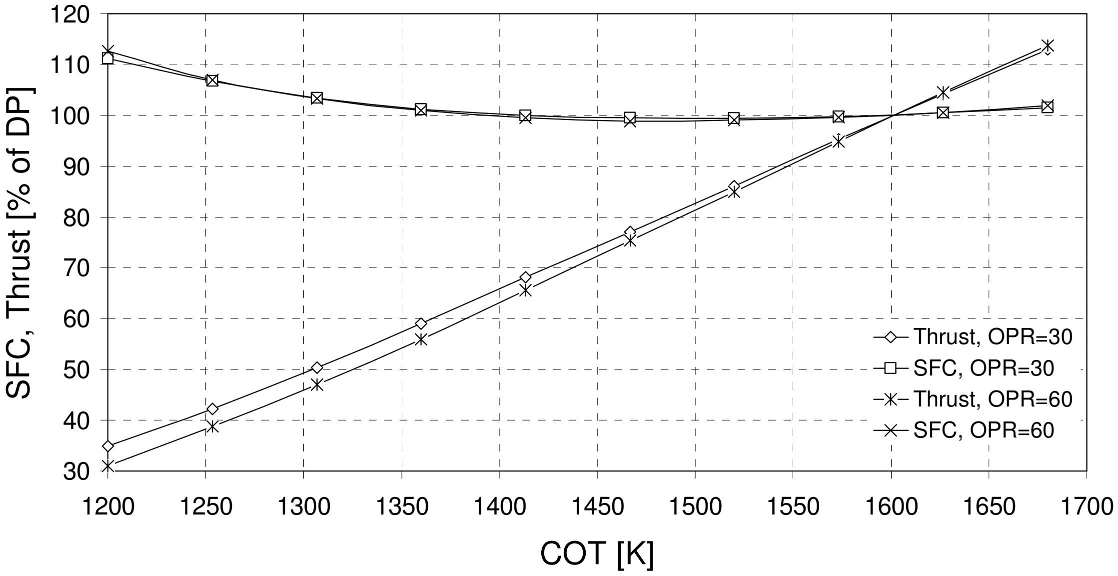

Figure 4-44: Off design behaviour of Turbofan at BPR=5 and DP-COT=1600K for two extreme OPRs.

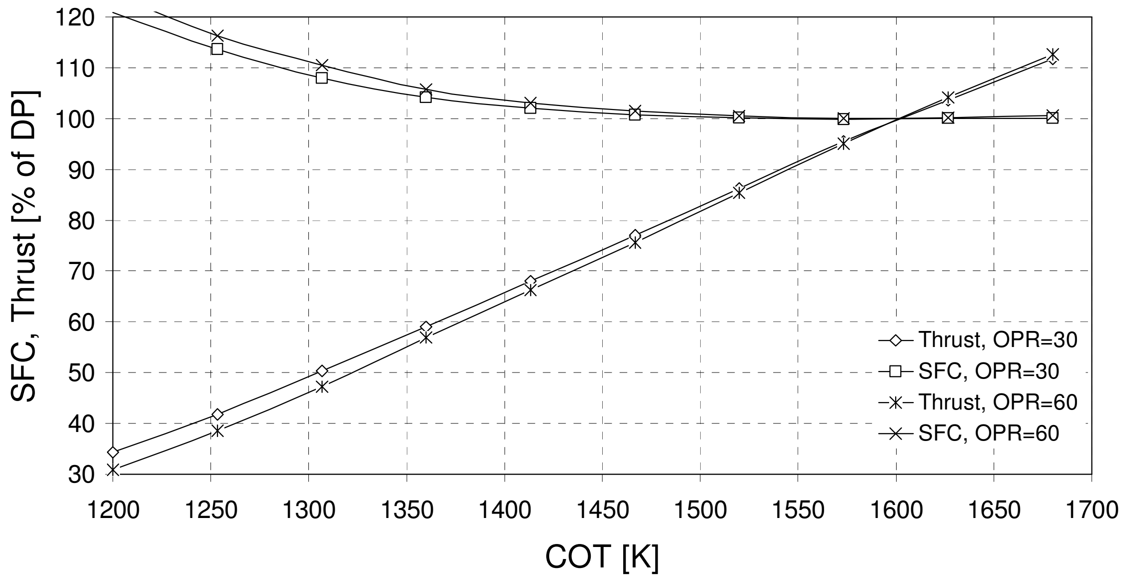

Figure 4-45: Off design behaviour of Recuperated Turbofan at BPR=5 and DP-COT=1600K for two extreme OPRs.

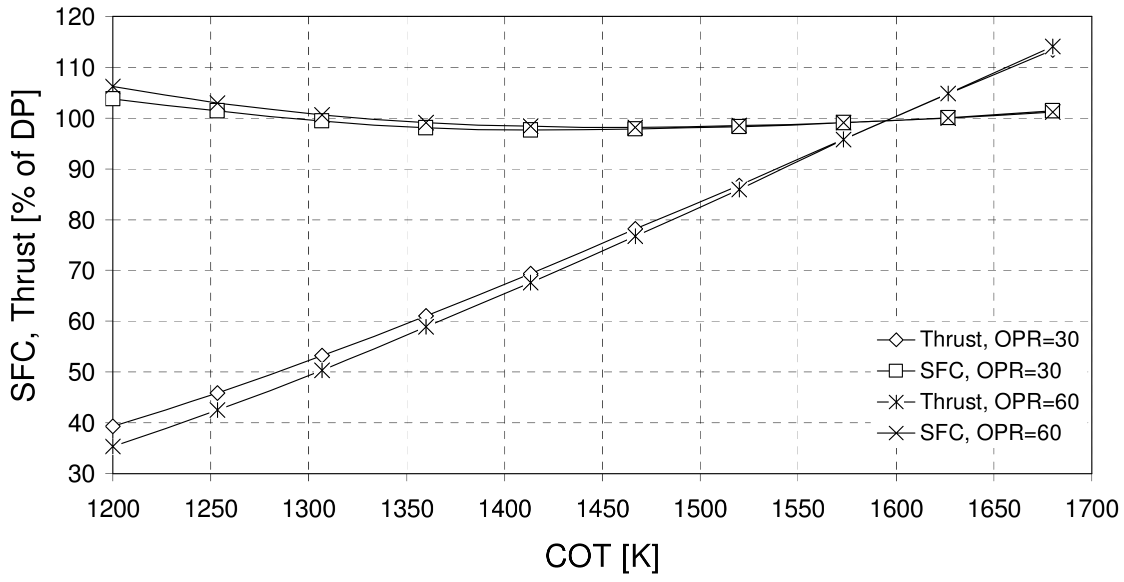

Figure 4-46: Off design behaviour of ICR Turbofan at BPR=5 and DP-COT=1600K for two extreme OPRs.

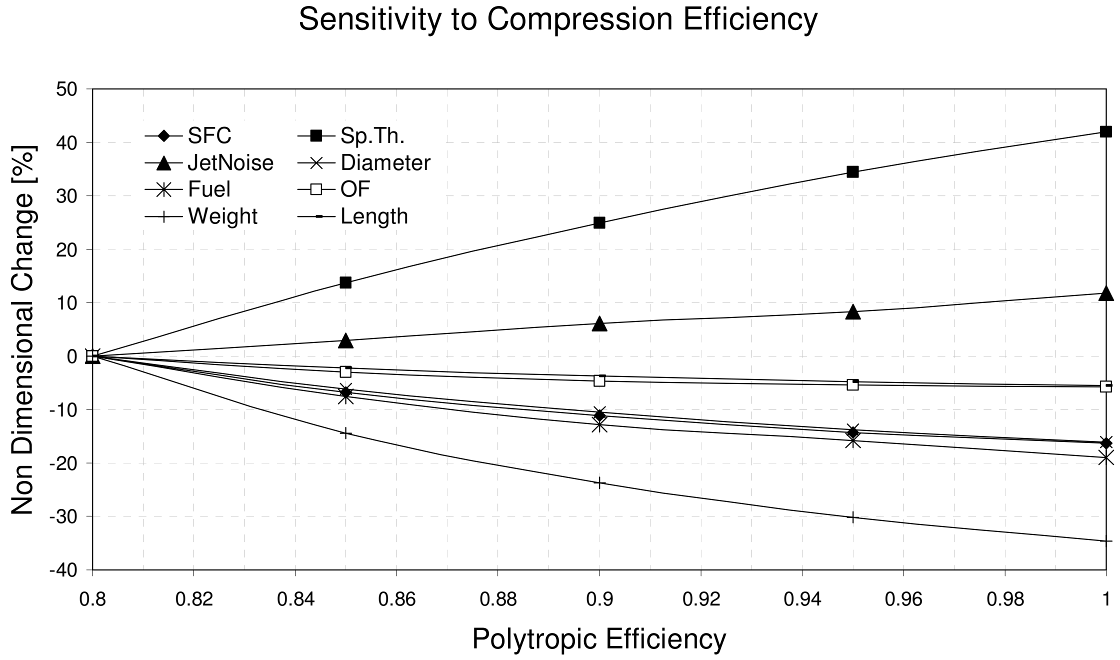

Figure 4-47: Sensitivity of analysis to compression polytropic efficiency.

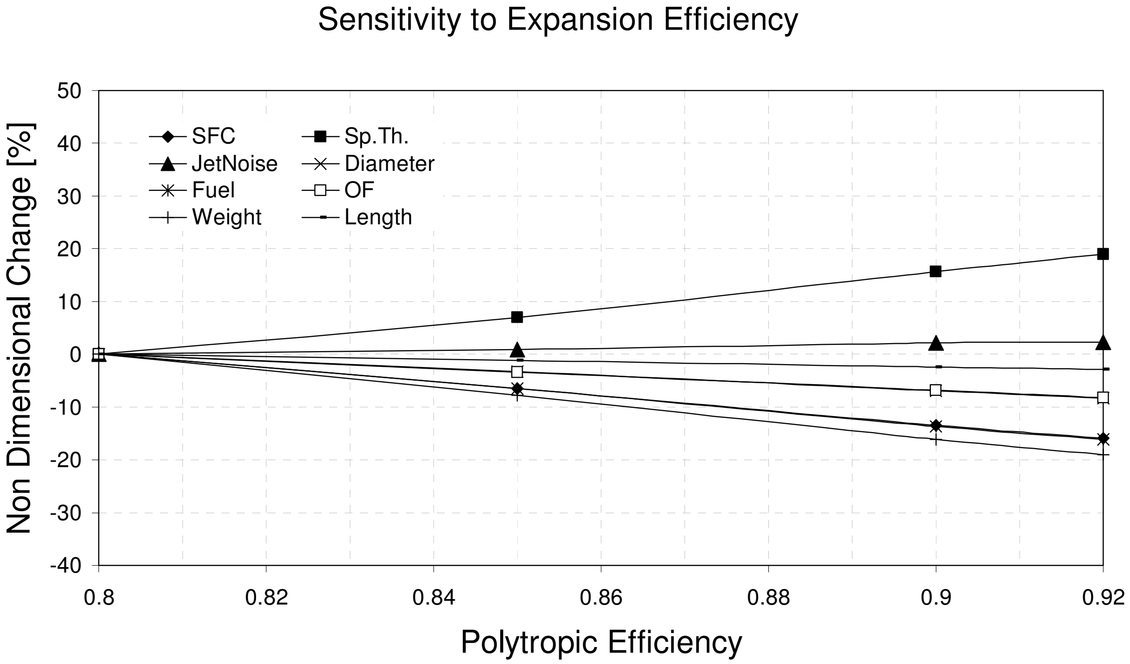

Figure 4-48: Sensitivity of analysis to expansion polytropic efficiency.

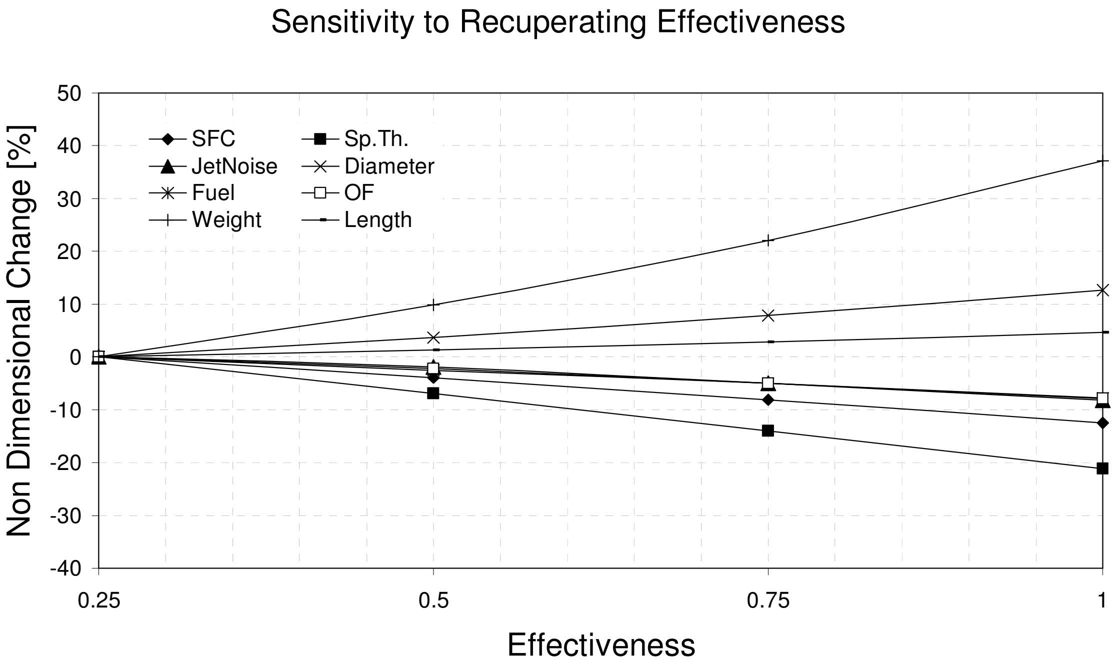

Figure 4-49: Sensitivity of analysis to heat exchanger effectiveness –recuperated cycle.

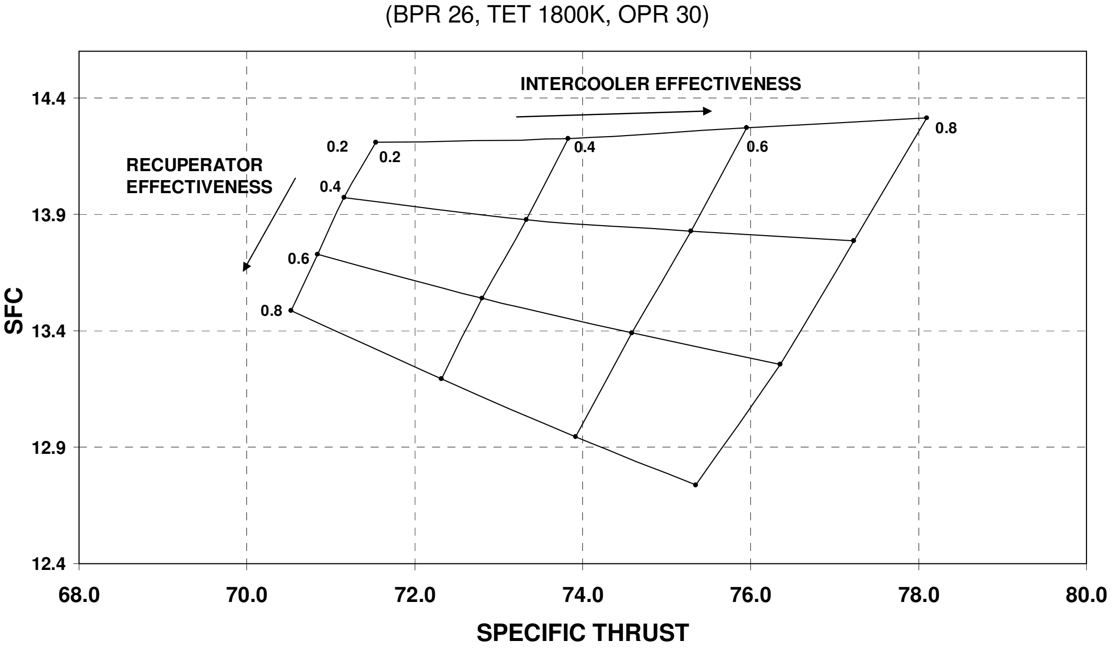

Figure 4-50: Sensitivity of ICR thermodynamic cycle on heat-exchanger effectiveness.

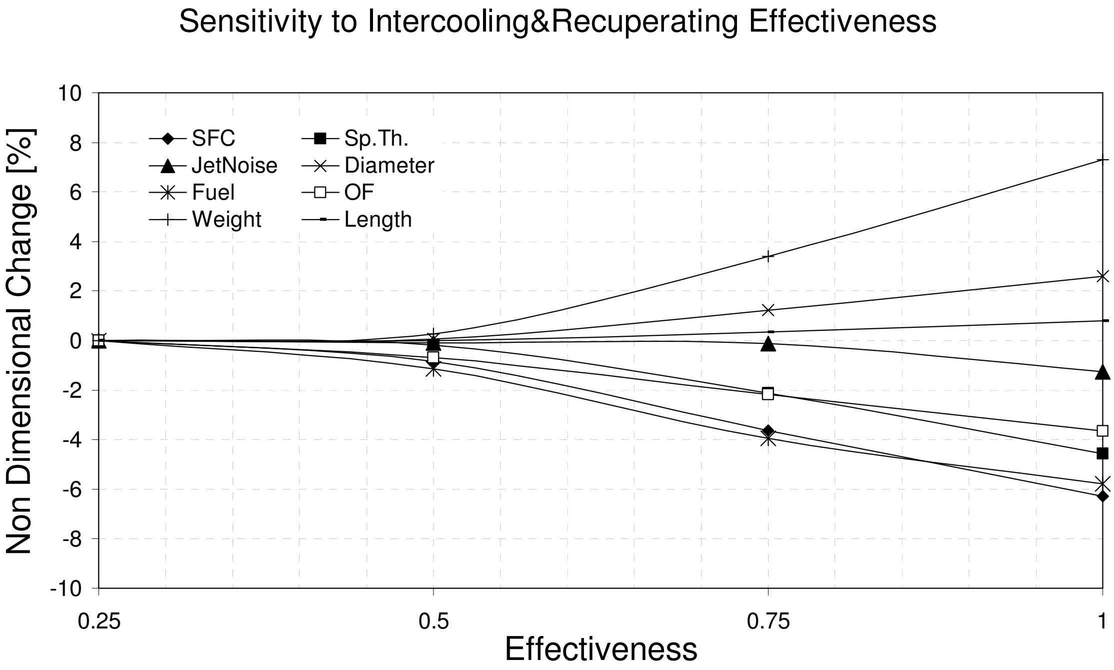

Figure 4-51: Sensitivity of analysis to heat exchanger effectiveness –intercooled recuperated cycle.

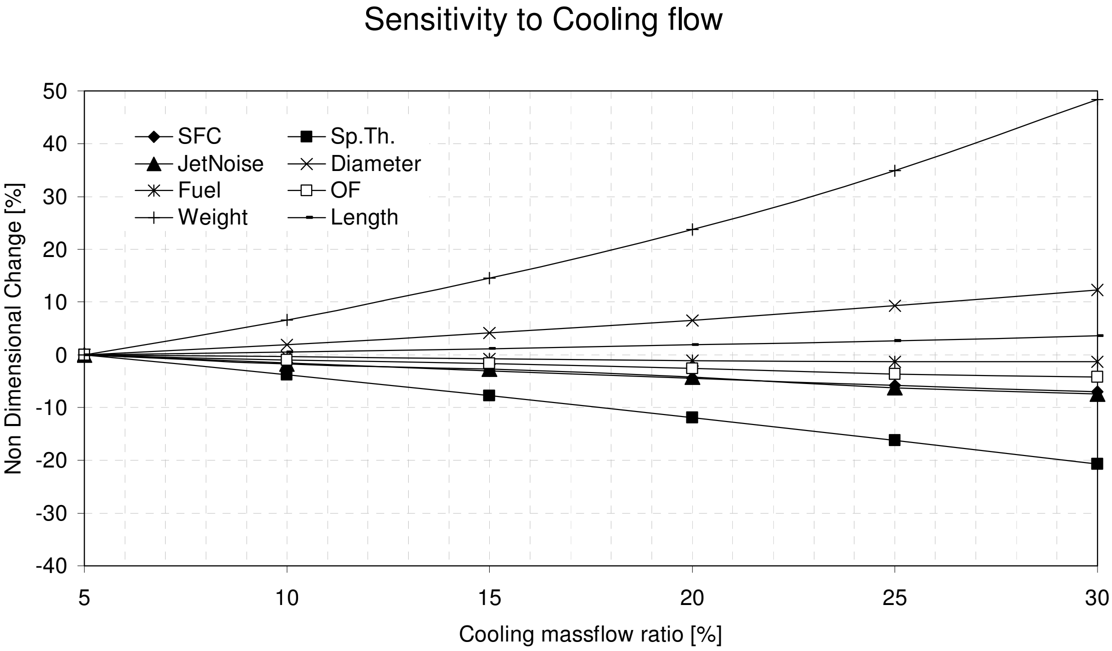

Figure 4-52: Sensitivity of results to turbine cooling flow.

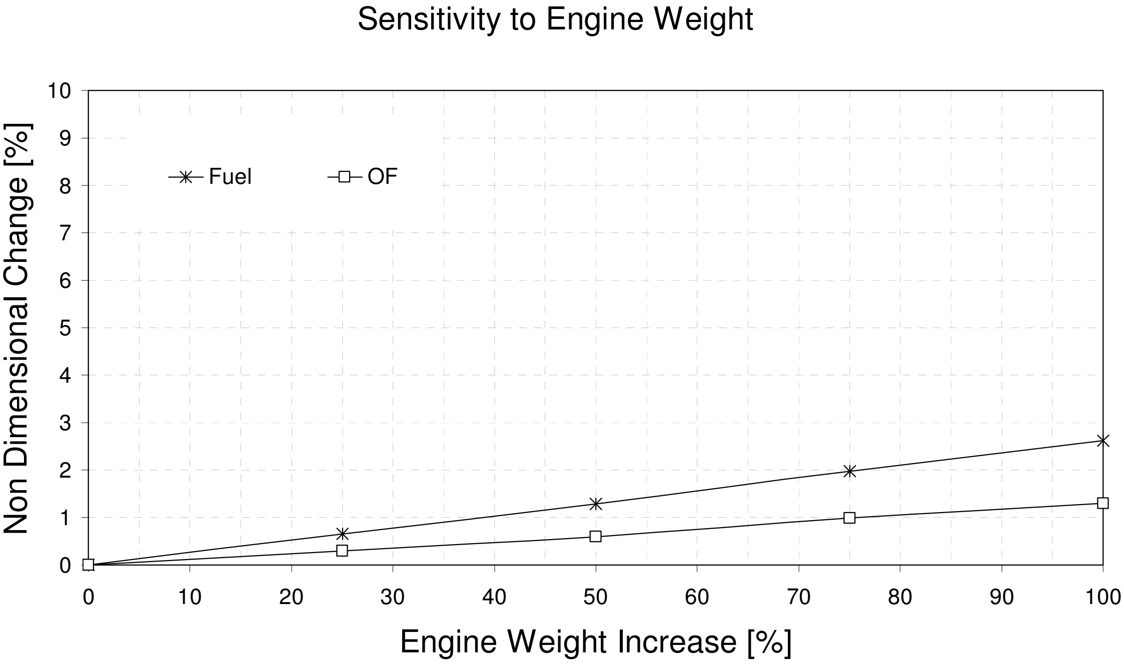

Figure 4-53: Sensitivity of total mission fuel to engine weight.

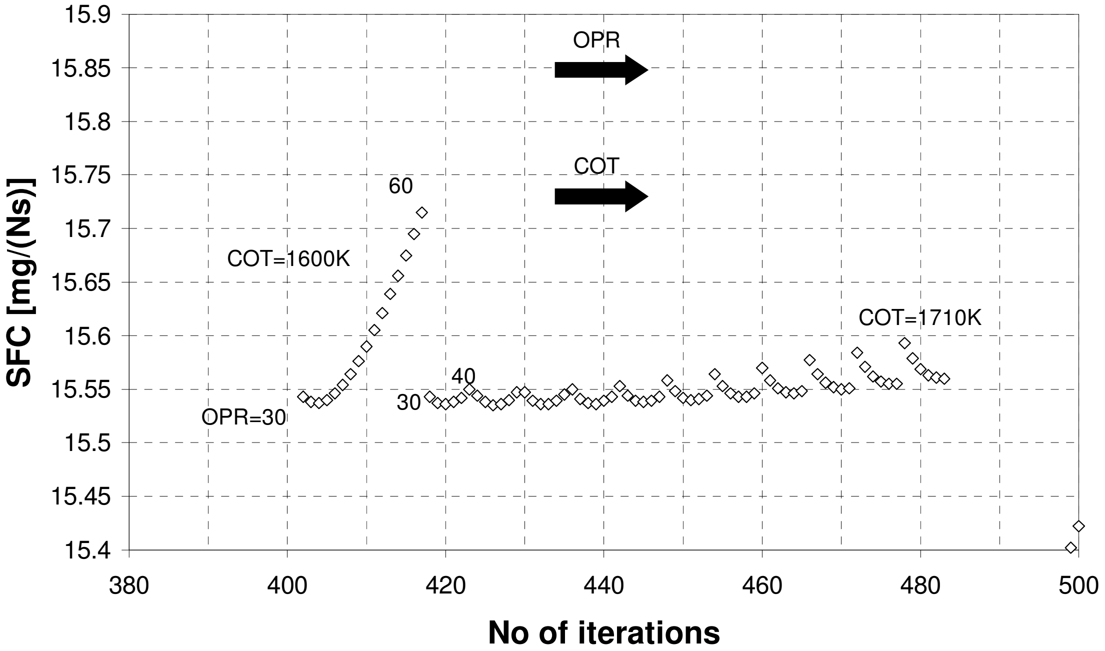

Figure 4-54: SFC evolution for BPR=7 –Intercooled Recuperated Turbofan.

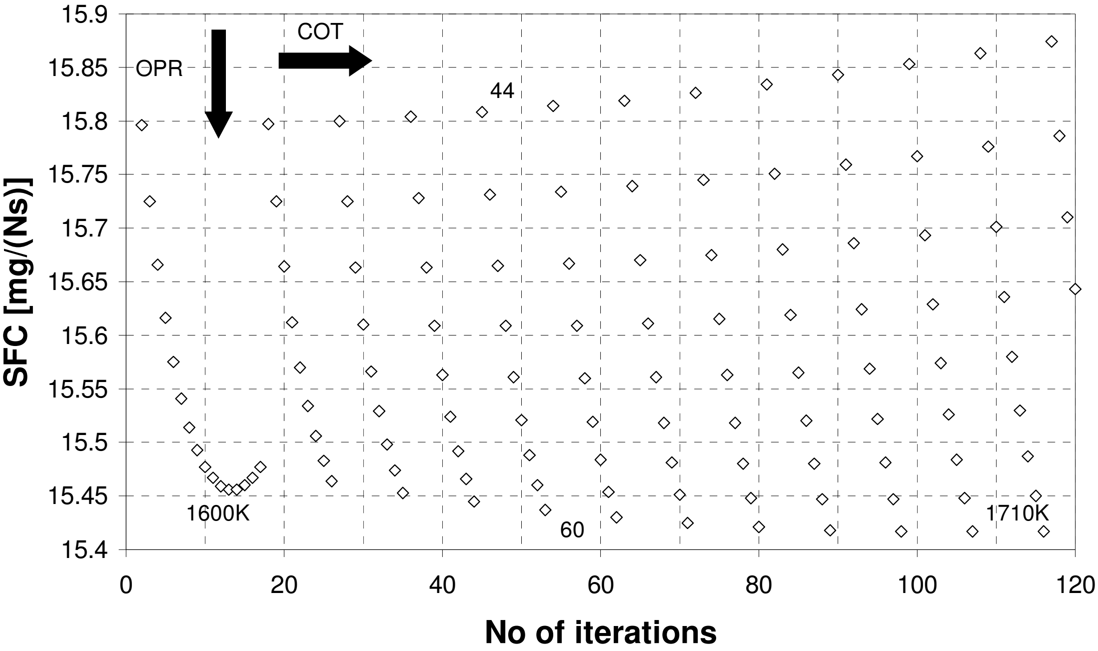

Figure 4-55: SFC evolution for BPR=7 –Recuperated Turbofan.

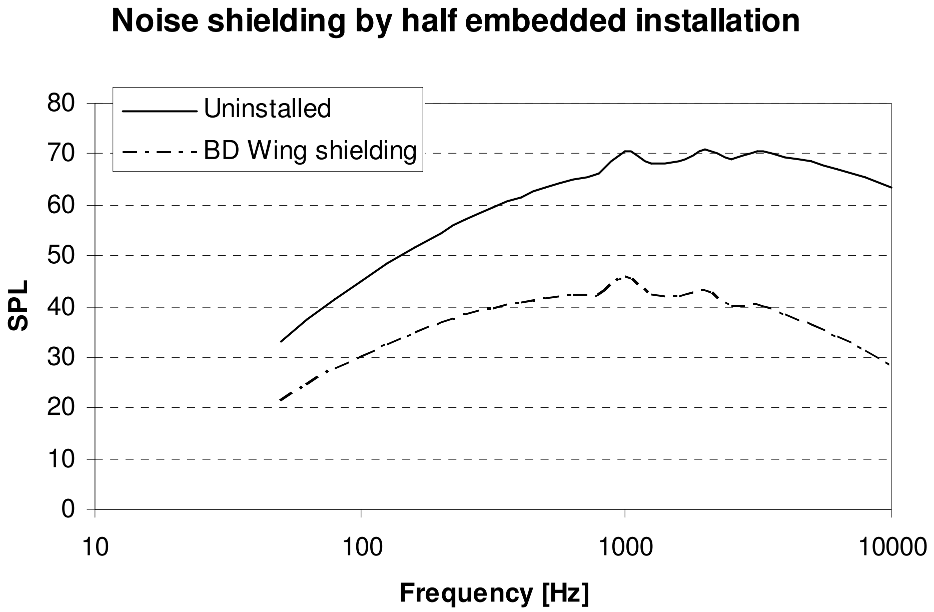

Figure 4-56: Effect of shielding on fan noise SPL spectrum.

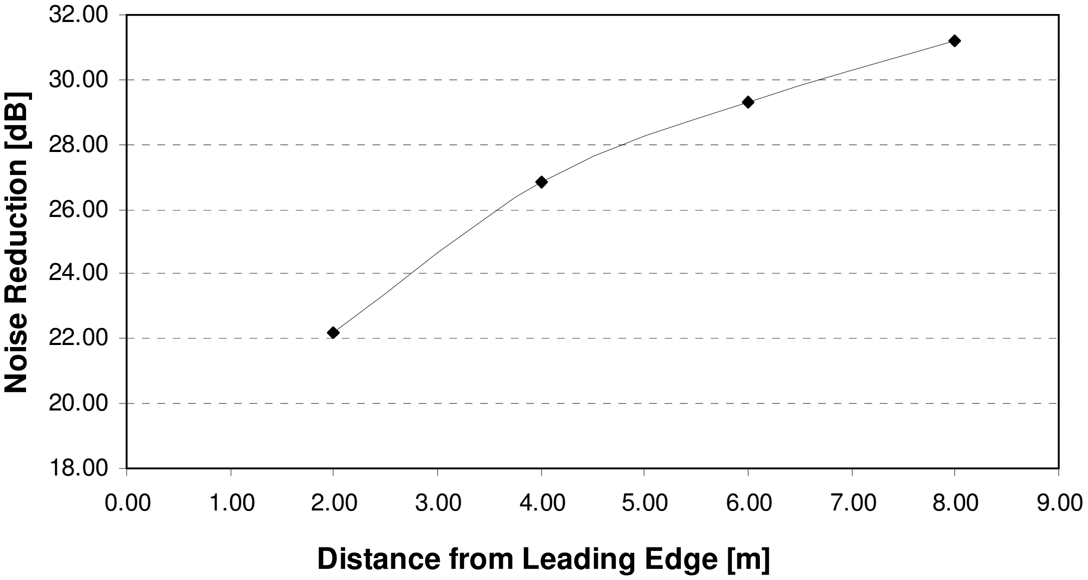

Figure 4-57: Effect of distance from leading edge to noise shielding.

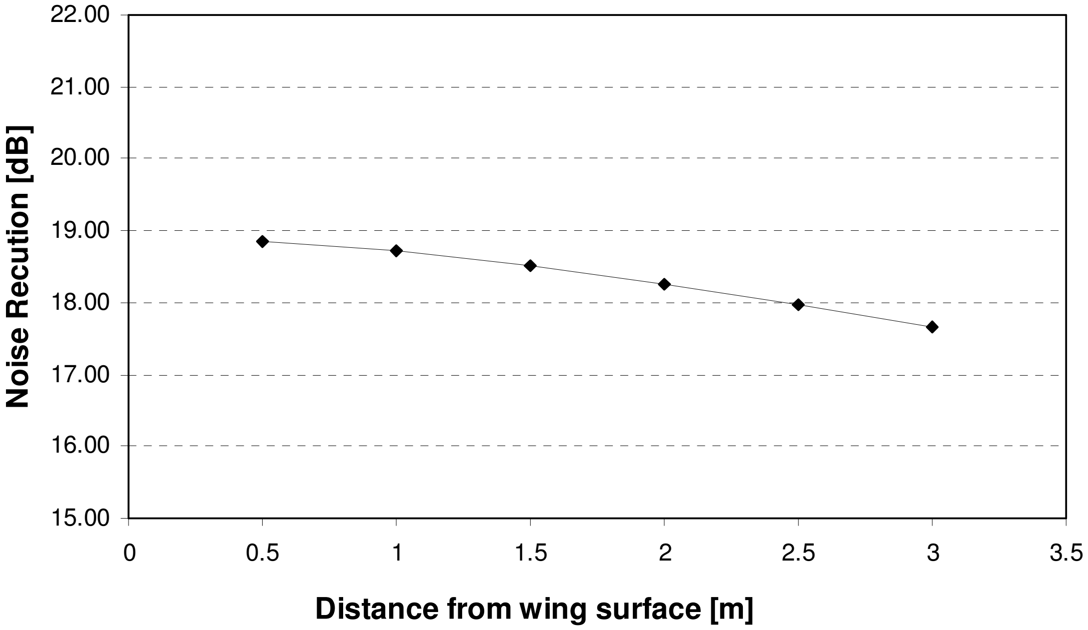

Figure 4-58: Effect of vertical distance on noise shielding (Axial distance 1m, Wedge angle 330^o).

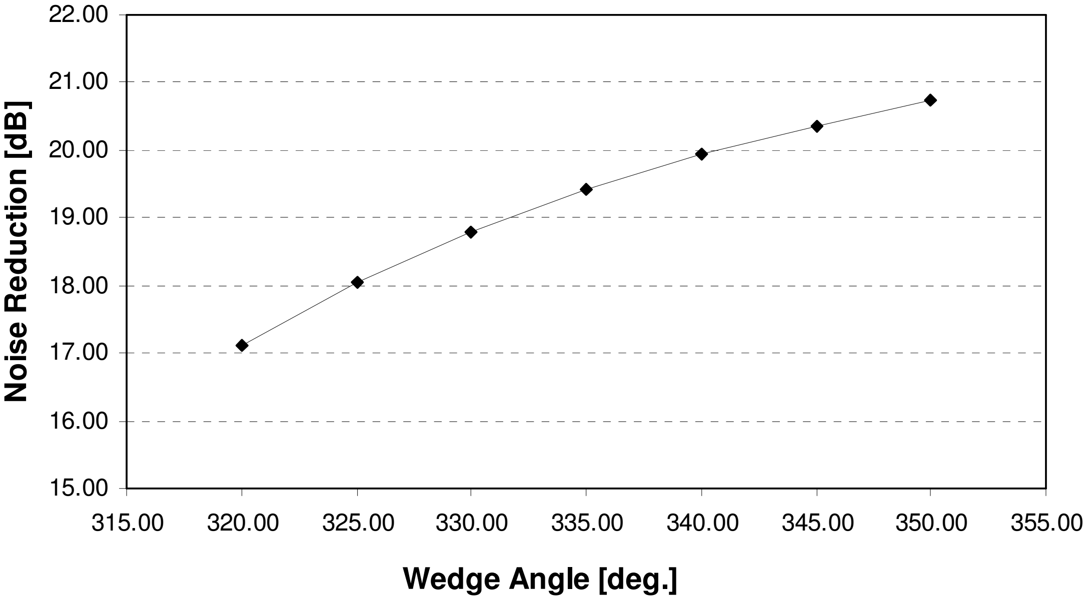

Figure 4-59: Effect of leading edge wedge angle on noise shielding (Axial distance 1m, vertical 1m).

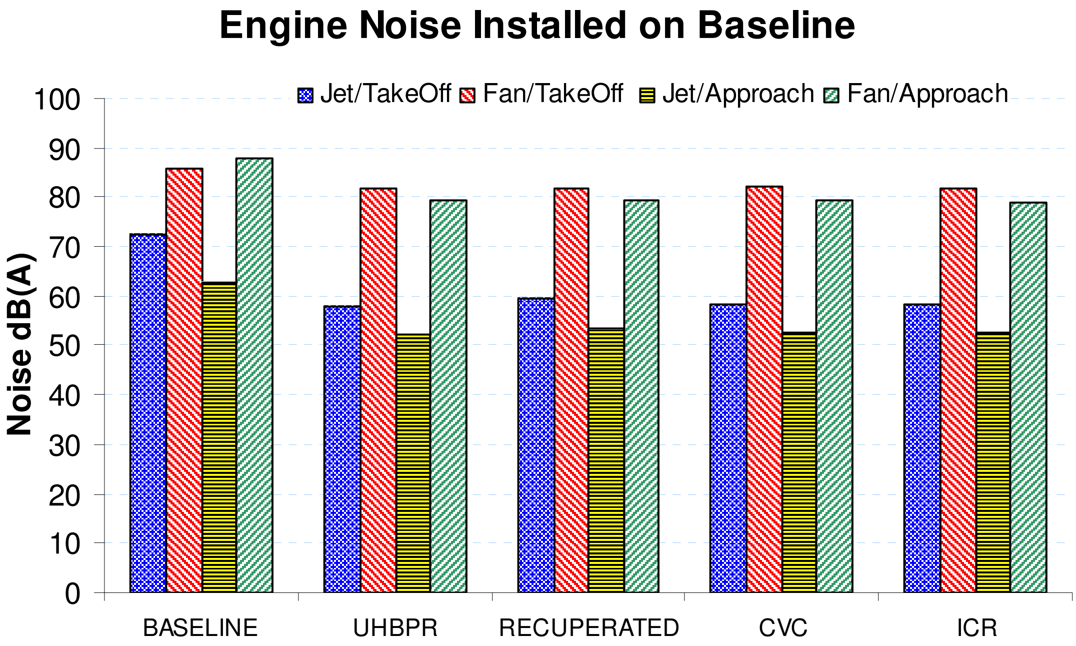

Figure 4-60: Engine noise installed on baseline airframe.

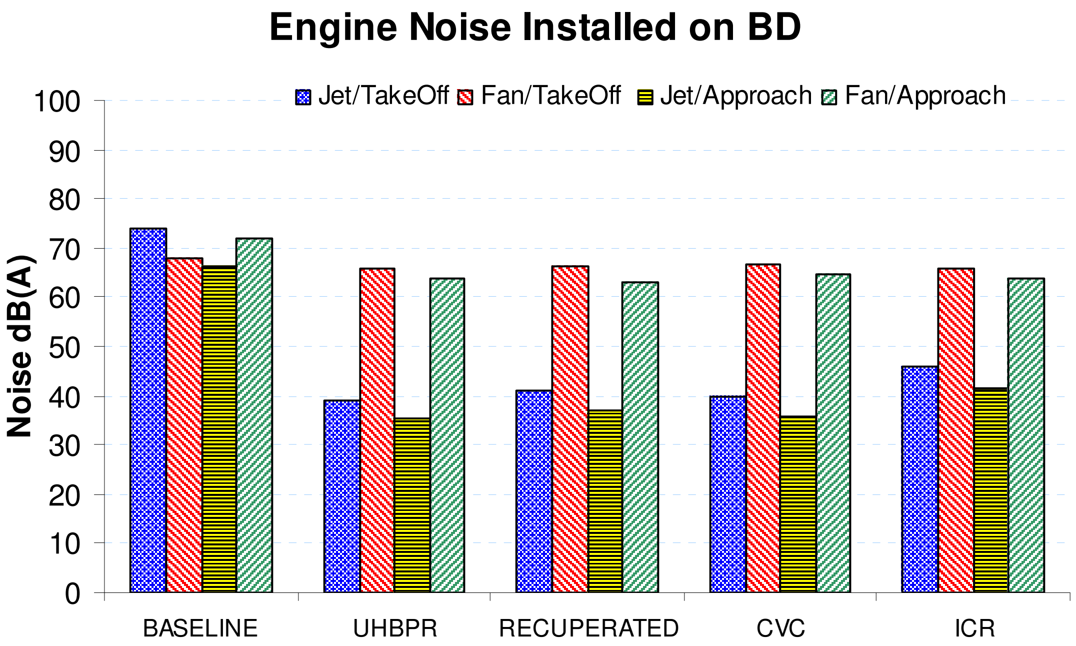

Figure 4-61: Engine noise installed on Broad Delta airframe.

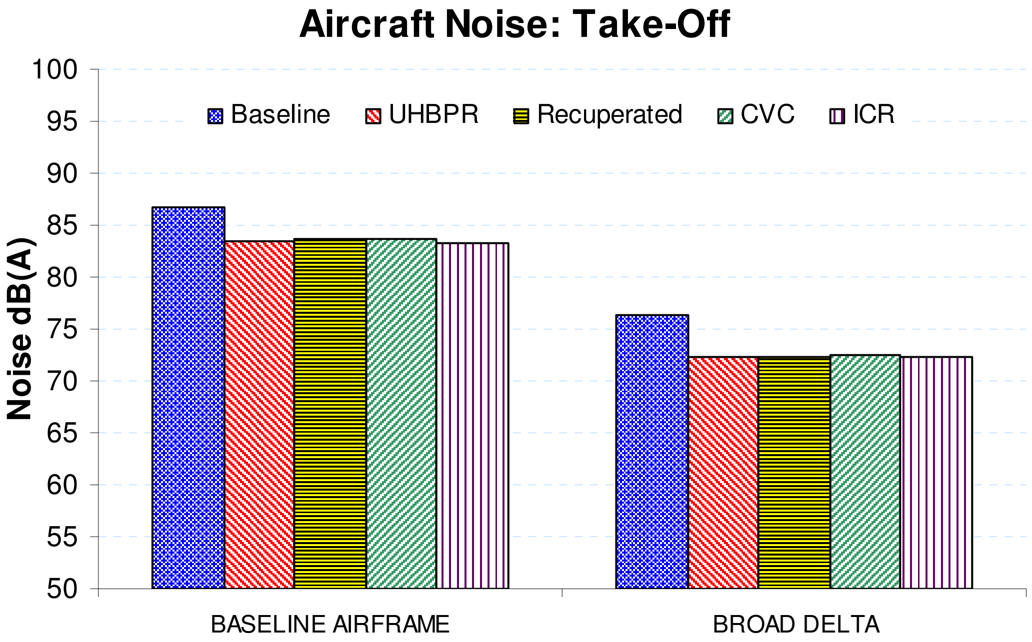

Figure 4-62: Aircraft total noise at take-off.

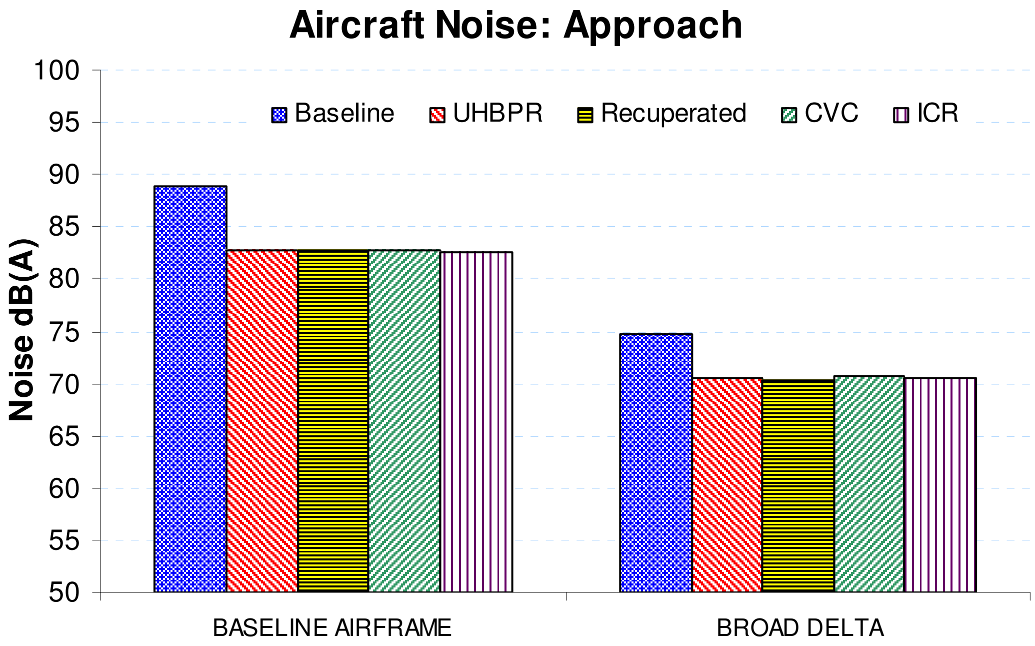

Figure 4-63: Aircraft total noise at approach.

5 Airframe-Engine Integration

The installation of the propulsion system on the airframe is a result of collaborative work between the engine and airframe teams. In the context of the ‘Silent Aircraft Initiative’, an installation that allows for maximum fan noise shielding has been decided. Such a solution proposes the half-embedding of the engine on the upper surface of the wing, resulting in a significant proportion of fan noise reflected upwards.

Embedding the gas turbine in the wing is a common practise for military applications, where minimum drag is desired, especially in supersonic speeds. However, the only example of embedded engines in civil aviation, the ‘Comet’, suffered the catastrophic effects of fatigue caused by this installation. Even though, manufacturing issues are not in the objectives of the project, it should be noted that, due to the significant progress in materials and design methods, any similar problems encountered in the future would be handled by structure analysis. Furthermore, a number of issues arise, regarding the effect of the installation on engine performance.

This chapter first discusses in detail the installation of an ultra high bypass ratio turbofan into a broad delta wing airframe as suggested by Mistry, [Mistry, 2008]. Then the three dimensional CFD analysis that has been undertaken by Truffi, [Truffi, 2007] and Rousselot, [Rousselot, 2007] under the author’s close supervision, is analysed. The main target of this work is the creation of a quasi 3D intake map, to be coupled with the enhanced fan representation model that is discussed in chapter 6.

5.1 Half-Embedded Intake-Nacelle Design

A novel airframe for civil aviation is the Broad Delta (BD) wing, [Doulgeris et al., 2006]. It comprises a conventional fuselage and a low aspect ratio wing. One successful BD was used as a long range tactical bomber, the Avro Vulcan, and was highly stable for an early tailless aircraft. This configuration is recommended for improved noise emissions and performance, due to limited lifting surfaces. The use of winglets, as it is illustrated in Figure 5-3, reduces the effects of the secondary flows emanating from the low aspect ratio of the wing. On the other hand, wing thickness at the root reaches 2.5 meters, so more than half of the engine can be buried in it, allowing for some space for the wing structure. The main geometrical data of the airframe are detailed in Table 1.

The major challenge emerging from such installation is the increase of the inlet stream tube wetted area, upstream the gas turbine. This condition results in highly non uniform and non symmetric inlet distortion that varies in both the circumferential and radial directions. Such phenomenon can be assessed with 3-D CFD simulation of the flow in the proximity of the engine intake. The results of such a study are useful for feeding a high fidelity engine model that can account for inlet distortion on overall performance. Previous work on conventional intakes has been presented in [Pachidis et al., 2006], followed by the use of streamline curvature method for calculating the effect of inlet distortion on GT performance [Templalexis et al., 2006]. Similar approach, using 3D streamline curvature is followed by [Hale et al., 2006], focused, mainly, in military intakes. Additionally, an enhanced performance prediction method –2-D CFD coupled with performance– has been presented in [Mund et al., 2007]. In the same manner, this chapter presents the generation of a quasi 3-D map, in order to be used in high fidelity fan-representation GT performance code.

The initial planning regarding the integration of the propulsion system into the airframe aimed at fully embedded engine in the wing. However, after the first broad delta wing airframe design, it was realized that such solution was not feasible for the following reasons. Firstly, it required high wing thickness, leading to significant flow acceleration in suction surface. Secondly, strict jet noise limits, led to ultra high bypass ratio, with an impact on maximum diameter. As a result, a compromise was accomplished by burying the engine as deep as possible in the wing and designing the exceeding part, according to podded nacelle guidelines –Williams, [Williams, 2005] and Seddon, [Seddon, 1985].

The propulsion system that has been chosen is a recuperated turbofan with BPR 20, COT 1700K and overall pressure ratio 40. The main engine data are included in Table 5-4. As previously discussed the recuperation process, has an impact on engine specific thrust and combined with high bypass ratio lead to high diameter, despite low static thrust requirement. However it lies under the limit of 2.7m set by the airframe designer, [Mistry, 2008]. At this point it should be noted that the engine and the airframe used in the CFD calculation are not the final designs presented in this thesis and [Mistry, 2008]. The reason is that grid creation, validation and CFD simulation are a long, demanding process and by the time the final cycle designs were ready –§4.4.5–, time constrains did not allow for further analysis to take place.

5.1.1 Podded Nacelle Design

As stated above, the upper part of the installation is based on conventional podded nacelle design, in an attempt to achieve smooth flow around the engine. There are identifiable parts in a nacelle; the forebody, the midbody and the afterbody. In the current study, a design without a midbody is chosen.

The design process starts with the definition of diameters. Critical role in this calculation plays Mach number at the fan face and at the throat of the intake, along with the engine mass flow. Table 5-1 summarises the flow conditions at three stations, far upstream, throat and fan face, at design point cruise condition. A value of Mach number 0.6 has been set at fan face leading to an area of 3.72 m^2. It can be noticed, that total pressure reduces, as a pressure recovery factor (PRF) of 0.99 has been utilized in the initial calculation.

In a further step, highlight area is calculated, based on a contraction ratio (A_H/A_{th}) of 1.35. Moreover, the highlight diameter is used for the calculation of the main forebody design parameters, which are the length (L_f) and the maximum diameter (D_{max}). These two parameters play significant role in the forebody drag, due to their effect on spillage drag. An iterative process resulted in the data, presented in Table 5-2. Maximum diameter and length to highlight diameter ratios have been varied in order to achieve satisfactory margins for mass flow ratio (MFR) and drag-rise Mach number (M_D), as shown in Equation 5-2 and Equation 5-3.

Equation 5-1:

$$MFR = \frac{A_0}{A_1}$$

Equation 5-2:

$$MFR_{margin} = MFR_{actual} - MFR_{critical}$$

Equation 5-3:

$$M_{margin} = M_{actual} - M_D$$

As their names declare, when the intake operates under MFR lower than critical, spillage drag occurs with an effect on total drag, while for freestream Mach number higher than M_D severe wave drag takes place. For this reason, safety margins of 0.2 and 0.1 having been applied –Table 5-2– and the resulting geometrical values are summarised in Table 5-5.

Equation 5-4:

$$MFR_{critical} = \left[\frac{1 - 4\left(\frac{1-D_H}{D_M}\right)^2}{\frac{L_F}{D_M}} \right]^{\frac{5}{2}}$$

Equation 5-5:

$$M_D = 1 - \frac{1}{8} \frac{\sqrt{1 - \left(\frac{D_H}{D_M}\right)^2}}{\frac{L_F}{D_M}}$$

The calculation of critical MFR and M_D is based on Equation 5-4 and Equation 5-5 respectively, as suggested by Stanhope, 1968. In the equations, the effect of maximum diameter (D_M), highlight diameter (D_H) and total forebody length (L_F) is apparent and these parameters appear in the codename of the NACA1 airfoil which is NACA1-76-132 and the X-Y coordinates can be found in the Appendix (§9.10).

In order to check the margins of the design, MFR has been calculated for two extreme cases; at cruise with engine at idle –COT set at 1200K– and during landing for same COT. For both cases, as shown in Table 5-3, MFR is greater than the critical value, meaning that no spillage is expected to occur.

In a further step, the coordinates of the lip and the diffuser are defined. The lip of the intake is a super-ellipse –Equation 5-6. On the other hand, a 3rd degree polynomial equation –Equation 5-7– has been applied for the diffuser, for smooth transition of the wall, from the lip, through the divergent region to the fan face.

Equation 5-6:

$$\left(\frac{y}{0.416}\right)^{2.25}+\left(\frac{x}{0.166}\right)^{2.5}=1$$

Equation 5-7:

$$y=-0.01297\cdot x^3+0.7092\cdot x^2-0.05235\cdot x+1.03986$$

After the definition of the forebody geometry, the calculation of the afterbody follows. The main geometrical parameters are the maximum diameter –equal to forebody's D_M–, the nozzle exit diameter (D_n) –input from cycle design–. They are positioned in a distance, defined by total engine length requirement and a cone is shaped having a circular arc profile. The circular arc radius is defined according to Equation 5-8 –as suggested in [Williams, 2006]–, where $M_{D,A}$ is equal to the forebody drag rise Mach number (M_D).

Equation 5-8:

$$R_A=\frac{0.04D_M}{\left(1-M_{D,A}\right)^2}$$

An important parameter in the design of the afterbody is the boattail chord angle. This angle defines the performance of the afterbody and should not exceed the value of 8^o, as this would lead to intense pressure gradients and flow separation, or even wave drag rise.

5.1.2 Installation on Broad Delta Wing

As previously discussed, this thesis presents a noise driven design method. As a result, priority is given on noise reducing solutions. In this manner an upper wing installation half-embedded installation has been chosen, for providing adequate fan noise shielding. Moreover, in order to minimise inlet distortion a channel has been opened through the wing, instead of an S-duct. An S-duct in this case, would feed air from the suction surface of the wing, where Mach number is expected to be high, causing further problems in the diffusion part of the intake. As a result, the wing channel upstream of the intake has been created after the intersection of the wing with a virtual cone of diameter equal to the throat (D_{th}).

According to the 4-engine configuration, two turbofans are installed on each wing. This condition, led to additional complexity, due to the interaction between the two nacelles. The limited time did not allow for addressing in detail this issue, by trimming the design, using 3D CFD techniques. As a result, the two nacelles were positioned, in order to be attached. This decision was made in order to diminish the passage between them that acts as a convergent-divergent nozzle, causing supersonic flow. Future analysis should include a blending of the two nacelles, based on the existing geometry.

A secondary design target is the maximising of fan noise shielding provided by the installation. This condition does not allow the implementation of bleed ports for the control of inlet distortion, especially under high angles of attack. However, variable inlet geometry should be subject of further work. Nevertheless, the design presented in this thesis, serves as a demonstrator for providing with qualitative data the PaCo-SLC Compressor model, in the form of a quasi 3D intake map.

5.2 *Method of intake map generation*

The map generation process is based on two main tools; a 0-D gas turbine performance simulation code, TURBOMATCH –§3.4–, and FLUENT, a three dimensional CFD analysis commercial code.

The process followed for the generation of one point in the map is outlined in Figure 5-4. This process simulates the direct relation between CFD and gas turbine performance codes. According to this, any entropy created in the intake, or upstream reduces inlet total pressure, affecting the operating point of the engine. The change of the operating point is connected with a change of the mass flow rate through the gas turbine, affecting the static pressure at the fan face, which is a boundary condition to the CFD calculation.

The engine throttle setting and flight conditions are defined by the user and are inputs to TURBOMATCH, which produces the boundary condition values for the CFD calculation –far-stream total pressure, static pressure at fan face, mass flow, and total temperature. It should be noted that an initial value (0.99) of pressure recovery is used in the first iteration. Then, the mass averaged P_t and mass flow at fan face are compared to the values from TURBOMATCH and the error is calculated using Equation 5-9.

Equation 5-9:

$$Error = \frac{\left| A_{TURBOMATCH} - A_{CFD} \right|}{A_{CFD}}$$

‘A’ stands for pressure recovery, mass flow or flight Mach number and if the convergence criterion is not satisfied for any of them, a new pressure recovery is guessed, based on the CFD value; it is the new input to TURBOMATCH and the process is repeated.

The intake map consists of several operational points defined by corrected mass flow –Equation 5-10– and pressure recovery factor –Equation 5-11.

Equation 5-10:

$$W_{corr} = \frac{W_2 \cdot \sqrt{Tt_2 / Tt_{ref}}}{Pt_2 / Pt_{ref}}$$

Equation 5-11:

$$PRF = \frac{Pt_2}{Pt_0}$$

The map contains data for two flight conditions; take-off and cruise, detailed in Table 5-6. Combustor outlet temperature has been varied according to common flight requirements. The variation at cruise between two extreme COTs –1200K to 1900K– gives a full operating line, while the temperatures at take-off have been chosen, in order to satisfy the airframe thrust requirement.

5.3 Grid Generation

5.3.1 Grid generation strategy

The challenge of this analysis lies in the creation of a grid, able to predict the flow patterns at the face of the propulsion systems, taking into account the whole aircraft; moving from large scale to small. In order to achieve this goal using available computational power the split of the problem into two has been decided. It should be noted that a first attempt of creating one single grid for the whole domain (of approximately 6×10^6 cells) increased computational time requirements further than the available resources. As a result, a 'big domain' and a 'small domain' grid have been constructed using GAMBIT commercial grid generator.

The purpose of the 'big domain' topology is to take into account the full airframe geometry and create a boundary condition –exit static pressure–for the 'small', detailed grid. This boundary condition plane is pointed in Figure 5-5. Its position has been chosen in order to minimise the computational domain, but also lay in a low pressure gradient area. This condition is satisfied for the inner nacelle (a), where the boundary condition plane lays at the afterbody area, shown in Figure 5-6. However, the plane meets the second nacelle (b) at the forebody, in an area, where not steep gradients appear as seen in Figure 5-7. It should be noted though, that the plane could not be positioned further downstream as it would be exposed to the exhaust plume of the inner engine.

5.3.2 Grid Size

As exhibited in Figure 5-8 and Figure 5-9, the size of the elements in the 'big domain' grid varies considerably. As a result, in the region of undisturbed ambient flow, the grid is coarse and becomes finer close to the installed engines, due to the use of size functions, in order to improve computational time. The effect of using size functions is clearly observed in Figure 5-9. Additionally, in order to avoid jet mixing that would affect convergence the engines are modeled as infinite bodies. Regarding, the upstream solid tube, it was used to eliminate the engine inlet boundary condition. Nevertheless, due to time constrains, the 'big domain' simulation was launched only for the two major flight conditions.

It can, also, be observed that several components –likely to perturb convergence– have been removed, such as the fin and the winglets. However, in order to simulate the effect of the winglets the wing has been modeled as infinite body with an extra brick added, to prevent tip vortex generation and secondary flows on suction surface, as shown in Figure 5-8. The extent of this secondary area and therefore the final size of the computational domain are chosen after a comparative study, presented in Table 5-7.

The criterion that is used for choosing the appropriate grid size is the maximum Mach number on the upper surface of the wing, indicative of the secondary flow that develops regionally, as shown in Figure 5-10. It is clear that the implementation of a virtual wing of equal length to the broad delta wing reduces the maximum Mach number by more than 19%.

A grid independence study shows the effect of grid density on solution. Table 5-8 contains the comparison to a denser grid (d), where an increase in density by 35% led to 1.6% higher Mach number. As a result, an unstructured mesh (c) containing 2000832 tetrahedral elements is chosen for the analysis.

5.3.3 Final Grid Quality

Relatively to grid quality, a check has shown that only 1 element is exceeding the aspect ratio (AR; ratio of major to minor cell edges) limit of 69. Three cells exhibit equiangle (EAS) skew (angle between two grid lines) higher than 0.97 and 24 have equisize skew (EVS) higher than 0.97 –limits as suggested by GAMBIT manual [online].

The ‘small domain’ grid is illustrated in Figure 5-11 and Figure 5-6. It features a combination of structured –inside the intake– and unstructured grid. More specific, two extra fine-meshed volumes are created; one inside the intake and one surrounding the nacelle. This configuration – shown in Figure 5-6 and Figure 5-12– is selected as the most appropriate for robustness and accuracy of the model for two reasons. The structured grid in the inner section of the intake can be considered as aligned to the main flow, reducing numerical diffusion. On the other hand, the highly curved, complex nacelle geometry requires the implementation of dense unstructured grid that eliminates negative volumes and limits the number of highly skewed cells.

The resulting grid consists of 676571 unstructured tetrahedrical elements and 589368 structured hexahedrical ones. With respect to mesh quality, only one is above AR limit, 16 above EAS and 101 exceed the EVS limit of 0.97. As already stated the simulation is focused on the inner part of the intake. For this reason, the structured hecahedrical cells have a maximum primary dimension of 10mm. As a result, the y^+ values in the intake are ranging between 500 and 1000, values that are acceptable for fully turbulent flow, as the maximum acceptable limit is 1000.

5.4 3D CFD Simulation

The simulation process starts with the ‘big domain’ creating the static pressure boundary condition for the ‘small domain’. In the ‘big domain’ case, a viscous, compressible, turbulent –standard k-ε– flow model is used, while the numerical scheme is pressure based, with first order upwind discretisation. The boundary conditions consist of far upstream uniform total pressure –ambient with flight Mach number–, far downstream uniform static pressure, whereas symmetry condition is used in order to reduce the number of cells and, therefore, computational time.

In the ‘small domain’ simulation, Wilcox k-ω turbulent model is used, along with second-order discretisation, for increased reliability at high Mach numbers. Concerning the boundary conditions, the static pressure outlet is derived from the ‘big domain’. Additionally, an ellipsoidal inlet is formed, as shown in Figure 5-6, in order to apply uniform inlet total pressure. Finally, an extra boundary condition is the static pressure at fan face, which is calculated by TURBOMATCH during the iterative process.

Figure 5-14 shows the maximum residuals for a typical case; flight condition is cruise and engine maximum temperature is set at 1800K. The convergence criterion is 0.0001 and as shown in Figure 5-14, all of the residuals go to much lower values except the continuity. Three regions can be identified, split by two peaks, resulting from the strategy that has been followed. In the first 400 iterations flight Mach number is set at 0.3 and flow model is laminar, in order to produce initial conditions, not affected by compressibility and turbulence effects –an initial value of M=0.8 led to divergence. After a satisfactory level of residuals is reached, Mach number is changed to 0.8, while flow model is kept laminar and in the last step a turbulent k-ε model is used for the final results.

Similar convergence strategy has been followed for the ‘small domain’ case, as well. However, there was no need for initialising with low flight Mach, because a laminar simulation at M=0.8 gave convergent results after 2500 iterations and another 1100 were needed for a fully converged turbulent flow field.

As mentioned before, every map point is the result of an iterative process. During this process, firstly the 'big domain' calculation runs for the particular flight condition, generating the boundary condition for the 'small domain'. After this, TURBOMATCH calculates the P_{st} boundary condition at the fan face and the flow simulation results in updated values of pressure recovery, mass flow and fan inlet Mach number.

The history of convergence of the process is illustrated in Figure 5-15, referring to both engines. It can be seen that, the error relative to PR reduces to lower than 0.2%, Mach number to lower than 2%, while the minimum mass flow error is 4%. This is a result of the inability of 0-D performance code to take into account compressibility effects. Another reason that could explain this difference is that mass flow is calculated by completely different methods in the two models. In Turbomatch, the mass flow is a result of mass averaged inlet total pressure and engine maximum temperature (COT) that define the engine operating point, thus mass flow. On the other hand, in the case of CFD, mass flow is defined by ambient conditions and static pressure at the fan face. On the top of this, the CFD calculation provides a three-dimensional profile that is mass averaged in order to be used in the 0-D GT performance code. The returning boundary condition to CFD, instead of a 3-D P_s profile, is a constant value for the whole annulus. The use of a quasi-3D representation of the fan could improve this condition and is the subject of further work.

5.5 Intake map – Discussion

Figure 5-17 illustrates total pressure on the surface of BD airframe and its evolution along the two intake channels. Even though, higher pressure gradients are apparent in the outer intake (b), the closer to the fuselage intake (a) experiences more intense flow distortion, as it is more deeply embedded in the wing and the intake channel is longer – thus there are greater viscous effects.

Another critical area is the leading edge of the wing at the intersection with the inlet channel. An acceleration of the flow appears, probably due to the sharp shape of the lip, illustrated in Figure 5-12.

The effect of installation is apparent in Figure 5-19 where P_t contours at the two fan faces are shown. The extended inlet channel, increases frictional losses, reducing P_t, while additional losses appear in the form of low P_t in the area where the nacelles blend with the wing. However, still, a considerable proportion of inlet flow can be considered as undistorted.

At low speed and altitude, PRF is significantly higher as shown in Figure 5-21: and Figure 5-22. The main reason is the low Reynolds number that has a favorable effect on frictional losses. On the other hand, low speed, combined with maximum engine mass flow –due to thrust requirement– leads to high Mass Flow Ratio (MFR) and generation of recirculation at the upper section of the intake, apparent in Figure 5-21. As shown in Equation 5-1, MFR is the ratio of the far-stream, cross-sectional area of the stream-tube that enters the engine, divided by the highlight area of the intake. When MFR exceeds 1, air accelerates when entering the intake and recirculation may occur in the divergent part of the inlet duct, with a negative effect on PRF. In general, though, losses are much less at take off and this is observed in Figure 5-22 as well, where the intake map for both cruise and take-off is illustrated.

It should be noted that the change of the MFR is not taken into consideration in the ‘big domain’, as the intake is regarded as infinite-length body. This condition introduces an error, especially in the outer installation (b), as the P_s boundary condition is applied on the forebody area. As a result, when engine throttle is higher than design point, the inlet stream tube has higher diameter than the one used in the ‘big domain’ model and the model predicts lower static pressure than actual. However the intake is designed for preventing spillage as discussed in §5.1.1, so no significant changes in the flow field are expected. A comparison of the near-intake flow field as predicted by the 'big' and the 'small' domain is illustrated in Figure 5-20, where similar trends appear for Mach number evolution. Future work though, includes the simulation without the use of two computational domains that should eliminate this uncertainty.

A comparison between the two intakes shows that in cruise, the outer installation (b) exhibits improved pressure recovery, due to shorter intake duct that leads to lower boundary layer thickness at the AIP. The effect of boundary layer thickness is in agreement to the findings of the experimental study conducted by Mossman and Randall, [Mossman & Randall, 1948] on submerged intakes. This condition reverses, at take-off, where the main loss generation mechanism is recirculation at the upper section of the intake. As shown in Figure 5-21, the outer inlet, which is less embedded –as the wing gets thinner towards the wing-tip–, has a broader area of low PRF, therefore outer engine performs under lower inlet pressure during takeoff. Additionally, as shown in the map, recirculation appears at ~580 kg/s corrected mass flow, or engine throttle setting at 1750K and a 0.5% step reduction in PRF is observed.

A general comment on the results is that low throttle settings lead to low engine mass flow and low Reynolds number, thus improved pressure recovery factor. Moreover, another outcome from Figure 5-22 is that special care needs to be given on engine control systems, if such an installation reaches production. This is because, as seen in the map, for same throttle settings, the two turbofans operate under different inlet pressure, something that has a considerable effect on thrust. Taking into account the fact that during take-off the behaviour reverses –2nd intake having lower PRF– a detailed electronic mapping in the control system is essential, in order to vary fuel flow of the two engines, so optimal thrust is produced for the whole flight envelope.

The map presented in Figure 5-22 illustrates mass averaged values for each operating point and is sufficient for implementation in a 0-D performance code. However, in a high fidelity representation of the low pressure system, a more detailed input is required.

Nevertheless, the flow in a half-embedded installation is non uniform as shown in Figure 5-19. As a result, a quasi three dimensional map is derived from the computational analysis data, in order to be installed on the high fidelity PaCo-SLC fan model. For this reason, at every operating point, 8 sets of PRF radial distributions are extracted from fan-face plane.

Two operating points at cruise and take-off are illustrated in Figure 5-23 and Figure 5-26, respectively. The 8 sections on fan annulus that correspond to each radial distribution are shown as well. It should be noted that the top section is the one highlighted by the arrow. A comparison between Figure 5-23 and Figure 5-19 makes apparent the level of fidelity that is achieved; i.e. the region of low pressure recovery at the low part of the annulus is well presented in Figure 5-23. During take-off, low altitude and Mach number lead to low corrected mass flow and low Reynolds number. As a result frictional losses are reduced and this is illustrated in Figure 5-26, where radial profiles appear to have shifted up, compared to cruise case. On the other hand the recirculation bubble is apparent as well, in the second profile from top, due to high MFR, as discussed before.

Tables of Chapter 5

		Symbol	∞	Throat	Fan
Mach number		M	0.8	0.73	0.6
Total Temperature	[K]	T	244.4	244.4	244.4
Total Pressure	[Pa]	P	28579	28579	28293
Static Temperature	[K]	T	216.6	220.8	227.9
Static Pressure	[Pa]	P	18748	20049	22182
Air Density	[kg/m^3]	P	0.3015	0.3163	0.3390
Area	[m^2]	A	3.2177	3.3291	3.7197

Table 5-1: Intake design-point flow data.

A_H/A_{th}	1.35
D_M/D_H	1.32
L_F/D_H	1.32
$MFR_{critical}$	0.5117
MFR_{margin}	0.2042
M_D	0.923
$M_{D\ margin}$	0.1184
R_A [m]	18.972
Boattail chord angle (^{o})	5.84

Table 5-2: Forebody design parameters.

Flight Condition	Mass Flow [kg/s]	MFR	MFR_{margin} [%]
Cruise, Idle, COT=1200K	178	0.556	0.045
Landing, Idle, COT=1200K	397	0.525	0.013

Table 5-3: Check of MFR margins.

BPR	20
OPR	40
COT [K]	1800
SLS Thrust [kN]	101
DP (ToC) SFC [mg/(N.s)]	14.6
DP (ToC) Mass Flow [kg/s]	229

Table 5-4: Engine data.

Contraction Ratio	1.35
Fan Diameter [m]	2.4
Max Engine Diameter [m]	3.1
Intake Highligh Diameter [m]	2.35
Throat Diameter [m]	2.05
Nozzle Diameter [m]	2.37
Forebody Length [m]	3.3
Afterbody Length [m]	3.7
Total Engine Length [m]	7

Table 5-5: Intake geometrical data.

	Cruise	Take-Off
Altitude [m]	12192	500
Mach	0.8	0.3
COT [K]	1200 to 1900	1700 to 1800

Table 5-6: Flight conditions.

	Virtual /Actual Wing Length [%]	Maximum Mach Change [%]
a	10	19.3
b	50	10
c	100	-

Table 5-7: Effect of virtual wing length.

	Grid Cells	Grid Change	Mach Change
c	2000832	-	-
d	2701123	+35 %	+1.6 %

Table 5-8: Comparison to a denser grid.

Figures of Chapter 5

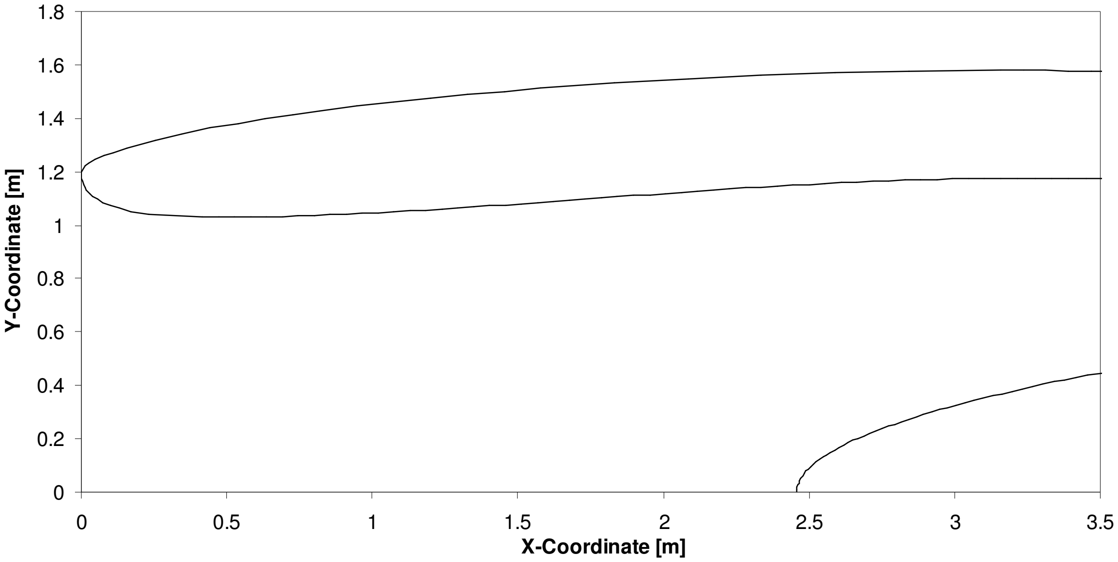

Figure 5-1: Engine installation cross section sketch (forebody).

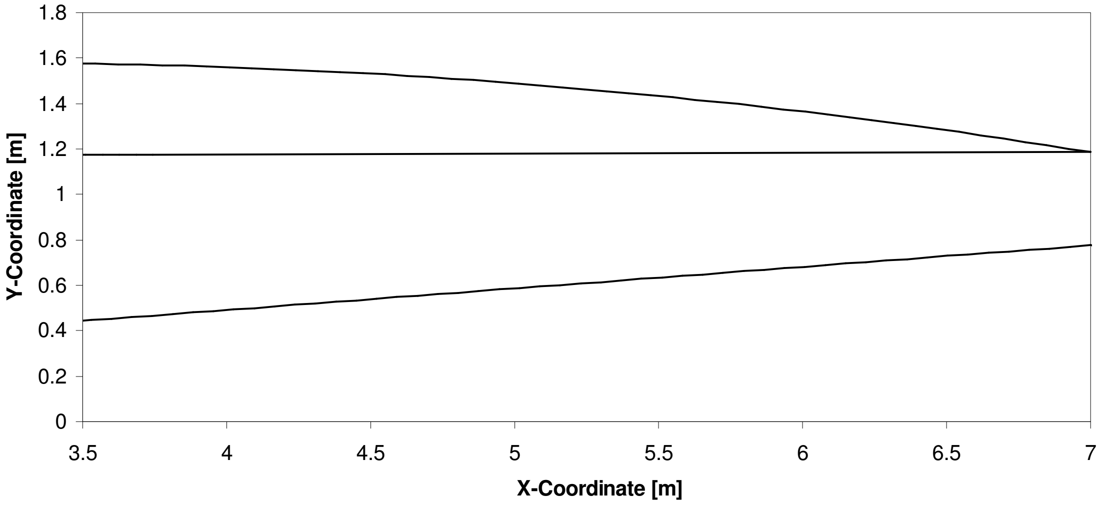

Figure 5-2: Engine installation cross section sketch (afterbody).

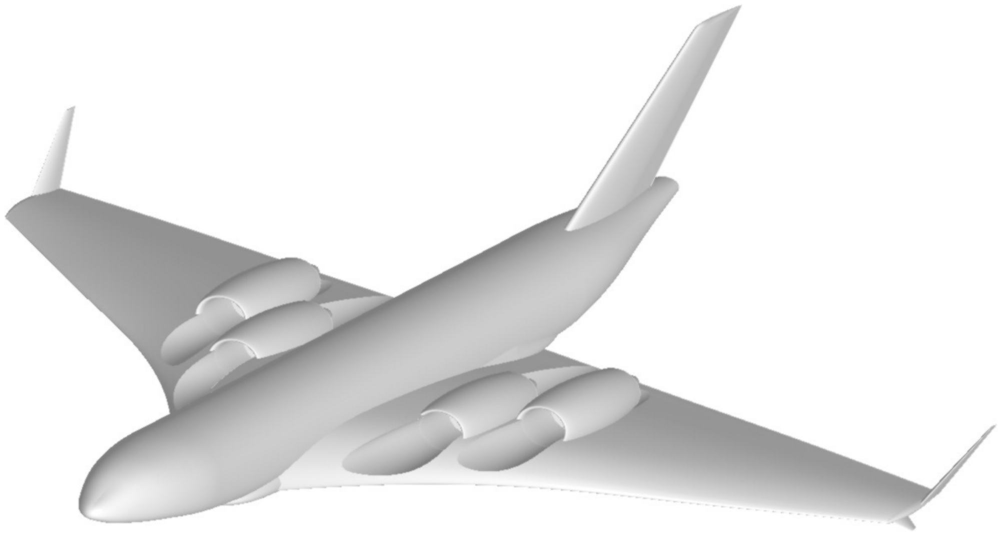

Figure 5-3: Broad delta wing aircraft.

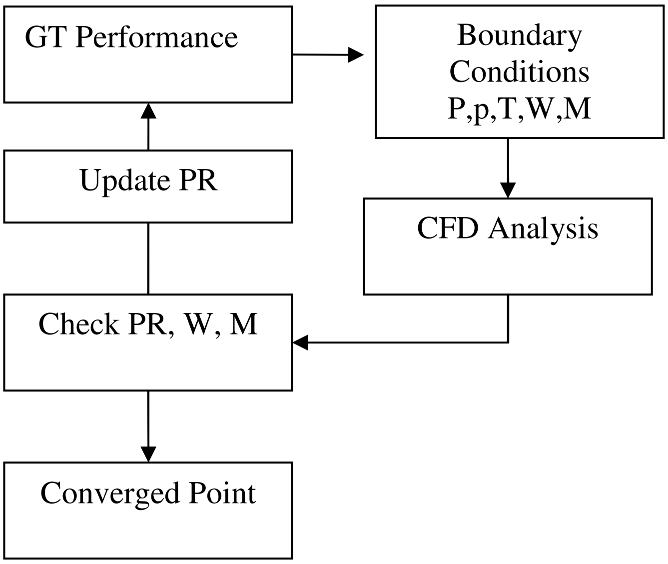

Figure 5-4: Map generation iterative process.

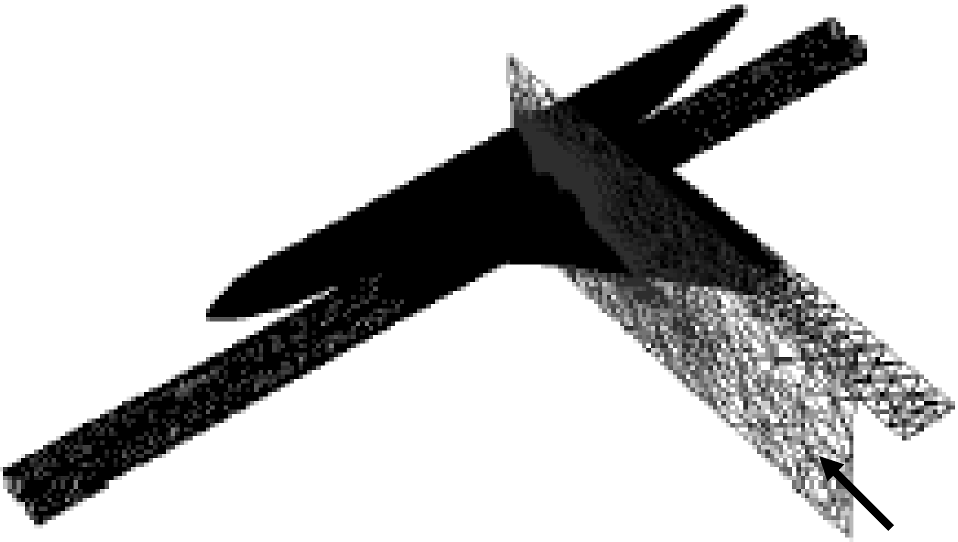

Figure 5-5: Boundary condition plane.

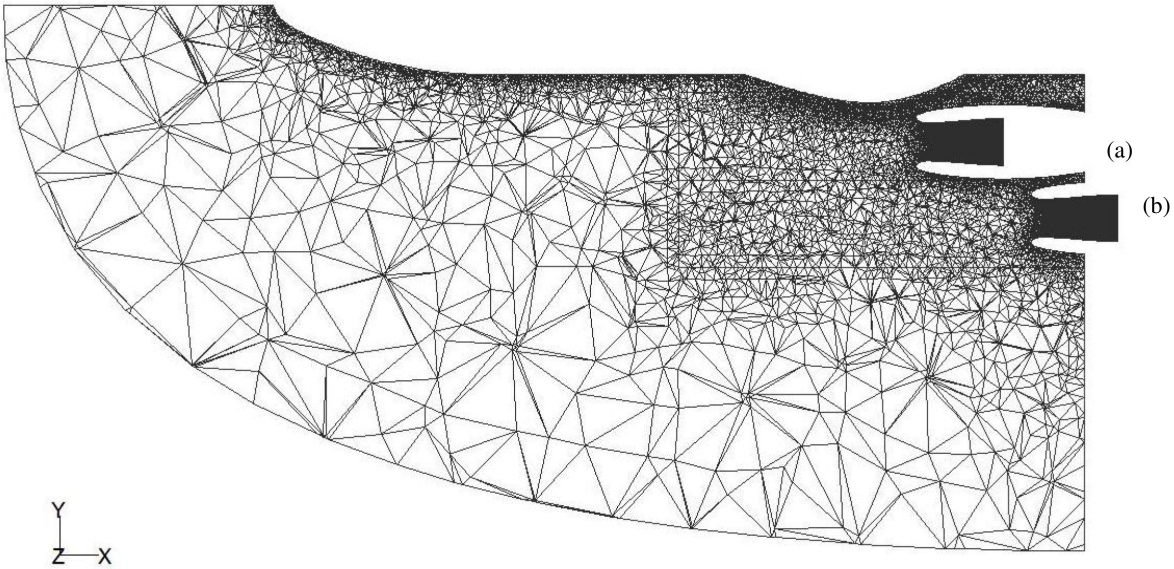

Figure 5-6: Small domain top view.

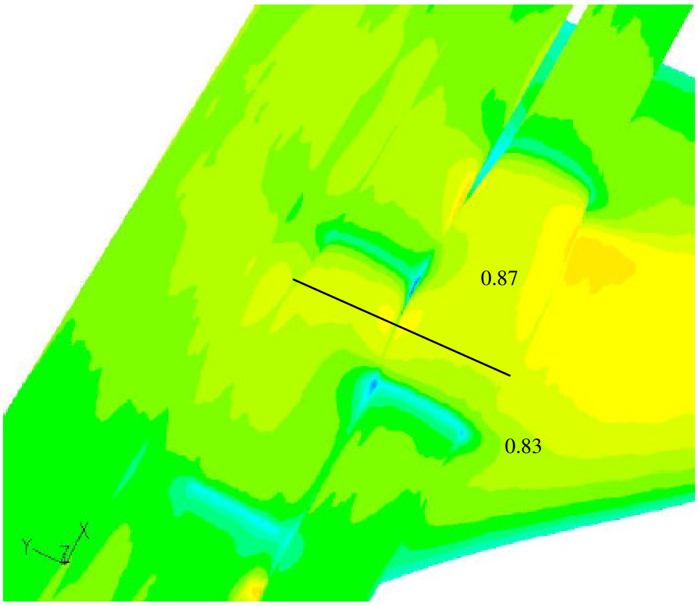

Figure 5-7: **Top view, two nacelles close-up, Mach number contours, at cruise.**

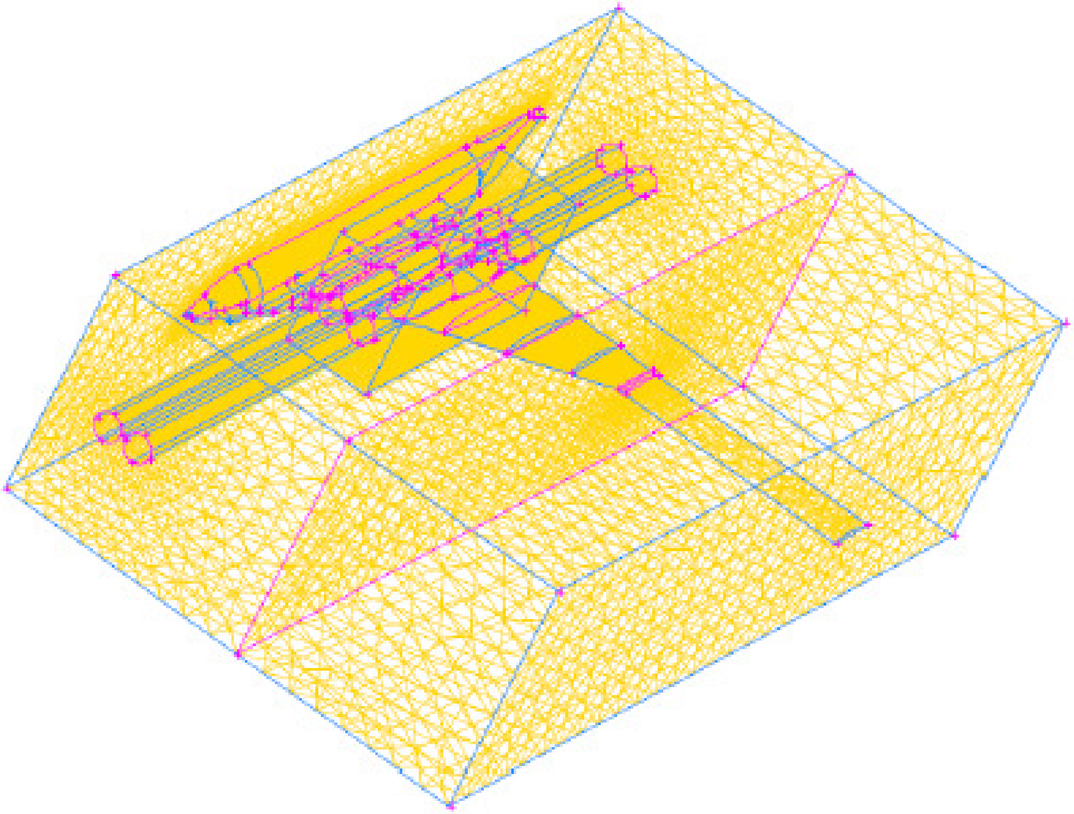

Figure 5-8: Big domain grid 3-D view.

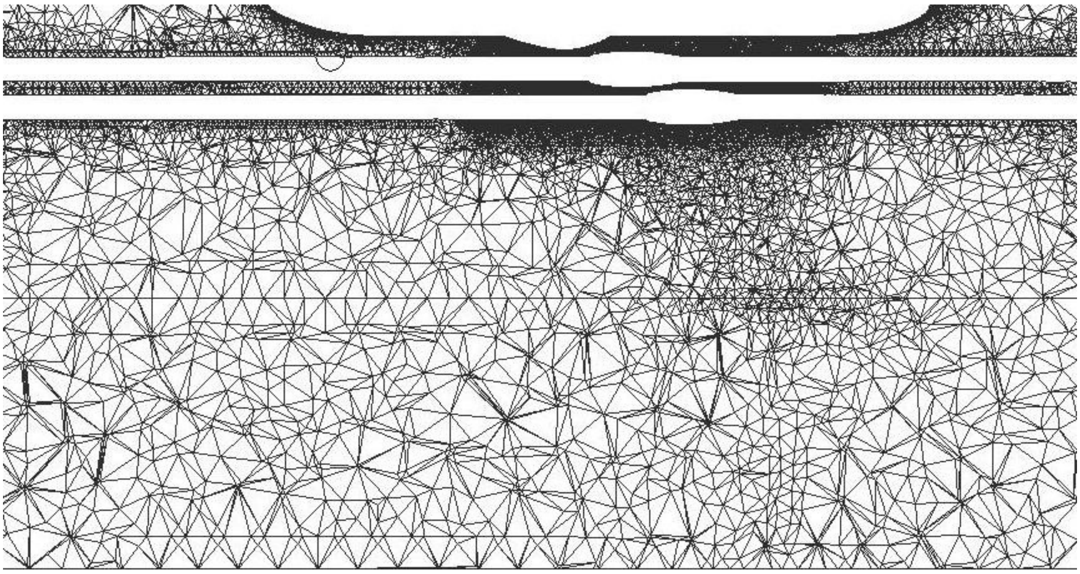

Figure 5-9: Big domain grid cut.

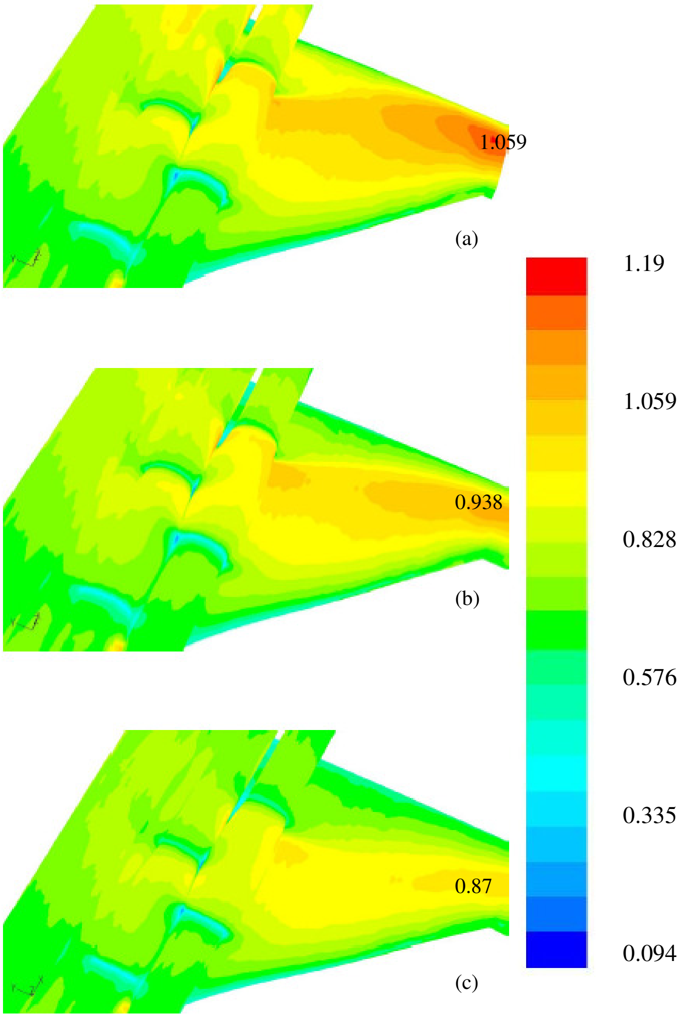

Figure 5-10: Mach number contours at suction surface of the wing, 3 virtual wing lengths, cruise condition.

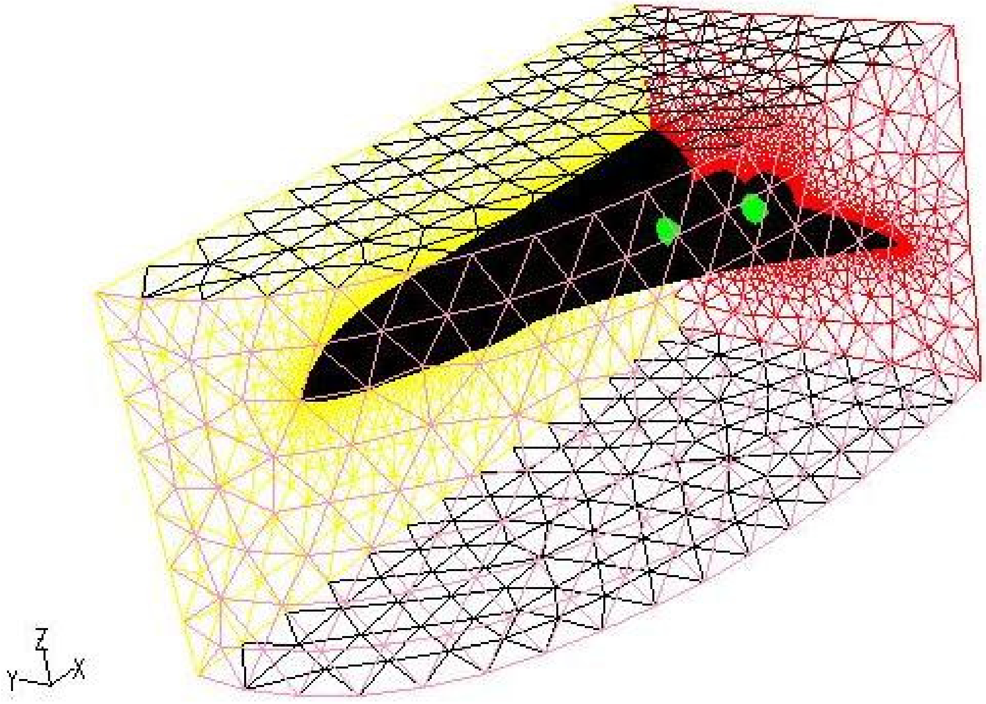

Figure 5-11: Small domain 3-D view.

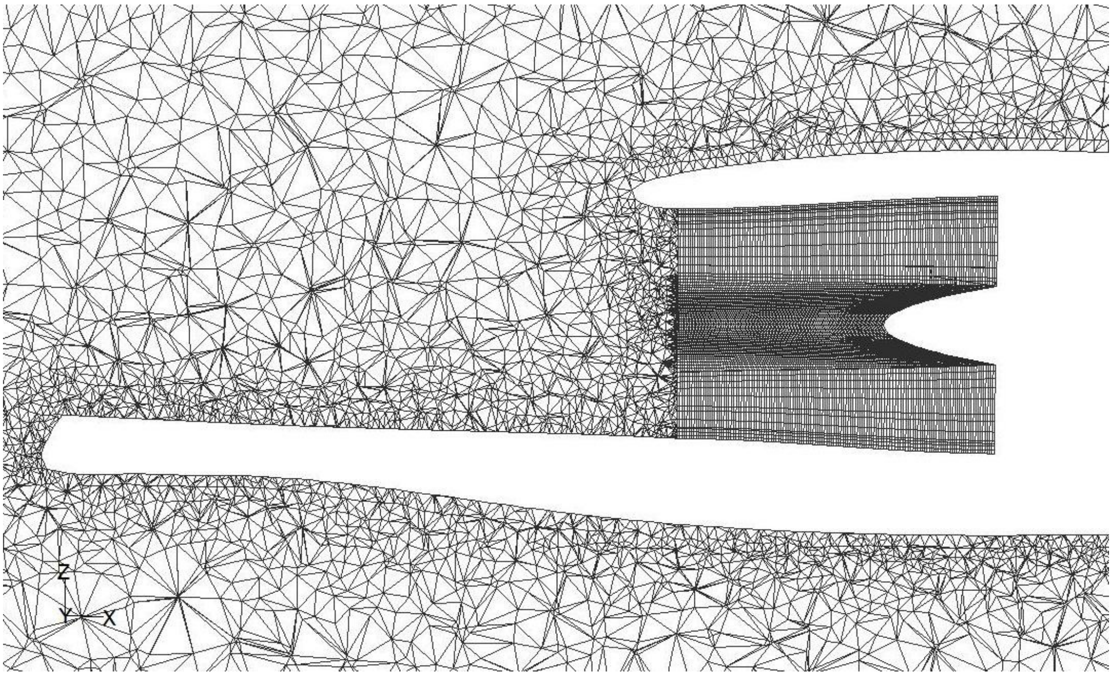

Figure 5-12: Small domain, meridional view of intake.

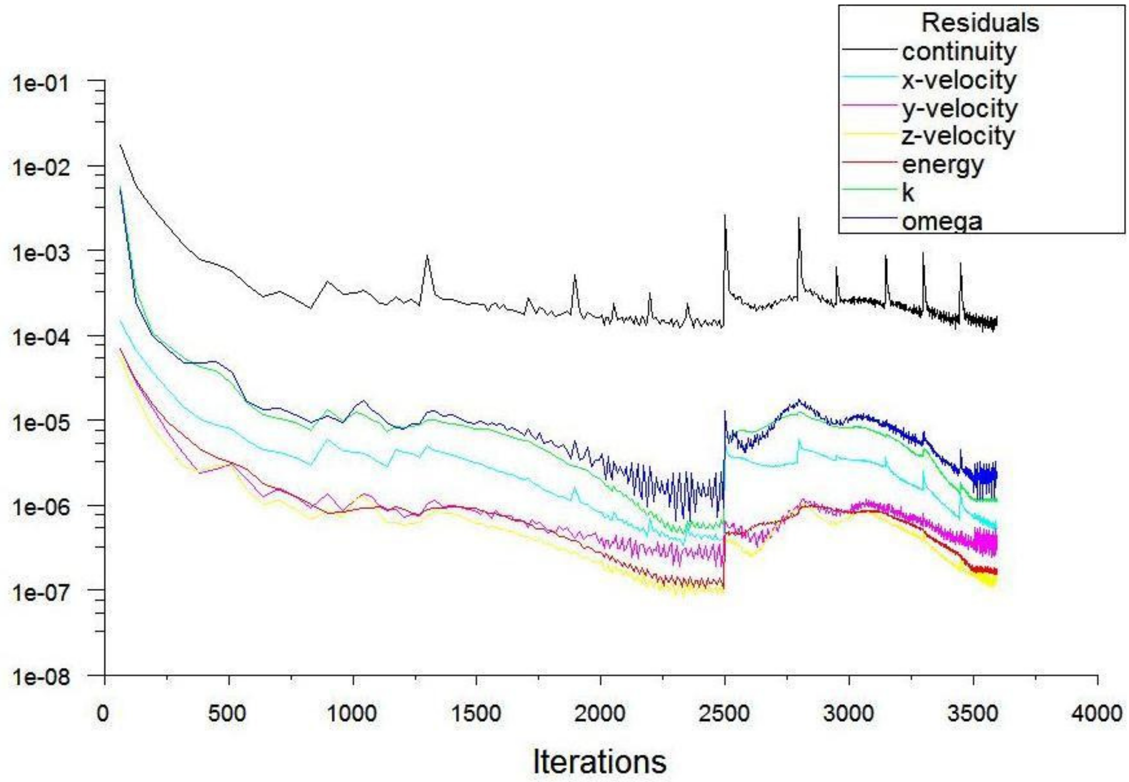

Figure 5-13: Convergence history for small domain.

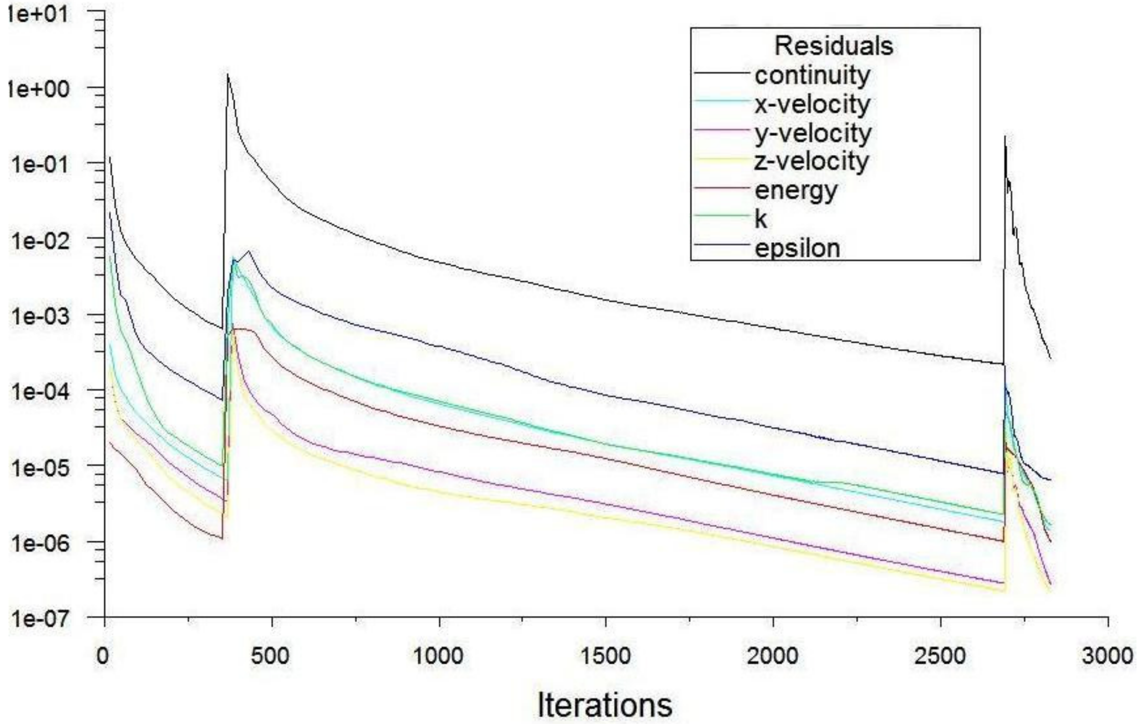

Figure 5-14: Convergence history for ‘big domain’.

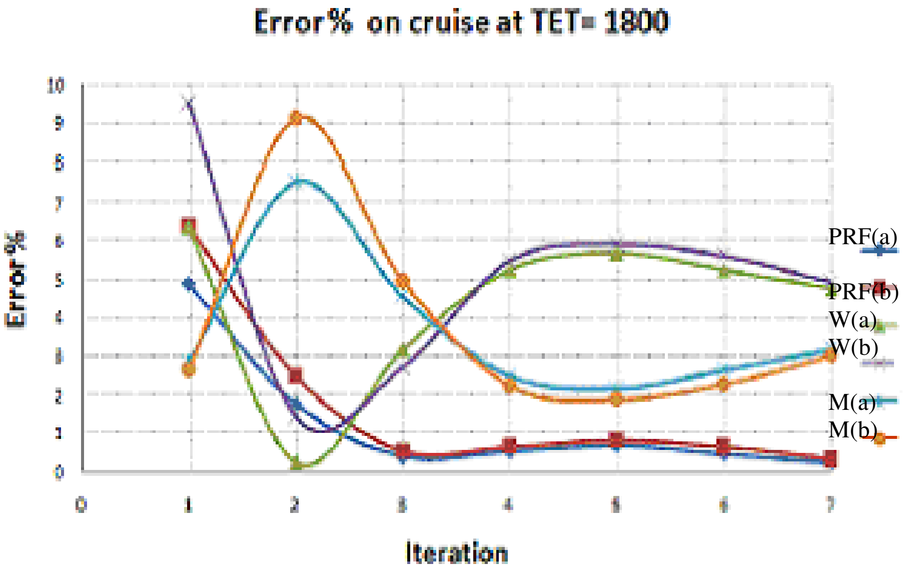

Figure 5-15: Convergence history of iterative process.

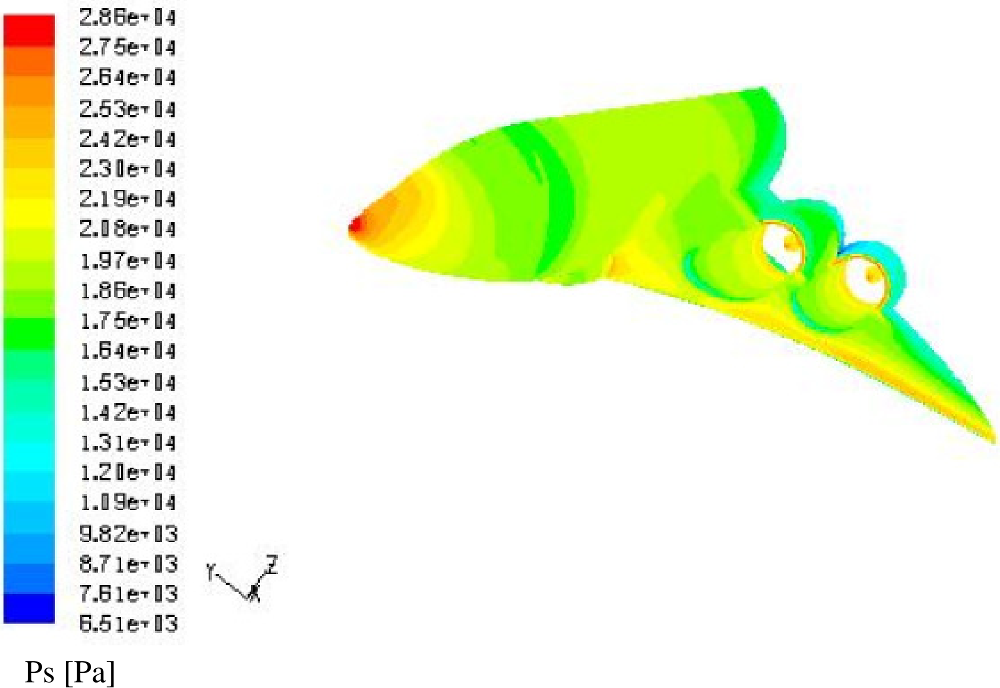

Figure 5-16: Small domain P_s contours at cruise and COT at 1800K.

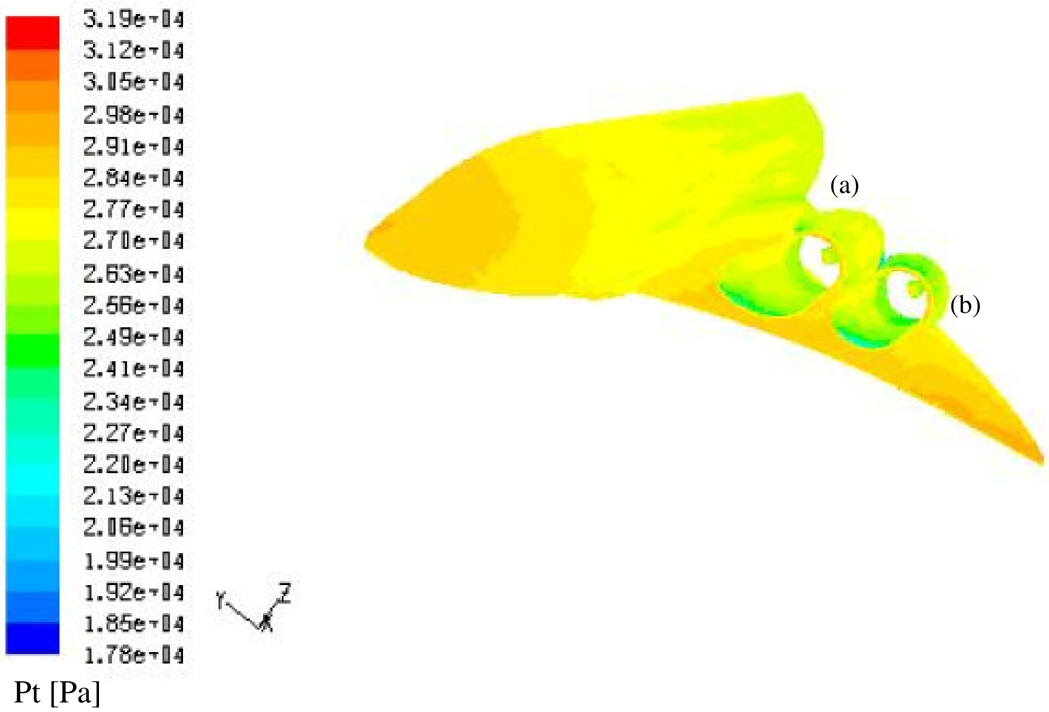

Figure 5-17: Small domain P_t contours at cruise and COT at 1800K.

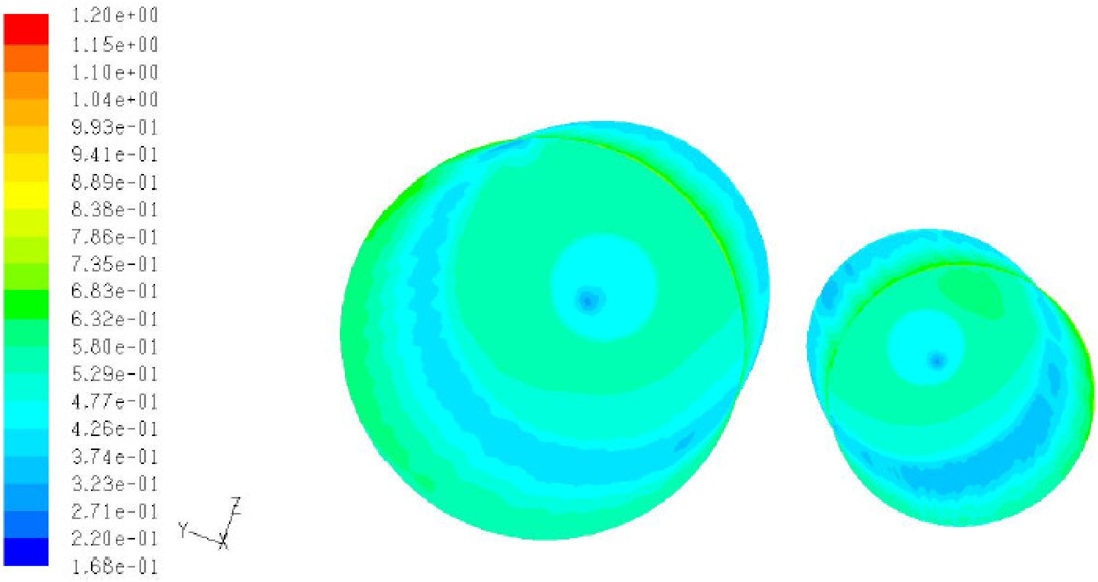

Figure 5-18: Small domain Pt contours at cruise and COT at 1800K.

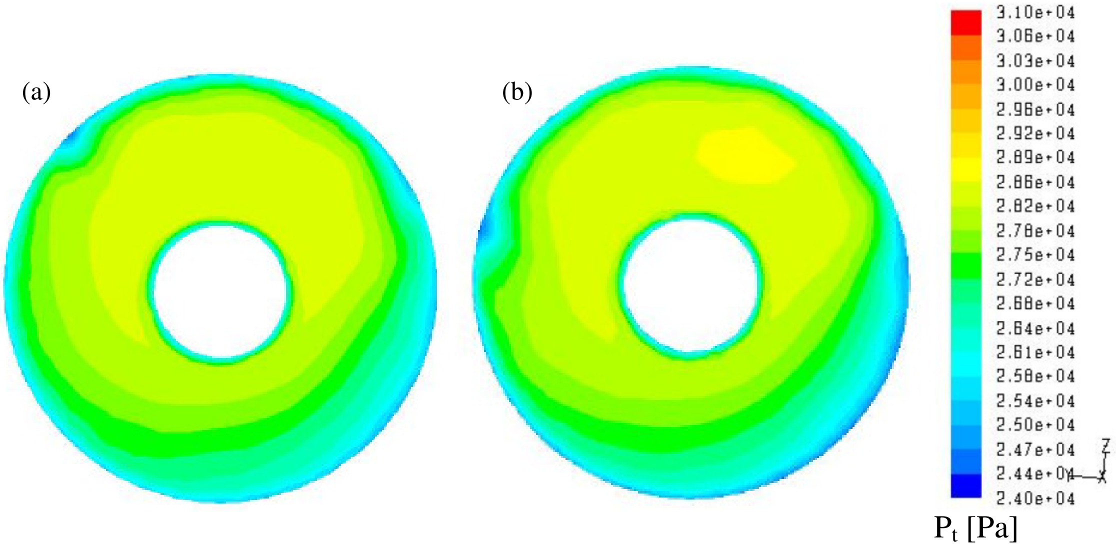

Figure 5-19: Fan intake Pt contours at cruise and COT at 1800K.

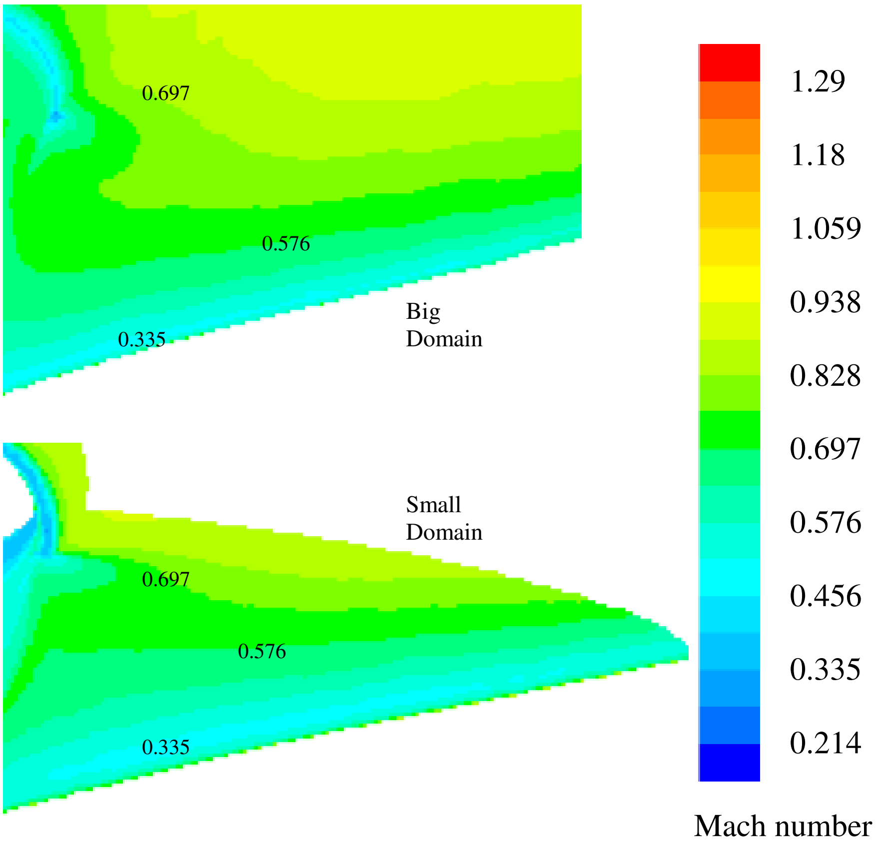

Figure 5-20: Wing detail of 'Big' and 'Small' domain flow field, Mach number contours at cruise and COT at 1800K.

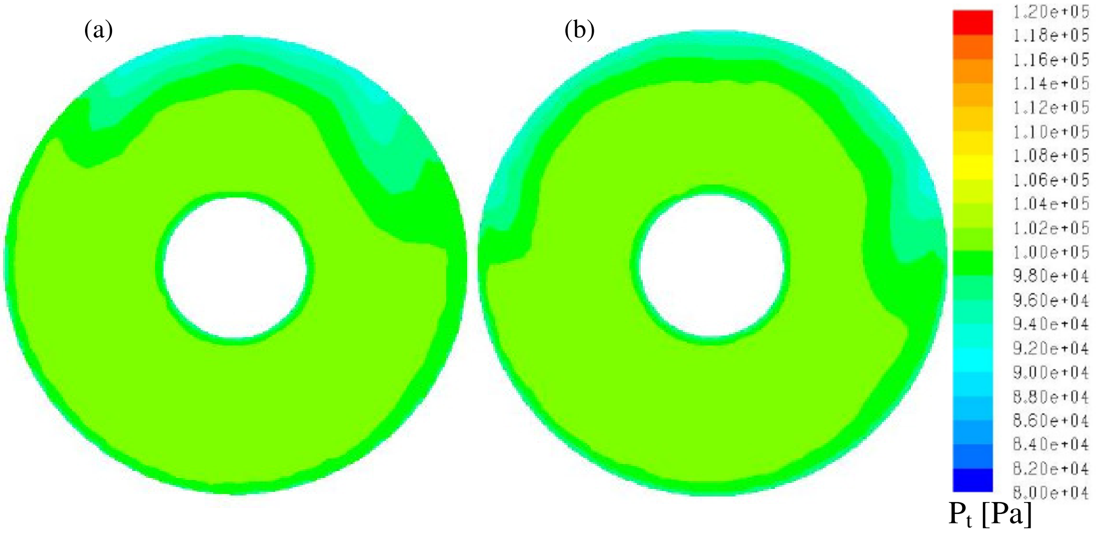

Figure 5-21: Fan intake Pt contours at take-off and COT at 1800K.

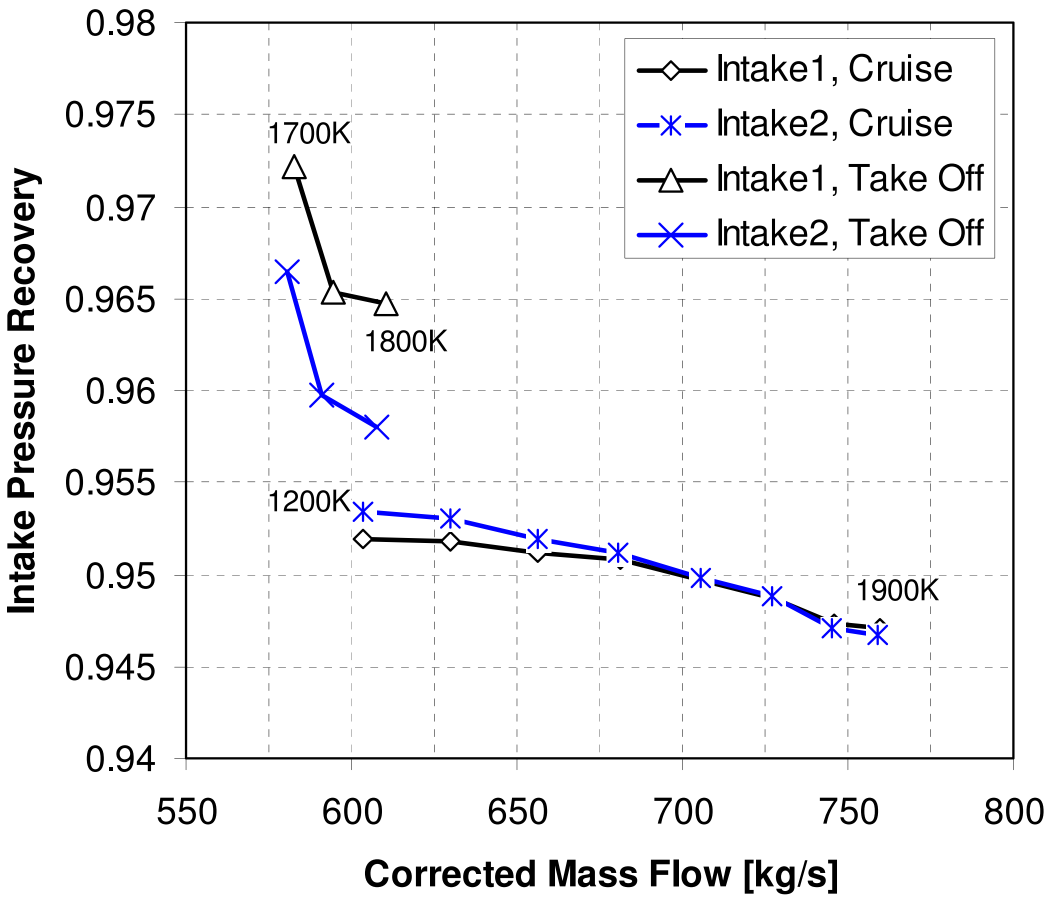

Figure 5-22: Intake map at cruise and take off.

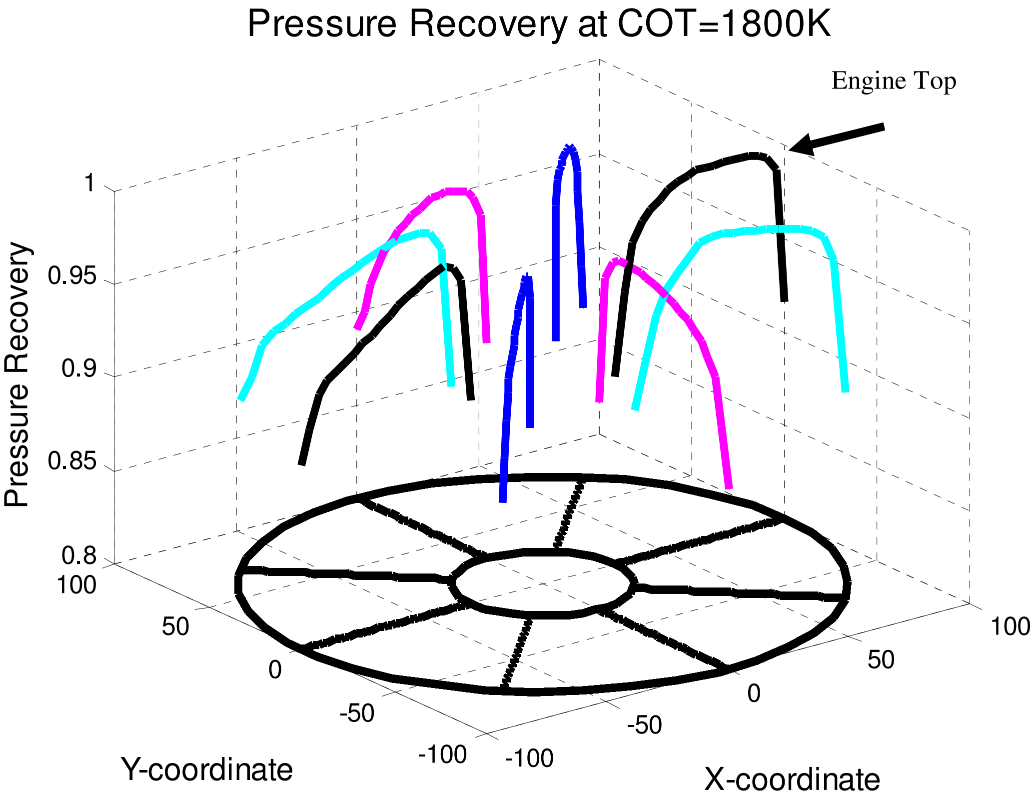

Figure 5-23: Pressure recovery profiles at cruise and COT at 1800K.

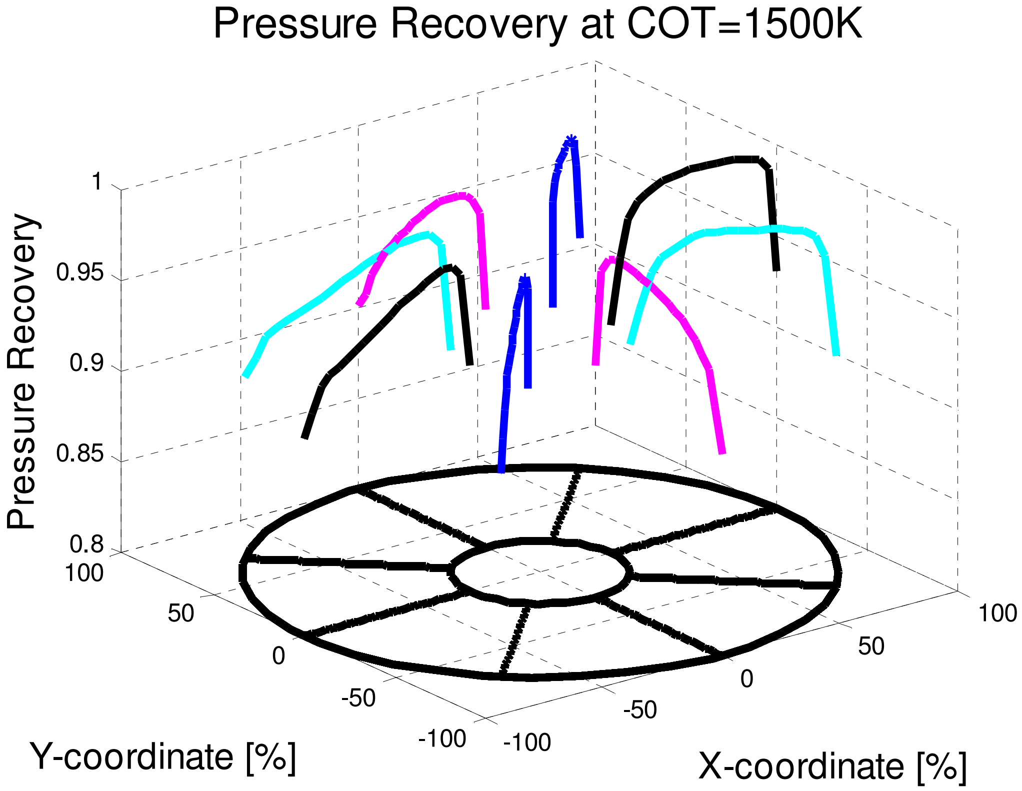

Figure 5-24: Pressure recovery profiles at cruise and COT at 1500K.

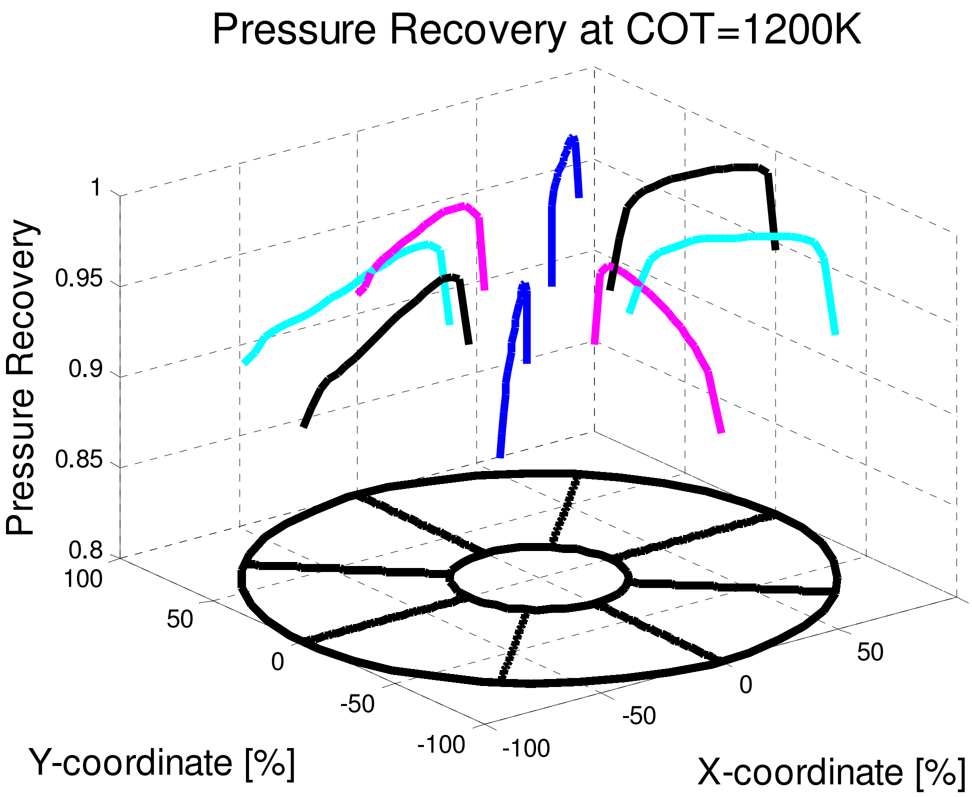

Figure 5-25: Pressure recovery profiles at cruise and COT at 1200K.

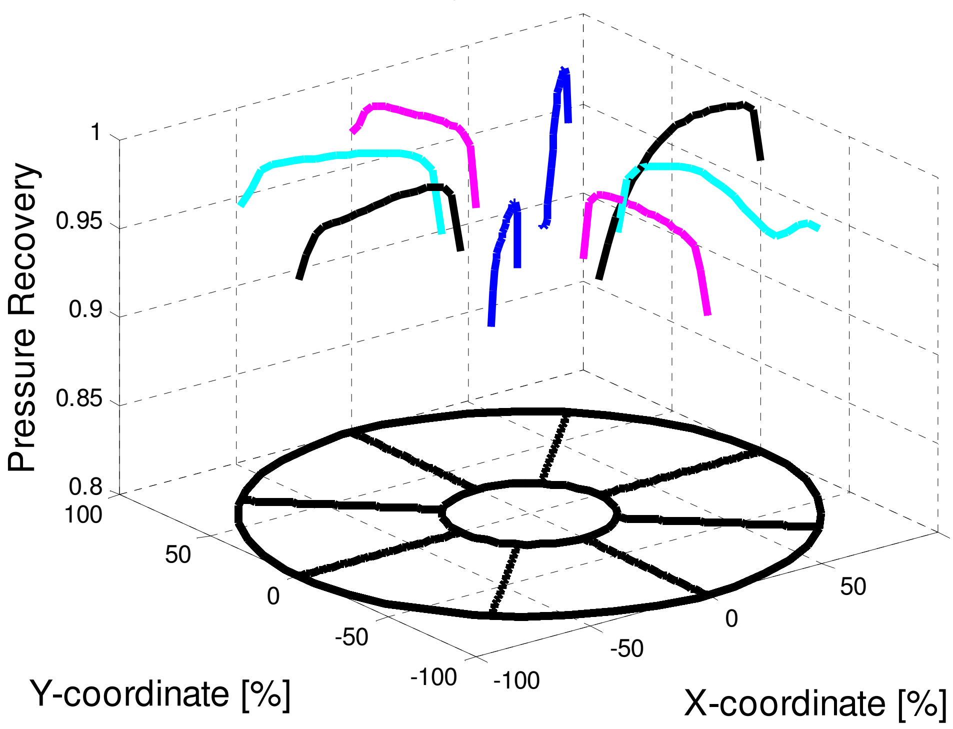

Figure 5-26: Pressure recovery profiles at take-off and COT at 1800K.

6 High Fidelity Engine Performance Analysis Under Inlet Distortion

Gas turbine performance simulation is broadly based on 0D component maps. In this case, engine components are represented by non-dimensional maps. As a result, complex 3D phenomena, such as inlet distortion are not taken into consideration. However, in cases of embedded or half-embedded installations, where the propulsion system is subject to distorted flow during the whole envelope, higher fidelity modelling of the engine is recommended.

This project focuses on the design of low noise propulsion systems. In this context, a half-embedded installation has been designed and tested, as discussed in Chapter 5. Such a design results in highly distorted engine inlet flow. Therefore, the impact of distortion on engine performance and stability is assessed by a high fidelity model of the low pressure compression system; the fan. The reason for focusing on the fan is that distortion is attenuated downstream the fan. As a result the downstream components are subject to lower distortion levels.

The method that has been discussed in §3.10 (PaCo-SLC), has been applied on a generic fan and a high bypass ratio turbofan. This chapter includes a discussion on fan stability and overall engine performance, based on the results of the high fidelity analysis.

6.1 Inlet Distortion

An installation study of an advanced propulsion system on a novel airframe has been thoroughly discussed in Chapter 6. In the scope of the study, three-dimensional CFD analysis has been used for producing a quasi 3D map for representation of the intake in engine performance modelling. This map has been implemented in an engine model using a method described in §3.10. The following results illustrate the strategy that has been followed in order to feed the PaCo-SLC model with appropriate inlet profiles of pressure recovery factor.

As discussed in §3.10, distortion index ‘K’ has been used for specifying distortion levels. The calculation of ‘K’ is based on intake maps that include radial profiles at 8 circumferential positions, varying with mass flow rate, as illustrated in Figure 6-1 to Figure 6-8. As a result, according to the value of inlet mass flow, linear interpolation is used for defining the radial profiles of pressure recovery factor at the 8 sections. The relatively small change of the radial profiles with mass flow, that is profound in figures1 to 8, allows for using linear interpolation with confidence. In a further step ‘K’ is calculated, using Equation 3-14. This index is based on circumferential distortion, therefore, PRF is area-averaged in the radial direction and the results are depicted in Figure 6-9. In this figure, the circumferential variation of pressure recovery factor is plotted in parallel with the circumferentially-area-averaged PRF, in a way, that the area with local PRF lower than average can be easily identified. It should be noted that each sector extends to an angle of 45^o and this is the value taken into consideration in the circumferentially-area-averaging process. In a following step, the area of low pressure is represented by a radial variation of PRF, resulting from area-averaging between all the low-PRF circumferential sectors.

Circumferential variations of PRF for four typical mass flow rates are extracted from the intake map and illustrated in Figure 6-9. The process discussed in the previous paragraph results in Figure 6-10, Figure 6-11, Figure 6-12 and Figure 6-13 for four different mass flow rates, respectively. Due to the fact that the low pressure area extends to 180^o, the model divided the circumference to two equal sectors; each sector being represented by a radial distribution of pressure recovery factor. Figure 6-10 to Figure 6-13 demonstrates the effect of mass flow on the shape and magnitude of inlet pressure radial distribution to the two parallel compressors. The low pressure profile exhibits intense pressure gradients, with low pressure at the tip, due to the effect of the intake channel through the wing, as discussed in §5.5. Furthermore, high mass flow results to lower pressure recovery for both sectors, and more intense negative radial pressure gradients towards the tip. This attribute is reflected in Figure 6-14, where ‘K’ appears to vary linearly with corrected mass flow rate.

The determination of the inlet radial profiles is an automatic process embedded in the PaCo-SLC model. In this way, the user needs to setup a CFD attained intake map. In a further step, the number of distorted sectors, the extent of distorted area and the distortion index are automatically calculated and used for the prediction of fan performance.

6.2 Fan Performance Analysis

Following the definition of input profiles to the parallel compressor streamline curvature code (PaCo-SLC), the method predicts fan performance under inlet distortion. The results are compared to clean inlet performance, in order to calculate the qualitative trends of loss on surge limits.

In the scope of the study of the effect of inlet distortion on fan performance, fan geometry is needed as input to the streamline curvature code. Several fan designs have been implemented. However SLC appeared unable to converge, due to high disorientation of the streamlines, during the iteration process. As a result, a generic fan has been used, based on the first stage of NASA TP 1493. The benefit from such solution is that SLC is already validated against experimental data for clean and radial distorted inlet conditions for this particular fan , [Pachidis, 2006], [Templalexis, 2006]. The geometrical input to SLC is included in the Appendix (§9.12).

Inlet distortion has a profound effect on fan performance. This is clearly demonstrated in Figure 6-15, Figure 6-16 and Figure 6-17, where radial distributions of total pressure and temperature at inlet and outlet of both parallel segments are plotted against radius. It should be noted that, the above mentioned plots refer to the surge point of the 100% speedline. In all the figures, radius is expressed as percentage of the maximum inlet radius. In this way, the reduction of annulus area at the exit of the fan is depicted. As shown in Figure 6-15, the two compressors exhibit similar outlet profiles of pressure, with a positive gradient towards the tip. However, the low inlet pressure region near the tip of the first compressor limits the increase of outlet pressure. Moreover, the Pt_{outlet} difference between the two segments appears to be proportional to their Pt_{inlet} difference, despite the increase of pressure ratio in the distorted area. This increase is the result of low regional inlet velocity, thus high incidence and blade loading, as shown in Figure 6-16. Additionally, similar behaviour is depicted in Figure 6-17. Even though inlet temperature distortion is negligible, higher pressure ratio at the distorted region, in addition to higher losses, lead to higher outlet temperature, across the whole radius.

Overall fan performance is depicted in Figure 6-18 and Figure 6-19. In these two figures, clean and distorted fan maps are plotted in terms of pressure ratio and efficiency against corrected mass flow per unit area. In such way, the loss in surge limits is clearly depicted, as the surge line of the distorted map has moved to lower pressure ratios and higher mass flows, reducing the area of stability available for the fan. Other than this, PaCo-SLC did not predict strong deviation between clean and distorted speedlines, in the region far from surge, in terms of the shape of the speedlines. With respect to efficiency, though, distortion has a negative effect, due to higher losses in the fan. As a result, efficiency levels are reduced through the whole fan map. It is noticed, that there are no PaCo-SLC results plotted for the 40% speedline. This is due to the absolute concurrence, between clean and distorted, something that is the case even for the 50% speedline. The main reason is the low slope of the speedline, combined with the low levels of inlet distortion.

In order to quantify the effect of loss in surge limit two values are used. They depict the percentage increase of surge mass flow and decrease of surge pressure ratio, as compared to the clean inlet surge limits. ‘ΔPRS’ (Equation 6-1) stands for loss in pressure ratio surge limit, while ‘ΔWS’ (Equation 3-3) is used for the increase of surge mass flow.

Equation 6-1

$$\Delta PRS = \frac{PR_{clean} - PR_{distorted}}{PR_{distorted}}$$

Equation 6-2

$$\Delta WS = \frac{MassFlow_{clean} - MassFlow_{distorted}}{MassFlow_{distorted}}$$

A comparison of the above mentioned factors with ‘K’, circumferential distortion index (definition of ‘K’, in §3.10) gives the sensitivity of the compression system to inlet distortion. This is depicted in Figure 6-20 and Figure 6-21. The linear relation between loss of surge pressure ratio and mass flow and distortion index can be expressed by a sensitivity factor (SF). This factor is calculated at ~0.65 for pressure ratio, using Equation 6-3 and 1.52 for mass flow using Equation 6-4, as depicted in the figures.

Equation 6-3

$$KS_{PR} \approx \frac{\Delta PRS}{K}$$

Equation 6-4

$$KS_{MF} \approx \frac{\Delta WS}{K}$$

6.3 Engine Performance

The assessment of fan sensitivity to inlet distortion is followed by assessing engine sensitivity. In the scope of this study, a generic high bypass ratio turbofan has been used. The effect of inlet distortion on propulsion system’s overall off-design performance, with the use of high fidelity modelling, has been analysed and compared to typical performance results.

A model of the turbofan has been created in TURBOMATCH, where the low pressure compression system has been replaced by the PaCO-SLC fan model. The data of the cycle used in the study are included in Table 6-1. A conventional generic turbofan has been implemented in the model, in order to be compatible with the pressure ratio of the NACA TP 1493. The reason is that no scaling factors have been used in the model, as this would be beyond the scope of this project. As a result, the use of moderate bypass ratio, that leads to optimum FPR ~1.5 is essential. Nevertheless, this generic turbofan is used as a demonstrator of the capabilities of the PaCo-SLC.

The turbofan model has been designed at top of climb condition. With constant flight conditions, an operating line has been created, with the use of fan rotational speed as handle. The same process has been followed, using once a conventional 0D compressor brick and then the PaCo-SLC model. For the case of inlet distortion, though, in the first case a conventional 0D map has been used, having a constant value for pressure recovery factor. On the other hand, a fan map from PaCo-SLC was implemented in the model, in parallel with the detailed intake map that allows the variation of PRF with mass flow.

The operating lines for clean and distorted inlet conditions are illustrated in Figure 6-22. A good agreement between the ‘clean’ operating lines of the streamline curvature code and 0D compressor is depicted. However, this is not the case for the distorted inlet, where the simple model under-predicts the effect of distortion, due to its inability of taking into consideration the variation of PRF with mass flow and the effects of distortion on fan performance. Additionally, the 0D model is based on a conventional Turbomatch compressor map, which even though it is scaled to coincide at the design point with the SLC map, it is not identical, as shown in [Pachidis, 2006, pp.218].

The calculation of the operating line allows to assess the stability of the fan, as the surge margin is defined using Equation 6-5.

Equation 6-5

$$SM = \frac{PR_{surge} - PR_{operating}}{PR_{operating}}$$

Fan surge margin is plotted against rotating speed in Figure 6-23, for clean and distorted inlet conditions. It is obvious that inlet distortion has a significant effect on the stability of the system, especially at high power settings. In the excess of design speed (90%), the fan operating line appears to approach the distorted surge limit, with the surge margin tending to zero. On the other hand, at low power settings, the loss of surge margin is much less, due to lower distortion levels.

The effect of inlet distortion on fan pressure ratio operating line is depicted in Figure 6-24. The fan appears to have increased its pressure ratio, due to lower mass flow that results from the response of the engine to lower inlet pressure. As opposed to this, overall pressure ratio is reduced as illustrated in Figure 6-25, because low inlet pressure at constant temperature is equivalent to inlet temperature increase. This leads to lower air density, increasing overall compressor work and reducing mass flow rate (Figure 6-26). This condition is magnified by component efficiencies degradation. For example, Figure 6-27 illustrates the reduction of fan efficiency due to inlet distortion, where the effect is less intense at low rotational speed, as a result of lower distortion levels.

Overall off-design performance results are depicted in Figure 6-28, Figure 6-29 and Figure 6-26. The off-design variation of specific fuel consumption, specific thrust and mass flow, shows a declining behaviour at low power settings, which is expected, as the reduction of speedline, reduces the work input and output of every component. Furthermore, these figures illustrate the performance loss due to inlet distortion. Consequently, the loss in SFC and specific thrust lies at ~5% at high thrust settings, something that is translated at 5% higher fuel consumption; i.e ~2000kg of extra fuel and ~6500kg of extra CO_2 emissions for a typical medium range mission. Additionally, the loss of thrust could be critical in a case of maximum thrust requirement.

Finally, the PaCo-SLC fan model is compared to a conventional compressor model in terms of the Δ(SFC) and Δ(specific thrust). The deviations are calculated using Equation 6-6. Results show the higher accuracy of the effect of distortion in the case of PaCo-SLC, where variable distortion with mass flow is taken into account. As a result the deviation of SFC reduces at low thrust settings, and the same appears at specific thrust. A different attribute is presented by Turbomatch 0D analysis, where the deviation of SFC and S.T. increase at low settings, as there is less energy (lower COT, rotational speed) available for counteracting the negative effect of low inlet pressure.

Equation 6-6

$$\Delta(X) = \frac{X_{distorted} - X_{clean}}{X_{clean}} 100\%$$

To conclude, the high fidelity performance analysis has shown improved results, in comparison to 0D conventional engine modelling. Additionally, even though the results can be considered as of qualitative nature, they can be used at preliminary cycle design, in order to take into consideration that surge may occur at high engine settings, in advanced installations such as the half-embedded.

Tables of Chapter 6

Generic Turbofan	
BPR (ToC)	9
OPR (ToC)	40
FPR (ToC)	1.505
COT (ToC) [K]	1800

Table 6-1: Turbofan engine data.

Figures of Chapter 6

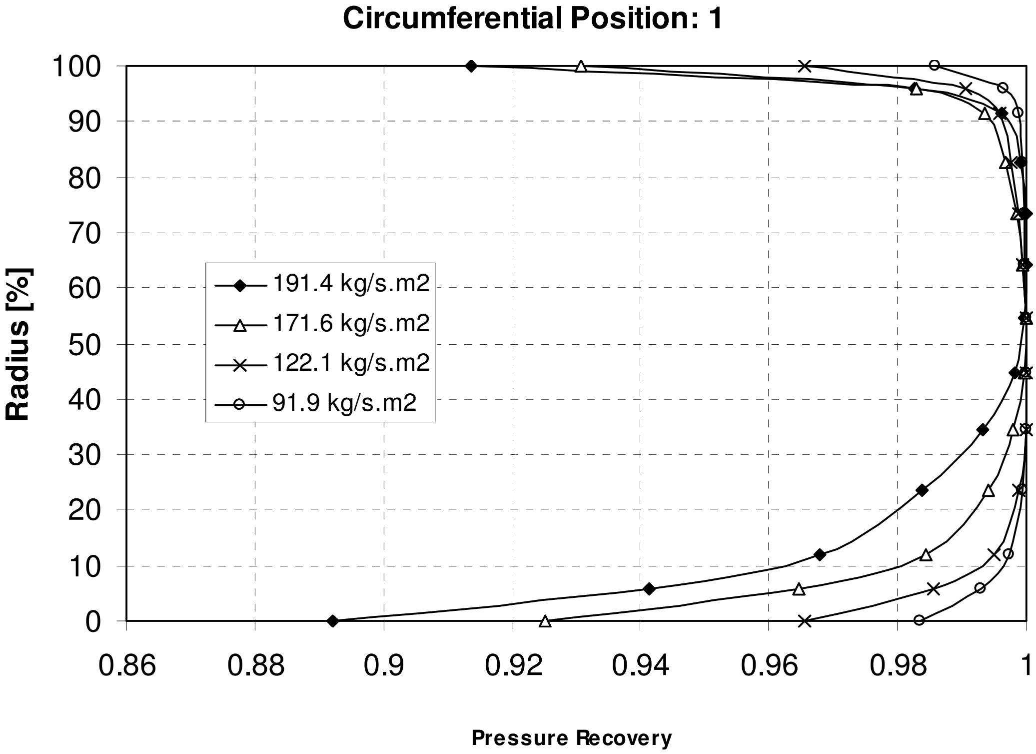

Figure 6-1: Pressure recovery Factor at section 1.

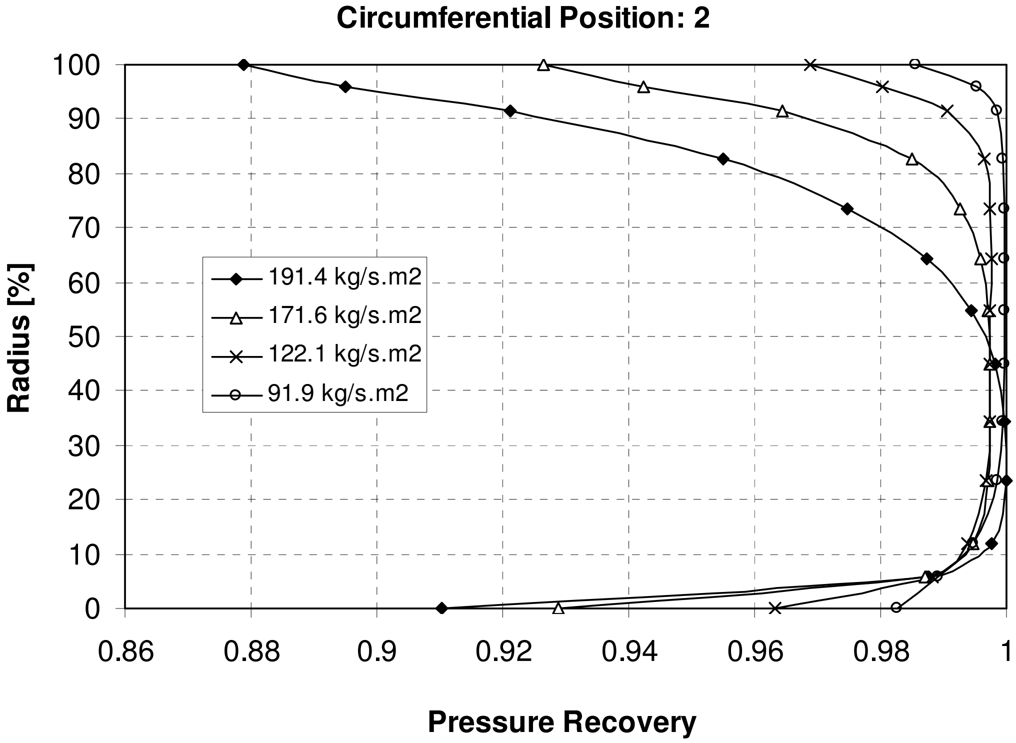

Figure 6-2: Pressure recovery Factor at section 2.

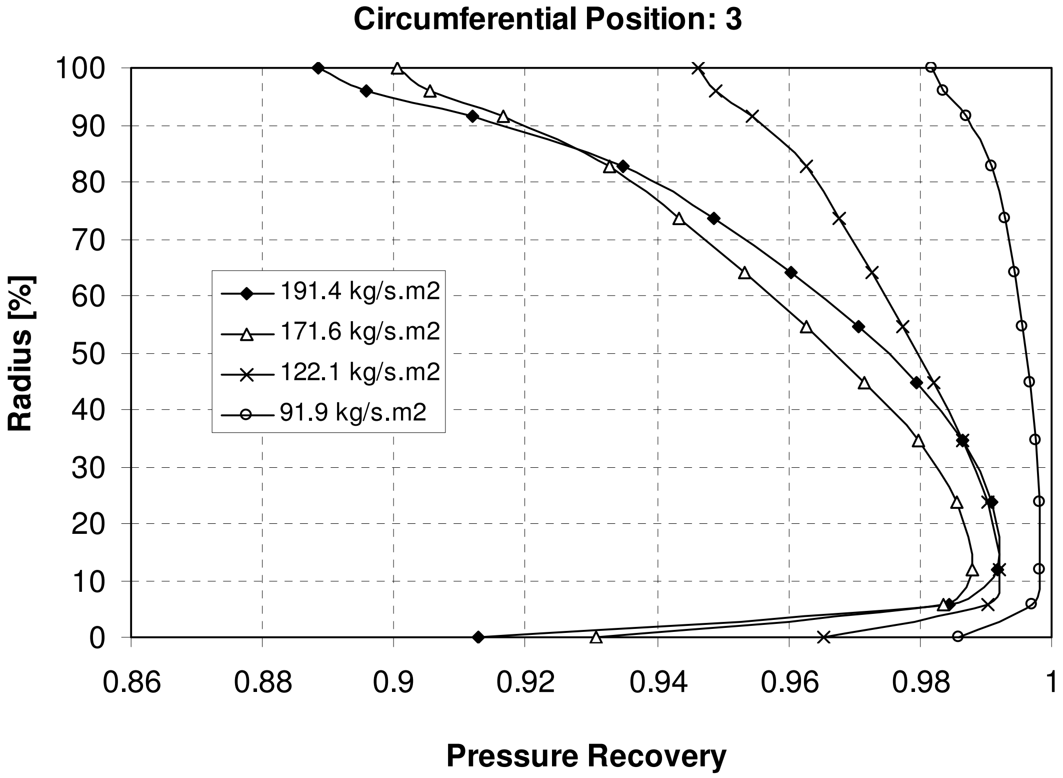

Figure 6-3: Pressure recovery Factor at section 3.

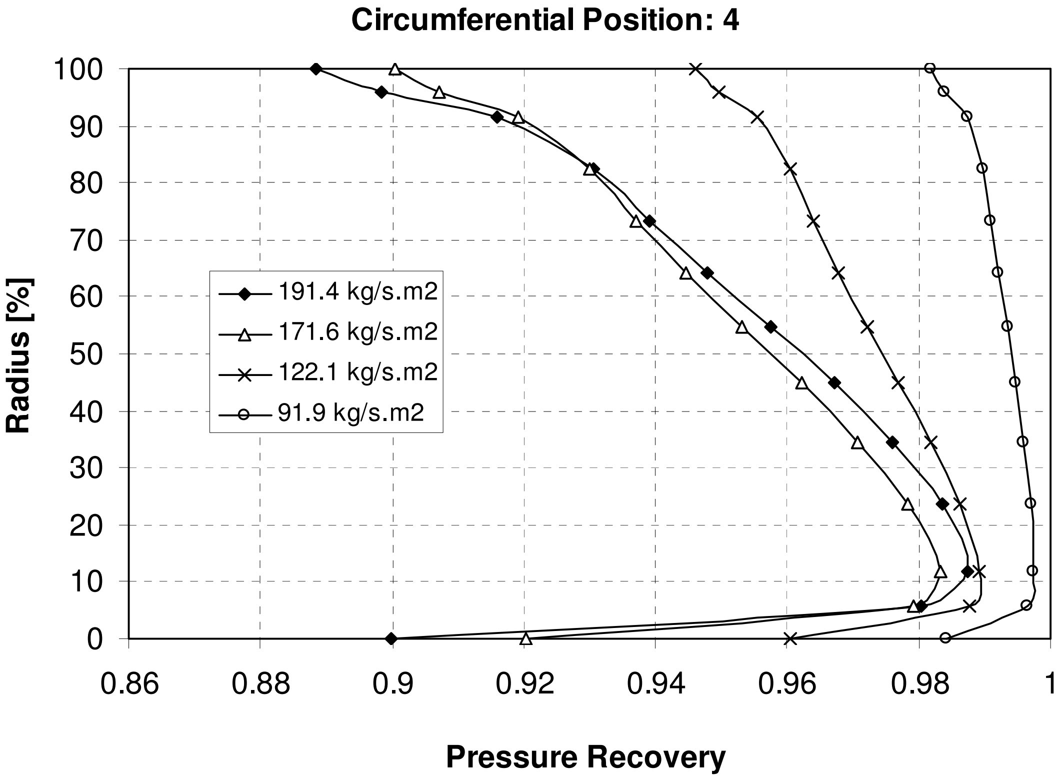

Figure 6-4: Pressure recovery Factor at section 4.

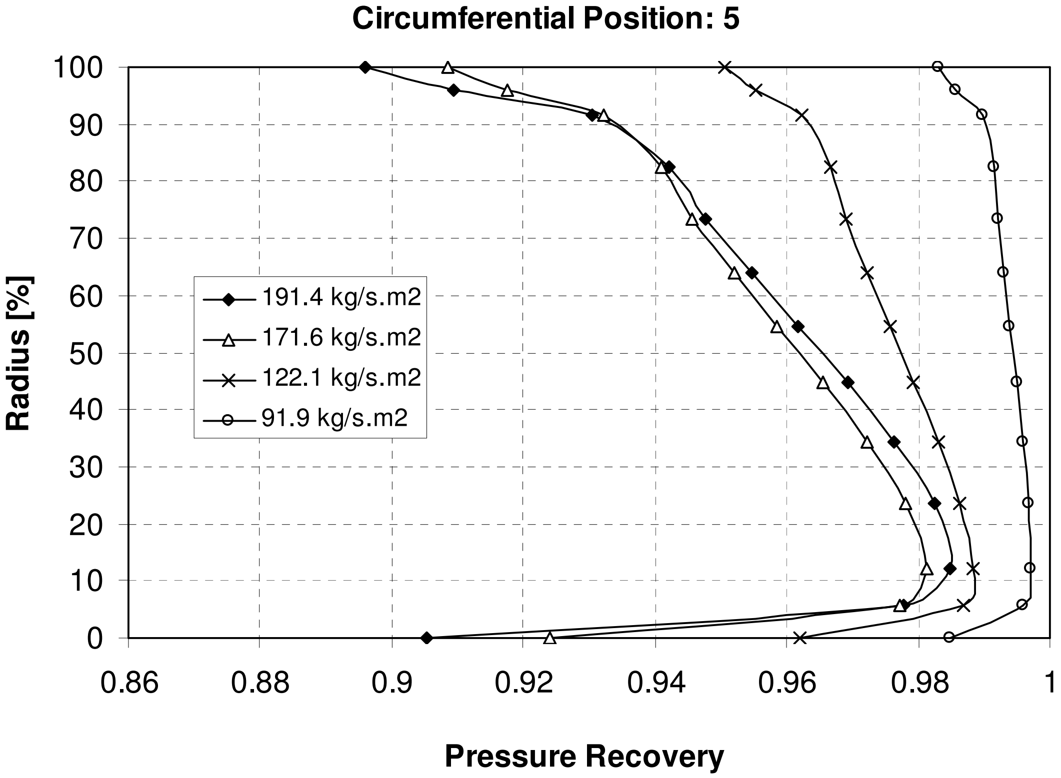

Figure 6-5: Pressure recovery Factor at section 5.

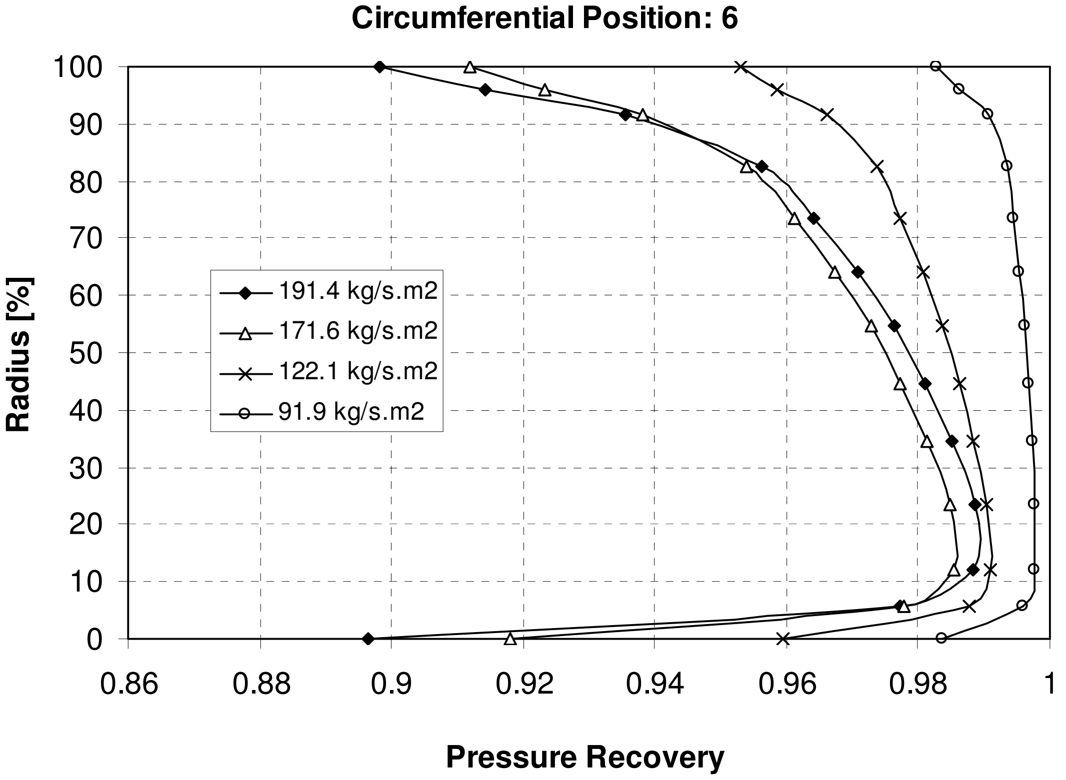

Figure 6-6: Pressure recovery Factor at section 6.

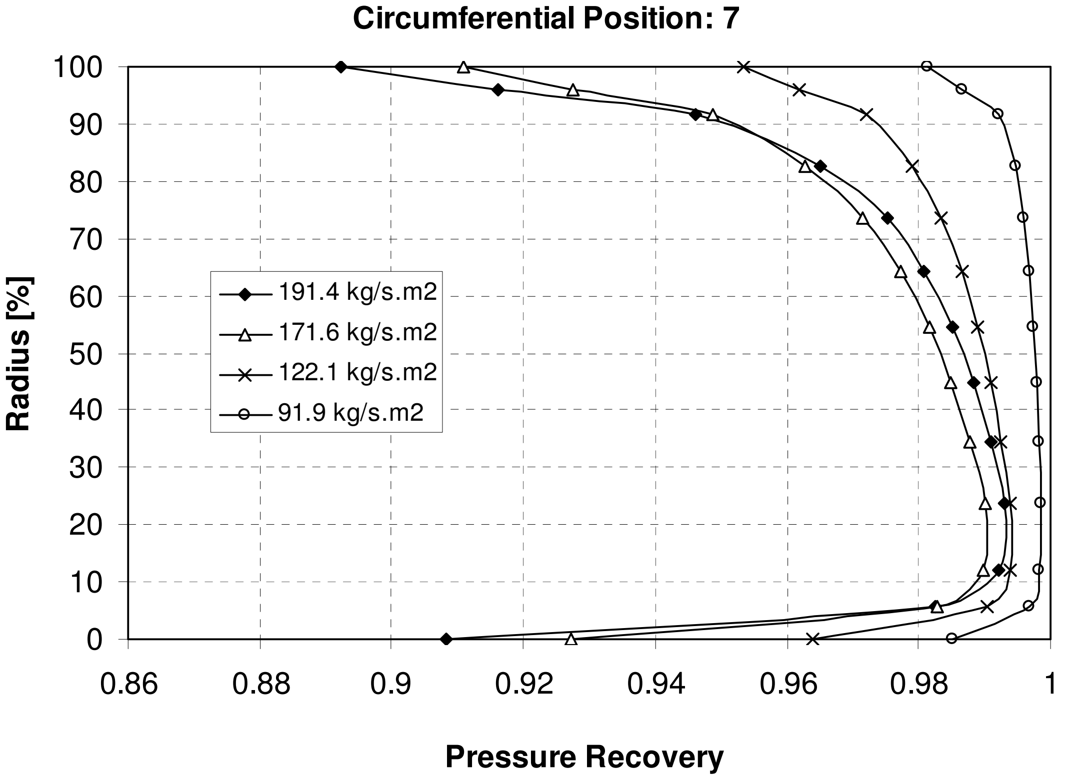

Figure 6-7: Pressure recovery Factor at section 7.

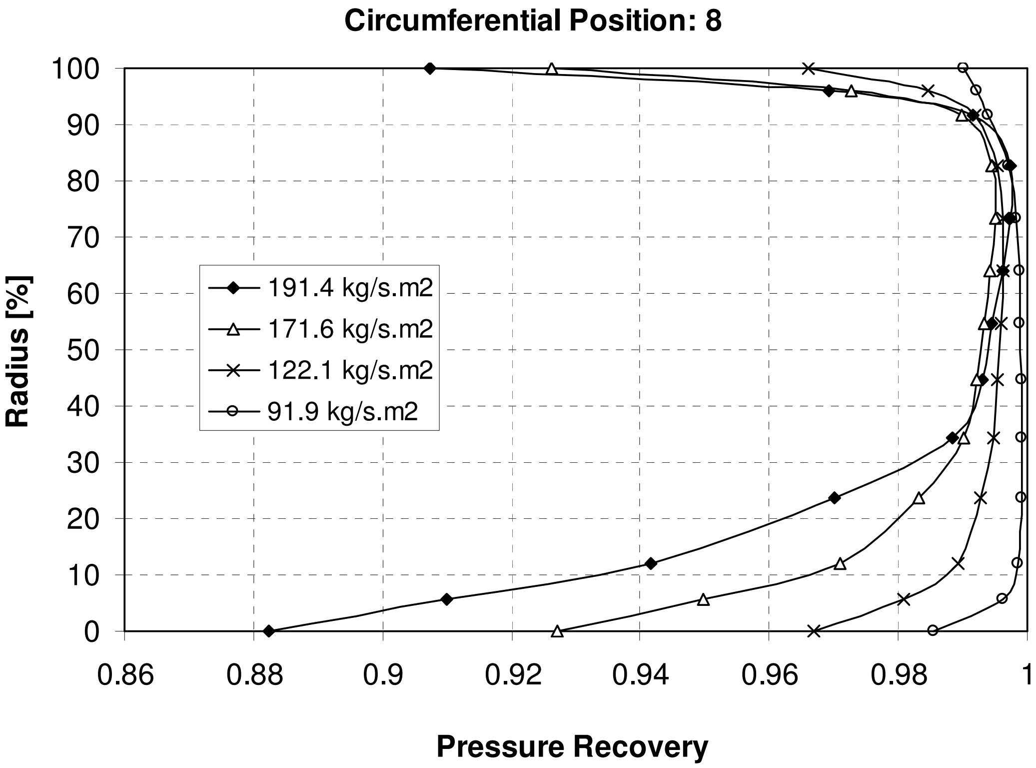

Figure 6-8: Pressure recovery Factor at section 8.

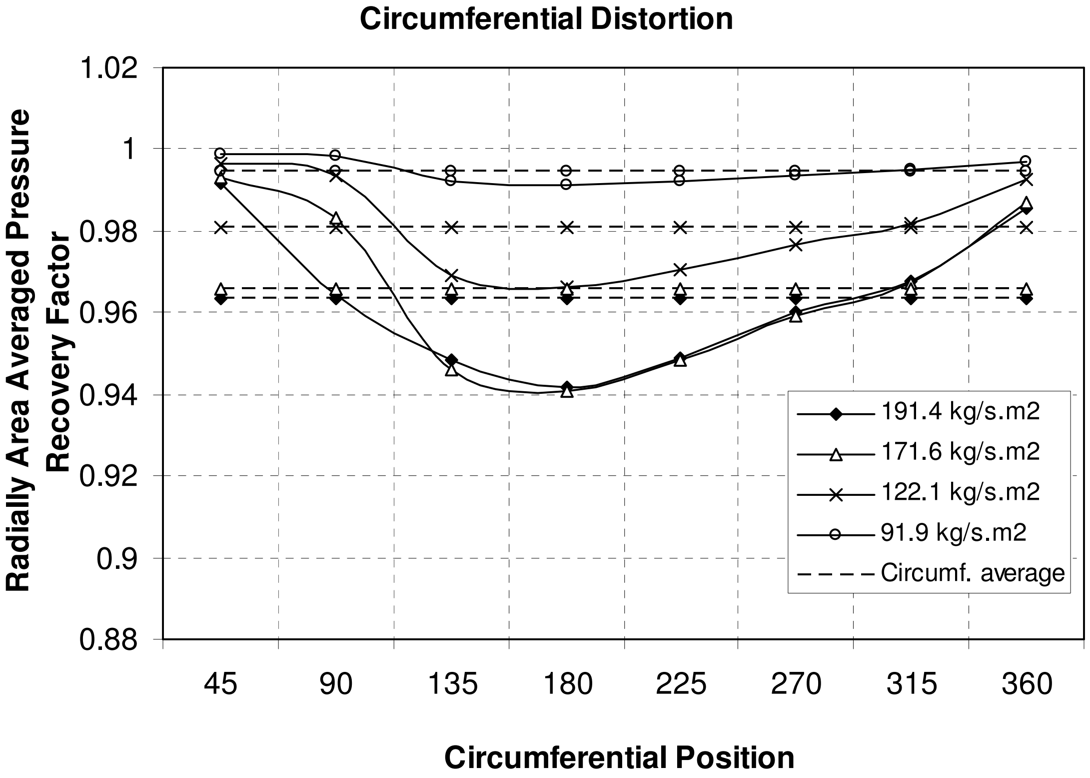

Figure 6-9: Circumferential distribution of PRF.

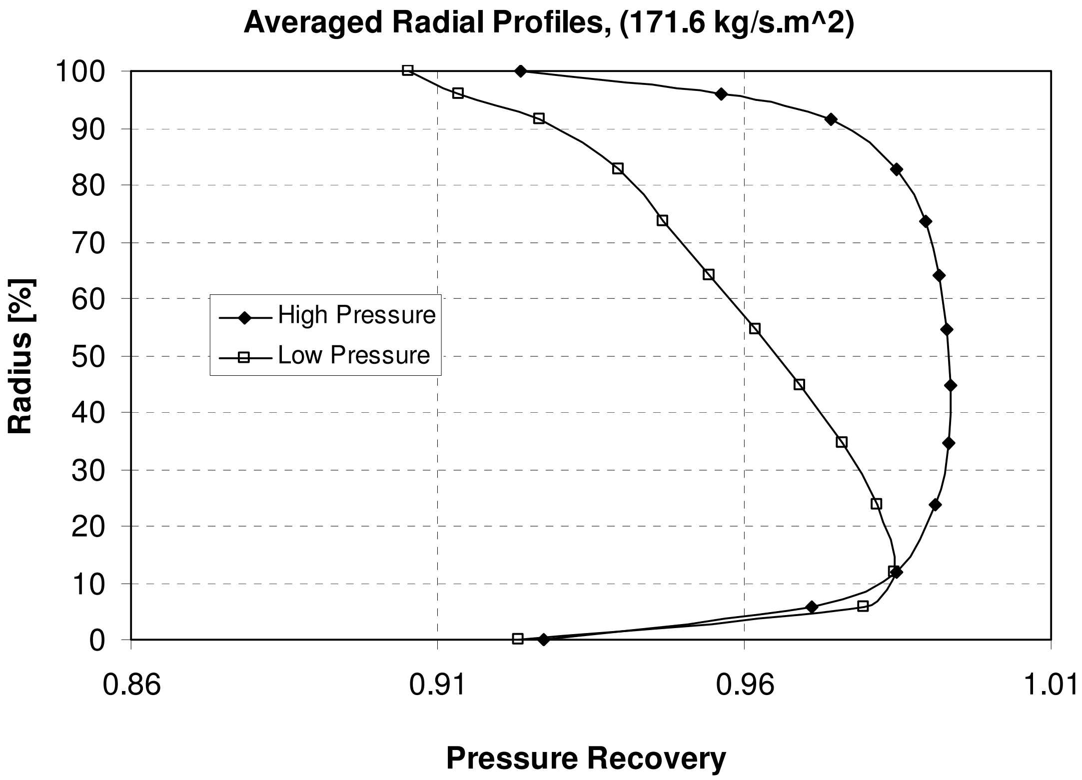

Figure 6-10: PaCo-SLC input PRF profiles at 171.6 kg/s.m^2 corrected mass flow.

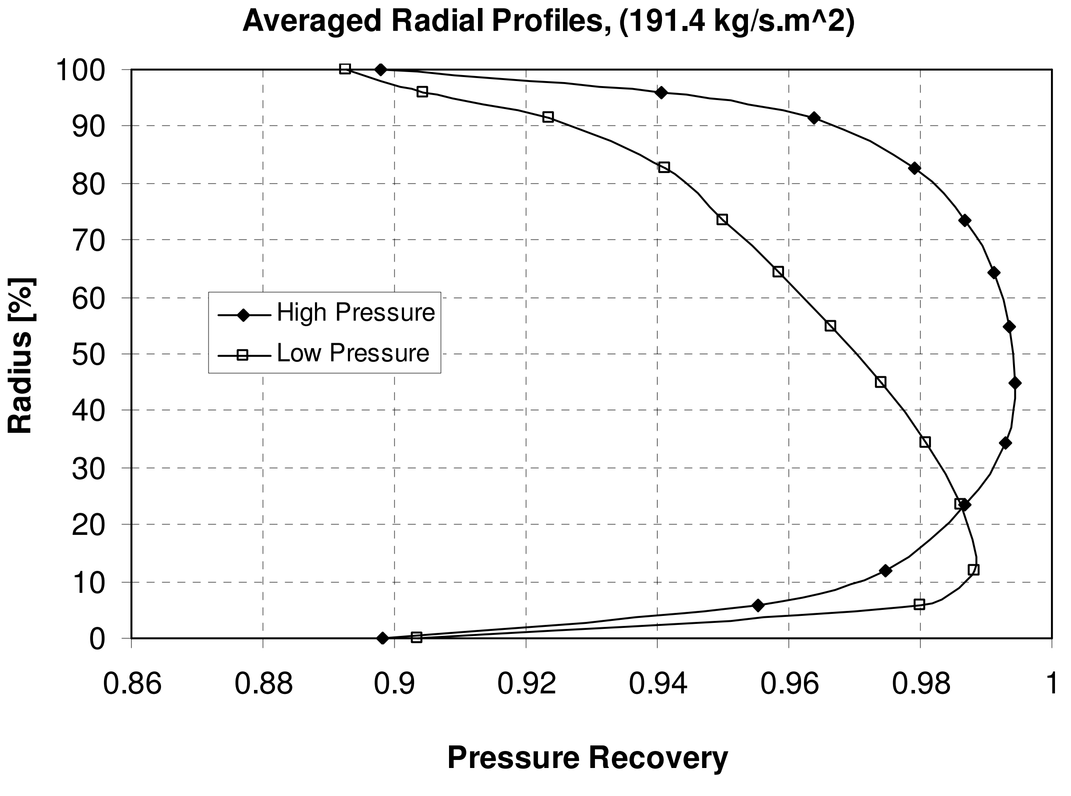

Figure 6-11: PaCo-SLC input PRF profiles at 191.4 kg/s.m^2 corrected mass flow.

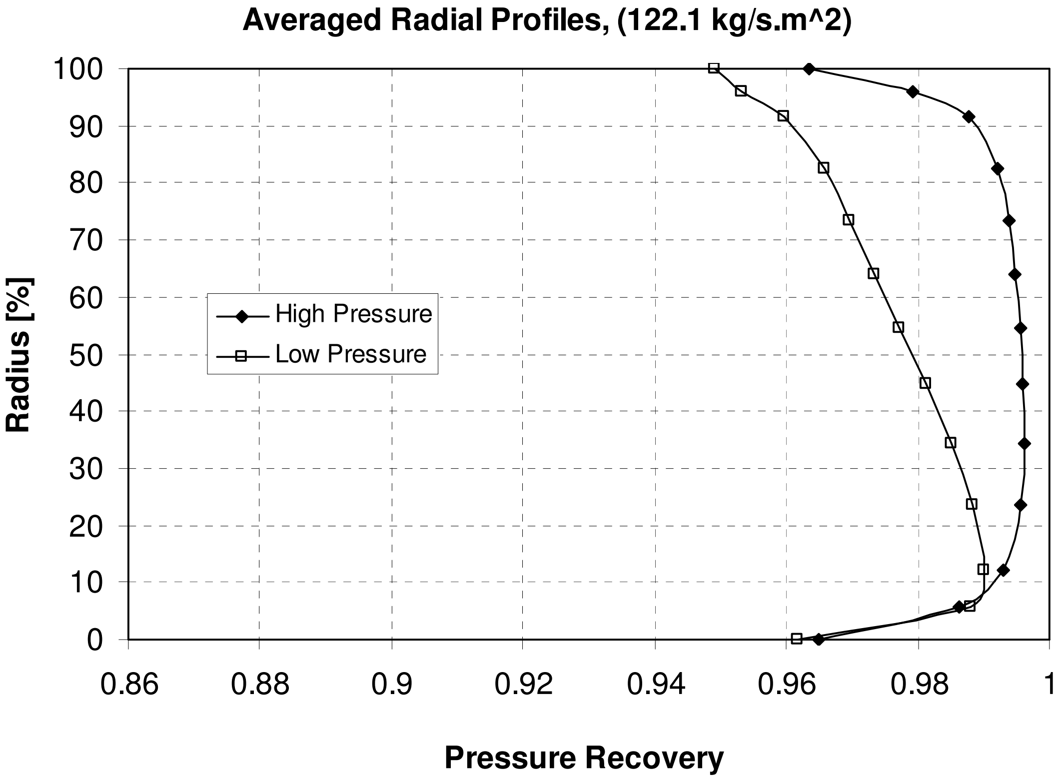

Figure 6-12: PaCo-SLC input PRF profiles at 122.1 kg/s.m^2 corrected mass flow.

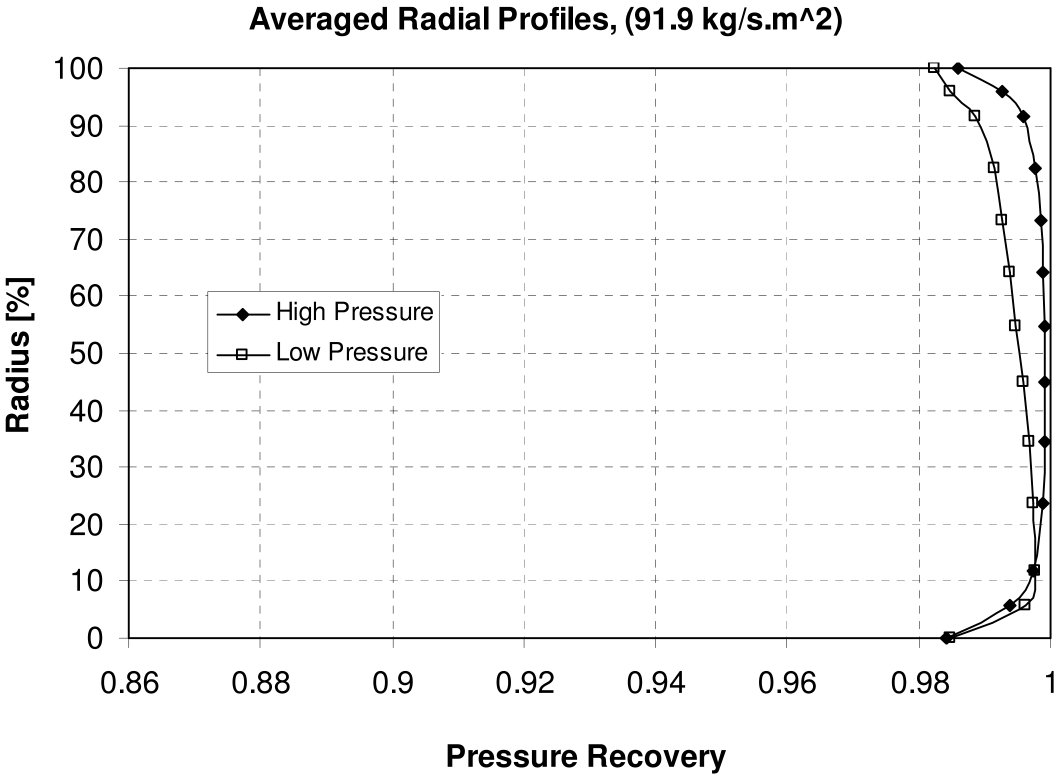

Figure 6-13: PaCo-SLC input PRF profiles at 91.9 kg/s.m^2 corrected mass flow.

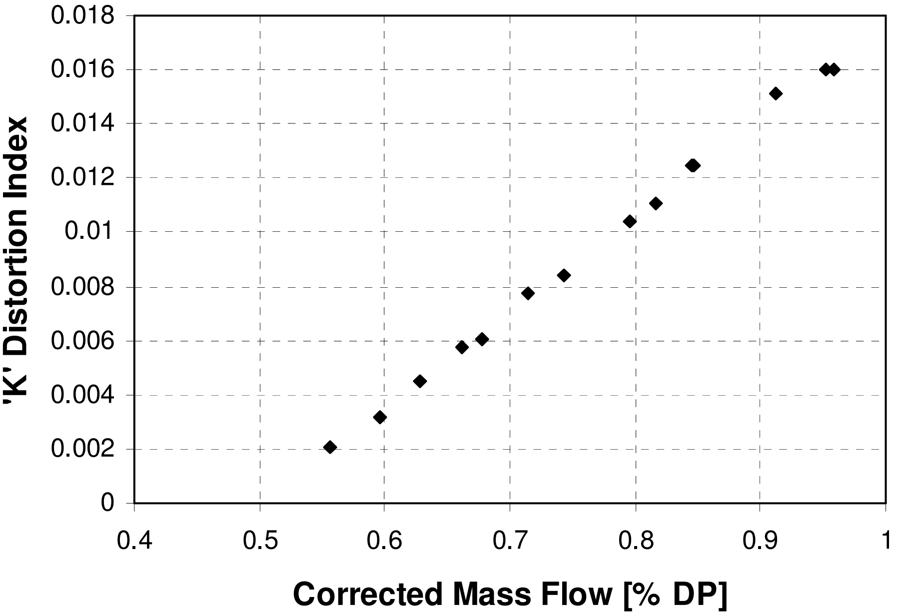

Figure 6-14: Variation of 'K' with corrected mass flow.

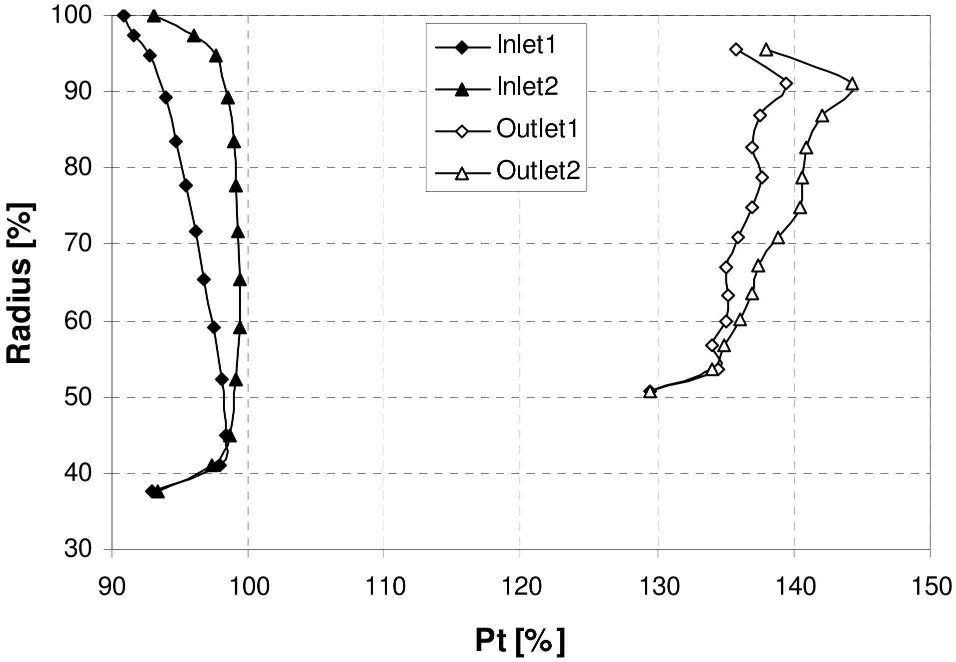

Figure 6-15: Fan inlet and outlet total pressure radial distributions.

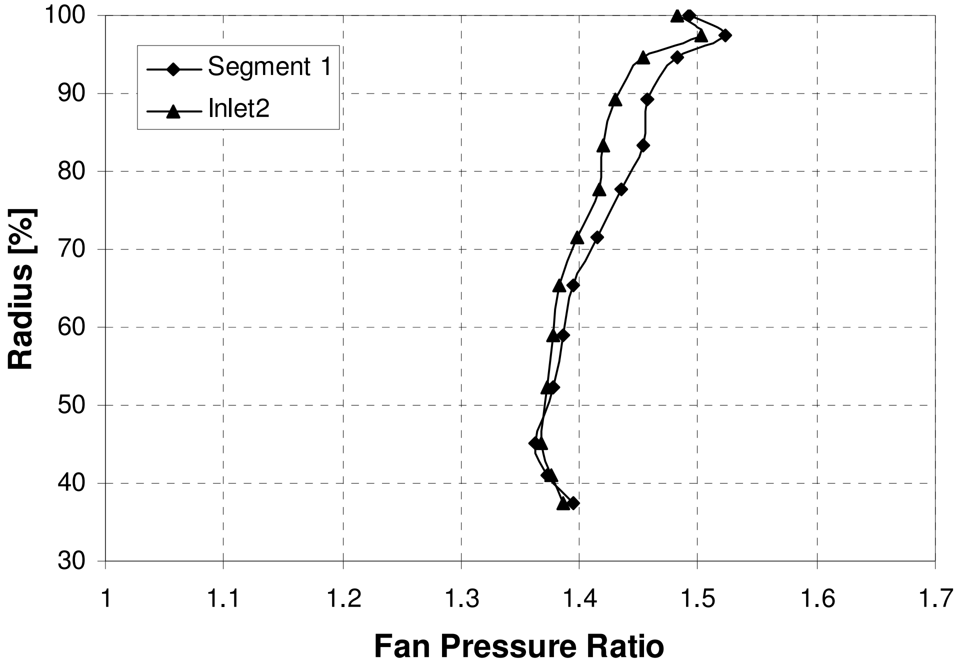

Figure 6-16: Fan pressure ratio radial distribution.

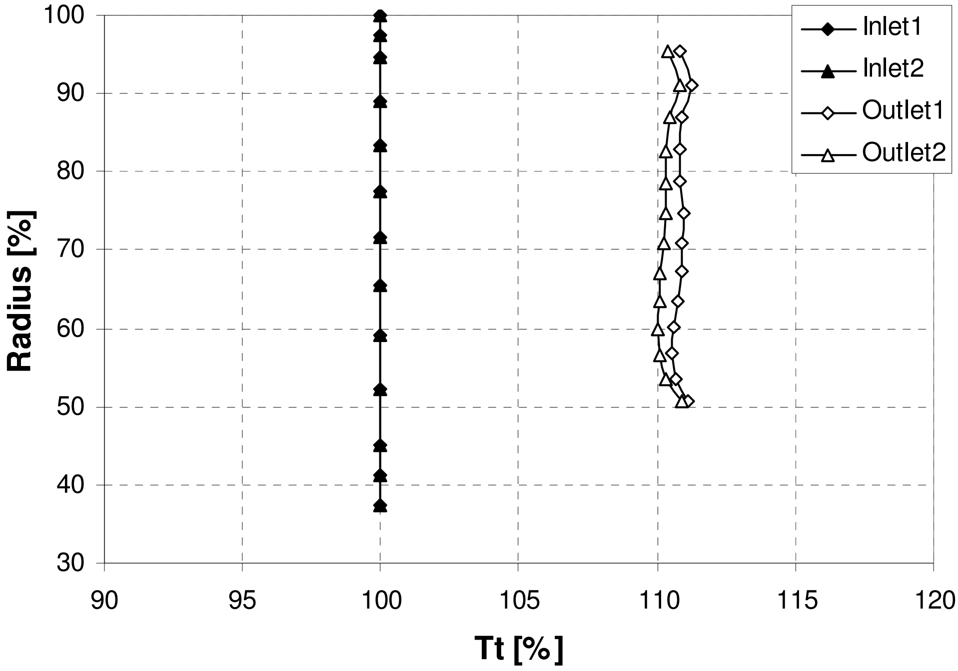

Figure 6-17: Fan inlet and outlet total temperature radial distributions.

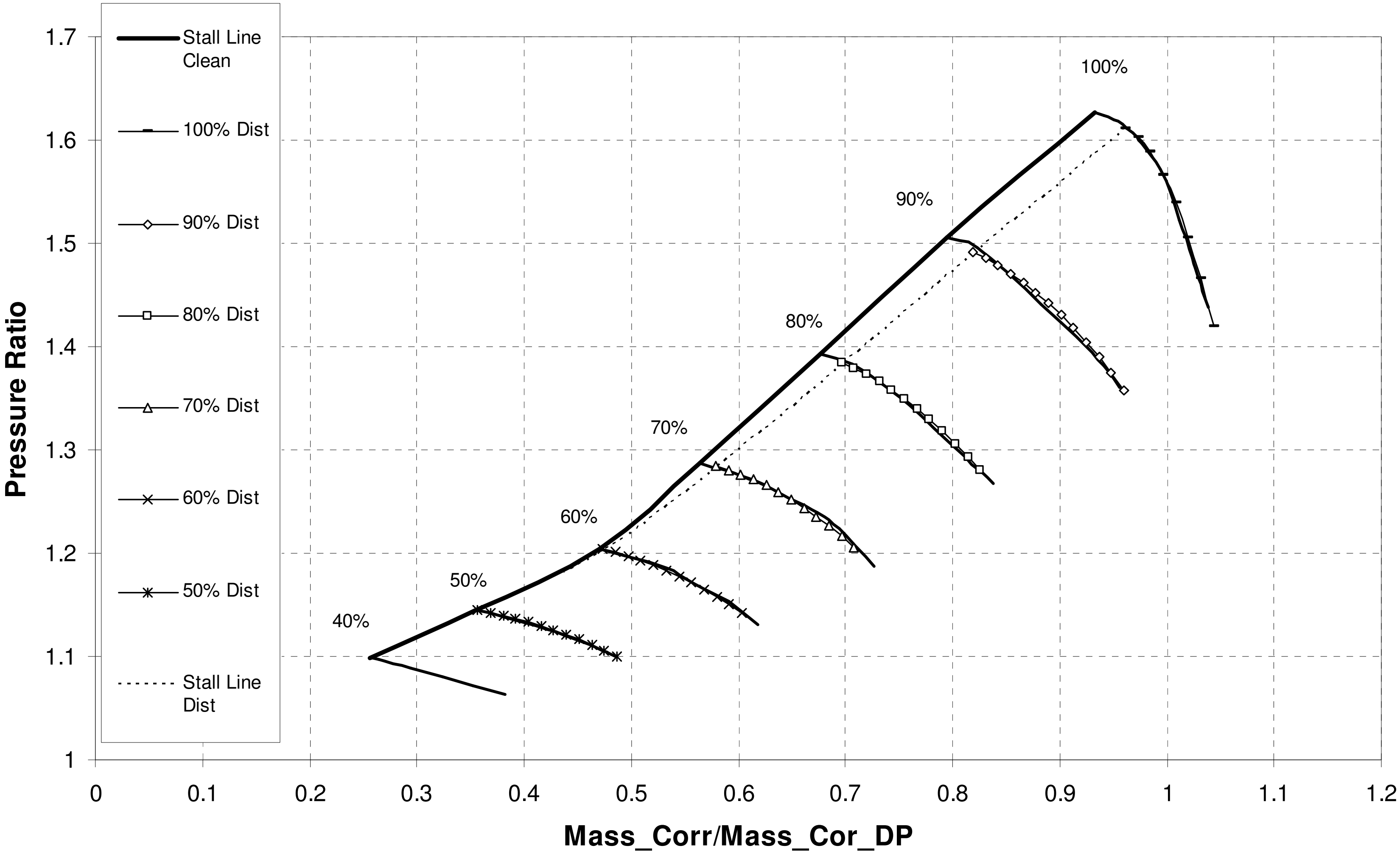

Figure 6-18: Fan pressure ratio Vs corrected mass flow; clean and distorted intake.

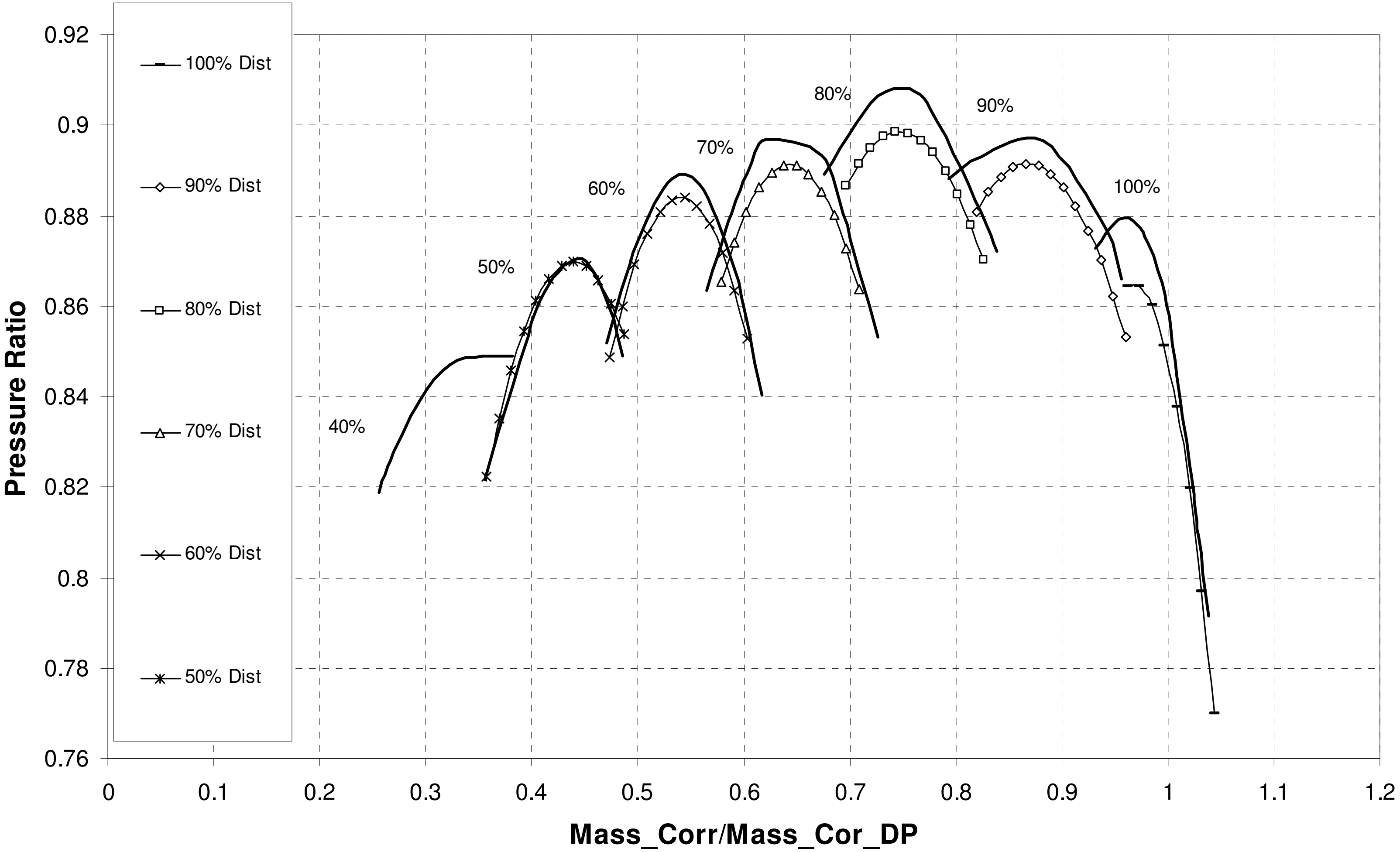

Figure 6-19: Fan efficiency Vs corrected mass flow; clean and distorted intake.

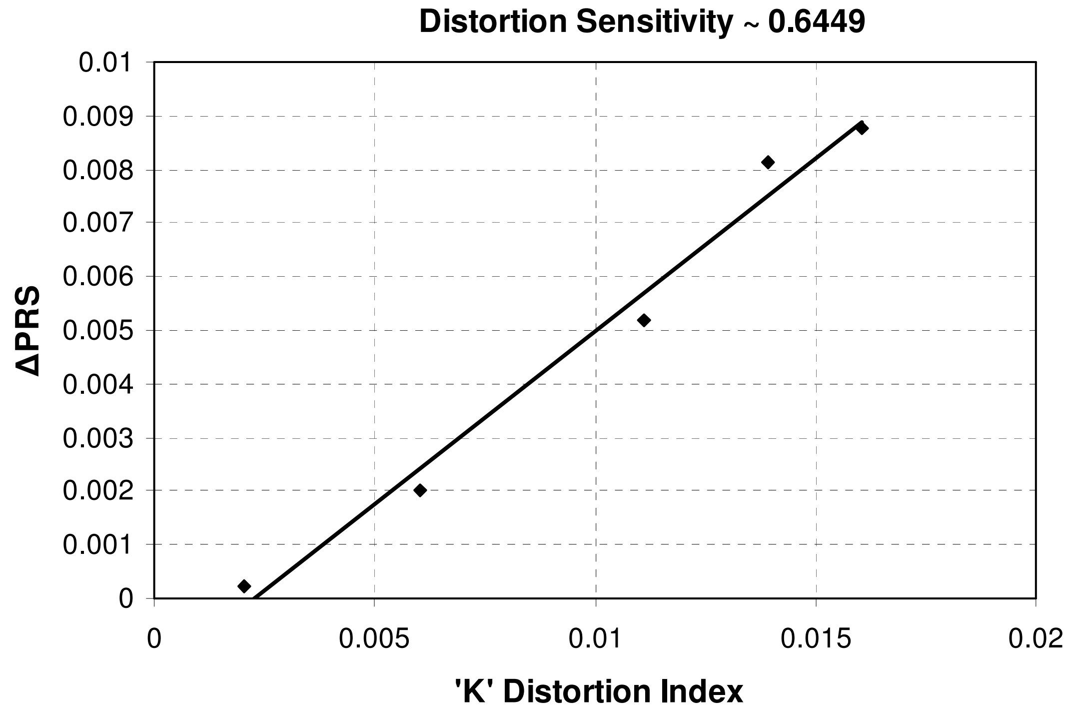

Figure 6-20: Pressure ratio distortion sensitivity of the fan.

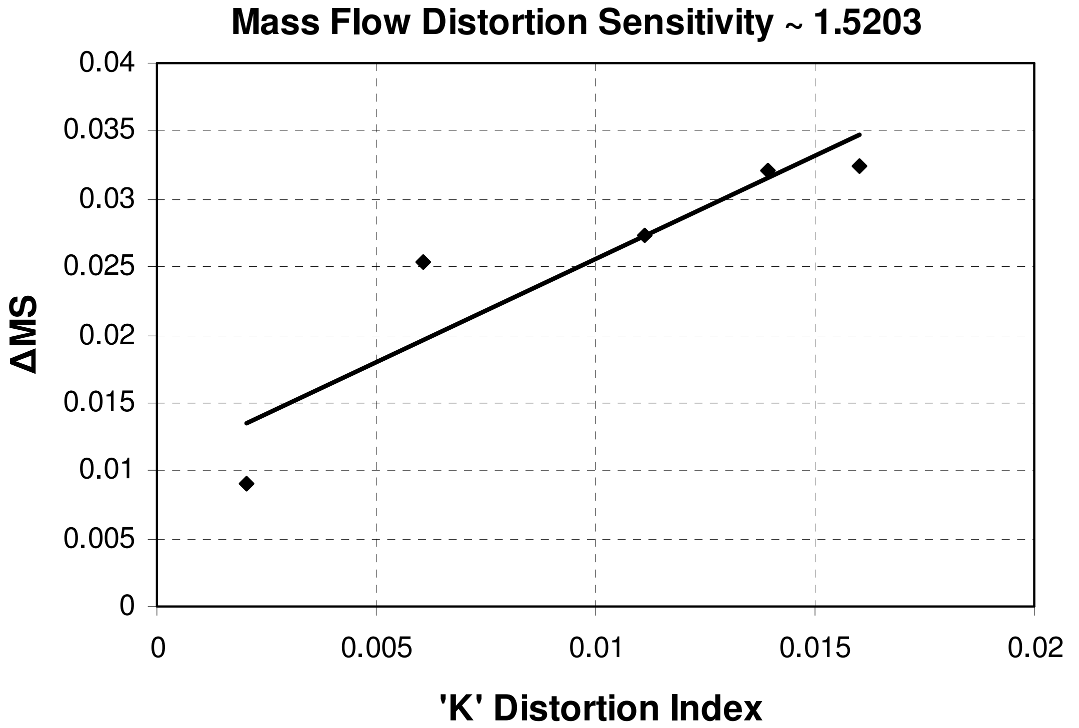

Figure 6-21: Mass flow distortion sensitivity of the fan.

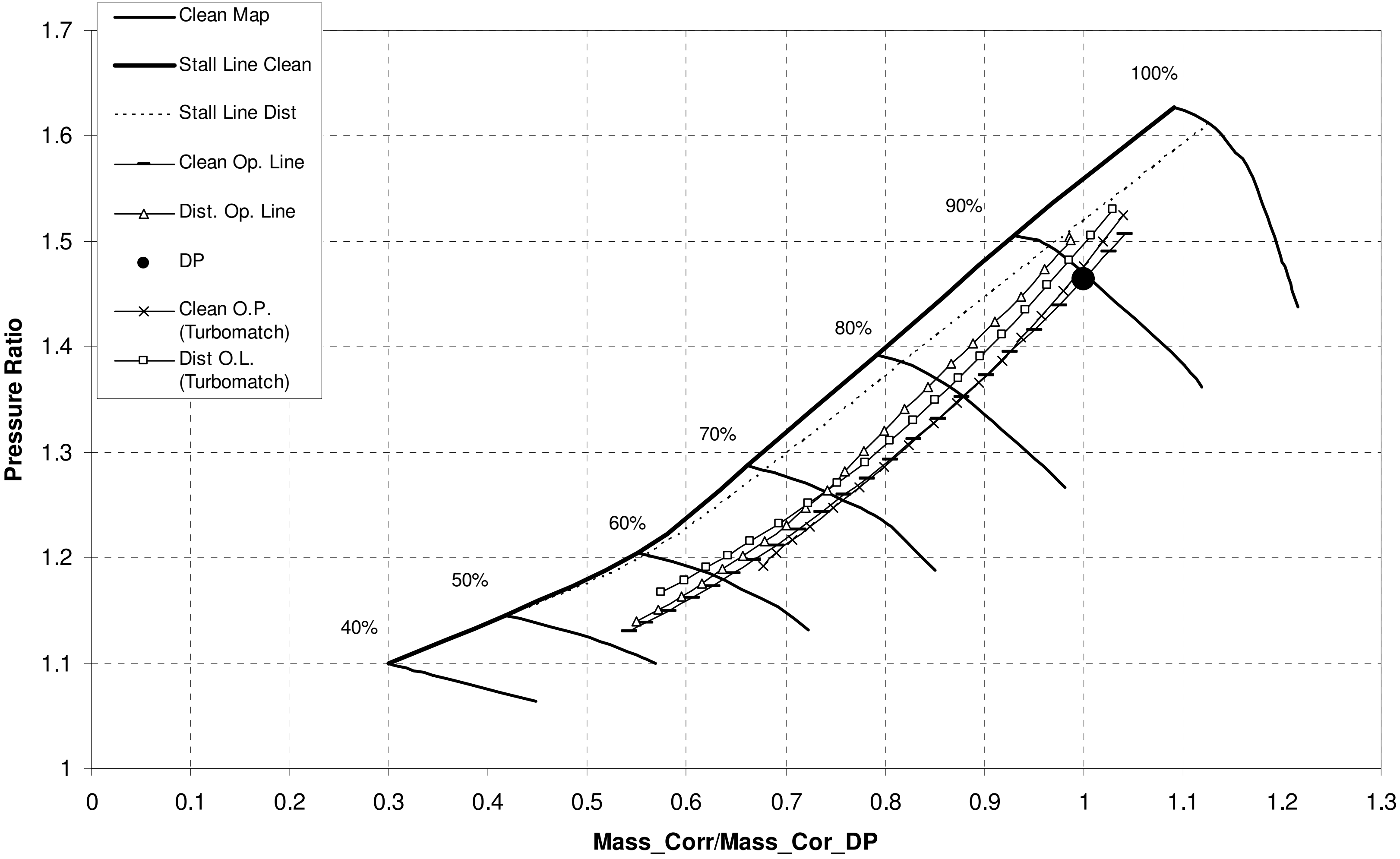

Figure 6-22: Fan operating lines.

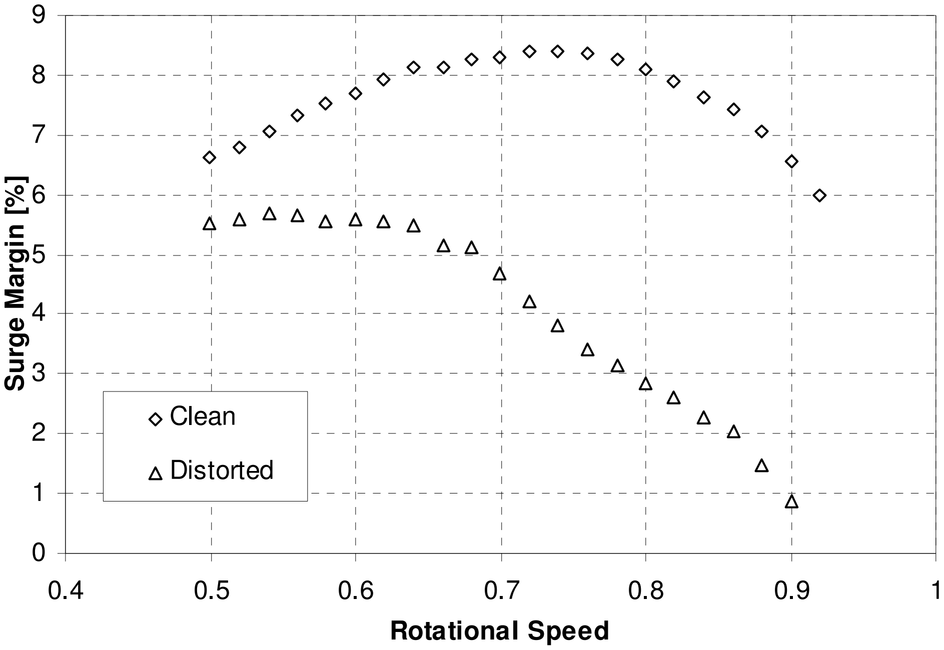

Figure 6-23: Fan surge margin loss.

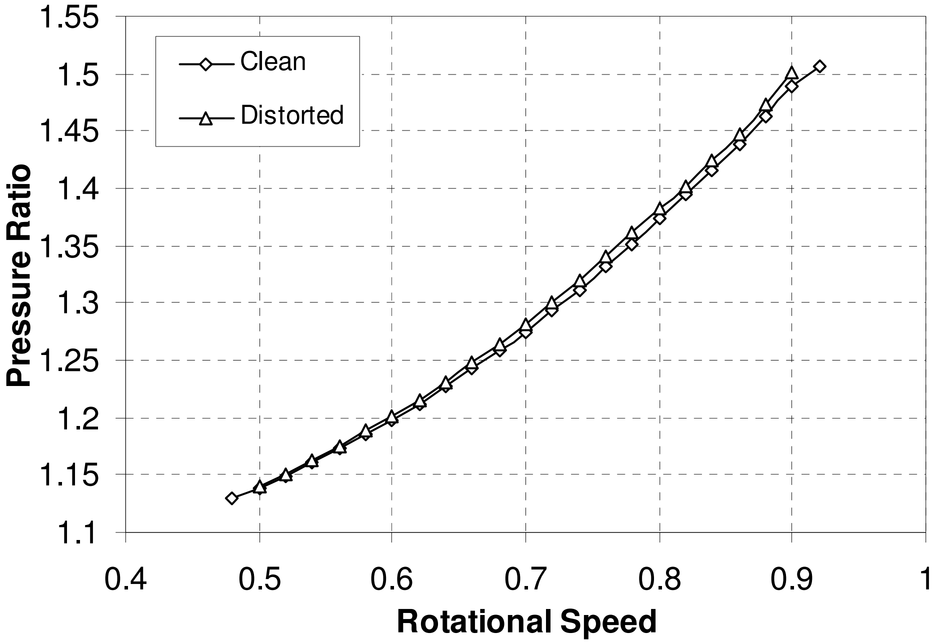

Figure 6-24: Pressure ratio Vs rotational speed for clean and distorted inlet.

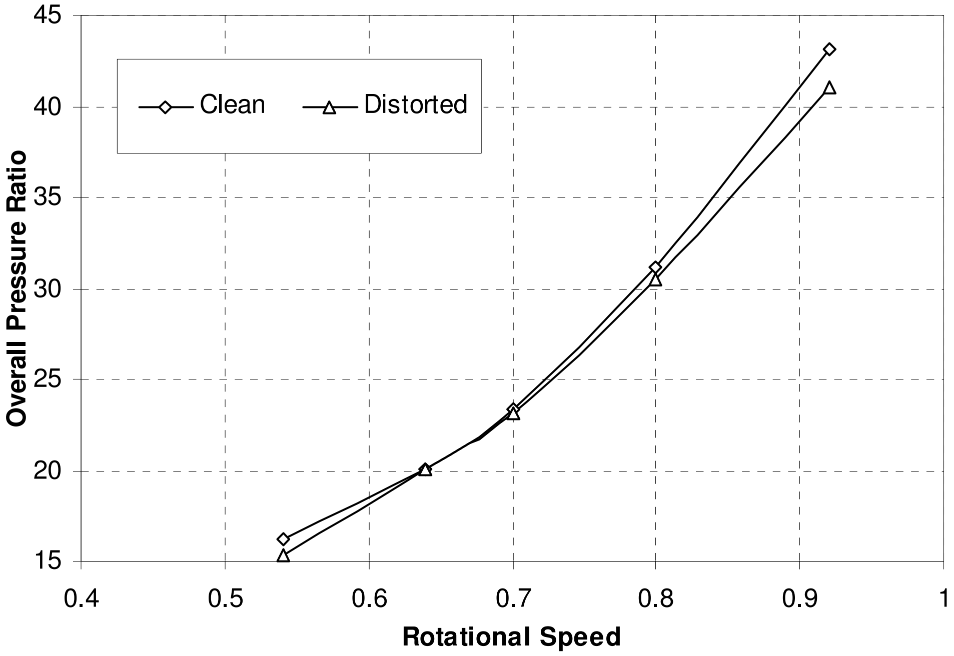

Figure 6-25: Overall pressure ratio Vs rotational speed for clean and distorted inlet.

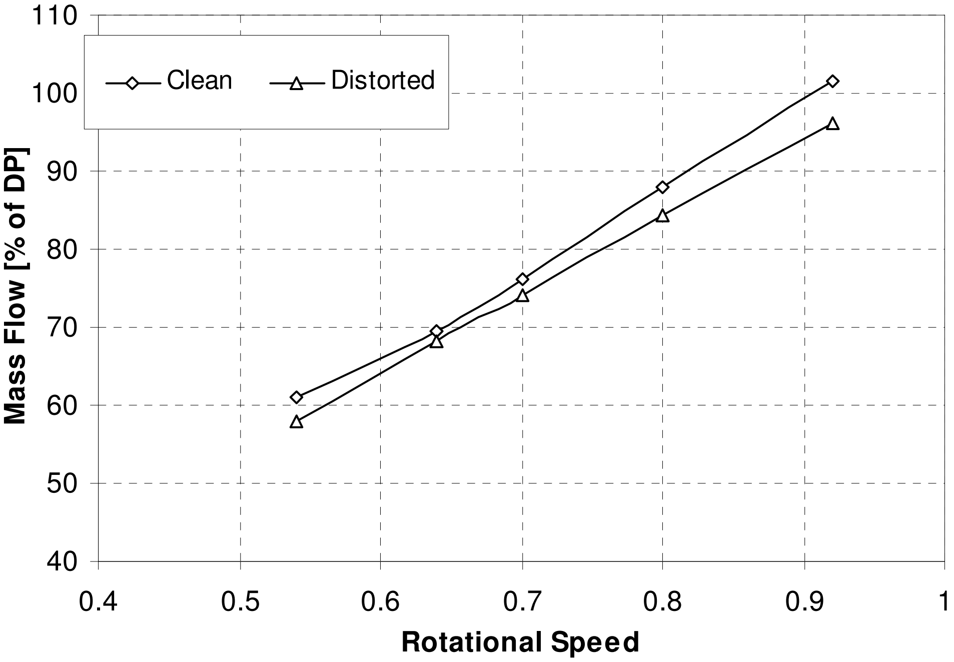

Figure 6-26: Engine mass flow Vs rotational speed for clean and distorted inlet.

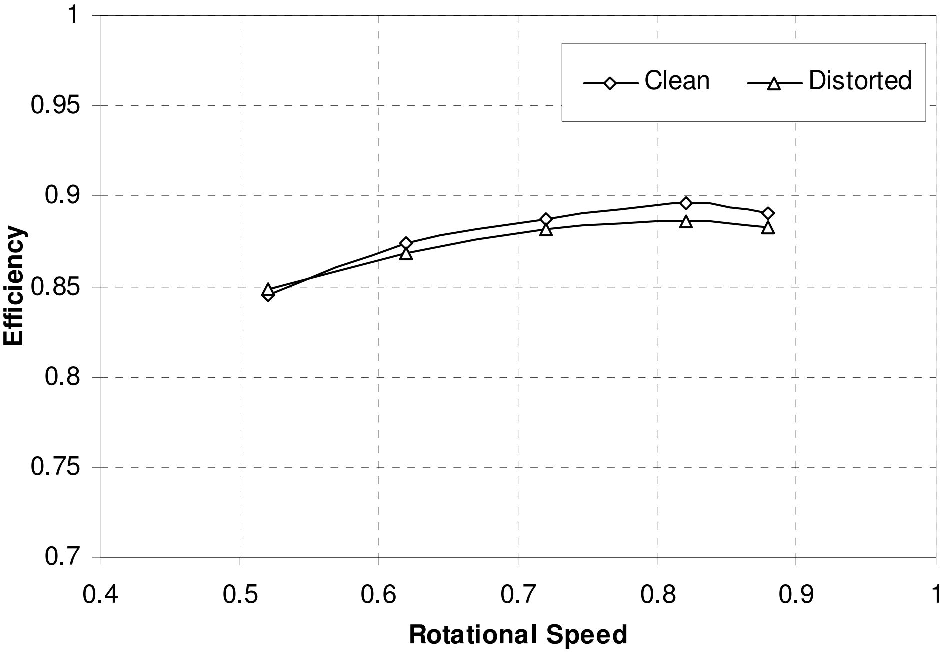

Figure 6-27: Fan efficiency Vs rotational speed for clean and distorted inlet.

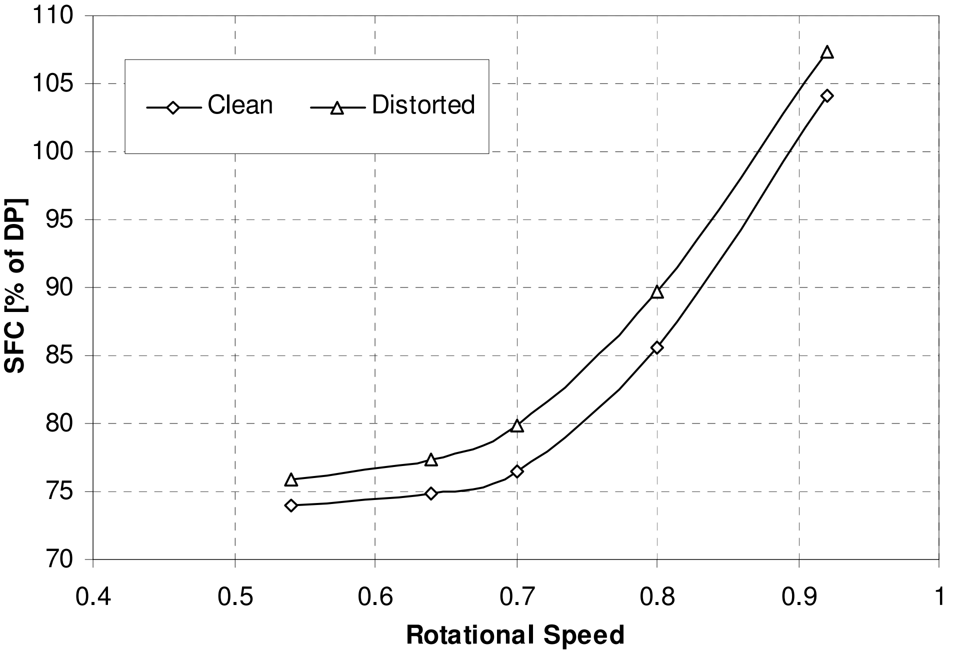

Figure 6-28: Specific fuel consumption Vs rotational speed for clean and distorted inlet.

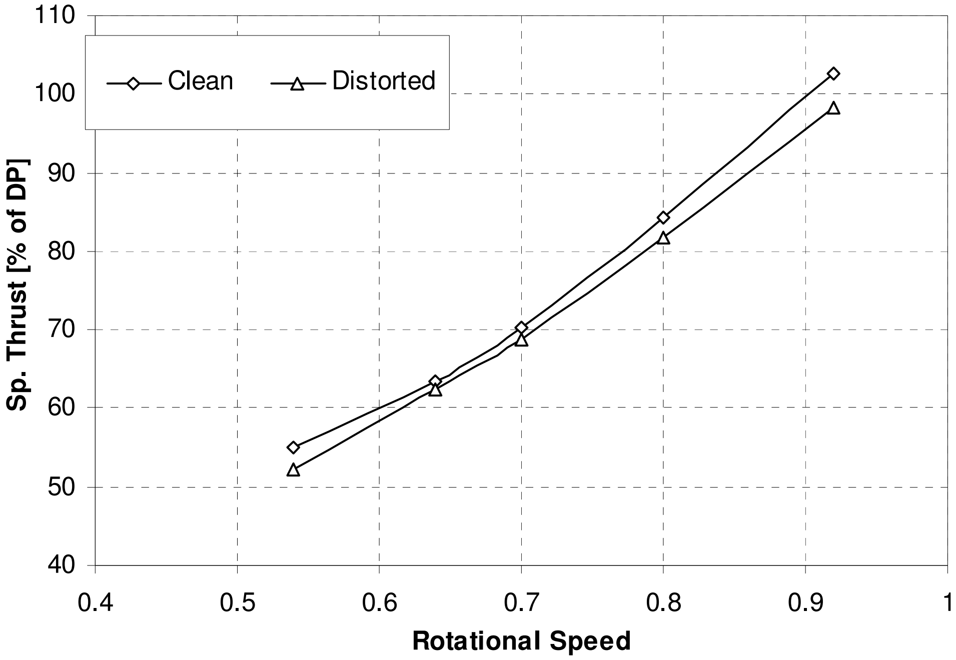

Figure 6-29: Specific thrust Vs rotational speed for clean and distorted inlet.

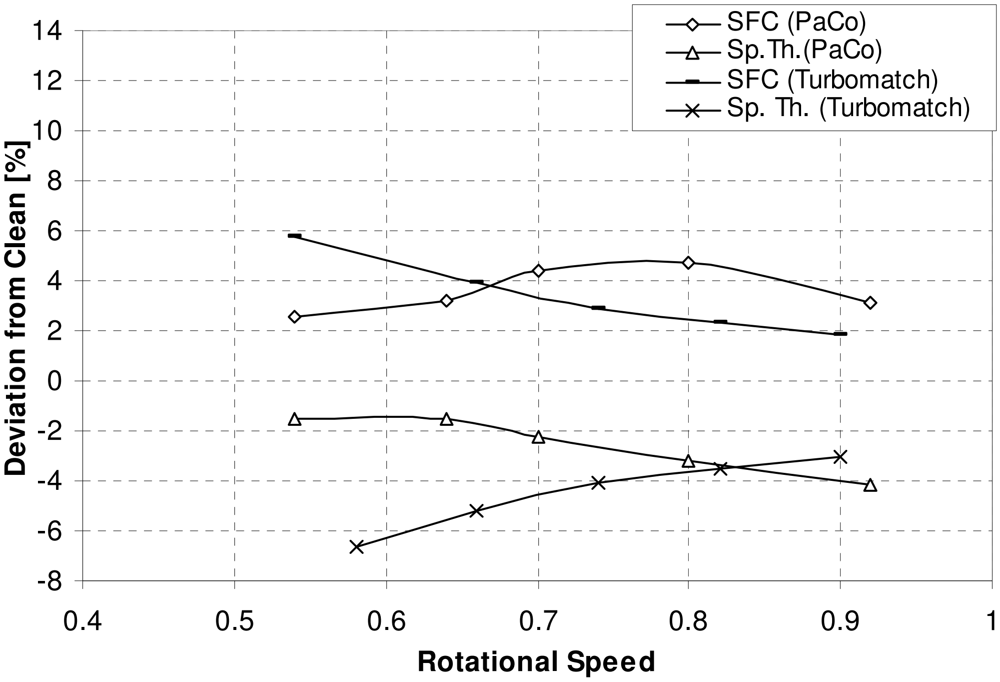

Figure 6-30: Loss of performance Vs rotational speed for PaCO and 0D fan models.

7 Conclusions and Future Work

This chapter summarises the main achievements of this thesis. Moreover, a discussion on the design and modelling methods that have been developed is followed by recommendations for future work and expansion of the models.

7.1 Achievements

The work presented in this thesis has contributed to the preliminary design and modelling of advanced propulsion systems, with principle target the reduction of engine noise emissions. The study asseses noise reduction of the two major sources, the fan and the jet. Jet noise is reduced by redesigning the propulsion cycle, while low fan noise is achieved by appropriate noise-shielding installation. In this manner, this thesis consists of three major parts; preliminary cycle design analysis –Chapter 4–, engine-airframe integration – Chapter 5– and analysis of the effect of installation on engine performance –Chapter 6.

In the first part of this study a preliminary design cycle method has been developed and applied on four advanced propulsion cycles. A novel airframe has been used as planform of the analysis and the results have shown significant jet noise reduction, accompanied by increased efficiency, leading to low fuel consumption and CO_2 emissions.

A completely different approach has been followed for reducing fan noise. In this scope, a novel installation has been suggested, where the engine has been half-embedded in the upper surface of the thick broad delta wing. The performance of the installation has been investigated with the aid of 3D computational fluid dynamics, showing the need for taking into account the effect of inlet distortion on engine performance.

In order to assess the effect of installation on engine performance a novel tool has been developed, for high fidelity modeling of the fan. This model has shown improved results, in comparison to 0D low fidelity engine analysis.

7.2 Conclusions

7.2.1 Advanced Propulsion Systems Preliminary Design

- A preliminary cycle design method has been proposed for designing advanced propulsion systems, with emphasis on noise reduction and fuel efficiency.
- The method incorporates the coupling of various modules in order to give an insight into the trade-offs between noise and total fuel consumption.
- All the tools are validated against measured data.
- Four advanced propulsion cycles are designed and compared to a baseline conventional turbofan. Ultra high BPR, recuperated, intercooled recuperated and constant volume combustion are the features of the novel cycles.
- The cycles are installed on a baseline airframe (type B767-300) and on a novel airframe; the Broad Delta wing.
- The superior performance of BD is obvious in the improved fuel efficiency and total noise emissions.
- A comparison between the cycles highlights the strong effect of high bypass ratio on engine performance, which dominates noise emissions.
- The most efficient cycle is the CVC, due to higher theoretical thermal efficiency that allows for high SFC and specific thrust, even with low COT and OPR. Moreover the ICR exhibits improved SFC and ST, as compared to the simple and the recuperated turbofans.
- The trade-off between noise and fuel is assessed by applying the method for fuel-optimised engines (which is the standard practice) and comparing them with the noise-optimised final cycles. For obtaining a benefit of ~30dBs in jet noise a penalty of ~10% increase of total mission fuel consumption has to be paid. Of

course, the final design may range between these two extreme conditions, according to the price of fuel and noise regulations that may become stricter in the future.

7.2.2 Half-embedded Installation

- Fan noise reduction is achieved by installing the engine in a way that noise is shielded by the wing. Such a configuration is the half-embedded on the upper part of a Broad Delta wing.
- The rationale of the design is to embed the engine as deep as possible, while designing the upper part of the intake –that exceeds the wing thickness–, according to conventional intake design method. Broad delta wing is ideal, due to high thickness near the root.
- The analysis of the intake with three dimensional CFD tools has shown a strong dependence of pressure recovery factor with boundary layer thickness at the aerodynamic inlet plane.
- A quasi 3D map of the intake has been created in order to be input to the engine performance model.

7.2.3 PaCo-SLC Fan Model

- Fan and engine performance sensitivity to inlet distortion has been assessed by a novel method that accounts for both circumferential and radial distortion.
- The fan is modelled using parallel compressor theory, in circumferential direction and streamline curvature in radial.
- A correction is applied in order to account for small extent of distortion, using θ_{crit} and ‘K’ distortion index.
- A correction for nozzle takes into account the effect of area variation from fan exit to nozzle exit.

- The model is validated against measured data. The same data have been used for identifying the critical angle of the fan. However, limited available experimental data allow for the use of the method as qualitative.
- The corrected PaCo-SLC model shows improved prediction of loss of surge limit, compared to classic parallel compressor model.
- The fan model has been impelemented in a Turbomatch model of a high bypass ratio generic turbofan, and off design engine performance has been predicted for inlet conditions that have been produced by CFD intake analysis.
- A linear relation has been found between loss in fan surge limit and distortion intensity.
- The effect of distortion on overall off-design engine performance has been studied, showing the linear loss of surge margin with distortion that may lead to surge at high throttle settings.
- The enhanced PaCo-SLC model has been compared to standard 0D compressor map, showing the enhanced capability of the model in predicting the effect of inlet distortion on off-design performance.

7.3 Discussion & Recommendations for Future Work

The present work is based on several assumptions. Some of the assumptions are imposed due to limited available time for this study, or due to strict project objectives. Therefore, recommendations for further work and expansion of the models are listed below.

7.3.1 Advanced Propulsion Systems Preliminary Design

- The results of the parametric analysis illustrate an additional characteristic of the method. The strong effect of engine weight model on fuel consumption is apparent in the results of the cycle design method. The engine model is the main chain between engine SFC and final fuel consumption, taking into account the effect of specific thrust, as it is assumed proportional to S.T. In this way, despite the fact that for a preliminary analysis, this model was found satisfying, a more accurate weight model should be implemented in future versions; a model that will calculate the weight of the components and not predict them. In this way, components such as gearbox, electric engines, multiple fans per engine, heat exchangers and constant volume combustors, instead of being added as correction factors, should be calculated analytically.

- A further improvement of the analysis is the complement of the parametric analysis with an optimisation technique, such as genetic algorithms or neural networks. In this way, the parametric analysis results can be evaluated against other optimisation methods. As a result, higher confidence on the result may be obtained.
- The parametric analysis can be enhanced with modules for prediction of NO_x, contrails and cirrus cloud. In this way, the method will be expanded for taking into account the radiative forcing of the engine.
- The design process of the intercooled recuperated turbofan assumed fixed position in the flowpath for the intercooling. This can be improved by adding a further optimisation loop, able to choose the most efficient position for intercooling, as the effect of intercooling varies with the first compressor delivery temperature.
- An optimisation loop regarding the position of the recuperator can further improve the recuperated turbofan. In a further detail, the position of the hot part of the heat exchanger can vary between the LP turbine and IP turbine exit, as in cases of low COT, or high OPR, where recuperation would improve if it was positioned between the two turbines, even though less work would be available for the LPT.
- This method is based on optimising for total mission fuel and noise. A further expansion can include the economical impact of fuel and noise consumption. This can be impelemented through an economic model that takes into account, fuel prices, purchase and operating costs and any environmental regulations. In this context, future scenarios, where more strict regulations are applied regarding noise, can show the viability of low-noise propulsion systems.

- The model of the constant volume combustion is based on an empirical correlation. An advanced model could be derived from detailed computational study of wave rotor combustors, that can be coupled with a turbomatch model for higher accuracy.
- One of the possible transmission solutions for the multiple fans per engine configuration is the geared fan. In this manner, a detailed gearbox calculation can further improve the design method, as the transmission losses have been kept constant through the whole process, in the current version. A future version, should be able to account for losses due to electrical transmission, as well.
- The 'Hermes' aircraft performance module can be expanded in multiple ways. A more detailed calculation of drag can be added, in order to take into account half embedded and deeply embedded configurations. Additionally, the calculation of fuselage can be expanded in a way that lift and drag from a non cylindrical configuration can be calculated. Moreover, the code can be expanded for calculating joint wing or tail-less configurations. In this way airframes, such as the blended wing body, or joint wing can be studied.
- In terms of mission profile, the 'Hermes' module can be improved in order to predict a more detailed mission. Taxi and contingency fuels should be calculated analytically from mission data, instead of using constant values.
- Modules for detailed take off and landing flight paths can be added in 'Hermes', predicting steep and slow take-off and approach conditions. In this way the calculation of effective perceived noise levels can be embedded in the model, in a way that actual nuisance levels are predicted.
- Additionally, Hermes can expand to calculate maneuvers during the critical segments of climb and approach.
- Distributed propulsion has not been taken into account in the present study. The beneficial effects of such configuration, though, need to be assessed in future version of 'Hermes'. This can be achieved by the implementation of empirical correlations, from open literature, on aircraft aerodynamics.
- Engine performance under distortion has not been taken into account in the preliminary cycle study. The reason was that the process included the

investigation of various cycles, making apparent the need for standard component maps and applicatoin of correction factors. However, the 'distorted' map was produced for a specific fan. Therefore, the implementation of this map in the design process was impractical. In a future version of 'Hermes', though, a Turbomatch model with PaCo-SLC can provide engine designs for safe operation under inlet distortion.

- In a further detail, 'Hermes' can define the engine operating condition that affects inlet distortion. In this way, the decoupled approach that has been followed in 'Hermes', where engine performance is included as a matrix, should be replaced by a coupled approach, where an iteration between 'Hermes' and Turbomatch is based on the relation between flight condition and distortion levels. In this context, the angle of attack should be taken into account, as well, affecting inlet distortion, thus engine and aircraft performance.
- Another expansion of 'Hermes' is the capability of using variable engine cycle. Initially, this can be achieved by adding more than one propulsion systems (i.e. variable BPR) and selecting the relevant flight segment for each one of them.
- Regarding the noise modules, it should be noted that noise has been evaluated in dBA and not in EPNDB, as a detailed calculation of the flight paths would be necessary. This can be taken into account, after an expansion of 'Hermes', as discussed in previous paragraph.
- Moreover, in the jet noise module, certain limitations apply, regarding velocity and area ratios between bypass and core streams. Therefore, the use of a more recent semi-empirical model is recommended.
- The noise shielding prediction model is one-dimensional and applicable only on fan noise, but it was the only available at the time. However, recent experimental research in the area can provide with novel shielding prediction methods for both fan and jet noise, that would be more suitable for aircraft applications.
- Another possible expansion of noise calculation, is the implementation of models for the noise generation from turbulence inside heat exchangers (recuperators, intercoolers).

- Even though, the constant volume combustion turbofan has exhibited competing fan and jet noise levels, noise from the novel combustor has not been taken into account. Noise prediction for such a device that incorporates complex pressure wave patterns could be computationally, or experimentally achieved. In a further step, the attenuation of combustion noise, through downstream components should be taken into account, as well.
- Even though, the assumption that fan and jet are the two major noise sources is considered valid, the investigation of other components, such as the low pressure turbine can be included in future versions of the method.

7.3.2 Half-embedded Installation

- Regarding the CFD modelling of the intake, in a future model, one single mesh should be used, from far upstream to far downstream. In this way, improved accuracy can be attained, due to the elimination of the error imposed by the use of constant boundary condition at the mid-chord of the wing.
- The performance of winglets should be assessed, for more realistic prediction of the flow field around the novel wing. This could be achieved under the condition that the prerequisite computational power is available.
- Additionally, the design of two intakes should be refined, by a detailed CFD analysis, in order to avoid any regions of high losses, or unacceptable acceleration of the flow, such as the region between the two nacelles.
- Intake performance needs to be assessed under extreme angles of attack, in order to provide data for a detailed coupling of ‘Hermes’ with Turbomatch, enhanced with Paco-SLC.
- In such configuration, variable leading edge should be subject of future research, in order to improve inlet distortion, thus engine performance.
- The effect of the position of the engines on the wing aerodynamic performance can be computationally assessed and optimised, taking into account noise shielding as well.

7.3.3 PaCo-SLC Fan Model

- Several modifications can be applied on the parallel compressor model, such as the implementation of the equation of momentum in order to take into account 1D flow phenomena.
- The mixing between the parallel segments is not taken into account in the present model. A future version can simulate this effect with the use of correction modules, especially for segments of small circumferential extent.
- The model of nozzle can be expanded by the application of mixing corrections, leading to higher accuracy.
- In the present study, the SLC model proved unable to converge using various geometrical inputs. As a result, a specific fan geometry has been used, for which the model has been validated in previous studies. This condition, though, has led to an inconsistency between intake CFD simulation and SLC model. In order to overcome this issue the intake map uses non dimensional data for the radius. Therefore, an error is involved, regarding the effect of diameter-based Reynolds number on boundary layer growth and distortion levels, due to the linear scaling of the distortion profiles. Such an error can be avoided by improvements in the robustness of the SLC code, in order to achieve convergence for various fan designs.
- Regarding the calibration of the parallel compressor, the critical angle has been identified, based on a single speedline, due to the lack of available data. A more detailed study should verify θ_{crit} for more speedlines of the fan map.
- An expansion of the PaCo-SLC model would be the direct coupling of the intake CFD module and the high fidelity fan representation (PaCo-SLC-Turbomatch). In such way, higher accuracy may be achieved, as direct exchange of 2D boundary condition data would take place. Additionally, such a model, should model with CFD the fan nozzle as well, producing an extra level of fidelity on engine modelling.

7.4 Further Discussion

This study has shown that significant engine noise reduction can be achieved, in the expense of fuel consumption. Under current conditions, where primary design target is fuel consumption, a novel low-noise propulsion system would not be a viable project, even though effort is spent in this direction by the industries. However, public awareness regarding the environmental impact of jet engines is growing and is expected to grow further in the future. As a result, more strict regulations are expected to be applied. Such condition, could initiate the debate on the viability of environmentally friendly propulsion systems.

Regarding engine modelling, it has been realised that the engineer has to apply several assumptions in order to result in competent designs under certain time limits and using specific available computational power. In the future, when adequate computational power will be available, direct modelling of the whole engine with the means of RANS CFD, or even DNS CFD should give the highest insight into flow phenomena inside gas turbines. However, through the years, it is evident that the evolution of computational tools has multiplied (instead of reducing) the need for engineers capable of making valid assumptions and providing with reliable results, under certain constraints.

8 References

Author's Publications

Journal

Mund, F.C., Doulgeris, G., Pilidis, P., Enhanced gas turbine performance simulation using a 2d representation of the low-pressure system for a high bypass turbofan. Journal of Engineering for Gas Turbines and Power, Vol.129, pp 761-768, July 2007.

Conference

Mund, F.C., Doulgeris, G., Pilidis, P., Enhanced gas turbine performance simulation using a 2d representation of the low-pressure system for a high bypass turbofan. Turboexpo 2006: Power for land, sea and air, May 8-11, 2006, Barcelona, Spain, 2006.

Fielding, J.P., Pilidis P., Mistry, S., Doulgeris, G., Development of silent airframe concepts and innovative cycle propulsion systems for reduction in aircraft noise, ICAS 2006: 25th International Congress of the Aeronautical Sciences, Hamburg, 2006.

Doulgeris, G., Mistry, S., Fielding, J.P., Pilidis P., Development of novel airframe and propulsion concepts for reduction in aircraft noise around airports, 07ATC-39, SAE 2007.

Rousselot, S., Truffi, D., Doulgeris, G., Mistry, S., Pachidis, V., Pilidis, P., Generation of a Quasi-3-D Map of a Half-Embedded Ultra High Bypass Ratio Turbofan Intake on the Wing of a Broad Delta Wing Airframe, Turboexpo 2008: Power for land, sea and air, June 9-13, 2008, Berlin, Germany, 2008.

Nettis, L., Javed, A., Doulgeris, G., Ogaji, S.O.T., Pilidis, P., De Bellis, F., Novel Cycles Deployment Study for a Silent Aircraft, Turboexpo 2008: Power for land, sea and air, June 9-13, 2008, Berlin, Germany, 2008.

Mistry, S., Doulgeris, G., Fielding, J.P., The Broad Delta Aircraft-Part 1; Viable Solution for Reducing Airframe Noise, Cranfield Multi-Strand Conference, 6-7 May 2008, UK, 2008.

Doulgeris G., Mistry, S., Pilidis, P., The Broad Delta Aircraft-Part 2; Silent Propulsion Systems Design Methodology, Cranfield Multi-Strand Conference, 6-7 May 2008, UK, 2008.

Poster

Doulgeris, G., Development of Low Noise Novel Propulsion Systems, Poster Conference/Contest, Cranfield University, 28 June 2007.

References in Alphabetical Order

A

Agarwal, A., Dowling, A.P., Low frequency acoustic shielding of engine noise by the silent aircraft airframe, AIAA 2005-2996, 2005.

Aleid, L., Variable Cycle Propulsion Systems for a Supersonic Civil Transport, PhD Thesis, Cranfield University, UK, 1997.

Antoine, E.A., Aircraft optimisation for minimal environmental impact, PhD Thesis, Stanford University, USA, 2004.

Arnulfo, L., Pilidis, P., Yin, J., Probert, D., Remote Lift-Fan Engines, IMechE, Vol 215, Part G, pp. 155-163, 2001.

B

Ballal, D.R., Progress in aero engine technology (1939-2003), 39th AIAA/ASME/SAE/ASEE Joint Propulsion Conference and Exhibit, 20-23 July 2003, Huntsville, Alabama.

Benveniste, D., Lei, V., Manneville, A., Optimisation of the propulsion system for a silent aircraft, [Online], URL: http://ocw.mit.edu/NR/rdonlyres/Aeronautics-and-Astronautics/16-888Spring-2004/078F4653-D089-41A2-AEF1-0A9A79BA606D/0/benven_lei_manv.pdf, Cited November 2005.

Berglund, B., Lindvall, T. Schwela, D. H. *Guidelines for community noise*, World Health Organisation, 1999.

Berton, J.J., Noise reduction potential of large over-the-wing mounted, advanced turbofan engines, NASA, TM-2000-210025, April 2000.

Bielak, G.W., Premo, J.W., Hersh, A.S., Advanced turbofan duct liner concepts, NASA, CR-1999-209002, February 1999.

Boggia, S., Rud, K., Intercooled Recuperated Gas Turbine Engine Concept, 41st AIAA/ASME/SAE/ASEE Joint Propulsion Conference&Exhibit, 10-13 July 2005, Tucson, Arizona, 2005.

Braithwaite, W., M., Graber, E., J., Mehalic, C., M., The Effect of Inlet Temperature and Pressure Distortion on Turbojet Performance, AIAA, 73-1316, 1973.

Brookfield, J.M., Turbofan Rotor/Stator Interaction Noise Reduction Through Trailing Edge Blowing, PhD Thesis, Massachusetts Institute of Technology, June 1998.

C
Callahan, G., M., Stenning, A., H., Attenuation of Inlet Flow Distortion Upstream of Axial Flow Compressors, AIAA 5th Propulsion Joint Specialist Conference, Colorado, June 1969.

Calogeras, J., E., Mehalic, C., M., Burstadt, P., L., Experimental Investigation of the Effect of Screen-Induced Total-Pressure Distortion on Turbojet Stall Margin, NASA-TM-X-2239, March 1971.

Centennial of flight, August 2007, [Online], URL:
http://www.centennialofflight.gov/essay/evolution_of_ technology/noise/tech25.htm,
Cited August 2007.

Chessel, C.I., Noise propagation along an impedance boundary, Journal of Acoustical Society of America, Vol.62, No.4, pp. 825-834, October 1977.

Crichton, D., de la Rosa Blanco, E., Law, T., Hileman, J., Design and Operation for Ultra Low Noise Take-Off, AIAA 2007-456, 2007.

Cumpsty, N.A., Compressor Aerodynamics, Longman Scientific & Technical, Longman Group UK ltd, 1989.

D
Dalton, W.N., Ultra high bypass ratio low noise engine study, Allison EDR 16083, NASA CR-2003-212523, 2003.

De la Rosa Blanco, E., Hall, C.A., Crichton, D., Challenges in the silent aircraft engine design, AIAA 2007-454, 2007.

Department for Transport, The future of air transport, UK Government, 2003.

Diedrich, A., Hileman, J., Tan, D., Willcox, K., Spakovszky, Z., Multidisciplinary design and optimisation of the silent aircraft, AIAA 2006-1323, 2006.

Dittmar, J.H., Elliot D.M., and Bock, L.A., Some Acoustic Results from the Pratt and Whitney Advanced Ducted Propulsor – Fan 1, NASA TM 1999-209049,NASA, 1999.

Doulgeris, G., Mistry, S., Fielding, J.P., Pilidis, P., Development of Novel Airframe and Propulsion Concepts for Reduction in Aircraft Noise Around Airports, SAE, 07ATC-39, 2007.

E
Elder, A., Prediction of the Effect of Distorted Inlet Flows on Fan and Compressor Stability, IMechE, C117/84, 1984.

Emerson, D.C., Magnetically Levitated Ducted Fan Being Developed as a Propulsor Option for Electric Flight, NASA Technical Report, 20050215595, 2005.

Engineering Sciences Data Unit, Combination of Levels in dB, ESDU, 66017, Issued March 1966.

Engineering Sciences Data Unit, Estimation of noise shielding by barriers, ESDU, 79011, Issued September 1979.

Engineering Sciences Data Unit, Prediction of noise generated by fans and compressors in turbojet and turbofan engines, ESDU, 98008, Issued April 1998.

Engineering Sciences Data Unit, Computer-based estimation procedure for coaxial jet noise- Including far-field subsonic jet mixing noise database for stationary, coplanar conical nozzles, ESDU, 01004, Issued May 2001.

Engineering Sciences Data Unit, An introduction to aircraft noise, ESDU, 02020, Issued December 2002.

F
Federal Aviation Administration / Airports & Traffic/Airport Noise, [Online],
URL: http://www.faa.gov/airports_airtraffic/airports/environmental/airport_noise/,
Sited August 2007

Federal Aviation Administration, General Electric Company; Model: CF6-80, Type Certificate Data Sheet E13NE, U.S. Department of Transportation, Revision 16, April 2000.

Fluent Manual, [Online], [URL]
http://www.cranfield.ac.uk/cww/ccdocs/documentation/fluent/fluent6.3/

Frick, C., W., Davis, W., F., Randall, L., M., Mossman, E., A., An Experimental Investigation of NACA Submerged-Duct Entrances, NACA ACR, 5120, Washington, October 1945.

G
Gambit User's Guide, [Online], [URL]:
http://www.cranfield.ac.uk/cww/ccdocs/documentation/fluent/fluent6.3/

Gerend, R.P., Roundhill, J.P., Correlation of gas turbine engine weights and dimensions, AIAA-70-669, 1970.

Gillian, R., Aircraft noise prediction program user's manual, NASA TM 84486, 1982.

Greener by Design, *Air travel – greener by design: The technology challenge*, 2001.

Greitzer, E., M., Griswold, H., R., Compressor-Diffuser Interaction with Circumferential Flow Distortion, Journal Mechanical Engineering Science, Vol. 18, No. 1, pp.25-38, 1976.

Greitzer, E., M., The Stability of Pumping Systems-The 1980 Freeman Scholar Lecture, Journal of Fluids Engineering, Vol. 103, pp.193-242, June 1981.

Greitzer, E., M., Moore, F., K., A Theory of Post-Stall Transients in Axial Compression Systems: Part I–Development of Equations, Journal of Engineering for Gas Turbines and Power, Vol. 108, pp.68-76, January 1986.

Greitzer, E., M., Moore, F., K., A Theory of Post-Stall Transients in Axial Compression Systems: Part II–Application, Journal of Engineering for Gas Turbines and Power, Vol. 108, pp.231-239, April 1986.

H

Halasz, C.W., Advanced Trailing Edge Blowing Concepts for Fan Noise Control: Experimental Validation, MSc Thesis, Virginia Polytechnic Institute, June 2005.

Hale, A., Davis, M., Sirbaugh, J., A Numerical Simulation Capability for Analysis of Aircraft Inlet-Engine Compatibility, Journal of Engineering for Gas Turbines, Vol. 128, Issue 3, pp.473-481, July 2006.

Hall, C.A., Crichton, D., Engine and Installation Configurations for a Silent Aircraft, ISABE-2005-1164, 2005.

Heidmann, M.F., Interim prediction method for fan and compressor source noise, NASA TM X-71763, 1979.

Harris, C.M., Handbook of noise control, McGraw-Hill, New York, 1957.

Higson, D. W., The Tip-Turbine Driven Propulsion Fan: Gas Generator Performance and Installation, MSc Thesis, Cranfield University, UK, 1999.

Howe, D., Aircraft conceptual design synthesis, PE Publishing, 2000, UK.

Hubbard, H.H., Aeroacoustics of Flight Vehicles: Theory and Practice; Volume 2: Noise Control, NASA Reference Publication 1259, Vol.2 WRDC, Technical Report 90-3052, August 1991.

Huete, J., Singh, R., A Novel Concept for the Next Generation Civil Supersonic Transport Propulsion System: The Retractable Fan, Journal of Aircraft Engineering and Aerospace Technology, Vol. 69, No 6, pp. 512-517, 1997.

I

ICAO, Environmental Unit, Aircraft Noise, [Online],
URL: http://ww.icao.int/icao/en/env/noise.htm, Sited August 2007.

J

Jaklitsch, R., Leto, A., Pratt, W., Schaefer, R., Tip-turbine lift package design, NASA Contractor Report, CR-72974, NASA, August 1971.

Jenkinson, L.R., Simpkin, P., Rhodes, D., Civil jet aircraft design, Arnold, London, 1999.

K

Kim, H.D., Saunders, J.D., Embedded Wing Propulsion Conceptual Study, NASA, TM-2003-212696, 2003.

King, J., The Tip Turbine Driven Propulsion Fan –Aerodynamic Considerations-, MSc Thesis, Cranfield University, UK, 1999.

Kryter, K.D., Scaling human reactions to the sound from aircraft, Journal of Acoustical Society of America, Vol.31, No.11, pp.1415-1429, 1959.

Kryter, K.D., Williams, C., Loudness and noisiness of sounds of different bandwidth, Journal of Acoustical Society of America, Vol.32, No.11, pp1523, 1960.

Ko, Y., The Multidisciplinary Design Optimization of a Distributed Propulsion Blended-Wing_Body Aircraft, PhD Thesis, Virginia Polytechnic Institute, 2003.

Kontos, K.B., Janardan, B.A., Gliebe, P.R., Improved NASA-ANOPP noise prediction computer code for advanced subsonic propulsion systems Volume 1: ANOPP evaluation and fan noise model improvement, NASA CR 195480, August 1996.

L

Laskaridis, P., Performance investigations and systems architectures for the more electric aircraft, PhD Thesis, School of Engineering, Cranfield University, 2005a.

Laskaridis, P., Pilidis, P., Kotsiopoulos, P., An integrated engine-aircraft performance platform for assessing new technologies in aeronautics, ISABE-2005-1165, 2005b.

Leifsson, L.T., Mason, W.H., Schetz, J.A., Haftka, R.T., Grossman, B., Multidisciplinary design optimisation of low airframe noise transport aircraft, AIAA-2006-0230, 2006.

Lieblien, S., Characteristics of Two-Dimensional Compressor Blade Cascades, NACA-RM-E57A28, Washington, March 1957.

Longley, J.P., Greitzer, E.M., Inlet Distortion Effects in Aircraft Propulsion System Integration, AGARD Lecture Series 183 on "Steady and Transient Performance Prediction of Gas Turbine Engines", June 1992.

Longley, J., P., Hynes, T., P., Stability of Flow Through Multistage Axial Compressors, Journal of Turbomachinery, Vol. 112, pp.126-132, January 1990.

Lowe, W.H., Sanger, R.W., Static performance of a 13.97-cm (5.5-inch) diameter model vtol lift fan, NASA Contractor Report, CR 2051, NASA, May 1972.

Lush, P.A., Measurements of subsonic jet noise and comparison with theory, Journal of Fluid Mechanics, Vol. 46, Part 3, pp.477-500, 1971.

M

Markopoulos, N., Neumeier, Y., Prasad, J., V., R., Zinn, B., T., An Extended Analytical Model for Compressor Rotating Stall and Surge, AIAA-99-2124, 1999.

Mazzawy, R., S., Multiple Segment Parallel Compressor Model for Circumferential Flow Distortion, Journal of Engineering for Power, pp.288-297, April 1977.

McDougall, N., M., Cumpsty, N., A., Hynes, T., P., Stall Inception in Axial Compressor, Journal of Turbomachinery, Vol. 112, pp.116-125, January 1990.

Milner, E., J., Wenzel, L., M., Performance of a J85-13 Compressor with Clean and Distorted Inlet Flow, NASA-TM-X-3304, December 1975.

Mistry, S., Development of Novel Airframes for Reduction in Aircraft Noise Around Airports, PhD Thesis, Cranfield University, UK, 2008.

Moore, F., K., A Theory of Rotating Stall of Multistage Axial Compressors, NASA-CR-3685, 1983.

Mossman, E.A., Randall, L.M., An Experimental Investigation of the Design Variables for NACA Submerged Duct Entrances, NACA, RM No.A7130, 1948.

Mund,F.C., Doulgeris, G., Pilidis, P., Enhanced Gas Turbine Performance Simulation Using a 2D Representation of the Low-Pressure System for a High Bypass Turbofan, Journal of Engineering for Gas Turbines and Power, Vol.129, pp 761-768, July 2007.

N

Najjar, Y., Al-Sharif, S.F., Thermodynamic optimisation of thrbofan cycle, Aircraft Engineering and Aerospace Technology: An International Journal, Vol.78, No.6, pp.467-480, 2006.

Nascimento, M.A.R., The Selective Bleed Variable Cycle Engine, PhD Thesis, Cranfield University, UK, 1992.

NEWAC, New Aero Engine Core Concepts, [Online], URL: http://www.newac.eu, Sited September 2007.

Noirot, S. M. R., Tip-Turbine Driven Propulsion Fan: Aerodynamic and Mechanical Considerations, MSc Thesis, Cranfield University, UK, 1999

P

Pachidis, V., The Turbomatch scheme; for aero/industrial gas turbine engine design point/off design performance calculation, Manual, Cranfield University, UK, October 1999.

Pachidis V., Gas turbine performance simulation, MSc Course notes, 'Thermal Power', Cranfield University, UK, 2005.

Pachidis, V., Gas Turbine Advanced Performance Simulation, PhD Thesis, Cranfield University, UK, 2006.

Pachidis, V., Pilidis, P., Talhouarn, F., Kalfas, A., Templalexis, I., A Fully Integrated Approach to Component Zooming, Journal of Engineering for Gas Turbines and Power, Vol.128, July 2006.

Pachidis, V., Pilidis, P., Templalexis, I., Korakianitis, T., Kotsiopoulos, P., Prediction of Engine Performance Under Compressor Inlet Flow Distortion Using Streamline Curvature, Journal of Engineering for Gas Turbine and Power, Vol. 129, pp.97-103, January 2007.

Palmer, J. R., The Turbomatch scheme; for aero/industrial gas turbine engine design point/off design performance calculation, Manual, Cranfield University, UK, 1993.

Papamoschou D., A new method for jet noise suppression in turbofan engines. 41st Aerospace Sciences Meeting and Exhibit, 6-9 January 2003, Reno, Nevada, AIAA 2003-1059,2003.

Parente, C. A., Arcas, N., Walker, B.E., Hersh, A.S., and Rice, E.J., Hybrid Active/Passive Jet Engine Noise Suppression System, NASA CR 1999-208875, NASA, 1999.

Plas, A.P., Madani, V., Crichton, D., Greitzer, E.M., Hynes, T.P., Hall, C.A., Performance of a Boundary Layer Ingestion (BLI) Propulsion System, AIAA-2007-450, 2007.

Pearson, H., McKenzie, A. B., Wakes in Axial Compressors, Journal of the Royal Aeronautical Society, July 1959.

Pierce, A.D., Diffraction of sound around corners and over wide barriers, Journal of Acoustical Society of America, Vol. 55, No.5, pp.941-955, May 1974.

Plourde, G., A., Stenning, A., H., Lehigh, U., Bethlehem, P., Attenuation of Circumferential Inlet Distortion in Multistage Axial Compressors, Journal of Aircraft, Vol. 5, pp.236-242, 1968.

R

Raman, G., McLaughlin, D.K., Highlights of Aeroacoustics Research in the U.S. – 1998, AIAA Paper 99-1915, 1999.

Reid, C., The Response of Axial Flow Compressor to Intake Flow Distortion, ASME 69-GT-29, 1969.

Rey, N., M., Tillman, G., Miller, M., Wynosky, T., Larking, M., Flamm, J., Bangert, L., Shape Memory Alloy Actuation for a Variable Area Fan Nozzle, Proceeding of SPIE, Vol. 4332, pp.371-382, Smart Structures and Materials, 2001.

Rodriguez, D., A 3D Multidisciplinary Design Method For Boundary Layer Ingesting Inlets, AIAA-2000-0424, 2000.

Rolls Royce,[Online], URL: http://www.rolls-royce.com/northamerica/history, Sited August 2007.

Rolls, S.L., Gerdes, R.M., Flight Evaluation of Tip-Turbine-Driven Fans for Lateral Control in a Hovering VTOL Aircraft, NASA Technical Note, TN D-5491, NASA, October 1969.

Rousselot, S., Etude Numerique des Deformations du Profil de Pression en Entrée de la Soufflante pour un Projet d'Avion Silencieux, These de Master SMA, Universite de Nantes, France, 2007.

S

Saiyed N., Mikkelsen K., Bridges J., Acoustics and thrust of separate flow exhaust nozzles with mixing devices for high-bypass-ratio engines. 6th AIAA/CEAS Aeroacoustics Conference, Lahaina, Hawaii, AIAA 2000-1961,2000.

Sanger, N., L., Performance of a 1.57-Pressure-Ratio Transonic Fan Stage With a Screen-Induced 90^o Circumferential Inlet Flow Distortion, NASA-TN-D-8163, February 1976.

Saravanamuttoo, H. I. H., Rogers, G. F. C., Cohen, H., Gas Turbine Theory, Pearson Education Limited 1951, 5th Edition 2001Smith, M.J.T., Aircraft Noise, Cmbridge University Press, 1989.

Schmidt, J., F., Ruggeri, R., S., Performance With and Without Inlet Radial Distortion of a Transonic Fan Stage Designed for Reduced Loading in the Tip Region, NASA-TP-1294, August 1978.

Seddon, J., Goldsmith, E. L., Intake Aerodynamics, Collins, London, 1985.

Smith, M. J. T., Aircraft Noise, Cambridge Aerospace Series, Cambridge University Press, New York, 1989.

Smith, C.F., Snyder, P.H., Emmerson, C.W., Nalim, M.R., Impact of the constant volume combustor on a supersonic turbofan engine, AIAA-2002-3916, 2002.

Snyder, P.H., Nalim, M.R., Alparslan, B., Gas dynamic cycle of the CVC, A novel detonation cycle, AIAA-2002-4069,2002.

Stanhope, F. W., The Performance of NACA 1-Series Intakes, Powerplant Research Report IAR 85002, Rolls Royce, UK, 1968.

Stenning, A., H., Inlet Distortion Effects in Axial Compressors, Journal of Fluids Engineering, Vol. 102, pp.7-13, March 1980 (a).

Stenning, A., H., Rotating Stall and Surge, Journal of Fluids Engineering, Vol. 102, pp.14-20, March 1980 (b).

Society of Automotive Engineers, Gas turbine coaxial exhaust flow noise prediction, SAE, Report AIR 1905, December 1985.

Society of Automotive Engineers, Aerospace Engineering Online / Top15 Technology Innovations for 1998 / 10.Pratt&Whitney's next leap in engine technology, [Online], URL: http://www.sae.org.aeromag/techinnovations , Sited September 2007.

Spearman, M.L., Some aviation growth events, AIAA 2002-0172, 2002.

Sutliff, D.L., Tweedt, D.L., Fite, E.B., Envia, E., Low-Speed Fan Noise Reduction with Trailing Edge Blowing, NASA Technical Memorandum, TM-2002-211559, 2002.

T

Templalexis, I., Gas Turbine Performance With Distorted Inlet Flow, PhD Thesis, Cranfield University, UK, 2006.

Templalexis I., Pilidis, P., Pachidis, V., Kotsiopoulos, P., Quasi-Three-Dimensional Compressor Performance Simulation Using Streamline Curvature and Multi-Parallel Compressor Theory, ASME, Proceeding of GT2006, GT2006-90812, 2006.

Truffi, D., Jet Engine Components Interaction for a Silent Aircraft, Final Thesis, Cranfield University, Universita Degli Studi Di Roma 'La Sapienza', 2007.

U

Urasek, D., C., Gorrell, W., T., Cunnan, W., S., Performance of Two-Stage Fan Having Low-Aspect-Ratio, First-Stage Rotor Blading, NASA-TP-1493, Technical Report 78-49, 1979.

V

Viswanathan K., An elegant concept for reduction of jet noise from turbofan engines, 10th AIAA/CEAS Aeroacoustics Conference, AIAA 2004-2975, 2004.

VITAL Project, EnVIronmentTALly Friendly Aero Engines, [Online], URL: http://www.project-vital.org, Sited September 2007.

W

Walsh, P. P., Fletcher, P., ‘Gas Turbine Performance’, Blackwell Publishing, 2nd Edition 2004.

Wenzel, L.M., Blaha, R., J., Analysis of Dynamic Inlet Distortion Applied to a Parallel Compressor Model, NASA-TM-X-3522, 1977.

Whellens, M.W., Singh, R., Pilidis, P., Taguchi, H., Genetic Algorithm Based Opitmisation of Intercooled Recuperated Turbofan Design, AIAA 2003-1210, 2003.

Williams, D., Propulsion Systems Performance & Integration, Lecture Notes, Thermal Power MSc, Cranfield University, 2005.

Won, H.T., Waters, M., Constant volume combustor implementation on a 50 passenger commercial regional transport mission simulation, AIAA-2003-4413, 2003

Woodward, R. P., Hughes, C. E., Noise Benefits of Increased Fan Bypass Nozzle Area, NASA, TM-2004-213396, 2004.

Woodward, R.P, Fite, E.B., Podboy, G.G., Noise Benefits fo Rotor Trailing Edge blowing for a Model Turbofan, NASA Technical Memorandum, TM-2007-214666, 2007.

Y

Yaros, S.F., et al., Synergistic Airframe-Propulsion Interactions and Integrations; A White Paper Prepared by the 1996-1997 Langley Aeronautics Technical Committee, NASA/TM-1998-207644, March 1998.

Yin, J., Hales, R., Pilidis, P., Curnock, B., 2-Shaft High-Bypass Ratio Turbofan Performance Calculation Using a New 2-D Fan Model, 37th AIAA/ASME/SAE/ASEE Joint Propulsion Conference, Salt Lake City, Utah, July 2001.

Yin, J., Pilidis, P., Influence of Inlet Profile on High-BPR Turbofan Performance Using a Radial Profile Map, ICAS 2002 Congress, 2002.

9 Appendix

9.1 Engine Weight Model

In the following section, the coefficients of the engine prediction method and their mathematical representation are discussed.

WT/Wo_{ref}

It is the relative reference engine weight to the engine air mass flow. The combination of this value with the new engine mass flow (Wo) form the linear part of the equation. For the GE CF6-80C2 the corresponding value is 4386.2/279.5=15.693.

KBPR

It is the coefficient that takes into account the effect of bypass ratio on the weight of the system. As illustrated in Figure 9-1, the relative engine weight decreases with bypass ratio, due to the decrease of the core size in relation to the total air mass flow. A curve that fits the data from Gerend [1970] is extrapolated to a maximum BPR of 30, showing a moderate decrease of KBPR that follows the trend of the available data. It can be noticed that the reference value has been shifted to a BPR of 5, as discussed in previous chapter.

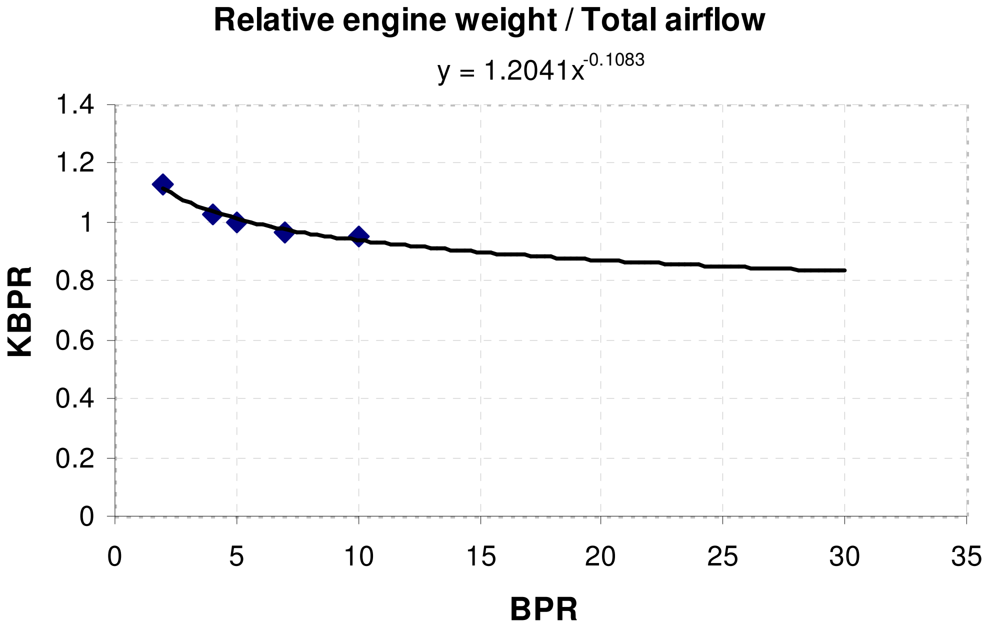

Figure 9-1: Relative engine weight correction factor.

KY

The KY factor stands for the possible advances in technology that could lead to engine weight reduction. This incorporates the use of lighter materials, combined with improvements in component design. Similarly to the previous case, the curve that fits the data assumes small future improvements in engine weight, as the technology levels in gas turbines are already very high.

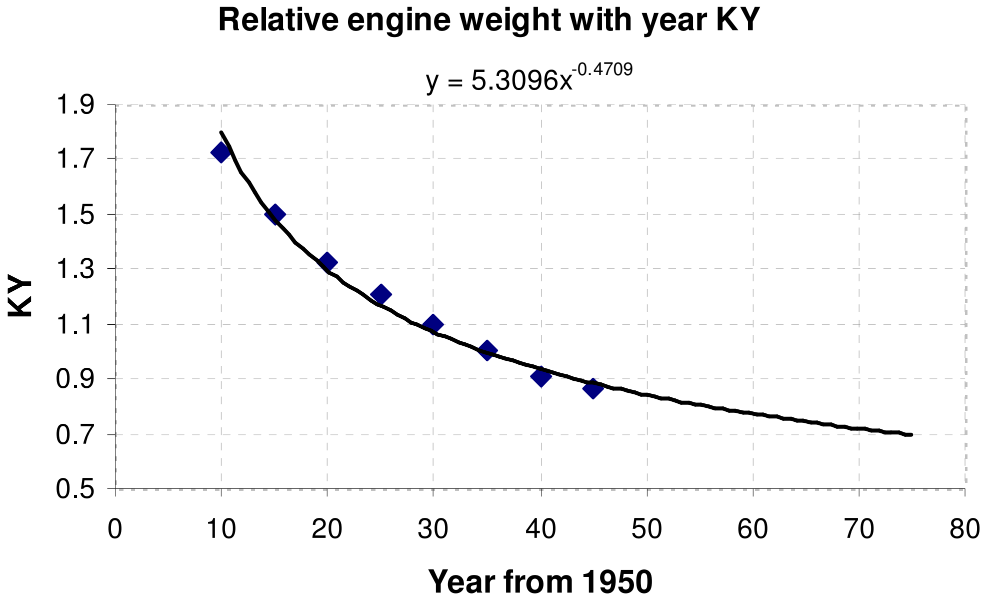

Figure 9-2: Relative engine weight with year.

KLIFE

This is a coefficient relative to the type of the engine. For a civil aircraft engine that is expected to have large service intervals a value of 1.07 has been chosen according to Gerend, [Gerend, 1970].

KM

The factor for flight Mach number does not affect the present study as the engine is operating in subsonic mode for the whole flight envelope. As a result, KM takes a value of 1.0.

KDUCT

It is referring to the additional weight, according to the type of nacelle that is used. If short nacelle is assumed KDUCT equals to 1.0.

KT_4

The increase of combustor outlet temperature is expected to increase the total weight, as it demands stronger structures. However the advances in technology, such as blade cooling and materials, mitigate the expected penalty. For this reason a linear expression based on Gerend has been implemented and is shown in Table 9-1.

KR_p

The overall pressure ratio has a detrimental effect on engine weight as it affects the number of stages of both compressors and turbines, leading to a linear relation between OPR and structure weight, which is translated to the equation shown in Table 9-1.

KW_e

For mass flows greater than 100kg/s the relation between relative gas generator weight and airflow is illustrated in Figure 9-3. It can be noticed that it is not linear, as a result of the fact that some components of the engine do not increase with increasing mass flow.

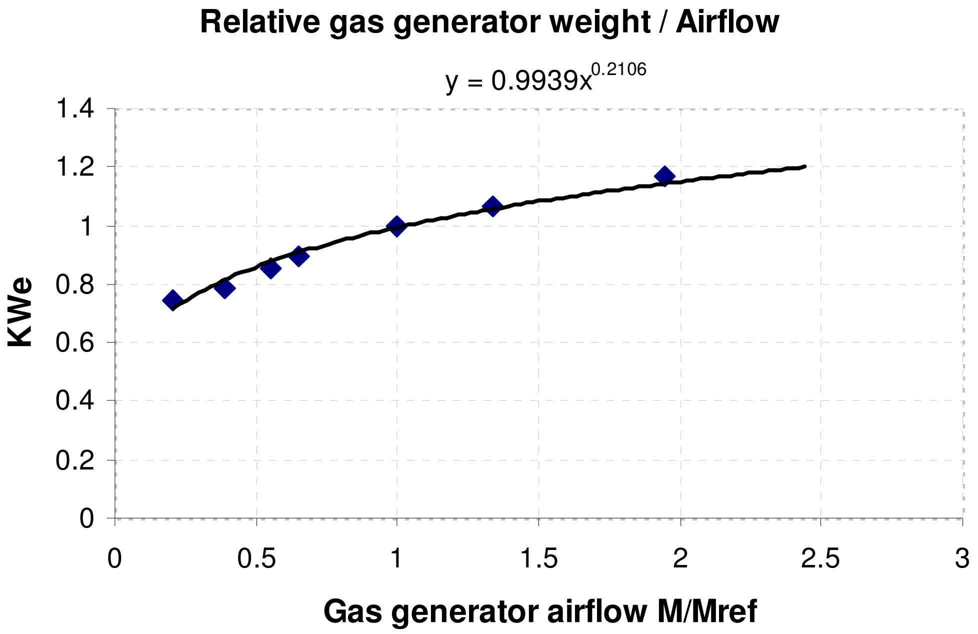

Figure 9-3: Relative core weight with core air mass flow.

KW_o

This correction factor takes into account the scaling law that has been assumed in the model. The model uses a power index of 1.3 for scaling the weight with mass flow.

K_{gg}

The use of K_{gg} depicts the breakdown of weight between the gas generator and the whole engine. As shown in Figure 9-4 the relative weight of the gas generator reduces with increasing bypass ratio, however not linearly as there are parts whose size is not changing with air mass flow. In this manner a curve that fits the original data and shows a reasonable behaviour at ultra high BPR has been chosen. The analytical expression of the curve is shown in Table 9-1.

KHX

The propulsion cycles featuring heat exchange, bear a weight penalty represented by [KHX] factor. This is proportional to the core mass flow and to a factor – [KHXt] – representing the heat exchanger weight impact on the baseline turbofan engine. The

[KHX] is calculated in accordance to the model proposed by Whellens [Whellens, 2003], using the equation in Table 9-1. The value of [KHXt] relies upon the relative weight of the heat exchangers to the core weight.

A value giving a 20% mass increase has been chosen for the intercooled-recuperated cycle, according to the suggestion by Boggia [Boggia, 2005], while half increase is expected for a configuration implementing only recuperation.

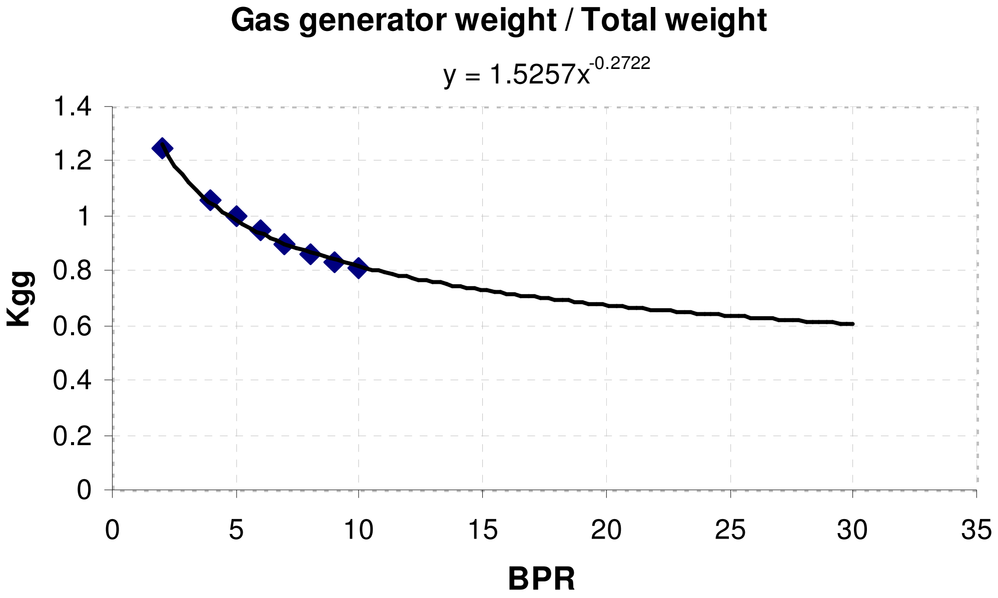

Figure 9-4: Core to total weight.

Weight Model Coefficients	
WT/Wo_{ref}	15.693
KBPR	$1.2041(BPR)^{-0.1083}$
KY	$5.3096(\Delta\ (Year))^{-0.4709}$
KLIFE	1.07 for long life civil turbofan
KM	1 for subsonic civil turbofan
KDUCT	1.0 for short cowl
KT4	$1+0.003\ \Delta(COT)$
KR_p	$1+(OPR-OPR_{ref})/36.14$
KHX	$[KHXt](Wo/Wo_{ref})(BPR_{ref}/BPR)$
KW_e	$0.9939(CoreMassFlow/Reference)^{0.2106}$
KW_o	$(Wo/Wo_{ref})^{0.3}$
K_{gg}	$1.5257(BPR)^{-0.2722}$

Table 9-1:Engine weight model correction factors

9.2 *Engine Length Model*

The correction factors, included in the length prediction method, and their analytical expressions are discussed below.

L_{ref}

It is the length of the reference engine. Even though Gerend [1970] used a turbojet, it was found that the use of a modern turbofan, would eliminate the cumulative prediction error, as the discrepancies between the reference and the novel cycles, in terms of BPR and OPR, would be lower.

KLW_e

The mass flow of the gas generator was found to affect the maximum length of the engine, as the core is the longest part of the engine. For this reason, a correlation is proposed by Gerend, [Gerend, 1970] that fits the engine database. A linear expression has been found to fit Gerend's results and is implemented into the model, shown in Table 9-2.

KLBPR

This correction factor comes to complement 'KLW_e', by quantifying the effect of bypass mass flow on engine length. BPR has a strong influence on length, mainly because it determines the number of stages of the low pressure turbine, but also, due to the geometrical changes of the fan (fan chord, spacing).

KLY

The year of manufacturing, is reflecting the technology level during that period. As it is expected, technology evolves in the direction of reducing engine length, due to improved, more compact components. Its analytical expression is illustrated in Table 9-2.

KLR_p

Engine length has been found to change linearly with overall pressure ratio for OPRs greater than 15. As stated above, OPR affects greatly the number of both compressor and turbine stages, having a linear effect on their dimensions as well. Table 9-2 shows this attribute.

KIGV

No inlet guide vanes are included in the design of ultra high bypass ratio civil turbofans. As a result the correction facto representing their use has been set to 1.

Length Model Coefficients	
L_{ref} [m]	4.274
KLW_e	$1+0.16(W_o/W_{oref}-1)$
KBPR	$1+0.04(BPR-BPR_{ref})$
KLY	$5.4(\Delta\ (Year))^{-0.48}$
KLR_p	$1+0.015(OPR-OPR_{ref})$
KIGV	1

Table 9-2: Engine length model correction factors.

9.3 Cycle Design Input

Table 9-3 depicts an input file for the design module used in the cycle design method. Four sections are recognisable in this file. The first includes data for the compression system of the engine and variables needed by the module that creates and updates Turbomatch input files. The second section refers to engine cycle initial values and range of variables, thrust requirements and fan design parameters. The third section is related to the objective function, while the last section defines in detail the off design condition, which is the condition of noise measuring.

Cycle Design Module Input File

Variables	Values
FPR Brick Data	7
Fan Efficiency	0.91
Fan Efficiency Brick Data	8
IPC Pressure Ratio Brick Data	22
IPC Efficiency	0.9
IPC Efficiency Brick Data	23
HPC Pressure Ratio Brick Data	28
HPC Efficiency	0.9
HPC Efficiency Brick Data	29
BPR (Initial Value)	25
BPR Brick Data	11
COT (Initial Value)	1800
FPR minimum	1.1
FPR maximum	1.4
FPR incremental change	0.01
OPR (Initial Value)	40
IPCR to HPCR ratio	1
Design Point Thrust	75000
Fan Inlet Mach	0.55
Fan Hub/Tip	0.4
a1	0.3
a2	0.6
OD_COT/DP_COT minimum	0.85
OD_COT/DP_COT maximum	1.2
Off design altitude	210
Off design Mach number	0.25
Off design Thrust	250000

Table 9-3: Cycle design input file.

9.4 Parametric Analysis Constraints Input

```
Min     Max          Intervals  !USED BY BOTH OPTIMISER&PARAMETRIC
5.      30.          25.      !ByPass Ratio
1600. 2000.          40.      !Turbine Entry Temperature
30.     60.          30.      !Overall Pressure Ratio
2.7                           !Maximum allowed fan diameter [m]
```

9.5 Baseline Engine Noise Calculation Data

Table 9-4, Table 9-6 and Table 9-5 illustrate the data involved in the calibration of the noise routines according to the FAA reference procedure. The liner impedance has been chosen from Bielak [Bielak, 1999].

JET CALCULATION

Variable	Core	Bypass
Jet Velocity [m/s]	352.3	296.3
Jet Area [m^2]	0.59	1.846
Jet Static Temperature [K]	656.7	305.2
Jet Total Temperature [K]	713.5`	348.7
Mass Flow Rate [kg/s]	106.0	600.39

Table 9-4: Jet noise calculation input data.

FAN CALCULATION

Variable	Value	Variable	Value
Rotor blades	30	Fan Tip Radius [m]	1.21
Stator Vanes	56	Fan Rot. Speed [RPM]	3288.2
Rotor-Stator [%chord]	150	Rel Tip Mach Design Point	1.5
Fan Temperature rise [K]	43.	Rel Tip Mach Off Design	1.345
Fan Mass Flow [kg/s]	705.7	Abs Tip Mach	1.238
Duct Length Inl or Aft [m]	4 or 1	Shocks per revolution	10

Table 9-5: Fan noise calculation input data.

LINER IMPEDANCE

Z1-23=(2,-2.78)	Z1-24=(2,-2)	Z1-25=(2,-1.6)
Z1-26=(2,-1.37)	Z1-27=(2,-1.13)	Z1-28=(2,-1.)
Z1-29=(1.78,-0.85)	Z1-30=(1.68,-0.79)	Z1-31=(1.53,-0.69)
Z1-32=(1.42,-0.58)	Z1-33=(1.34,-0.53)	Z1-34=(1.3,-0.4)
Z1-35=(1.25,-0.33)	Z1-36=(1.19,-0.31)	Z1-37=(1.17,-0.26)
Z1-38=(1.1,-0.24)		

Table 9-6: Liner calculation input data.

9.6 *Hermes Input Files*

Baseline aircraft geometry and missions details

Baseline Aircraft Geometry and Mission Details	
Wing Geometry	
Wing area, Sw	258.45
Aspect ratio, A	8
Span , bw	45.47
Thickness chord ratio, Ctw	0.11
Sweep angle (in radians), Yow	30
Taper ratio, Trw	0.25
Root thickness ratio, RTRw	0.11
Outer thickness ratio, OTRw	0.109
Tailplane Geometry	
Tailplane area, St	65.16
Span, bt	17.8
Thickness chord ratio, Ctt	0.069
Sweep angle (in radians), Yot	30
Taper ratio, Trt	0.35
Root thinkness ratio, RTRt	0.055
Outer thikness ratio, OTRt	0.11
Fin Geometry	
Fin area, Sf	39.09
Span , bf	18.62
Thickness chord ratio, Ctf	0.069
Sweep angle (in radians), Yof	45
Taper ratio, Trf	0.345
Root thinkness ratio, RTRf	0.0546
Outer thikness ratio, OTRf	0.111
Fuselage Geometry	
Diameter, DFc	5.03
Length, Lc	53.67
Engine Geometry	
Diameter, De	2.69
Length , Le	4.267
Mission / Weight Specifications	
Airframe weight, w_afr	78384.4
Number of Engines, EngNo	2
Engine weight, (kg/engine)	4472.4
Payload weight, kg	23750
Fuel weight, kg	39119
Maximum payload weight, kg	30000
Maximum fuel weight, kg	42000
Maximum landing weight, kg	115047
Maximum take-off weight, kg	160000
Realtive contingency fuel(%)	0
Range to be flown (km)	7412
Mission to be flown	2
number of cruise segments	4
Cruise fuel check Interval	30

Cruise altitudes	40/41.66/43.33/45
Cruise Mach numbers	0.8
Cruise temperature deviation from ISA	0
Engine SFC during Landing, SFC_Land	20
Approach speed (TAS)	120
Deviation from standard atmosphere for Landing	0
Duration of Landing phase in minutes	6

BDVT geometry and missions details

Broad Delta V-Tail Geometry & Details	
Wing Geometry	
Wing area, Sw	354.63
Aspect ratio, A	3.11
Span , bw	33.21
Thickness chord ratio, Ctw	0.10125
Sweep angle (degrees), Yow	31.06
Taper ratio, Trw	0.5279
Root thickness ratio, RTRw	2.343
Outer thickness ratio, OTRw	0.6
Tailplane Geometry	
Tailplane area, St	65.92
Span, bt	10.09
Thickness chord ratio, Ctt	0.041
Sweep angle (degrees), Yot	49.7
Taper ratio, Trt	0.422
Root thinkness ratio, RTRt	0.15
Outer thikness ratio, OTRt	0.06
Fin Geometry	
Fin area, Sf	28.4
Span , bf	3.53
Thickness chord ratio, Ctf	0.0405
Sweep angle (degrees), Yof	52.8
Taper ratio, Trf	0.51
Root thinkness ratio, RTRf	0.127
Outer thikness ratio, OTRf	0.065
Fuselage Geometry	
Diameter, DFc	5.03
Length, Lc	53.67
Engine Geometry	
Diameter, De (T772 = 2.474m)	2.69
Length , Le (T772 = 3.912m)	4.267
Mission / Weight Specifications	

Airframe weight, w_afr 86803.	64059.9
Number of Engines, EngNo	4
Engine weight, (kg/engine)	3671.9
Payload weight, (kg)	18548
Fuel weight, (kg)	39119
Maximum payload weight, (kg)	30000
Maximum fuel weight, (kg)	42000
Maximum landing weight, (kg)	115047
Maximum take-off weight, (kg)	137000
Realtive contigency fuel to remain after landing (%)	0

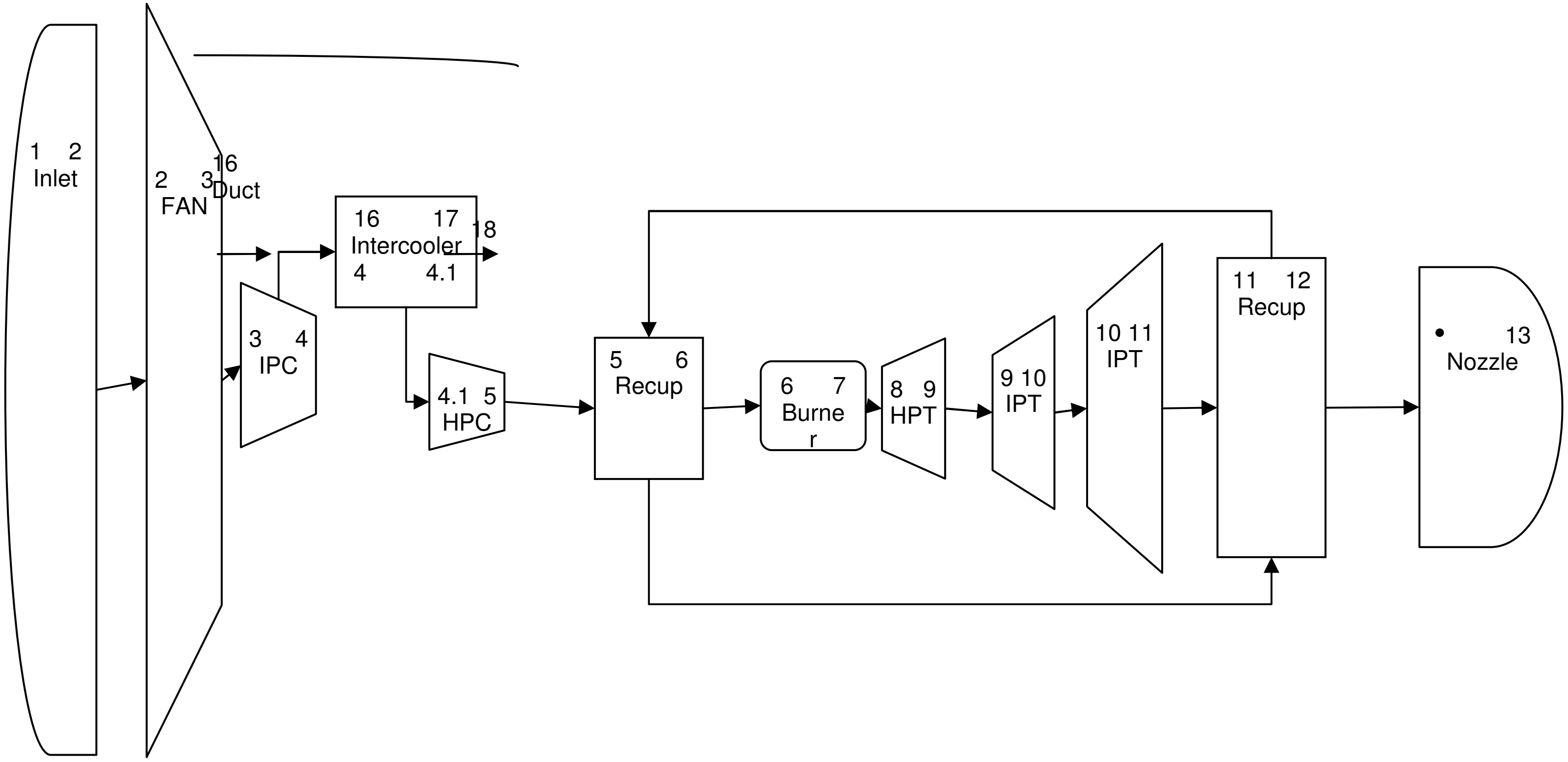

9.7 *Intercooled-Recuperated Engine Scheme with Engine Station Numbering*

9.8 Turbomatch Engine Models

Turbofan Engine Model

```
////
DP SI KE CT FP
-1
-1
INTAKE  S1-2        D1-4          R100
COMPRE  S2-3        D5-10         R101   V5    V6
PREMAS  S3,4,14     D11-14                V11
DUCTER  S14-15      D15-18        R102
NOZCON  S15-16,1    D19           R103
COMPRE  S4-5        D20-25        R104   V20   V21
COMPRE  S5-6        D26-31        R105   V26   V27
PREMAS  S6,7,17     D32-35
DUCTER  S17-18      D36-39        R106
BURNER  S7-8        D40-42        R107
MIXEES  S8,18,9
TURBIN  S9-10       D43-50,105,51         V44
TURBIN  S10-11      D52-59,104,60         V53
TURBIN  S11-12      D61-68,101,69         V62
NOZCON  S12-13,1    D70           R108
PERFOR  S1,0,0      D71-74,103,100,102,108,0,107,0,0,0
CODEND
////
1   12192.    ! ALTITUDE                               ! INTAKE - Aeroplane inlet
2   10.0      ! ISA DEVIATION
3   0.8       ! MACH NO.
4   0.99      ! PRESSURE RECOVERY
5 0.8         ! COMP : Z ! FAN                         !Fan
6 0.8         ! RELATIVE ROTATIONAL SPEED
7 1.6         ! PRESSURE RATIO (OPR=35.8)
8 0.9         ! ISENTROPIC EFFICIENCY
9 0.0         ! ERROR SELECTOR
10 2.0        ! MAP-NUMBER
11  0.133333    ! LAMDA
12  0.0       ! MASS FLOW LOSS
13  1.0       ! PRESSURE FACTOR
14  0.0       ! PRESSURE LOSS
15  0.0       ! REHEAT SELECTOR                        ! Bypass duct
16  0.01      ! PRESSURE LOSS 1%
17  0.0       ! REHEAT COMB.EFFICIENCY
18  0.0       ! MAX REHEAT FUEL FLOW
19  -1.0      ! Fan Exhaust Nozzle: fixed Area         !Bypass Convergent Zozzle
20  0.85       ! SURGE MARGIN                 !  IP COMPRESSOR
21  1.0        ! ROTATIONAL SPEED
22  5.188      ! PRESSURE RATIO
23  0.846      ! EFFICIENCY
24  1.0        ! ERROR SELECTOR
25  5.0        ! MAP NUMBER
26  0.85       ! SURGE MARGIN                 !  HP COMPRESSOR
27  1.0        ! ROTATIONAL SPEED
28  5.188      ! PRESSURE RATIO
29  0.851      ! EFFICIENCY
```

```
30  1.0      ! ERROR SELECTOR
31  5.0      ! MAP NUMBER
32  0.80     ! BYPASS RATIO              !  HPT Turbine COOLING BYPASS
33  0.0      ! MASS FLOW LOSS
34  1.0      ! PRESSURE FACTOR
35  0.0      ! PRESSURE LOSS
36  0.0      ! REHEAT SELECTOR                    !  Ducter Cooling
37  0.01     ! PRESSURE LOSS 1%
38  0.0      ! REHEAT COMB.EFFICIENCY
39  0.0      ! MAX REHEAT FUEL FLOW
40  0.06     ! PRESSURE LOSS             !  BURNER
41  0.998    ! COMBUSTION EFFICIENCY
42  -1.0     ! FUEL FLOW
43  0.0      ! AUX.WORK                           !  TURBINE-HP
44  0.8      ! REL NON-D MASS FLOW
45  0.6      ! REL NON-D SPEED
46  0.885    ! EFFICIENCY
47 -1.0      ! REL ROT.SPEED(COMP TURB=-1)
48  3.0      ! COMP NO. FROM LOW END
49  3.0      ! TURBINE MAP
50 -1.0      ! POWER LAW
51  0.0      ! NGV
52  0.0      ! AUX.WORK                           !  TURBINE-IP
53  0.8      ! REL NON-D MASS FLOW
54  0.6      ! REL NON-D SPEED
55  0.909    ! EFFICIENCY
56 -1.0      ! REL ROT.SPEED
57  2.0      ! COMP NO. FROM LOW END
58  3.0      ! TURBINE MAP
59 -1.0      ! POWER LAW
60  0.0      ! NGV
61  0.0      ! AUX.WORK                           !  TURBINE-LP
62  0.8      ! REL NON-D MASS FLOW
63  0.6      ! REL NON-D SPEED
64  0.915    ! EFFICIENCY
65 -1.0      ! REL ROT.SPEED
66  1.0      ! COMP NO. FROM LOW END
67  3.0      ! TURBINE MAP
68 -1.0      ! POWER LAW
69  0.0      ! NGV
70 -1.0      ! SWITHCH, AREA FIXED     !  Core CONVERGENT NOZZLE
71 -1.0      ! POWER (-1=TURBOJET/FAN)          !  PERFORMANCE
72 -1.0      ! PROPELLER EFFICIENCY(")
73  0.0      ! SCALING INDEX
74  0.0      ! REQ'D D.P. THRUST
-1
1 2  295.0    ! INLET MASS FLOW(Kg/s)
8 6  1600.0   ! TET(K)
-1
```

CVC Engine Model

```
////
DP SI KE VA FP
-1
-1
INTAKE  S1-2        D1-4          R100
COMPRE  S2-3        D5-11         R101   V5    V6
PREMAS  S3,4,14     D12-15               V12
DUCTER  S14-15      D16-19        R102
NOZCON  S15-16,1    D20           R103
COMPRE  S4-5        D21-27        R104   V21   V22
COMPRE  S5-6        D28-34        R105   V28   V29
PREMAS  S6,7,17     D35-38
DUCTER  S17-18      D39-42        R106
BURNER  S7-8        D43-45        R107
ARITHY              D202-208        R110
ARITHY              D210-216        R111
ARITHY              D46-52        R108
ARITHY              D53-59
ARITHY              D218-224
ARITHY              D225-231
TURBIN  S8-9        D60-67,105,68        V61
MIXEES  S9,18,10
TURBIN  S10-11      D69-76,104,77        V70
TURBIN  S11-12      D78-85,101,86        V79
NOZCON  S12-13,1  D87           R109
ARITHY              D92-99
PERFOR  S1,0,0      D88-91,103,100,102,109,0,107,0,0,0
CODEND
////
1   12192.000      ! INTAKE - Aeroplane inlet
2       10.000
3       0.800
4       0.990
5       0.800        !Fan
6       0.900
7       1.30
8       0.893
9       0.000
10       1.000
11       0.
12       0.111  ! PREMAS -  Bypass - Main
13       0.000
14       1.000
15       0.000
16       0.000   ! Bypass duct
17       0.010
18       0.000
19       0.000
20      -1.000   !Bypass Convergent Zozzle
21       0.850   !  IP COMPRESSOR
22       1.000
23       5.188
24       0.808
25       1.000
26       4.000
```

```
27      0.
28      0.850   !  HP COMPRESSOR
29      1.000
30      5.188
31      0.814
32      1.000
33      5.000
34      0.
35      0.800   !  HPT Turbine COOLING BYPASS
36      0.000
37      1.000
38      0.000
39      0.000   !  Ducter Cooling
40      0.010
41      0.000
42      0.000
43      0.060   !  BURNER
44      0.998
45     -1.000
201      0.445     !CONSTANT FACTOR FOR CVC
202      3.        !ARITHY
203      -1
204      110        !0.445*Pin
205      8         !P low
206      4
207      -1
208      201
209      0.9        !K-FACTOR FOR CVC!   VARIABLE  : 0.5<k<1.
210      3.         !ARITHY
211      -1
212      111        !0.445*Pin*k_factor
213      -1
214      110
215      -1
216      209
46      4.          !  CONSTANT VOLUME ARITHY
47      -1
48      108         !TET/CIT
49      8
50      6
51      7
52      6
53      3.          !CONSTANT VOLUME ARITHY II
54      8
55      4           !P8=P8*TET/CIT
56      8
57      4
58      -1
59      108
217      0.502     !CONSTANT FACTOR FOR CVC
218      3.        !CONSTANT VOLUME ARITHY III
219      8
220      4         !P8=0.502*P8*TET/CIT
221      8
222      4
223      -1
```

```
224     217
225     1.   !CONSTANT VOLUME ARITHY IV
226     8
227     4      !P8=0.502*P8*TET/CIT + 0.445*Pin*k_factor
228     8
229     4
230     -1
231     111
60     0.000    !  TURBINE-HP
61     0.800
62     0.600
63     0.885
64    -1.000
65     3.000
66     5.
67    -1.000
68     0.000
69     0.000    !  TURBINE-IP
70     0.800
71     0.600
72     0.909
73    -1.000
74     2.000
75     5.
76    -1.000
77     0.000
78     0.000    !  TURBINE-LP
79     0.800
80     0.600
81     0.915
82    -1.000
83     1.000
84     4.
85    -1.000
86     0.00
87    -1.000    !  Core CONVERGENT NOZZLE
88    -1.000    !  PERFORMANCE
89    -1.000
90     0.000
91     0.000
92  4.         !ARITHY FOR THE GAMMA CORRECTION OF FUEL FLOW
93  -1
94  107
95  -1
96  107
97  -1
98  99
99  1.33           !GAMMA OF HOT GASES
-1
1   2  295.000
8   6 1800.000
-1
```

Recuperated Turbofan Model

```
////
DP SI KE CT FP
-1
-1
INTAKE  S1-2         D1-4          R100
COMPRE  S2-3         D5-10          R101   V5    V6
PREMAS  S3,4,16      D11-14                V11
DUCTER  S16-17       D15-18         R102
NOZCON  S17-18,1   D19            R103
COMPRE  S4-5         D20-25         R104   V20   V21
COMPRE  S5-6         D26-31         R105   V26   V27
PREMAS  S6,7,19      D32-35
DUCTER  S19-20       D36-39         R106
HETCOL  S7-8         D201-204
BURNER  S8-9         D40-42         R107
MIXEES  S9,20,10
TURBIN  S10-11        D43-50,105,51         V44
TURBIN  S11-12        D52-59,104,60         V53
HETHOT  S7,12-13      D205-208
TURBIN  S13-14        D61-68,101,69         V62
NOZCON  S14-15,1     D70            R108
PERFOR  S1,0,0          D71-74,103,100,102,108,0,107,0,0,0
CODEND
////
1   12192.     ! ALTITUDE                                         ! INTAKE - Aeroplane inlet
2   10.0        ! ISA DEVIATION
3   0.8        ! MACH NO.
4   0.99       ! PRESSURE RECOVERY
5 0.8          ! COMP : Z ! FAN                         !Fan
6 0.8          ! RELATIVE ROTATIONAL SPEED
7 1.6          ! PRESSURE RATIO (OPR=35.8)
8 0.9          ! ISENTROPIC EFFICIENCY
9 0.0          ! ERROR SELECTOR
10 2.0         ! MAP-NUMBER
11  0.1111    ! LAMDA (BYPASS RATIO 8.5)          ! PREMAS -  Bypass - Main
12  0.0        ! MASS FLOW LOSS
13  1.0        ! PRESSURE FACTOR
14  0.0        ! PRESSURE LOSS
15  0.0        ! REHEAT SELECTOR                     ! Bypass duct
16  0.01        ! PRESSURE LOSS 1%
17  0.0        ! REHEAT COMB.EFFICIENCY
18  0.0        ! MAX REHEAT FUEL FLOW
19  -1.0       ! Fan Exhaust Nozzle: fixed Area           !Bypass Convergent Zozzle
20  0.85        ! SURGE MARGIN                !  IP COMPRESSOR
21  1.0        ! ROTATIONAL SPEED
22  5.188       ! PRESSURE RATIO
23  0.846       ! EFFICIENCY
24  1.0        ! ERROR SELECTOR
25  5.0        ! MAP NUMBER
26  0.85        ! SURGE MARGIN                !  HP COMPRESSOR
27  1.0        ! ROTATIONAL SPEED
28  5.188       ! PRESSURE RATIO
29  0.851       ! EFFICIENCY
30  1.0        ! ERROR SELECTOR
```

```
31  5.0      ! MAP NUMBER
32  0.80      ! BYPASS RATIO              !  HPT Turbine COOLING BYPASS
33  0.0      ! MASS FLOW LOSS
34  1.0      ! PRESSURE FACTOR
35  0.0      ! PRESSURE LOSS
36  0.0      ! REHEAT SELECTOR                  !  Ducter Cooling
37  0.01      ! PRESSURE LOSS 1%
38  0.0      ! REHEAT COMB.EFFICIENCY
39  0.0      ! MAX REHEAT FUEL FLOW
201 0.02       ! pressure loss        !HETCOL FOR RECUPERATOR
202 0.7       ! effectiveness
203 3.0       ! type
204 0.0       ! deltaW/w
40  0.06      ! PRESSURE LOSS              !  BURNER
41  0.998      ! COMBUSTION EFFICIENCY
42  -1.0     ! FUEL FLOW
43  0.0      ! AUX.WORK                         !  TURBINE-HP
44  0.8      ! REL NON-D MASS FLOW
45  0.6      ! REL NON-D SPEED
46  0.885      ! EFFICIENCY
47 -1.0      ! REL ROT.SPEED(COMP TURB=-1)
48  3.0      ! COMP NO. FROM LOW END
49  3.0      ! TURBINE MAP
50 -1.0      ! POWER LAW
51  0.0      ! NGV
52  0.0      ! AUX.WORK                         !  TURBINE-IP
53  0.8      ! REL NON-D MASS FLOW
54  0.6      ! REL NON-D SPEED
55  0.909      ! EFFICIENCY
56 -1.0      ! REL ROT.SPEED
57  2.0      ! COMP NO. FROM LOW END
58  3.0      ! TURBINE MAP
59 -1.0      ! POWER LAW
60  0.0      ! NGV
205 0.02            ! pressure loss        !HETHOT FOR RECUPERATOR
206 .7            ! effectiveness
207 3.0             ! type
208 0.0             ! deltaW/w
61  0.0      ! AUX.WORK                         !  TURBINE-LP
62  0.8      ! REL NON-D MASS FLOW
63  0.6      ! REL NON-D SPEED
64  0.915      ! EFFICIENCY
65 -1.0      ! REL ROT.SPEED
66  1.0      ! COMP NO. FROM LOW END
67  3.0      ! TURBINE MAP
68 -1.0      ! POWER LAW
69  0.0      ! NGV
70 -1.0      ! SWITHCH, AREA FIXED      !  Core CONVERGENT NOZZLE
71 -1.0      ! POWER (-1=TURBOJET/FAN)          !  PERFORMANCE
72 -1.0      ! PROPELLER EFFICIENCY(")
73  0.0      ! SCALING INDEX
74  0.0      ! REQ'D D.P. THRUST
-1
1 2  400.0    ! INLET MASS FLOW(Kg/s)
9 6  1800.0     ! TET(K)
-1
```

Intercooled Recuperated Turbofan Model

```
////
 DP SI KE CT FP
-1
-1
INTAKE  S1-2        D1-4           R100
COMPRE  S2-3        D5-10          R101   V5    V6
PREMAS  S3,4,19     D11-14                V11
DUCTER  S19-20      D15-18         R102
COMPRE  S4-5        D20-25         R104   V20   V21
DUCTER  S5-6        D81-84         R221
ARITHY              D301-307       R400           !INTERCOOLER BRICKS
ARITHY              D308-314       R401
ARITHY              D316-322       R402
ARITHY              D323-327
ARITHY              D328-334       R403           !BYPASS FLOW HEATING BRICKS
ARITHY              D335-341       R404
ARITHY              D342-348       R405
ARITHY              D349-353
COMPRE  S6-7        D26-31         R105   V26   V27
PREMAS  S7,8,17     D32-35
DUCTER  S17-18      D36-39         R106
HETCOL  S8-9        D85-88                        ! HEAT EXCHANGER COLD SIDE
BURNER  S9-10       D40-42         R107
MIXEES  S10,18,11
TURBIN  S11-12      D43-50,105,51         V44
TURBIN  S12-13      D52-59,104,60         V53
TURBIN  S13-14      D61-68,101,69         V62
HETHOT  S8,14,15    D75-78                        ! HEAT EXCHANGER HOT SIDE
NOZCON  S15-16,1    D70            R108
NOZCON  S20-21,1    D19            R103
OUTPBD              D400-405,500
PERFOR  S1,0,0      D71-74,103,100,102,108,0,107,400,0,0,0
CODEND
////
1 12192.
2 0.
3 0.8
4 0.99
 ! COMPRE - Fan uses Trent 800
 5    0.8       ! SURGE MARGINE
 6    0.8       ! ROTATIONAL SPEED,N1
 7   1.90       ! FAN PRESSURE RATIO
 8   0.893      ! EFFICIENCY
 9   0.0        ! ERROR SELECTOR
 10  1.0        ! MAP NUMBER
 ! PREMAS -  Bypass - Main
 11  0.1111     ! LAMDA (BYPASS RATIO 8.0)
 12  0.0        ! MASS FLOW LOSS
 13  1.0        ! PRESSURE FACTOR
 14  0.0        ! PRESSURE LOSS
 ! Bypass duct
 15  0.0        ! REHEAT SELECTOR
 16  0.02       ! PRESSURE LOSS 1%
 17  0.0        ! REHEAT COMB.EFFICIENCY
 18  0.0        ! MAX REHEAT FUEL FLOW
```

```
!Bypass Convergent Zozzle
19  -1.0       ! Fan Exhaust Nozzle: fixed Area
!  IP COMPRESSOR
20  0.85        ! SURGE MARGIN
21  1.0        ! ROTATIONAL SPEED
22  5.188       ! PRESSURE RATIO
23  0.808       ! EFFICIENCY
24  1.0        ! ERROR SELECTOR
25  4.0        ! MAP NUMBER
! INTERCOOLER
81  0.0        ! REHEAT SELECTOR
82  0.02        ! PRESSURE LOSS 1%
83  0.0        ! REHEAT COMB.EFFICIENCY
84  0.0        ! MAX REHEAT FUEL FLOW
500 0.7         ! EFFECTIVENESS          !CHANGE EFFECTIVNESS HERE
!ARITHY
301 2          !SUBTRACT
302 -1
303 400         !(T5-T3)
304 5          !COMPRESSOR OUTLET
305 6          !T5
306 3          !FAN OUTLET
307 6          !T3
! ARITHY
308  3          !MULTIPLY
309 -1
310 401         !EFF*(T5-T3)
311 -1
312 500         !EFFECTIVENESS
313 -1
314 400         !R400 (T5-T3)
! ARITHY
316 2          !SUBTRACT
317 -1
318 402         !T5-EFF*(T5-T3)
319 5
320 6          !T5
321 -1
322 401         !R401 EFF*(T5-T3)
! ARITHY
323 5          !EQUAL
324 6
325 6          !T6
326 -1
327 402         !T6=[T5-EFF*(T5-T3)]
! ARITHY
328 2          !SUBTRACT
329 -1
330 403         !(T5-T6)
331 5
332 6          !T5
333 6
334 6          !T6
! ARITHY
335  3         !Multiply
336 -1
```

```
 337 404        !(T5-T6)/BPR
 338 -1
 339 403        !(T5-T6)
 340 -1
 341 11        !(1/BPR)
 ! ARITHY
 342  1         !ADD
 343 -1
 344 405        !T21
 345 3
 346 6          !T3
 347 -1
 348 404        !(T5-T6)/BPR
 !ARITHY
 349 5          !EQUAL
 350 20
 351 6          !T20
 352 -1
 353 405        !T20=[T3+(T5-T3)/BPR]
 !  HP COMPRESSOR
 26  0.85       ! SURGE MARGIN
 27  1.0        ! ROTATIONAL SPEED
 28  5.188      ! PRESSURE RATIO
 29  0.814      ! EFFICIENCY
 30  1.0        ! ERROR SELECTOR
 31  5.0        ! MAP NUMBER
 !  HPT Turbine COOLING BYPASS
 32  0.80       ! BYPASS RATIO
 33  0.0        ! MASS FLOW LOSS
 34  1.0        ! PRESSURE FACTOR
 35  0.0        ! PRESSURE LOSS
 !  Ducter Cooling
 36  0.0        ! REHEAT SELECTOR
 37  0.01       ! PRESSURE LOSS 1%
 38  0.0        ! REHEAT COMB.EFFICIENCY
 39  0.0        ! MAX REHEAT FUEL FLOW
 !  HEAT EXCHANGER COLD SIDE
 85  0.02       !COLD SIDE TOTAL PRESSURE LOSS/COLD SIDE INLET TOTAL PRESSURE
 86  0.7        !HEAT EXCHANGER EFFECTIVENESS
 87  1.0        !1 FOR RECUPERATOR 3 FOR REGENERATOR
 88  0.0        !MASS FLOW LEAKAGE (COLD SIDE TO HOT SIDE/COLD SIDE INLET MASS
FLOW)
 !  BURNER
 40  0.06       ! PRESSURE LOSS
 41  0.998      ! COMBUSTION EFFICIENCY
 42  -1.0       ! FUEL FLOW
 !  TURBINE-HP
 43  0.0        ! AUX.WORK
 44  0.8        ! REL NON-D MASS FLOW
 45  0.6        ! REL NON-D SPEED
 46  0.885      ! EFFICIENCY
 47 -1.0        ! REL ROT.SPEED(COMP TURB=-1)
 48  3.0        ! COMP NO. FROM LOW END
 49  3.0        ! TURBINE MAP
 50 -1.0        ! POWER LAW
 51  0.0        ! NGV
```

```
 !  TURBINE-IP
 52  0.0        ! AUX.WORK
 53  0.8        ! REL NON-D MASS FLOW
 54  0.6        ! REL NON-D SPEED
 55  0.909       ! EFFICIENCY
 56 -1.0        ! REL ROT.SPEED
 57  2.0        ! COMP NO. FROM LOW END
 58  3.0        ! TURBINE MAP
 59 -1.0        ! POWER LAW
 60  0.0        ! NGV
 !  TURBINE-LP
 61  0.0        ! AUX.WORK
 62  0.8        ! REL NON-D MASS FLOW
 63  0.6        ! REL NON-D SPEED
 64  0.915       ! EFFICIENCY
 65 -1.0        ! REL ROT.SPEED
 66  1.0        ! COMP NO. FROM LOW END
 67  3.0        ! TURBINE MAP
 68 -1.0        ! POWER LAW
 69  0.0        ! NGV
!  HEAT EXCHANGER HOT SIDE
 75  0.02        !HOT SIDE TOTAL PRESSURE LOSS/HOT SIDE INLET TOTAL PRESSURE
 76  0.7        !HEAT EXCHANGER EFFECTIVENESS
 77  1.0        !1 FOR RECUPERATOR 3 FOR REGENERATOR
 78  0.0        !MASS FLOW LEAKAGE (COLD SIDE TO HOT SIDE/COLD SIDE INLET MASS
FLOW)
!  Core CONVERGENT NOZZLE
 70 -1.0        ! SWITHCH, AREA FIXED
 !  PERFORMANCE
 71 -1.0        ! POWER (-1=TURBOJET/FAN)
 72 -1.0        ! PROPELLER EFFICIENCY(")
 73  0.0        ! SCALING INDEX
 74  0.0        ! REQ'D D.P. THRUST
 -1
  1 2  400.0     ! INLET MASS FLOW(Kg/s)
  10 6 1800.0    ! TET(K)
 -1
 -3
```

9.9 PaCo-SLC Input

PaCo-SLC / Validation version input file (pc_input.dat)

```
_______________Circumferential Parallel Compressor Inlet Conditions_______________

288.15                    !AirInletAbsTotTemp [K]
101325.                   !AirInletAbsTotPress [Pa]
2                         !NumberOfCircmfSegments
180.                      !ExtOfDistortedArea [deg]
13                        !NumberOfRadialPositions
____2 Equal Sectors 180deg__________1st Segment relative values_________________
RadialPosition %Span  TotPress(%) TotTemp(%) AbsAng RCoord
1      0      101.2558      100.0000      0.0000 25.53
2      0      101.4336      100.0000      0.0000 24.88
3      0      101.6036      100.0000      0.0000 24.178
4      0      101.9206      100.0000      0.0000 22.753
5      0      102.2066      100.0000      0.0000 21.294
6      0      102.4617      100.0000      0.0000 19.81
7      0      102.6858      100.0000      0.0000 18.291
8      0      102.8791      100.0000      0.0000 16.723
9      0      103.0414      100.0000      0.0000 15.081
10     0      103.1727      100.0000      0.0000 13.349
11     0      103.2732      100.0000      0.0000 11.493
12     0      103.3118      100.0000      0.0000 10.503
13     0      103.3427      100.0000      0.0000 9.583
_______________2nd Segment relative values_____________________________________
RadialPosition %Span  TotPress(%) TotTemp(%) AbsAng RCoord
1      0      95.2541       100.0000      0.0000 25.53
2      0      95.6126       100.0000      0.0000 24.88
3      0      95.9452       100.0000      0.0000 24.178
4      0      96.5326       100.0000      0.0000 22.753
5      0      97.0161       100.0000      0.0000 21.294
6      0      97.3959       100.0000      0.0000 19.81
7      0      97.6719       100.0000      0.0000 18.291
8      0      97.8441       100.0000      0.0000 16.723
9      0      97.9126       100.0000      0.0000 15.081
10     0      97.8772       100.0000      0.0000 13.349
11     0      97.7381       100.0000      0.0000 11.493
12     0      97.6296       100.0000      0.0000 10.503
13     0      97.4952       100.0000      0.0000 9.583
```

PaCo-SLC / Turbomatch Version Input (pc_input.dat)

```
______________Circumferential Parallel Compressor Inlet Conditions______________

288.15                        !AirInletAbsTotTemp [K]
101325.                       !AirInletAbsTotPress [Pa]
1                             !NumberOfCircmfSegments
360.                          !ExtOfDistortedArea [deg]
13                            !NumberOfRadialPositions
!MAIN INPUT DATA COMMUNICATED TO TURBOMATCH
16.                           !InputMassFlow
0.6                           !NonDimRotSpeed
16042.8                       !RotSpeed_DP
!GEOMETRICAL DATA FOR NOZZLE CORRECTION
0.17591                       !FanInletArea kg/s
0.13426                       !FanExitArea
0.11                          !NozzleExitArea
!NOZZLE MACH CORRECTION
2                             !Switch_Pst
0.1                           !Relaxation Factor for Mach number calculation at nozzle
!RECOVERY FROM SLC CRASHING
0.3                           !massflowstep when SLC does not converge
10                            !Limit of steps
!DATA FOR MAIN PACO PROCESS
1.                            !Pst error     !(Pa)
50.                           !maxiter
0.5                           !Under relaxation_factor   Suggested 0.2-0.3
```

9.10 Engine Nacelle Outer Coordinates

X	Y	
0	1.196084	Forebody
0.01263	1.22146	
0.02526	1.231794	
0.04736	1.244769	
0.07894	1.259505	
0.11052	1.272404	
0.15788	1.289321	
0.25261	1.317836	
0.34734	1.342102	
0.44207	1.363191	
0.5368	1.381333	
0.63153	1.397791	
0.72626	1.412948	
0.82099	1.427072	
0.9473	1.444448	
1.0736	1.460485	
1.19991	1.475259	
1.32622	1.488809	
1.45252	1.501286	
1.57883	1.512577	
1.83144	1.53271	
2.08406	1.548976	
2.33667	1.561531	
2.58928	1.570678	
2.8419	1.576534	
3.15766	1.578831	
3.23504	1.578673	Afterbody
3.31242	1.5782	
3.3898	1.57741	
3.46718	1.576306	
3.54454	1.574886	
3.62191	1.57315	
3.69926	1.571099	
3.77661	1.568732	
3.85394	1.56605	
3.93127	1.563052	
4.00858	1.559739	
4.08588	1.556111	
4.16316	1.552167	
4.24042	1.547908	
4.31767	1.543335	
4.3949	1.538446	
4.4721	1.533242	
4.54929	1.527723	
4.62645	1.52189	
4.70359	1.515742	
4.7807	1.509279	
4.85778	1.502502	
4.93484	1.49541	
5.01187	1.488005	
5.08886	1.480285	
5.16583	1.472251	
5.24276	1.463903	
5.31965	1.455242	
5.39651	1.446267	
5.47333	1.436979	
5.55012	1.427377	
5.62686	1.417462	
5.70357	1.407235	
5.78023	1.396694	
5.85684	1.385841	
5.93342	1.374676	
6.00994	1.363198	
6.08642	1.351409	
6.16285	1.339307	
6.23923	1.326894	
6.31556	1.31417	
6.39183	1.301134	
6.46806	1.287787	
6.54422	1.274129	
6.84832	1.216396	
6.92419	1.201188	
7	1.185671	nozzle

9.11 Engine Nacelle Internal Coordinates

X	Y
0	1.196084
0.000213	1.184973
0.001204	1.173863
0.003329	1.162752
0.006871	1.151642
0.012098	1.140531
0.019295	1.12942
0.028784	1.11831
0.040962	1.107199
0.056345	1.096089
0.075648	1.084978
0.09995	1.073867
0.131039	1.062757
0.172382	1.051646
0.232935	1.040536
0.416647	1.029425
0.471467	1.029596
0.526288	1.030099
0.581108	1.030921
0.635928	1.032048
0.690748	1.033465
0.745569	1.03516
0.800389	1.037118
0.855209	1.039325
0.91003	1.041768
0.96485	1.044432
1.01967	1.047304
1.07449	1.05037
1.129311	1.053617
1.184131	1.057029
1.238951	1.060594
1.293772	1.064297
1.348592	1.068125
1.403412	1.072064
1.458232	1.076099
1.513053	1.080218
1.567873	1.084406
1.622693	1.08865
1.677514	1.092935
1.732334	1.097248
1.787154	1.101574
1.841975	1.105901
1.896795	1.110214
1.951615	1.114499
2.006435	1.118743
2.061256	1.122931

2.116076	1.12705
2.170896	1.131085
2.225717	1.135024
2.280537	1.138852
2.335357	1.142555
2.390177	1.14612
2.444998	1.149532
2.499818	1.152779
2.554638	1.155845
2.609459	1.158717
2.664279	1.161381
2.719099	1.163824
2.773919	1.166031
2.82874	1.167989
2.88356	1.169683
2.93838	1.171101
2.993201	1.172228
3.048021	1.17305
3.102841	1.173553
3.157662	1.173724
3.216348	1.173724
3.275034	1.173724
3.33372	1.173724
3.392406	1.173724
3.451092	1.173724
3.509779	1.173724
3.568465	1.173724
3.627151	1.173724
3.685837	1.173724
3.744523	1.173724
7	1.185671

9.12 SLC Input

Streamline Curvature Geometrical Input

```
**********Axial-Flow Compressor and Blade Geometry Input Data**********

NoOfBladeRows              :  2
NoOfStrlines               : 13
NoOfBladeChordLocations            : 26
NoOfBoundLayerAuxPoints            : 40
DPRotationalSpeed       : 16042.8
```

```
1st Stage Rotor(Clockwise Rotation)
---------------
BladeRowType            :  2
NoOfBlades              : 22
AirInletBlockageFactor   :  1.0000
AirOutletBlockageFactor  :  1.0000
BladeProfile            :  65s

%Chord      T/C
  0.00    0.0000
  0.50    1.5440
  0.75    1.2427
  1.25    0.9352
  2.50    0.6296
  5.00    0.4354
  7.50    0.3529
 10.00    0.3040
 15.00    0.2444
 20.00    0.2072
 25.00    0.1801
 30.00    0.1587
 35.00    0.1407
 40.00    0.1249
 45.00    0.1103
 50.00    0.0962
 55.00    0.0824
 60.00    0.0691
 65.00    0.0566
 70.00    0.0451
 75.00    0.0345
 80.00    0.0248
 85.00    0.0163
 90.00    0.0090
 95.00    0.0032
100.00    0.0000
```

RadialPosition	%Span	InRCoord	OutRCo	InZCoord	OutZCo	Pitch/Chord	Stag	InletAng	OutletAng	Tmax/C	TipRadius/Tmax
Tip 13	100.0	25.5300	24.7730	2.5780	6.6070	0.7700	-63.8600	-66.6100	-54.0600	2.9037	6.2174
12	95.0	24.8800	24.1250	2.3970	6.7670	0.7536	-61.5900	-64.5600	-53.1500	2.9301	6.1617
11	90.0	24.1780	23.4780	2.2360	6.8960	0.7270	-59.6300	-62.8300	-52.5000	3.0800	6.1070
10	80.0	22.7530	22.1840	2.0130	7.0610	0.6916	-56.9400	-60.8500	-51.6000	3.3301	6.0502
9	70.0	21.2940	20.8890	1.7980	7.2500	0.6498	-54.0100	-59.0100	-48.2500	3.8835	5.9945
8	60.0	19.8100	19.5950	1.5730	7.5000	0.6075	-50.3500	-56.8100	-43.2400	4.5666	5.9388
7	50.0	18.2910	18.3010	1.3350	7.8060	0.5643	-45.8400	-54.2700	-36.7000	5.3564	5.8831
6	40.0	16.7230	17.0060	1.0660	8.1280	0.5200	-40.4500	-51.4000	-29.0500	6.1960	5.8273
5	30.0	15.0810	15.7120	0.8050	8.5140	0.4739	-33.6500	-47.4400	-19.5300	7.0397	5.7716
4	20.0	13.3490	14.4180	0.5280	8.8370	0.4259	-25.9800	-43.7900	-7.6000	7.7873	5.7159
3	10.0	11.4930	13.1230	0.2360	9.0140	0.3841	-19.4000	-41.4000	6.3900	8.2698	5.6602
2	5.0	10.5030	12.4760	0.1100	9.0650	0.3490	-14.0200	-40.3000	13.8200	8.4674	5.6045
Hub 1	0.0	9.5830	11.8290	0.0000	9.1040	0.3211	-10.0600	-39.3500	21.3800	8.5486	5.5487

```
1st Stage Stator
----------------

BladeRowType              :  3
NoOfBlades                : 34
AirInletBlockageFactor    :  1.0000
AirOutletBlockageFactor   :  1.0000
BladeProfile              :  65s

%Chord     T/C
  0.00    0.0000
  0.50    1.5440
  0.75    1.2427
  1.25    0.9352
  2.50    0.6296
  5.00    0.4354
  7.50    0.3529
 10.00    0.3040
 15.00    0.2444
 20.00    0.2072
 25.00    0.1801
 30.00    0.1587
 35.00    0.1407
 40.00    0.1249
 45.00    0.1103
 50.00    0.0962
 55.00    0.0824
 60.00    0.0691
 65.00    0.0566
 70.00    0.0451
 75.00    0.0345
 80.00    0.0248
 85.00    0.0163
 90.00    0.0090
 95.00    0.0032
100.00    0.0000
```

RadialPosition	%Span	InRCoord	OutRCoord	InZCoord	OutZCoord	Pitch/Chord	StaggerAng	InletAng	OutletAng	Tmax/C	TipRadius/Tmax
Tip 13	100.0	24.3840	24.3840	12.6350	18.2610	0.7868	10.9700	38.8300	-16.9800	8.0324	16.3043
12	95.0	23.7860	23.7960	12.6260	18.2510	0.7675	10.9800	36.1100	-14.1000	7.9274	16.0793
11	90.0	23.2090	23.2510	12.6230	18.2440	0.7422	11.2300	34.4700	-12.0400	7.8026	15.6411
10	80.0	22.0330	22.1220	12.6360	18.2410	0.7117	12.1600	34.4000	-10.1100	7.6284	15.1030
9	70.0	20.8480	20.9830	12.6460	18.2370	0.6743	12.7500	34.8100	-9.3400	7.4346	14.4366
8	60.0	19.6590	19.8470	12.6610	18.2350	0.6369	13.4600	35.7300	-8.8600	7.2226	13.6304
7	50.0	18.4600	18.7120	12.6800	18.2350	0.5988	14.2700	37.0900	-8.6300	7.0107	12.8060
6	40.0	17.2500	17.5750	12.6990	18.2330	0.5609	15.0300	38.6500	-8.7300	6.8149	11.9066
5	30.0	16.0210	16.4320	12.7220	18.2320	0.5222	15.9000	40.5500	-8.9500	6.6006	11.1016
4	20.0	14.7770	15.2910	12.7500	18.2330	0.4833	16.7900	42.9700	-9.8600	6.3828	10.2861
3	10.0	13.5190	14.1570	12.7790	18.2390	0.4485	17.4700	46.0800	-11.6000	6.1979	9.5238
2	5.0	12.8830	13.5950	12.7940	18.2460	0.4241	17.7000	47.9400	-13.1200	6.0680	8.7143
Hub 1	0.0	12.1890	12.9310	12.8110	18.2540	0.4024	17.8400	50.0400	-15.0400	5.9592	7.9942

9.13 High Fidelity Turbomatch Input

```
////
OD SI KE CT FP
-1
-1
INTAKE  S1,2      D1,2,3,4                          R300
COMP2D  S2,3      D5,6,7,8,9,10                     R301 V5
PREMAS  S3,4,15   D12,13,14,15                           V12
COMPRE  S4,5      D16,17,18,19,20,21                R302 V16 V17
PREMAS  S5,6,17   D23,24,25,26
PREMAS  S17,18,19 D27,28,29,30
BURNER  S6,7      D31,32,33                         R303 W7,6
MIXEES  S7,19,8
TURBIN  S8,9      D34,35,36,37,38,39,40,41,302              V35
MIXEES  S9,18,10
TURBIN  S10,11    D44,45,46,47,48,49,50,51,301              V45
NOZCON  S15,16,1  D66                               R307
NOZCON  S11,12,1  D65                               R306
PERFOR  S1,0,0    D67,68,69,70,306,300,303,307,0,0,0,0,0
CODEND

DATA////
1  12192.
2  0.0
3  0.8
4  -1.0

!COMPRESSOR PACO-SLC MODEL
5  0.9
6  0.9
7  0.0
8  0.0
9  0.0
10  0.0

!PREMAS
12  0.1
13  0.0
14  1.0
15  0.0

!COMPRESSOR
16  0.75
17  1.0
18  15.
19  0.84
20  0.0
21  1.0

!PREMAS
23  0.82
24  0.0
25  1.0
```

```
26  0.0

!PREMAS
27  0.3
28  0.0
29  1.0
30  0.0
!BURNER
31  0.05
32  0.99
33 -1.0
!TURBINE
34  0.0
35  0.7
36  0.7
37  0.86
38 -1.0
39  2.0
40  1.0
41 -1.0
!TURBINE
44  0.0
45  0.7
46  0.5
47  0.89
48 -1.0
49  1.0
50  2.0
51 -1.0
!DUCTER
54  0.0
55  0.05
56  0.0
57  0.0
!MIXFUL
58  1.0
59  1.0
60  0.275
!DUCTER
61  0.0
62  0.05
63  0.0
64  0.0
!NOZCON
65 -1.0
!PERFOR
67 -1.0
68 -1.0
69  0.0
70  0.0
-1
1 2 100.
7 6 1800.0
-1
-3
```

9.14 PC-SLC Output File

```
  ___PC-SLC RESULTS___
    Averaged Results
 PrRatioTot Efficiency MassFlow NonDimMass CorrMass
   1.5998    0.8730   32.7498  0.005498   32.8201

    Circumferential Sectors
 Sector  MassFlow   PrRatioTot  Efficiency
 1     31.7000      1.6245      0.8734     33.5573
 2     33.4179      1.5840      0.8728     32.6200

    Radial Distributions
 Sector=          1
 Radial   Ptot        Ttot      Pst
  1   140048.2       328.4    121913.1
  2   142081.6       327.5    124307.7
  3   144532.2       327.8    126882.2
  4   146469.6       328.4    129124.4
  5   148125.4       329.3    131134.0
  6   149585.5       330.1    132962.8
  7   152386.4       331.0    135386.1
  8   156061.8       331.9    138205.2
  9   159226.2       332.7    140828.7
 10   161660.9       333.5    143234.2
 11   164278.0       334.5    145832.5
 12   167590.7       336.0    148843.3
 13   164519.9       334.5    149206.2
 Sector=          2
 Radial   Ptot        Ttot      Pst
  1   152145.3       337.3    127687.7
  2   153205.0       335.5    129548.6
  3   154513.4       335.0    131542.4
  4   155735.0       335.0    133439.7
  5   156907.0       335.2    135231.5
  6   157663.9       335.6    136776.9
  7   160001.1       336.0    138923.4
  8   164382.6       336.7    141911.1
  9   168046.4       337.3    144715.0
 10   170717.3       337.8    147339.4
 11   172945.5       338.3    149921.8
 12   175139.7       339.3    152556.3
 13   172180.7       337.7    153438.0
```